Investigation of Coupled Processes in Argillite Rock: FY19 Progress

Spent Fuel and Waste Disposition

Prepared for
U.S. Department of Energy
Spent Fuel and Waste Science and Technology

Jonny Rutqvist, Yves Guglielmi, Kunwhi Kim, Hao Xu, Hang Deng, Pei Li, Mengsu Hu, Carl Steefel, Ben Gilbert, Antonio Rinaldi, Peter Nico, Sharon Borglin, Patricia Fox, Jens Birkholzer

Lawrence Berkeley National Laboratory

May 17, 2019
LBNL-2001202
SFWD Working Document: External Release

This page is intentionally left blank.

Revision 0
02/14/2019

APPENDIX E

NTRD DOCUMENT COVER SHEET [1]

Name/Title of Deliverable/Milestone/Revision No.	Investigation of Coupled Processes in Argillite Rock: FY19 Progress M3SF-19LB010301031
Work Package Title and Number	Argillite Disposal R&D – LBNL/Argillite International Collaboration – LBNL
Work Package WBS Number	SF-19LB01030103 /SF-19LB01030107
Responsible Work Package Manager	Jonny Rutqvist (signature on file)
	(Name/Signature)

Date Submitted **5/17/2019**

Quality Rigor Level for Deliverable/Milestone[2]	☐ QRL-1 Nuclear Data	☐ QRL-2	☐ QRL-3	☒ QRL 4 Lab-specific [3]

This deliverable was prepared in accordance with Lawrence Berkeley National Laboratory (LBNL)
(Participant/National Laboratory Name)

QA program which meets the requirements of
☒ DOE Order 414.1 ☐ NQA-1 ☐ Other

This Deliverable was subjected to:

☐ Technical Review	☐ Peer Review
Technical Review (TR)	**Peer Review (PR)**
Review Documentation Provided	**Review Documentation Provided**
☐ Signed TR Report or,	☐ Signed PR Report or,
☐ Signed TR Concurrence Sheet or,	☐ Signed PR Concurrence Sheet or,
☒ Signature of TR Reviewer(s) below	☐ Signature of PR Reviewer(s) below
Name and Signature of Reviewers	**Name and Signature of Reviewers**
Pierre Jeanne: Sections 2, 3, 4, 5, 6, 8, 9	Liange Zheng: Sections 1, 7, 10, 11, 12, 13
(Signature on file)	(Signature on file)
Boris Faybishenko: All Sections	
(Signature on file)	

NOTE 1: *Appendix E should be filled out and submitted with each deliverable. Or, if the PICS:NE system permits, completely enter all applicable information in the PICS:NE Deliverable Form. The requirement is to ensure that all applicable information is entered either in the PICS:NE system or by using the FCT Document Cover Sheet.*

- *In some cases there may be a milestone where an item is being fabricated, maintenance is being performed on a facility, or a document is being issued through a formal document control process where it specifically calls out a formal review of the document. In these cases, documentation (e.g., inspection report, maintenance request, work planning package documentation or the documented review of the issued document through the document control process) of the completion of the activity, along with the Document Cover Sheet, is sufficient to demonstrate achieving the milestone.*

NOTE 2: *If QRL 1, 2, or 3 is not assigned, then the QRL 4 box must be checked, and the work is understood to be performed using laboratory specific QA requirements. This includes any deliverable developed in conformance with the respective National Laboratory / Participant, DOE or NNSA-approved QA Program*

NOTE 3: *If the lab has an NQA-1 program and the work to be conducted requires an NQA-1 program, then the QRL-1 box must be checked in the work Package and on the Appendix E cover sheet and the work must be performed in accordance with the Lab's NQA-1 program. The QRL-4 box should not be checked*

TABLE OF CONTENTS

LIST OF FIGURES

LIST OF TABLES

ACRONYMS

ALC	Micro-tunnel experiment at Bure
ANDRA	French National Radioactive Waste Management Agency
BBM	Barcelona Basic Model
BExM	Barcelona Expansive Clay Model
BGR	Bundesanstalt für Geowissenschaften und Rohstoffe
BGS	British Geological Survey
CDM	Continuum Damage Mechanics
CFD	Computed Fluid Dynamics
CIEMAT	Centro De Investigaciones Energéticas, Medio Ambientales Y Tecnológicas
COx	Callovo-Oxfordian Claystone
DECOVALEX	DEvelopment of COupled Models and their VAlidation against EXperiments
DFN	Discrete fracture network
DOE	Department of Energy
DRZ	Disturbed rock zone
DSID	Deviatoric Stress Induced Damage
EBS	Engineered barrier system
EDZ	Excavation damaged zone
EOS	Equation of State
FBG	Fiber Bragg gratings
FE	Full-scale emplacement
FEPs	Features, Events, and Processes
FLAC	Fast Lagrangian analysis of continua
FOP	Fault Opening Pressure
FY	Fiscal year
GDSA	Generic Disposal Systems Analysis
H1	Heater #1
H2	Heater #2
H3	Heater #3
HLW	High-Level Waste
HM	Hydro-mechanical
IRSN	Institut de Radioprotection et de Sûreté Nucléaire

KAERI	Korea Atomic Energy Research Institute
KBS	Kärnbränslesäkerhet/Nuclear Fuel Safety
LASGIT	Large Scale Gas Injection Test
LBM	Lattice Boltzmann method
LBNL	Lawrence Berkeley National Laboratory
MHM	Meuse/Haute-Marne
MULES	Multidimensional universal limiter with explicit solution
NAGRA	National Cooperative for the Disposal of Radioactive Waste, Switzerland
NMM	Numerical manifold method
NWMO	Canada - The Nuclear Waste Management Organization
OpenFOAM	Open Field Operation and Manipulation
PA	Performance assessment
R&D	Research & Development
RBSN	Rigid-Body-Spring Network
REV	Representative Elementary Volume
RWM	Radioactive Waste Management Limited
SFWST	Spent Fuel and Waste Science and Technology
SIMFIP	Step-Rate Injection Method for Fracture In-situ Properties
STP	Standard temperature and pressure
SURF	Sanford Underground Research Facility
TED	Thermal Borehole Experiment at Bure
TH	Thermal-hydrological
THC	Thermo-hydro-chemical
THM	Thermo-hydro-mechanical
THMC	Thermal-hydrological-mechanical-chemical
TOUGH	Transport of Unsaturated Groundwater and Heat
TPHM	Two-part Hooke's model
TSX	Tunnel Sealing Experiment
UFD	Used Fuel Disposition
UFDC	Used Fuel Disposition Campaign
UFZ	Helmholtz-Centre for Environmental Research
UPC	Universitat Politècnica de Catalunya
URLs	Underground Research Laboratory
VOF	Volume of fluid

This page is intentionally left blank.

1. INTRODUCTION

Shale and argillite geological formations have been considered as potential host rocks for geological disposal of high-level radioactive waste (HLW) throughout the world because of their low permeability, low diffusion coefficient, high retention capacity for radionuclides, and capability to self-seal fractures. Low permeability of clay and shale rock is well-known in the hydrogeology community, because these rocks are usually serve as aquitards that severely limit groundwater movement, and in petroleum industry, because they act as caprocks limiting the rise of buoyant petroleum fluids. While fractures can occur in argillite and shale, these formations often demonstrate the tendency to self-seal fractures, reducing the effects of fractures on bulk permeability. Other favorable characteristics of argillite/shale are the strong sorptive behavior for many radionuclides, reducing conditions because of the lack of oxygen transport from the surface, and chemical buffering the effects of materials introduced during repository construction, operation, and emplaced materials.

The focus of research within the Spent Fuel and Waste Science and Technology (SFWST), formerly called Used Fuel Disposal (UFD), Campaign is on repository-induced interactions that may affect the key safety characteristics of engineered barrier system (EBS) bentonite and host rock. These include thermal-hydrological-mechanical-chemical (THMC) processes that occur because of repository construction and waste emplacement. Some of the key questions addressed in this report include the formation of an excavation damaged zone (EDZ) near tunnels and the evolution of near field coupled thermo-hydro-mechanical (THM) processes after the waste emplacement. In particular, this report describes our efforts to model these processes with confidence.

Within the SFWST program, LBNL's work on argillite disposal research & development (R&D) started in 2010 by leveraging on previous experience on coupled THM processes modeling within domestic and international nuclear waste programs (Rutqvist et al., 2001; 2002; 2011). Much of this work has been dedicated to the development and validation of coupled THM simulators for modeling of near-field coupled processes. From a safety assessment perspective, near-field coupled processes are relatively short-lived,,but could give rise to permanent changes, such as the formation of a thermally altered or a damaged zone around excavations, and which could provide a pathway for transport of radionuclides if released from a waste package (Figure 1-1). For a repository hosted in clay-rock, the mechanical evolution and swelling of the protective buffer surrounding the waste package (often bentonite) are imperative to its functions, such as to provide long-term mechanical support to seal the EDZ. At the same time, the mechanical evolution of the buffer is governed by complex coupled interactions of temperature and hydraulics, micro and macro structures of clay, as well as the host rock. Currently, more advanced constitutive mechanical models are being applied, but those require a large number of input parameters for describing processes at the different structural levels. It is therefore important to test and validate the models at a relevant field scale, in addition to verification and validation against independent analytical and numerical solutions and well-controlled laboratory experiments.

Coupled THM processes can also occur at the repository scale as shown in Figure 1-2. This could include activation of faults or fractures, or potential creation of new fractures due to thermal stress and so-called thermal pressurization, which is a process of pressure increase by thermal expansion of pore-fluids that are trapped by low permeability in a porous argillite host rock. Another potential source of near field coupled THM processes is gas generation within the waste package as well as seismic motion from a distant earthquake. The potential implication for repository performance related to the activation of faults includes creation of (permeable) flow paths, induced seismicity and potential shear load on a waste canister.

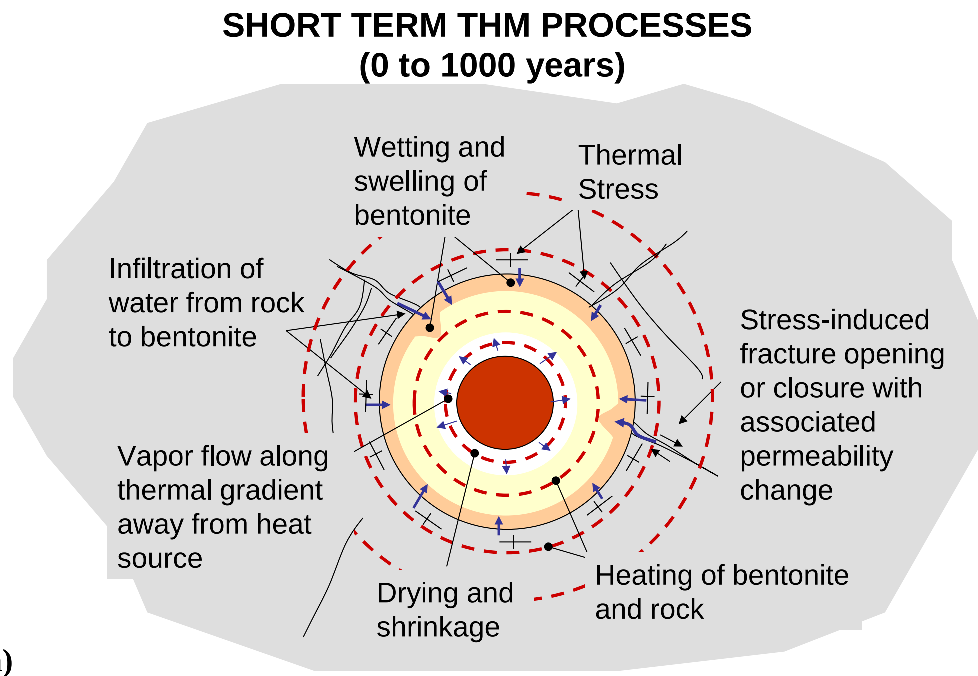

(a)

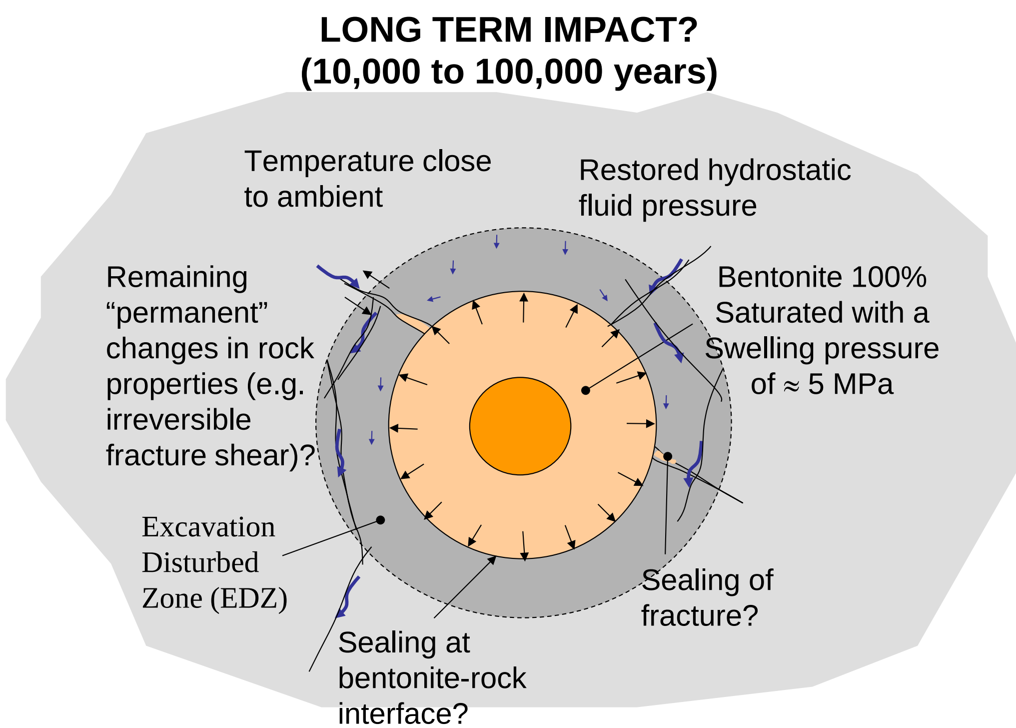

(b)

Figure 1-1. Schematic illustration of coupled THM processes driven by heat released from the waste package: (a) short-term THM processes, and (b) long-term impact of early time coupled THM processes.

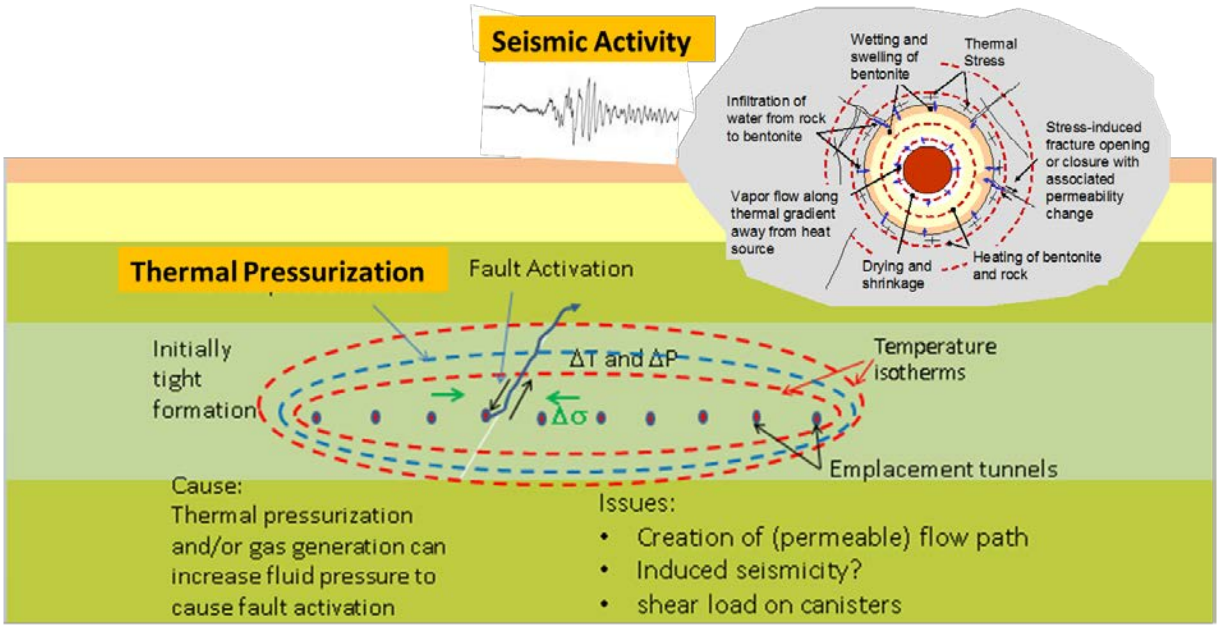

Figure 1-2. Schematic of coupled THM responses in a repository in the near field (upper right) and at the repository scale caused by heating, thermal pressurization and potential gas generation.

LBNL is developing two complementary coupled simulation approaches to model THM processes (Figure 1-3). TOUGH-FLAC, based on linking LBNL's TOUGH2 multiphase fluid flow simulator with the FLAC3D geomechanics code, provides an efficient continuum modeling approach with state-of-the-art constitutive models for bentonite and host rock (Rutqvist et al., 2002; Rutqvist 2011; 2017). The complementary TOUGH-RBSN simulator, based on linking the TOUGH2 simulator with the Rigid-Body-Spring Network (RBSN) model, enables explicit modeling of discrete fractures and fracturing (Asahina et al. 2014; Kim et al., 2017). The TOUGH-RBSN is most suitable for detailed analysis of fracturing in laboratory samples as well as within the EDZ, whereas TOUGH-FLAC enables modeling of the evolution of the EBS, EDZ and surrounding host rock at a larger scale (Figure 1-2). TOUGH-FLAC with appropriated constitutive models is also used to calculate the evolution of permeability and transport properties in the EDZ, which can then be used as input to future safety assessment models and Geologic Disposal Safety Analysis (GDSA).

In addition, work is ongoing for the development of modeling related to fault activation. This includes for example, capabilities for modeling of fault slip, induced seismicity and associated changes in fault permeability. Figure 1-4 presents one such model, involving the TOUGH-FLAC simulator, with discrete representation of a fault plane, a slip weakening fault rupture model, and with the potential for modeling seismic wave propagation as available in the FLAC3D code. This model can also be applied for modeling of activation and creation of new flow paths as a result over pressure by gas generation or thermal pressurization, as illustrated in Figure 1-2.

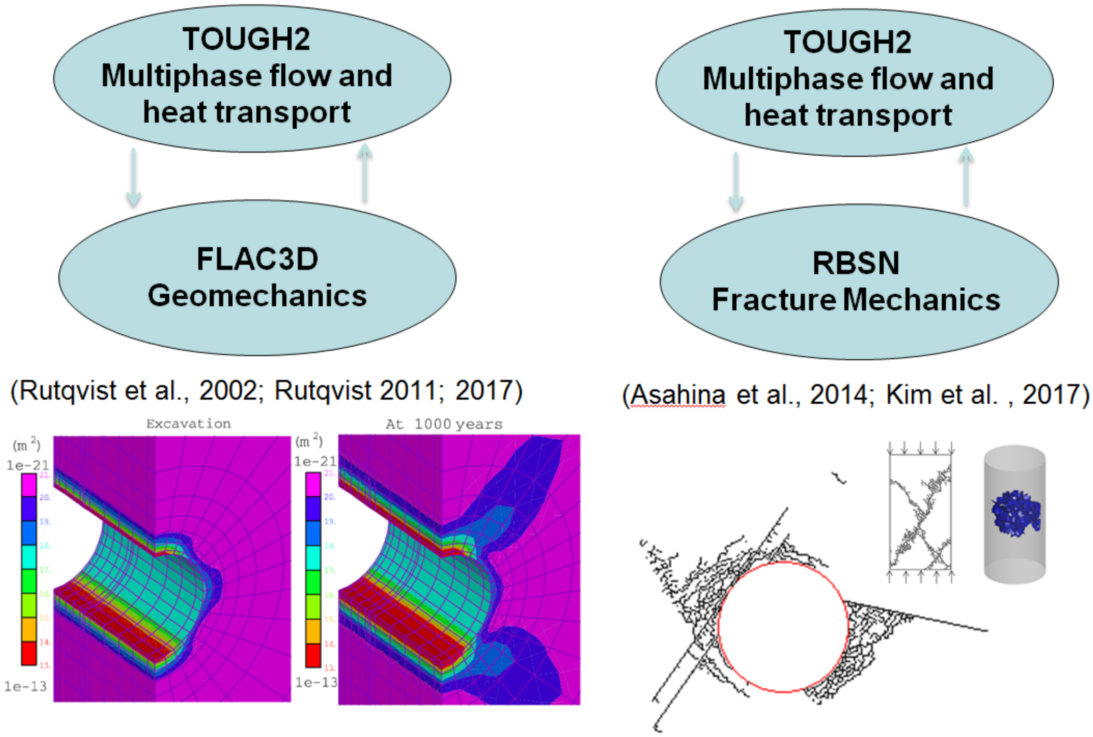

Figure 1-3. TOUGH-FLAC (left) and TOUGH-RBSN (right) models developed for coupled THM process analysis.

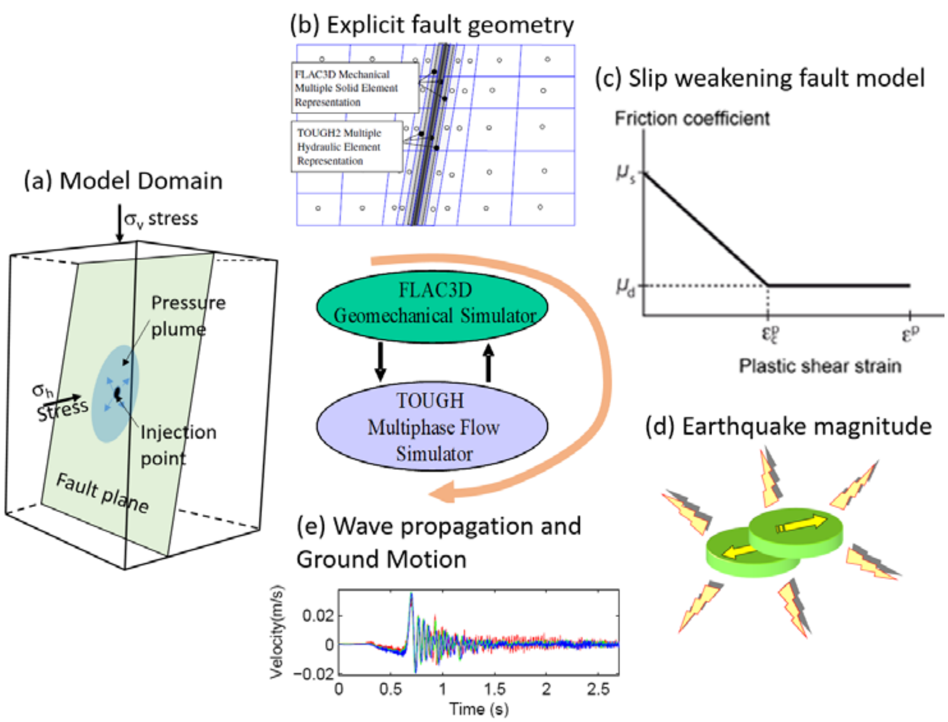

Figure 1-4. Fault activation modeling approach using TOUGH-FLAC (Rutqvist and Rinaldi, 2019).

In this report, we present our FY2019 progress to date and plans for the rest of FY2019 on these activities. The document delivers milestone M3SF-19LB010301031 “Investigation of Coupled Processes in Argillite Rock” in the LBNL Argillite R&D Work Package (SF-19LB01030103) with input from Activity SF-19LB010301071 “LBNL FY19 Argillite International Collaboration” in the LBNL Argillite International Collaboration Work Package (SF-19LB01030107). These activities address key Features, Events, and Processes (FEPs), which have been ranked in importance from medium to high, as listed in Table 7 of the Used Fuel Disposition Campaign Disposal Research and Development Roadmap (FCR&D-USED-2011-000065 REV 1) (Nutt, 2012). Specifically, they address FEP 2.2.01, Excavation Disturbed Zone, for clay/shale, by investigating how coupled processes affect EDZ evolution; FEP 2.2.05, Flow and Transport Pathways; and FEP 2.2.08, Hydrologic Processes, and FEP 2.2.07, Mechanical Processes, as well as FEP 2.2.12, Gas Sources and Effects.

The activities documented in this report also address a number of research topics identified in Research & Development (R&D) Plan for Used Fuel Disposition Campaign (UFDC) Natural System Evaluation and Tool Development (Wang 2011), including Topics S3, Disposal System Modeling – Natural System; P1, Development of Discrete Fracture Network (DFN) Model; P14, Technical Basis for Thermal Loading Limits; and P15, Modeling of Disturbed Rock Zone (DRZ) Evolution (Clay Repository).

In Sections 2 and 3 of this report, we present the current status of the TOUGH-FLAC and TOUGH-RBSN simulators for modeling coupled THM processes in argillite, including fracturing. In Sections 4 and 5, we present the results of the validation of the TOUGH-FLAC model against *in situ* heater experiments at the Mont Terri Underground Research Laboratory (URL) in Switzerland and at the URL in Bure, France. The heater experiments modeled are the Mont Terri FE (Full-scale Emplacement) Experiment, conducted as part of the Mont Terri Project, and the TED and ALC experiments conducted in Callovo-Oxfordian claystone (COx) at the Meuse/Haute-Marne (MHM) URL in Bure, France. Modeling of the TED and ALC heater experiments is conducted as part of a modeling task (Task E) of the international DECOVALEX-2019 project. DECOVALEX, which stands for DEvelopment of COupled Models and their VALidation against EXperiments, is an international collaborative activity, in which DOE and LBNL gain access to unique laboratory and field data defined as modeling test cases. DECOVALEX tasks are studied collectively among several international groups to better understand the processes and to improve numerical models, which could eventually be applied in the performance assessment for nuclear waste disposal in clay host rocks and bentonite backfill. Section 6 presents LBNL’s activities focused on modeling gas migration in bentonite related to Task A of the international DECOVALEX project. Section 7 describes pore-scale modeling of gas bubble migration. Sections 8 through 10 present the results of fundamental research on fracture and fault behavior, at a larger scale (Sections 8 and 9) related to field-scale fault slip experiments at Mont Terri, and at the micro-scale in a new research task (Section 10). Section 11 presents another new research task on coupled microbial-abiotic processes in EBS and host rock materials. Finally, in Section 12, we present thoughts on the integration of coupled THM processes models into the Geologic Disposal Safety Assessment (GDSA) and Performance Assessment (PA). Section 13 provides a summary of the progress and plans for the rest of FY2019.

This page is intentionally left blank.

2. STATUS OF TOUGH-FLAC SIMULATOR

The TOUGH-FLAC simulator (Rutqvist et al., 2002; Rutqvist, 2011), used within the SFWST Argillite R&D work package, has been adapted for modeling coupled THM processes associated with bentonite backfilled repositories in argillite host rocks. For rigorous modeling of the THM behavior of bentonite-based (swelling) buffer and back-fill materials, the BBM (Barcelona Basic Model) and BExM (Barcelona Expansive Model) have been implemented into TOUGH-FLAC (Rutqvist et al., 2011; 2014b; Vilarrasa et al., 2016). Constitutive models to describe anisotropic THM behavior of shale rock have also been adapted. This model development has been accompanied by extensive testing, verification and validation, including participation within international collaborative projects such as DECOVALEX. In the following subsections, we present more details on the status of the TOUGH-FLAC, including the status of the numerical framework for coupled THM modeling and geomechanical constitutive models, followed by a list of completed verification and validation examples, as well as new verifications against analytical solutions.

2.1 TOUGH-FLAC Framework

As mentioned in the introduction, the TOUGH-FLAC simulator (Rutqvist 2011; 2017) is based on linking the TOUGH2 multiphase flow and heat transport simulator (Pruess et al., 2012) with the FLAC3D geomechanical simulator (Itasca 2011). In this approach, TOUGH2 (Pruess et al., 2012) is used for solving multiphase flow and heat transport equations, whereas FLAC3D (Itasca, 2011) is used for solving geomechanical stress-strain equations.

For analysis of coupled THM problems, TOUGH2 and FLAC3D are executed on compatible numerical grids and linked through a coupled THM model (Figure 2-1) with coupling functions to pass relevant information between the field equations, which are solved in the respective codes. In the coupling scheme between TOUGH2 and FLAC3D, the TOUGH2 multiphase pressures, saturation, and temperature are provided to update temperature, and pore pressure to FLAC3D (Figure 2-1). After data transfer, FLAC3D internally calculates thermal expansion, swelling, and effective stress. Conversely, element stress or deformation from FLAC3D is supplied to TOUGH2 to correct element porosity, permeability, and capillary pressure for the fluid-flow simulation in TOUGH2. The corrections of hydraulic properties are based on material-specific functions.

In a TOUGH-FLAC simulation, the calculation is stepped forward in time with the transient multiphase fluid flow analysis in TOUGH2, and at each time step or at the TOUGH2 Newton iteration level, a quasi-static mechanical analysis is conducted with FLAC3D to calculate stress-induced changes in porosity and intrinsic permeability (Figure 2-2). In this scheme, the fluid-flow sequence is solved first under fixed stress with a porosity correction $\Delta\Phi_c$ derived from the constitutive equations of solid:

$$\mathrm{d}\Phi = \left(\frac{b^2}{K} + \frac{b-\phi}{K_s}\right)\mathrm{d}p + \phi\alpha_s\mathrm{d}T - \Delta\Phi_c \tag{2.1}$$

$$\Delta\Phi_c = -\frac{b}{K}\mathrm{d}\sigma_v = -\frac{b}{K}(K\mathrm{d}\epsilon_v - b\mathrm{d}p - K\alpha\mathrm{d}T) \tag{2.2}$$

where K is the bulk modulus of porous medium, K_s is the bulk modulus of solid skeleton, b is the Biot's coefficient, p is the pore pressure, ϕ is the porosity, α_s is the volumetric thermal expansion coefficient of solid grains, T is the absolute temperature, σ_v is the mean stress, and ϵ_v is the volumetric strain. The resulting pressure and temperature are prescribed in the mechanical sequence. This corresponds to so-called stress-fixed iterations in the sequential scheme, in which the solution becomes unconditionally stable. The resulting THM analysis may be explicit sequential, meaning that the porosity and permeability is evaluated only at the beginning of each time step, or the analysis may be implicit sequential, with permeability and porosity updated on the Newton iteration level toward the end of the time step using an iterative process.

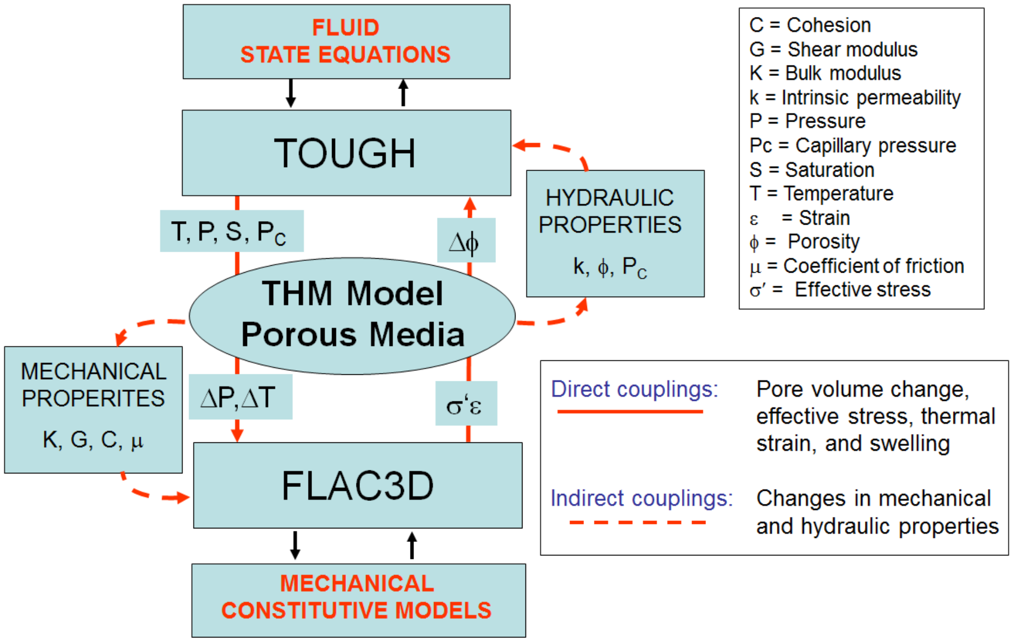

Figure 2-1. Schematic of linking of TOUGH2 and FLAC3D in a coupled TOUGH-FLAC simulation.

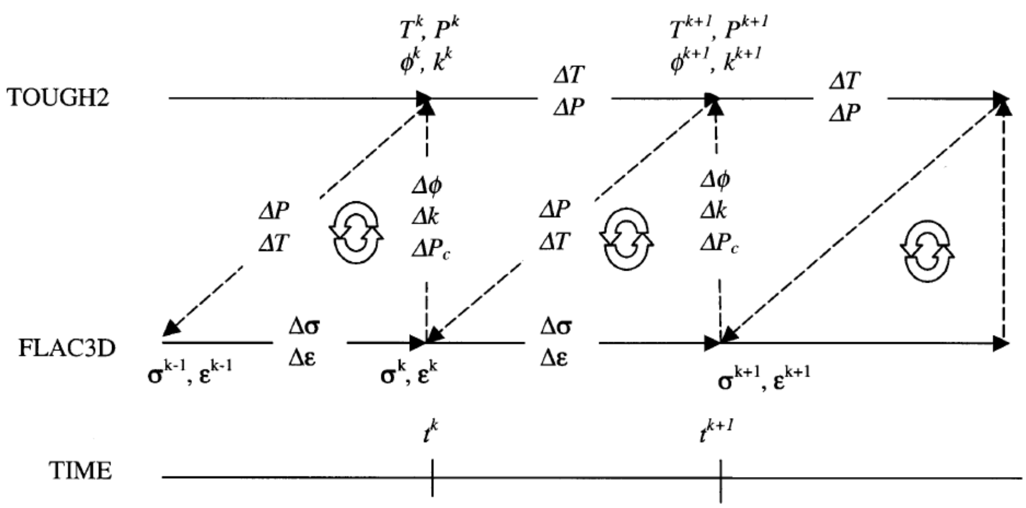

Figure 2-2. Schematic of a numerical procedure of linked TOUGH2 and FLAC3D simulations, with subscript *k* signifying time step.

2.2 Bentonite Constitutive THM Models in TOUGH-FLAC

Since 2010, the TOUGH-FLAC simulator has been adapted and applied to modeling issues related to nuclear waste disposal with bentonite backfilled tunnels (Rutqvist et al., 2011; 2014b). This includes implementation of the BBM (Alonso et al., 1990) for the mechanical behavior of unsaturated soils, which has been applied for modeling of bentonite backfill behavior (Rutqvist et al., 2011). The model can describe many typical features of unsaturated soil mechanical behavior, including wetting-induced swelling or collapse strains, depending on the magnitude of applied stress, as well as the increase in shear strength and apparent preconsolidation stress with suction (Gens et al., 2006). Figure 2-3 presents the yield surface of the BBM model in *q-p-s* space. The shaded surface corresponds to the elastic region at fully water-saturated conditions. The figure also shows how the yield surface expands at unsaturated and dryer conditions when suction increases. There is an increase in both the apparent pre-consolidation pressure along the load collapse (LC) yield surface and by the increasing tensile strength, which in turn leads to an increased cohesion and shear strength.

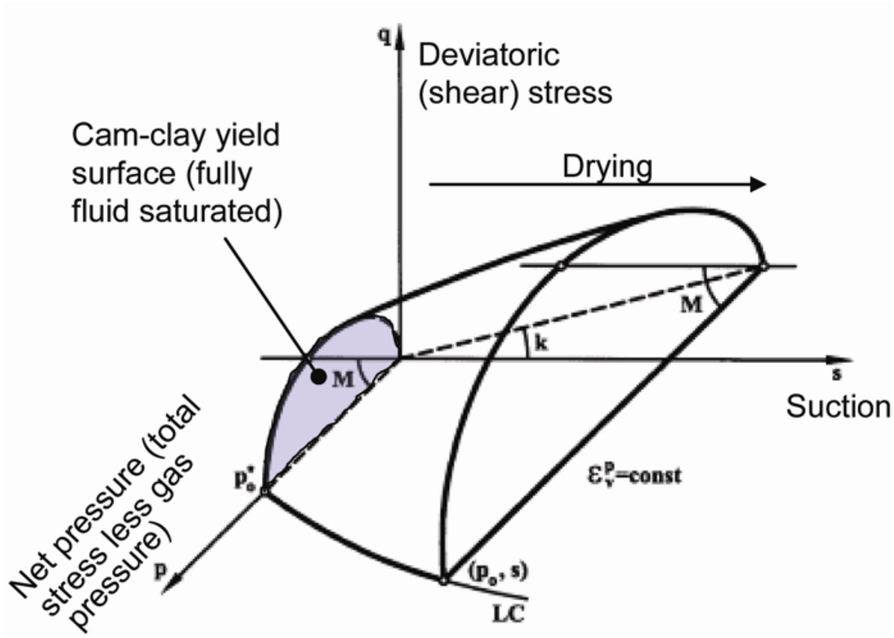

Figure 2-3. BBM constitutive model showing the yield surface in q-p-s space.

The BBM has been used for modeling bentonite-buffer behavior in various national nuclear waste programs in Europe and Japan. For example, the BBM was successfully applied to model the coupled THM behavior of unsaturated bentonite clay associated with the full-scale engineered barrier experiment (FEBEX) *in situ* heater test at the Grimsel Test Site, Switzerland (Gens et al., 2009). The BBM has also been applied to other types of bentonite-sand mixtures based on MX-80, considered as an option for an isolating buffer in the Swedish KBS-3 repository concept (Kristensson and Åkesson 2008). As part of the Used Fuel Disposition (UFD) program, Rutqvist et al. (2014b) used the BBM for modeling of coupled THM processes around a generic repository in a clay host formation. In the last few years, as part of the UFD and current SFWST program, the BBM has been extended to a dual-structure model, corresponding to the Barcelona Expansive Model (BExM). In a dual-structure model, the material consists of two structural levels: a microstructure, in which the interactions occur at the particle level, and a macrostructure that accounts for the overall fabric arrangement of the material comprising aggregates and macropores (Figure 2-4) (Gens et al., 2006, Sánchez et al., 2005, Gens and Alonso 1992). A dual-structure model has important features for modeling the mechanical behavior of a bentonite buffer, such as irreversible strain during suction cycles. Moreover, a dual-structure model provides the necessary link between chemistry and mechanics, enabling us to develop a coupled THMC model for the analysis of long-term EBS behavior. This approach enables mechanistic modeling of processes important for long-term buffer stability, including effects of pore-water salinity on swelling (loss of swelling), conversion of smectite to nonexpansive mineral forms (loss of swelling), and swelling pressure versus exchangeable cations. Details of the development, testing and applications of the dual-structure model, were first presented in the FY2014 UFD milestone report titled "Investigation of Coupled THMC Processes and Reactive Transport: FY14 Progress" (Rutqvist et al. 2014a), and have also been published in a journal paper (Vilarrasa et al., 2016).

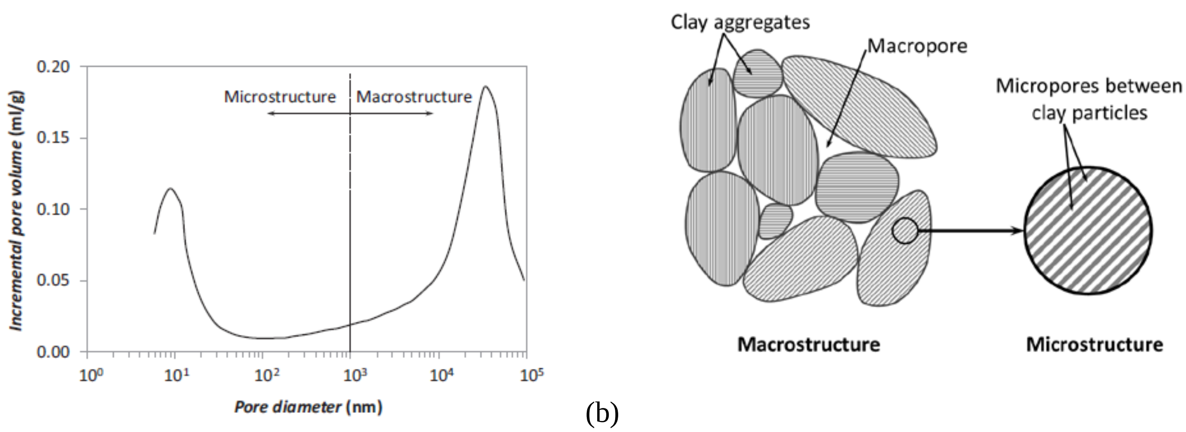

Figure 2-4. (a) Pore size distribution, and (b) schematic representation of the two structural levels considered in the dual structure model. Clay particles are represented by the gray lines (Vilarrasa et al., 2016).

The model implementation of BExM was further tested and validated as documented in the FY2016 milestone report titled "DR Argillite Disposal R&D at LBNL" (Zheng et al., 2016) by modeling (1) one swelling pressure test on Boom clay pellets, (2) two cyclic wetting-drying tests on one type of expansive clay, and (3) two tests with combination of loading paths on compacted bentonite samples. Based on the simulation results, the model is capable to reproduce the observed behavior of expansive clays during experiments associated with suction changes. The computation results we obtained with BExM agree well with the experiment data, and also follow the same tendency of results presented by BExM developers (Zheng et al., 2016). However, considerable uncertainties still exists in the use of the BExM model, because of complexities in the underlying processes and the large number of parameters needed to define the constitutive dual-structure behavior of clays.

2.3 Shale Constitutive THM Models in TOUGH-FLAC

Constitutive models of coupled THM processes in Argillite have been developed based on the results of modeling of a number of *in situ* experiments at Mont Terri and Bure underground research laboratories (URL's), considering anisotropic properties of clay and shale elasticity, strength, thermal conductivity, permeability, and thermal expansion.

The FLAC3D ubiquitous joint model can handle anisotropic strength properties of shale, and this model has been commonly used for geomechanical modeling of Opalinus Clay at Mont Terri (Corkum and Martin, 2007). The theory and implementation of this model in FLAC3D is described in the FLAC3D manual (Itasca, 2011). The model accounts for an orientation of weakness (weak plane) in a Mohr-Coulomb constitutive model. The criterion for failure on the plane of a given orientation is based on the escalation of a composite Mohr-Coulomb envelope with the tension cutoff. The rock-strength input parameters include the friction angle and the tension cutoff with weaker properties for the weak (joint) planes compared to that of the intermediate intact rock. Figure 2-5 shows the results of a simulation involving a horizontal emplacement tunnel in Opalinus Clay with the horizontal bedding (Rutqvist et al., 2014b). On top and bottom of the emplacement tunnel we can see a shear failure that occurred along bedding planes, whereas the volumetric strain in the isotropic matrix rock is uniformly distributed around the tunnel.

The results of modeling of heater experiments at Mont Terri and Bure showed the need to take into account anisotropic thermal conductivity to match temperature measurements observed at the experiments (Garitte et al., 2017). Anisotropic thermal conductivity is not standard in TOUGH2 and TOUGH-FLAC and was implemented into the TOUGH2 source code. Anisotropic permeability can be considered in the standard TOUGH2 code for rectilinear grid.

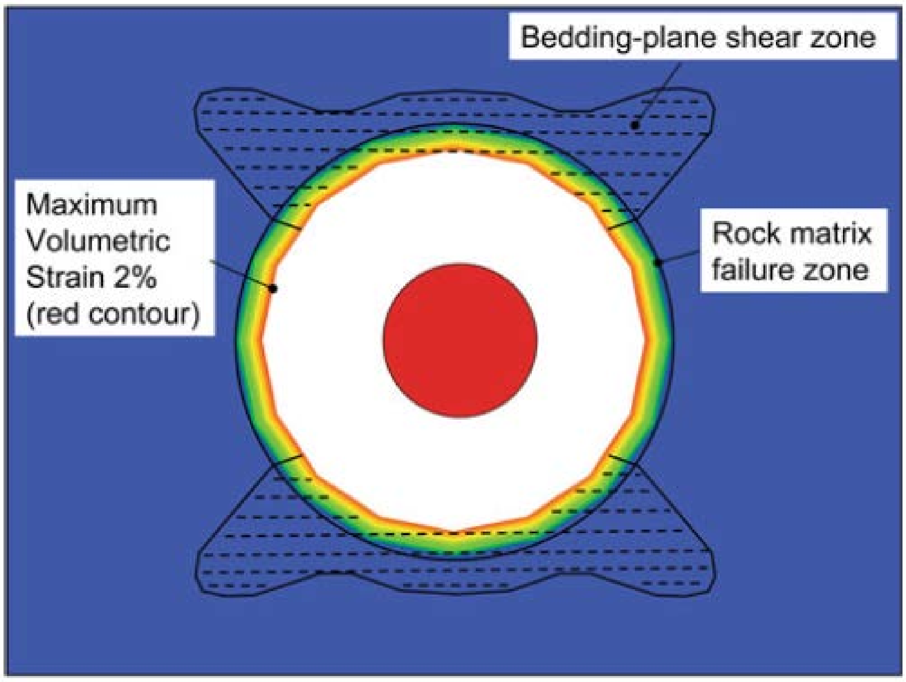

Figure 2-5. Volumetric strain contour and extent of failure zones related to horizontal bedding planes and rock matrix (Rutqvist et al., 2014b).

2.4 EDZ Models in TOUGH-FLAC

The EDZ is one of the most important features taken into account in the performance assessment of repositories in argillite, and was assigned the highest research priority ranking in the 2011 UFD Road Map (Nutt, 2012). Models of different sophistications have been developed and applied to model the EDZ using TOUGH-FLAC, including

1) Empirical stress-permeability model;

2) Non-linear elastic and brittle failure model; and

3) Anisotropic continuum damage model.

The three models are summarized in the following subsections.

2.4.1 Empirical stress-permeability model

An empirical stress-permeability model calibrated against *in situ* EDZ data is described in Rutqvist (2015). The empirical EDZ model was applied in a previous phase of the DECOVALEX project related to nuclear waste disposal in crystalline rock (Rutqvist et al., 2009). The empirical EDZ model was calibrated against EDZ data from the Tunnel Sealing Experiment (TSX) experiment conducted at the underground research laboratory in Manitoba, Canada (Martino et al., 2004).

The permeability around the tunnel was simulated using the empirical stress-permeability relationship in which permeability is a function of the effective mean stress, σ'_m, and deviatoric stress, σ_d, according to (Rutqvist et al., 2009):

$$k = [k_r + \Delta k_{\max} \exp(\beta_1 \sigma'_m)] \cdot \exp(\gamma \Delta \sigma_d) \tag{2.3}$$

where k_r is residual (or irreducible) permeability at high compressive mean stress, Δk_{max}, β_1 and γ are fitting constants, and $\Delta\sigma_d$ is the change in deviatoric stress relative to a critical deviatoric stress for onset of shear-induced permeability.

Figure 2-6 compares simulated and measured permeability changes for β_1 = 4×10^{-7} Pa^{-1}, k_r = 2×10^{-21} m^2, Δk_{max} = 8×10^{-17} m^2, γ = 3×10^{-7} Pa^{-1}, and with the critical deviatoric stress for onset of shear-induced permeability set to 55 MPa.

The 55 MPa critical deviatoric stress roughly coincides with the extent of a cluster of microseismic events at the top of the tunnel and is also about a factor of 0.3 of the instantaneous uniaxial compressive stress of small-scale core samples, which is consistent with the stress level at which crack initiation was observed in studies of Lac du Bonnet granitic samples (Martin and Chandler, 1994). Thus, it is an example taken from a crystalline rock site, whereas such calibration could also be made using in situ data from an Argillite rock site, such as Mont Terri.

A model prediction for the longer term EDZ evolution of a nuclear waste emplacement tunnel was conducted based on the relationship calibrated against field measurements of EDZ during excavation (Ngyuen et al., 2009). Figure 2-7 presents the EDZ permeability distribution after excavation and at 1000 years after emplacement when the thermal-mechanical stress might be the highest. Figure 2-7 shows that there is some increase in EDZ permeability at 1000 years compared to that after excavation, though the changes are small.

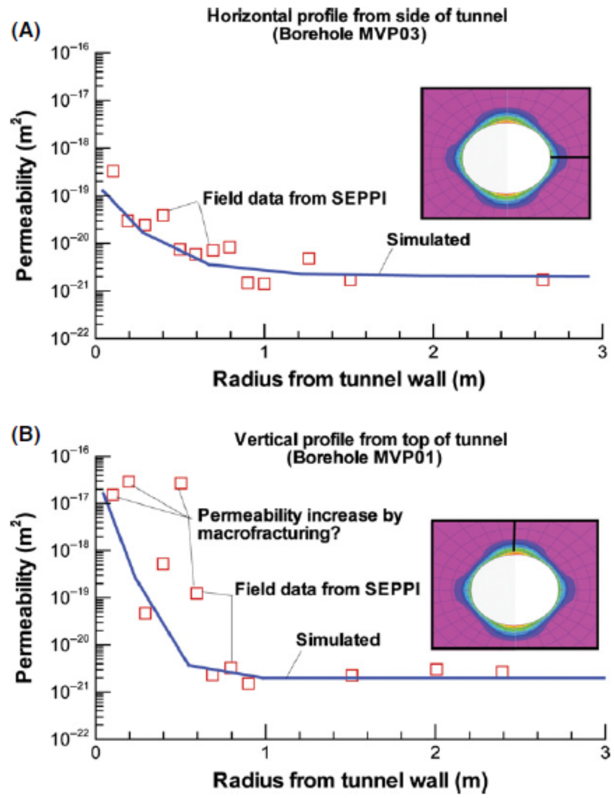

Figure 2-6. Simulated and measured permeability changes around the TSX tunnel (Rutqvist et al. 2009). Permeability versus radius: (A) along a horizontal profile from the side of the tunnel, and (B) a vertical profile from the top of the tunnel.

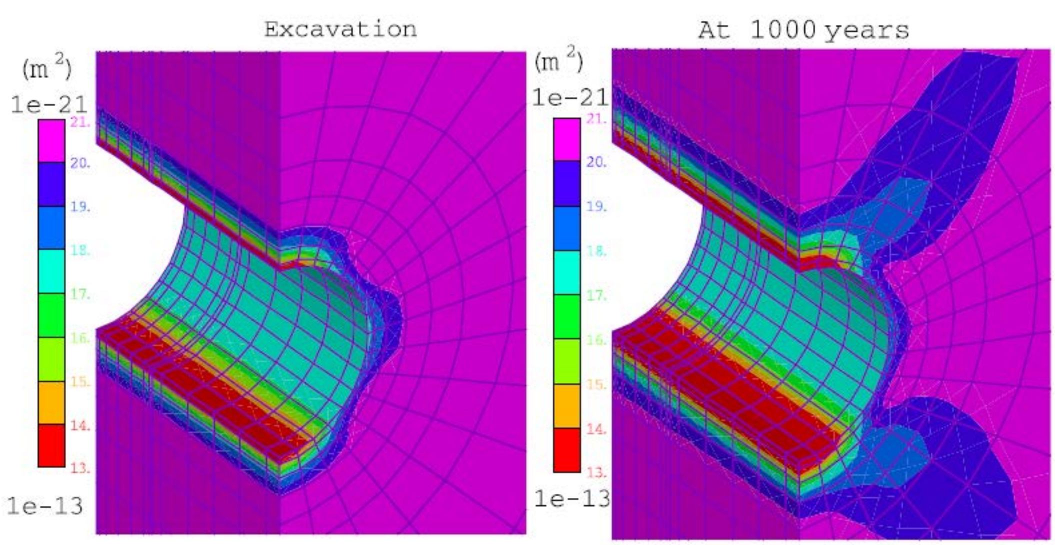

Figure 2-7. Calculated permeability distribution for generic repository emplacement tunnel in crystalline rocks using the empirical stress-permeability relation (Nguyen et al., 2009).

2.4.2 Non-linear elastic and brittle failure model

A non-linear elastic and brittle failure model was implemented in TOUGH-FLAC and demonstrated in the FY2012 Milestone Report titled "Report on Modeling Coupled Processes in the Near Field of a Clay Repository" (Liu et al., 2012). The non-linear elastic model, denoted the two-part Hooke's model (TPHM), provided a new constitutive relationship and associated formulations regarding rock hydraulic/mechanical properties. The usefulness and validity of the TPHM were demonstrated by the consistency between simulation results and field observations at the Mont Terri URL. The brittle failure model was applied using a fine-grid numerical approach, based on the explicit incorporation of small-scale heterogeneity of mechanical properties. Using the combination of the TPHM and the fine-grid numerical approach of the results of investigations were compared with field results at Mont Terri.

Figure 2-8 shows an example of calculated brittle failure and permeability changes around a tunnel in a host rock representing Opalinus Clay. The model simulation captured both the observed displacements and the size of the damage zone. Moreover, the fine-grid numerical approach, together with an explicit incorporation of the small-scale heterogeneity of mechanical properties, was able to capture the overall behavior of the EDZ, as demonstrated by the consistency between the simulated and the observed EDZ size, which was about 1 m on the side of the tunnel. The calculated permeability values are especially high in the EDZ within the tunnel sidewalls, varying between 2.39×10^{-14} m^2 and 7.45×10^{-13} m^2, which are consistent with measured data from pneumatic borehole injection tests at the Mont Terri Laborator (Bossart et al., 2002; Bossart et al., 2004). Such a model validated against field data could also be used to calculate EDZ evolution over the longer term. However, while the current model addresses permeability changes induced during excavation, it does not address sealing and healing processes that might be important over the long term.

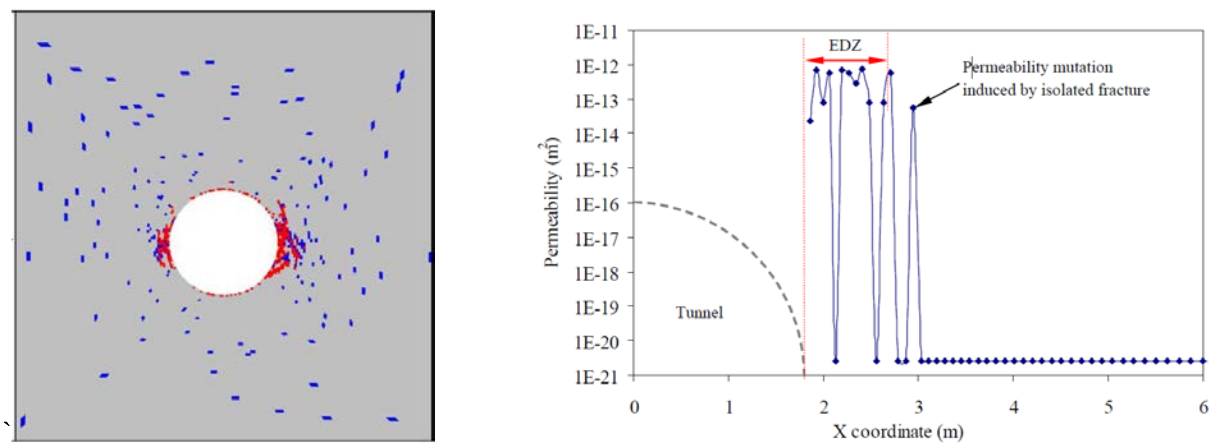

(a) (b)

Figure 2-8. (a) Calculated brittle failure (tension failure marked by RED color and shear failure marked by BLUE color), and (b) permeability changes around an excavation in argillite (Liu et al., 2012).

2.4.3 Anisotropic continuum damage model

In FY2017, an anisotropic damage model named Deviatoric Stress Induced Damage (DSID) was implemented into the simulator to account for crack propagation due to microstructure changes (Zheng et al., 2017). This new damage model is hyper-elastic, i.e., the stress-strain relationship was derived from the expression of a thermodynamic potential, and was derived based on Continuum Damage Mechanics (CDM), which avoids to model cracks at the micro-scale, as opposed to micro-mechanics. Damage effects are analyzed at the scale of Representative Elementary Volume (REV) with the concept of effective stress to account for the reduction of undamaged areas (Chaboche, 1992). REV is the smallest volume over which a measurement can be made that will yield a value representative of the whole, and it ranges from 10^{-3} m to 0.1 m, depending on the material and the focused problem. The model implementation has been validated by comparison with modeling several laboratory experiments on granite and by comparing computation results with different codes. The agreements between simulation and experimental results proved that the damage model was implemented correctly in our simulator and was capable to reproduce the same non-linear mechanical behavior due to damage propagation. For instance, the damage model was utilized to predict the evolution of the disturbed rock zone (DRZ) around emplacement tunnels, where the model enabled to capture the micro-crack propagation induced by the excavation (Figure 2-9).

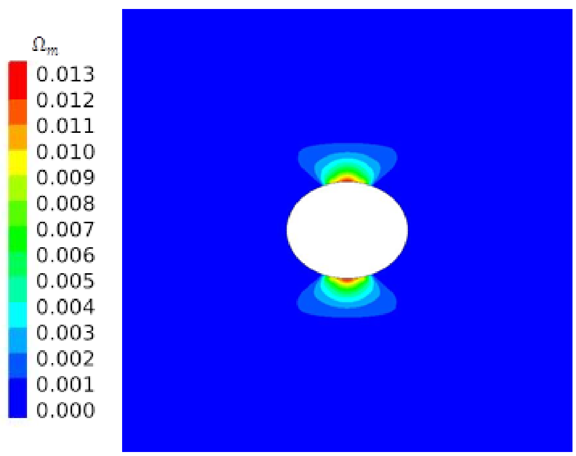

Figure 2-9. The simulation result of damage distribution at TSX experiment.

2.5 Development of TOUGH3-FLAC6

The recent development of the TOUGH3 code allows for a faster and more reliable fluid flow simulator. At the same time, new versions of FLAC3D are released periodically, allowing for new features and faster execution. In the framework of the current activities, we have coupled for the first time the newly developed TOUGH3 (Jung et al., 2017) with the version 6.0 of FLAC3D (Itasca, 2018). After verifying the correctness of the solution compared to the previous version,/ we evaluated the performance of the newly developed approach, which allowed for running on a multi-processors machine. We maintained the sequential coupling between the two codes as described above, and accounted for the main modification:

(1) Using TOUGH3 for parallel processing of fluid flow,
(2) Accounting for Python flexibility (as embedded in FLAC3D) and using a binary file exchange, to speed up read/write operation,

(3) No need to restart FLAC3D each time step, avoiding restore/save of state file that can be quite large for large models.

In MPI codes, and in particular for TOUGH3, a processor is designed as "IOProcessors" and takes care of all the input/output functionality of the code. The coupling approach for TOUGH3 and FLAC3D is described in Figure 2-10. FLAC3D is started at the beginning of the simulation. Then, for each time step, before starting the iterations for solving the fluid flow problem, TOUGH3 invokes a subroutine to gather the information from all the processors. Such information (pressure, temperature, saturation and capillary pressure) are written to binary file TOU_FLA by the IOProcessor, and write a flag file, read by FLAC3D. All this stage is basically done in serial by the IOProcessor, while all the other *n* processors are idle. Given the right flag, FLAC3D (i) reads the TOU_FLA file (with Python), (ii) solves for the mechanical equilibrium (in parallel), (iii) writes the FLA_TOU file to transfer information to TOUGH3 (with Python), and finally (iv) modify the flag file for TOUGH. At this stage, the subroutine invoked previously by TOUGH3 is waiting for the right flag, then the IOProcessor serially reads the FLA_TOU file and distributes the variables/properties (bulk modulus, Biot's coefficient, strain, and stress) to all *n* processors. Finally, the parallel computing can restart with the calculation of mechanically-induced changes of flow properties and with continuation of the iterations to finish the current time step.

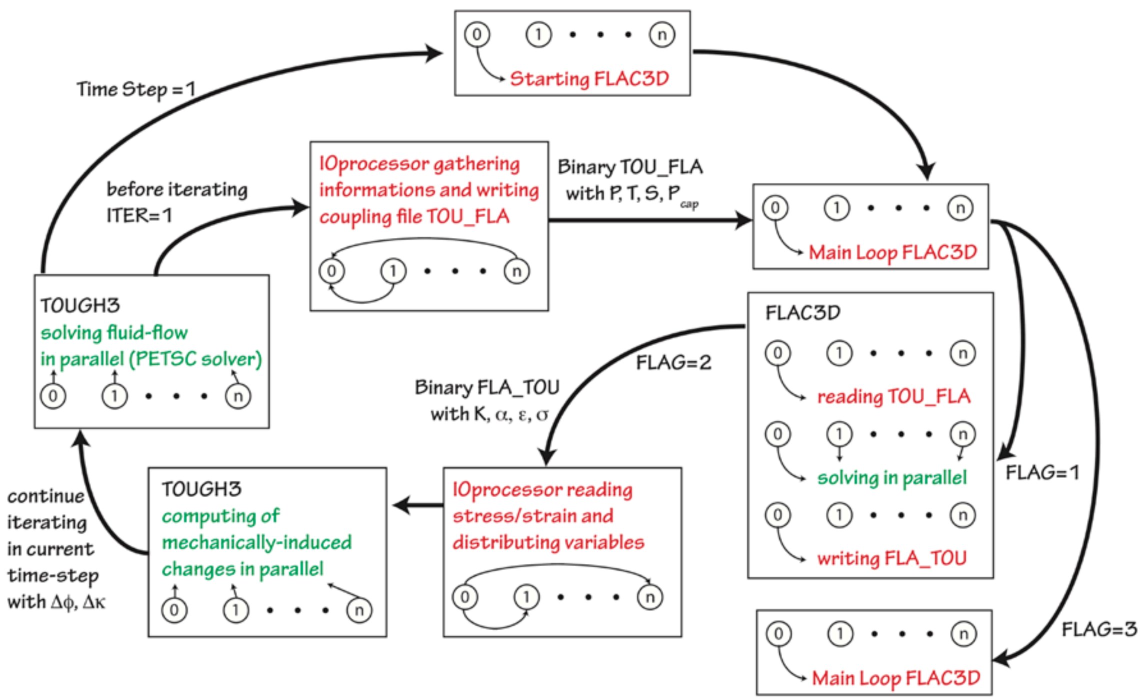

Figure 2-10. Illustration of a coupling between TOUGH3 and FLAC3D for each time step. Green parts are executed in parallel, while red parts are executed in serial. P, T, S, P_{cap} are pore pressure, temperature, saturation, and capillary pressure, respectively. K, α, ε, σ are bulk modulus, Biot's coefficient, strain, and stress, and Δϕ and Δκ stand for porosity and permeability changes.

One of the limitations of FLAC3D is that it runs only on Windows-based machines. Then, to make use of the MPI parallelization provided in TOUGH3, we compiled the code in the Cygwin environment, which also allows for calling to Windows-based programs (i.e., FLAC3D batch).

All simulations presented here were run on a large workstation with two 6-core CPUs Intel Xeon E5-2643 at 3.40 GHz and equipped with 64 GB RAM. This hardware configuration allows for using up to

12 processors, and it provides a relatively good scaling for TOUGH3-only models with a simulation being up to 6X faster, when run in parallel compared to serial for a mesh with about 850,000 elements.

Figure 2-11 shows the performance of TOUGH3-FLAC compared to TOUGH2-FLAC5. Similarly to the previous version, the code reaches peak performance by using only few threads in FLAC3D (3/4 core, 6/8 threads) for a mesh with 50’000 elements (Fig. 2-11a). The total execution time decreased from about 1300 s with the old model to about 400 seconds, when accounting for the maximum number of threads (Fig. 2-11b). By varying the number of elements, we observed a similar scaling/improvement in performance, up to 3.5 when using 10 cores/20 threads (Fig. 2-11c). Worth to note that the current hardware is not optimal for FLAC3D, which works better on single, multi-threaded processor: indeed, we observe a rupture in performance scaling when the second processor is used. To highlight the role of TOUGH3, it is useful to compare the scaling with the number of cores but fixing the threads in FLAC3D (Fig, 2-11d). With respect to TOUGH2-FLAC5, most of the improvement is achieved by optimizing the coupling between the two codes. The use of TOUGH3 is quantified in about 8% and 5% speed increase when using 50’000 and 200’000 elements, respectively. TOUGH3-FLAC6 is about 4 times faster than TOUGH2-FLAC5 for a mesh as large as 200’000 elements.

The developed approach is currently being used in the framework of BenVaSim code benchmarking, with excellent matching to analytical solutions. In the next phase, we will focus on (1) testing performances for larger meshes, and (2) applying a newly developed approach to conditions relevant to nuclear waste disposal.

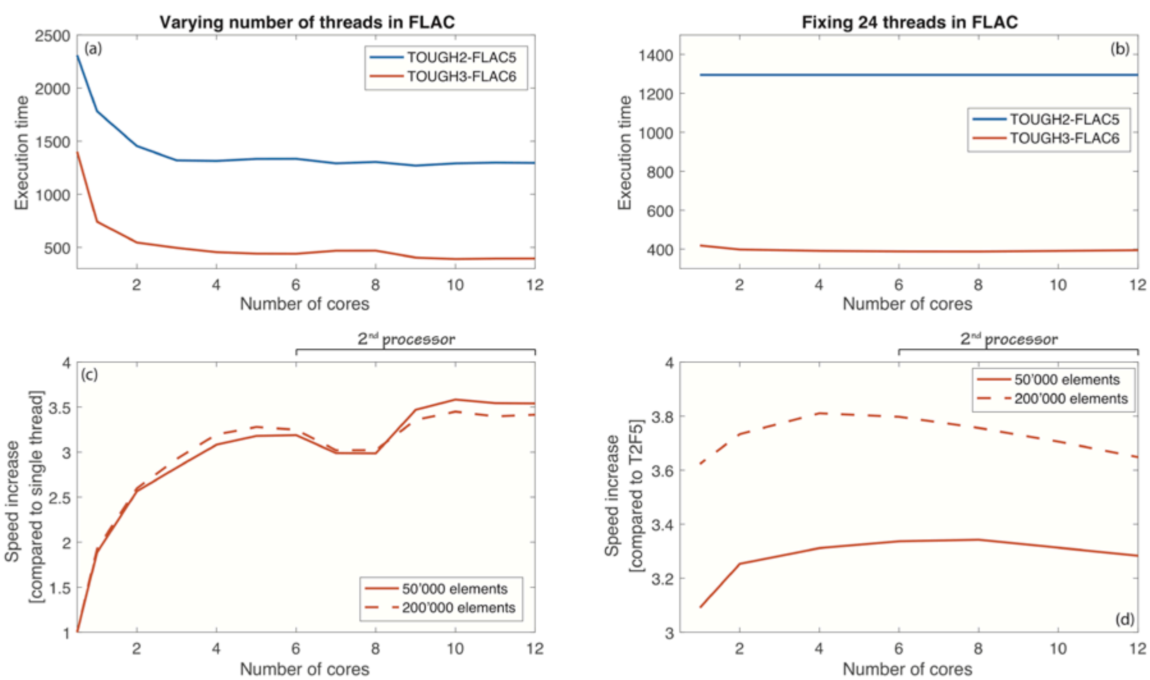

Figure 2-11. (a) Comparison of execution time as function of the number of cores/threads for TOUGH3-FLAC6 (red) and TOUGH2-FLAC5 (blue). (b) Comparison between T3F6 and T2F5 as function of number of cores while fixing the number of threads to 24 in FLAC3D. (c) Execution speed improvement for 50’000 (solid) and 200’000 (dashed) elements as function of the number of cores/threads. (d) Execution speed improvement with respect to old version as a function of number of cores while fixing 24 threads in FLAC for 50’000 (solid) and 200’000 (dashed) elements.

This page is intentionally left blank.

3. STATUS OF TOUGH-RBSN SIMULATOR

The TOUGH-RBSN simulator has been used for modeling coupled THM processes related to fracture/damage behavior (Asahina et al., 2014; Kim et al., 2017), for which the TOUGH2 code demonstrated multiphase flow and mass transport and the rigid-body-spring network (RBSN) model representing mechanical and fracture-damage behavior, respectively. The coupling modules, implemented in each of the modeling codes, update material properties and mechanical boundary conditions with the outputs of primary variables of physical quantities in sequential coupling time steps. This section presents more details on the TOUGH-RBSN simulator, including modeling of anisotropic deformation and fracture development in argillite rocks, followed by validation examples, and the status of the validation and verification works using the TOUGH-RBSN framework.

3.1 Representation of Anisotropy in Geomechanics Models

Some sedimentary rocks (e.g., shales) have directional fabrics such as bedding, foliation, and flow structures, which result in anisotropic features in bulk-scale mechanical responses. For example, clay rocks exhibit transversely isotropic elastic properties, in which Young's modulus is greater in the direction parallel to bedding than normal to the bedding (Bossart, 2012). Anisotropic features may also impact spatial evolution of mechanical failure. In order to represent those anisotropic features, we have implemented a novel scheme in the RBSN code.

3.1.1 Anisotropy of elastic deformability

Figure 3-1 shows the arrangements of spring sets within a Voronoi grid and the corresponding lattice elements. A 2D description is provided herein for simplicity, although this scheme has been developed within a 3D modeling framework. In the ordinary RBSN model, the spring sets are oriented to their individual local coordinates defined by the Voronoi diagram. However, in a new scheme, all spring sets are aligned to the principal bedding direction. The spring coefficients are defined in global fabric coordinates, where two orthogonal *N*- and *P*-axes are normal and parallel to bedding, respectively. Spring coefficients of a transversely isotropic material are calculated by using two different Young's moduli related to the bedding direction:

$$k_N = E_N \frac{A_{ij}}{h_{ij}}, \quad k_P = E_P \frac{A_{ij}}{h_{ij}}, \quad k_\phi = E_N \frac{I_\phi}{h_{ij}} \tag{3.1}$$

where E_N and E_P are Young's moduli normal and parallel to bedding, respectively.

Three distinct coordinate systems are considered for representation of kinematic quantities: global *X*-*Y* coordinates based on domain construction; local *x*-*y* coordinates for individual elements; and global *N*-*P* coordinates related to the orientation of a fabric. For each spring set, the spring stiffness matrix is established in *N*-*P* coordinates:

$$\mathbf{k}_b = \begin{bmatrix} k_N & & \\ & k_P & \\ & & k_\phi \end{bmatrix} \tag{3.2}$$

Although the derivation is invariant to coordinate systems, it is more convenient for matrix formulation to represent and manipulate the stiffness quantities in local *x*-*y* coordinates rather than in global *N*-*P* coordinates. Thus, the spring stiffness matrix, $\mathbf{k}_b$, is transformed to local *x*-*y* coordinates using following coordinate transformation (McGuire and Gallagher, 1979):

$$\mathbf{k}_s = \boldsymbol{\gamma}^T \, \mathbf{k}_b \, \boldsymbol{\gamma} \tag{3.3}$$

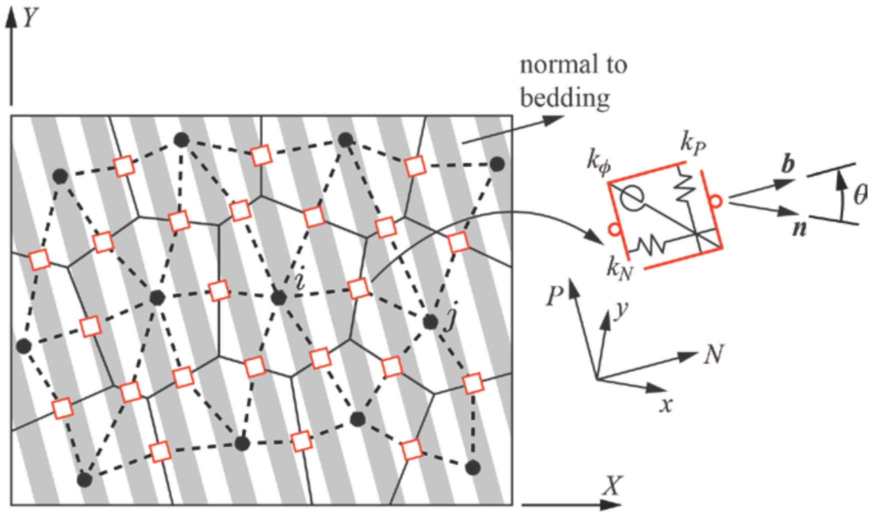

Figure 3-1. Arrangements of the spring sets in the identical lattice structure, where the spring coefficients comply with transversely isotropic elastic properties.

where $\boldsymbol{\gamma}$ is the 3×3 coordinate transformation matrix from local (*x*-*y*) to global fabric (*N*-*P*) coordinates:

$$\boldsymbol{\gamma} = \begin{bmatrix} Nx & Ny & 0 \\ Px & Py & 0 \\ 0 & 0 & 1 \end{bmatrix} \tag{3.4}$$

The first 2×2 entries in $\boldsymbol{\gamma}$ are the direction cosines between the bedding direction and the local coordinate axes. The element stiffness matrix, $\mathbf{k}_e$ (with respect to local *x*-*y* coordinates), is obtained by post- and pre-multiplication of $\mathbf{k}_s$ by the geometric transformation matrix that relates the generalized relative displacements at the spring set to the nodal displacements. Detailed formulation is presented elsewhere (Bolander and Saito, 1998; Berton and Bolander, 2006).

Finally, the element stiffness matrix is transformed to global coordinates:

$$\mathbf{K}_e = \mathbf{\Gamma}^T \, \mathbf{k}_e \, \mathbf{\Gamma} \tag{3.5}$$

where $\mathbf{\Gamma}$ is the coordinate transformation matrix from global domain *X*-*Y* to local *x*-*y* coordinates.

3.1.2 Anisotropy of strength and failure

In this study, Mohr-Coulomb type criteria are used to determine failure of local lattice elements. The stress state of a lattice element is represented with a Mohr circle in the stress space, and the Mohr circle is assessed by a failure surface defined with strength parameters. Herein, the weak-plane failure model is used to represent strength anisotropy. The model assumes that the inherent strength is the same in all directions of a rock material, except for one set of parallel planes where the strength is lower. This model concept has a physical basis because the bedding planes in sedimentary rocks may be planes of weakness.

Figure 3-2 describes an example where a lattice element undergoes the weak-plain failure along the bedding plane. Two different sets of strength parameters are necessary to define the failure surfaces, which are explicitly available from typical laboratory test results. First, intrinsic strength parameters (cohesive strength c, friction angle β, and tension cut-off f_t) define a failure envelope that represents isotropic failure in all directions except the direction of bedding. If the stress state of a lattice element is such that the Mohr circle exceeds the envelope, the material will undergo failure like that in an isotropic material, that is so called intrinsic failure. For the anisotropic failure on the bedding planes, the weak plane criterion is given by lower values of the cohesion c_w, friction angle β_w, and tensile strength $f_{t,w}$. A point on the Mohr circle represents the stress state about the bedding plane, which should be compared with the weak failure surface. In Figure 3-2, the Mohr circle has not touched the intrinsic failure envelop, but the point for the stress state along the bedding plane hit the weak failure envelop, so this element will undergo failure along the bedding plane.

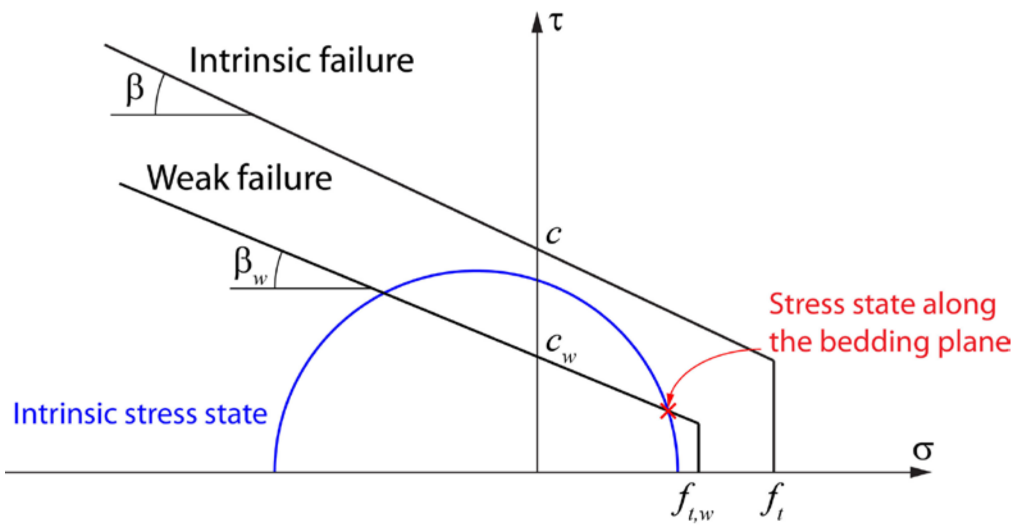

Figure 3-2. Weak-plane failure model with two different Mohr-Coulomb type criteria for intrinsic failure and weak failure.

3.1.3 Simulations of anisotropic damage and fracture in clay rocks

This section presents the validity of the modeling scheme for anisotropic failure behavior observed in the field site, the HG-A microtunnel. The 1-m diameter microtunnel is located in the Mont Terri underground research laboratory (URL) near Saint-Ursanne, Switzerland. The rock of the test site is relatively homogeneous at the meter-scale, but pronounced bedding was discovered at finer scales (Marschall et al., 2006). The rock formation is highly fractured with frequencies of 0.3 to 1 m, although the fracture permeability is not significant, which indicates that fractures are mostly closed under natural stress conditions (Marschall et al., 2006; 2008).

Figure 3-3 shows the excavation damage of the microtunnel. Partial damage and exfoliations have occurred along the microtunnel wall, which are mainly attributed to the anisotropic strength characteristics of the rock. The relative weakness is orthogonal to the bedding and the weakness near faults, intercepting the tunnel, results in the non-uniform damage around the excavation wall. In this study, we investigate the effects of anisotropic strength parameters and fault formations on the damage characteristics, and three modeling cases are simulated with different geomechanical settings as described in Figure 3-4.

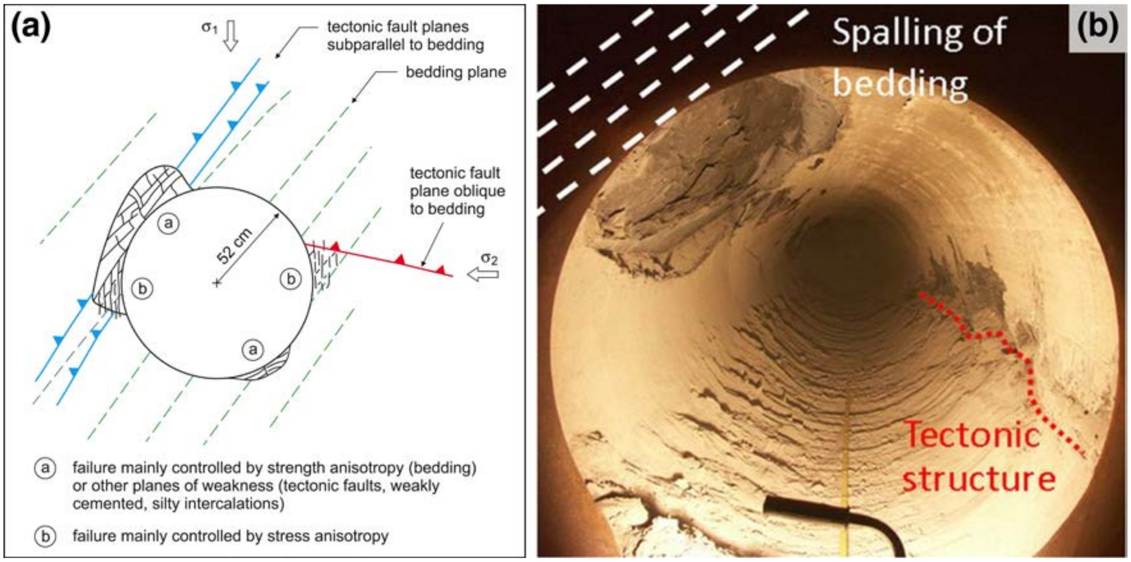

Figure 3-3. Excavation damage of the HG-A microtunnel: (a) conceptual diagram of the damaged zones and fault traces around the tunnel; and (b) observed damage formation along the tunnel (Lanyon et al., 2009; Marschall et al., 2006).

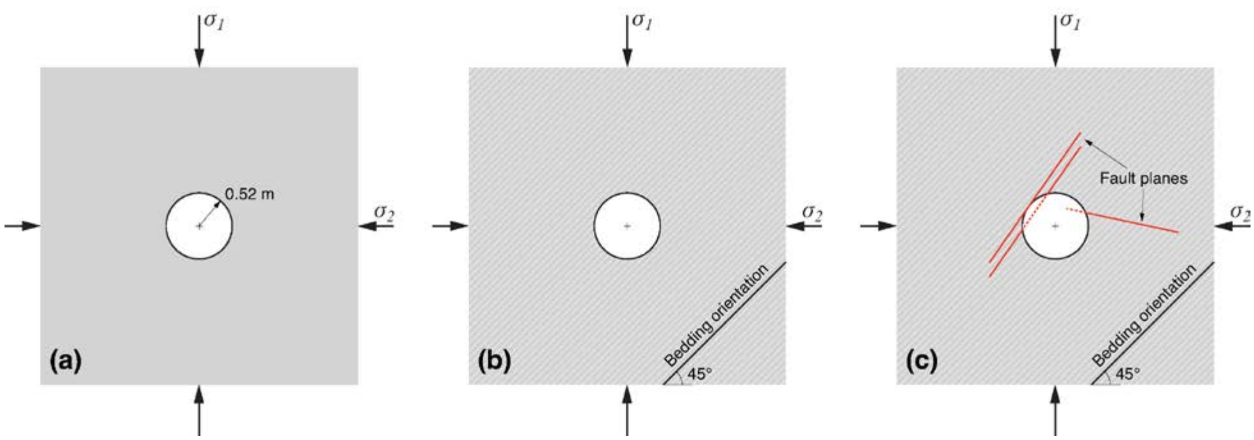

Figure 3-4. Modeling cases for three different geomechanical settings: (a) Case I–for in-plane isotropy and intact formation; (b) Case II–for in-plane anisotropy and intact formation; and (c) Case III–for in-plane anisotropy and fault formation.

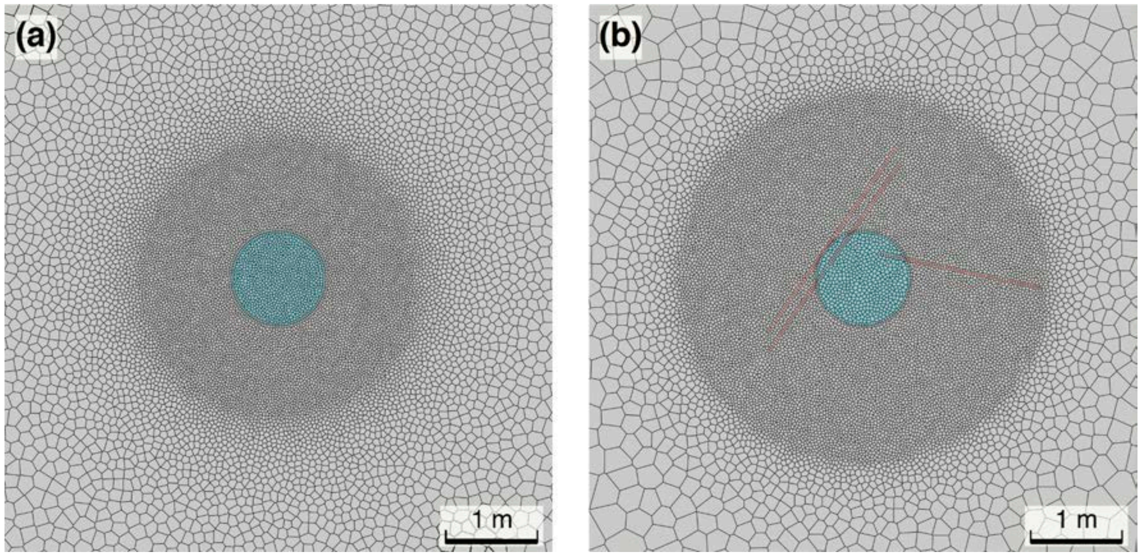

Figure 3-5. Voronoi discretization for modeling tunnel geometries in (a) intact formation (Cases I and II) and (b) fault formation (Case III).

Table 3-1. Anisotropic mechanical properties of the Opalinus Clay (Bossart, 2012).

Mechanical parameters	Parallel to bedding	Normal to bedding
Young's modulus (GPa)	15.5	9.5
Uniaxial tensile strength (MPa)	2.0	1.0
Cohesion (MPa)	5.5	2.2
Internal friction angle (degrees)	25	25

Figure 3-5 presents discretizations of a 10-m square domain with a gradual nodal density, where a circular subdomain for excavation is defined at the center. The bedding planes are assumed to be aligned at 45° from the horizontal axis. The anisotropic elastic and strength parameters of the rock matrix are listed in Table 3-1. The observed fault planes are precisely modeled into a grid (see Figure 3-3a), for which the weaker strength parameters are assigned: tensile strength $f_{t,f} = 0.5$ MPa; cohesion $c_f = 1.0$ MPa; and friction angle $\beta_f = 23°$. These parameters values are lower than parallel bedding parameters and are taken from Bossart (2012).

Far-field confining stresses are applied at the boundary edges: 4.5 MPa in the horizontal direction and 6.5 MPa in the vertical direction (Martin and Lanyon, 2003), and the pore pressure of 1.5 MPa is applied over the domain at the initial stage. A one-step preliminary simulation is conducted to grasp the initial stress state for the given stress and pressure configurations, so the main simulation starts with the underformed condition. An excavation process can be demonstrated by gradually reducing the elastic parameters, internal stress and pressure in the excavation zone over the loading steps. Herein, an exponential function is adopted, by which the values will be decreased to about 10^{-6} of the initial configurations after 100 loading steps.

The resulting failure patterns and stress distributions for each case are presented in Figures 3-6 to 3-8. For Case I with isotropic parameters, the damage pattern is mainly affected by the confining stress state. In Figure 3-6, more brisk failure occurs along the direction of minor principal stress and the stress distributions are symmetric about the confining stress directions. On the other hand, Case II with anisotropic parameters exhibits tilted damage pattern, and the failure tangent is sub-parallel to the bedding planes (Figure 3-7). The effects of fault planes on the failure patterns can be interpreted by a comparison of Figures 3-7 and 3-8. The matrix domain is homogenous in the material composition, thus the failure pattern and stress distributions are quite symmetric without fault planes (Figure 3-7). However, in the presence of faults (Figure 3-8), a distinct shear fracture develops along the fault planes, and then fractures grow from the fault planes. One notable feature in the fracture pattern with fault planes is that the fracture growth is somewhat limited by the fault planes, and the resulting fracture pattern is not symmetric due to the stress contour perturbed by the fault planes.

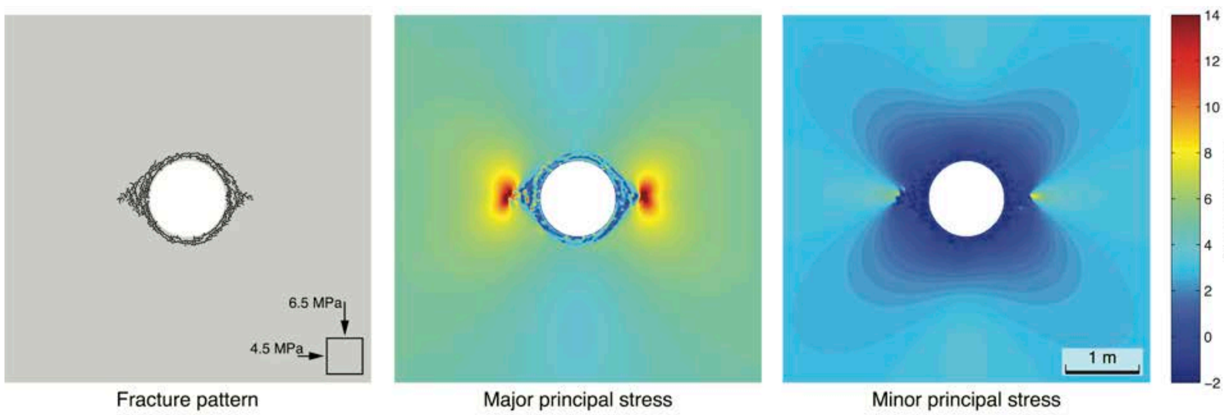

Figure 3-6. Results at the final stage of the simulation for Case I with in-plane isotropy and intact formation.

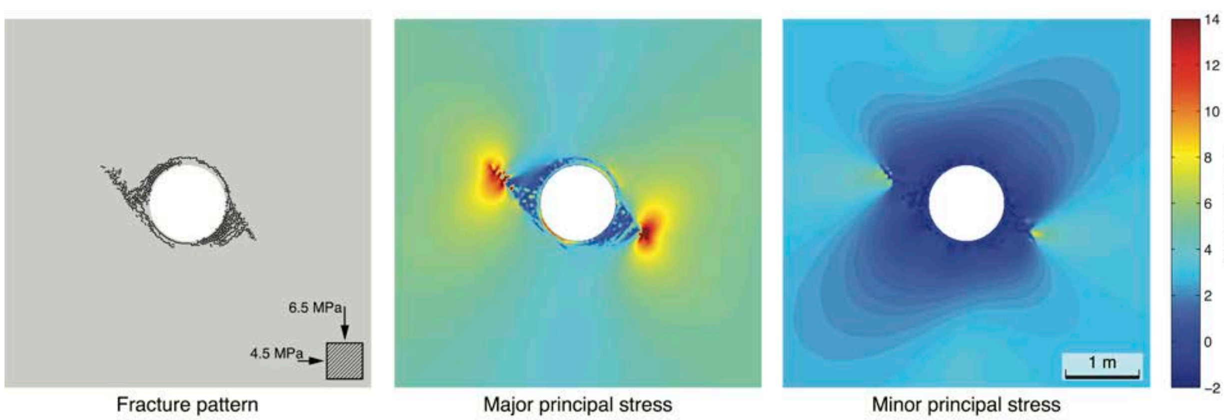

Figure 3-7. Results at the final stage of the simulation for Case II with in-plane anisotropy and intact formation.

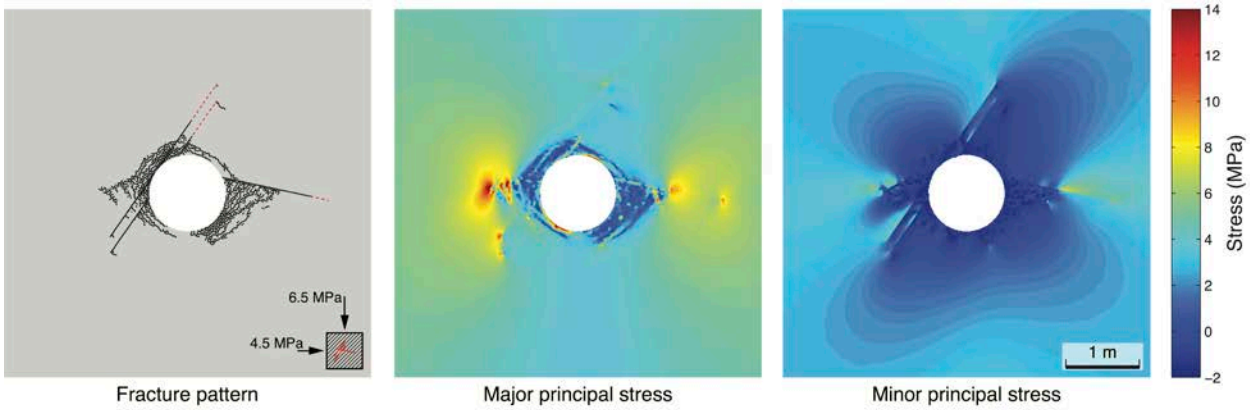

Figure 3-8. Results at the final stage of the simulation for Case III with in-plane anisotropy and fault formation.

3.2 Status of TOUGH-RBSN Verification and Validation

Coupled THM processes, including fracture propagation, within argillaceous rocks and clay rich geomaterials have been simulated using the TOUGH-RBSN code with adequate constitutive models, which are verified and validated against laboratory tests and analytical solutions. In the following, completed verifications and validations of TOUGH-RBSN are listed with the references in which those activities are documented.

- Simulations of swelling stress development and desiccation cracking in geomaterials validated against independent laboratory test data (Asahina et al., 2014)
- Hydraulic fracture propagation in rock-analogue samples made of soda-lime glass with a designed fracture geometry (Kim et al., 2017)
- Excavation damage and fracture development influenced by the deformation and strength anisotropy of clay rocks (Kim et al., in preparation)

In addition, LBNL is currently involved in DECOVALEX-2019, an international collaborative activity for validating various modeling approaches against laboratory and field collected datasets. TOUGH-RBSN has been used to model two-phase liquid and gas flow in a saturated bentonite sample with dilatant flow path and fracture generation. Intermediate results for 1D gas flow have been presented in Tamayo-Mas et al. (2018), including an extensive comparison of simulation results using 11 different modeling approaches with laboratory test data. The TOUGH-RBSN models, based on relevant conceptual models, exhibit key responses such as pressure/stress evolution in a plausible match with the experimental data. In FY2019, we have focused on 3D modeling of spherical gas flow in bentonite samples, and the conceptual models and the updated results are presented in Section 6.

This page is intentionally left blank.

4. FE EXPERIMENT AT THE MONT TERRI SITE (MONT TERRI PROJECT)

In this section, we present the current status of the FE Experiment at Mont Terri and updated results of TOUGH-FLAC modeling of the experiment. In particular, in FY2019 we have extended the modeling for comparison with over 4 years of field data from the experiment. In the following, we first provide a description and status of the FE Experiment and then present the results of current THM modeling.

4.1 Description and Status of the Mont Terri FE experiment

The Mont Terri FE experiment is undertaken by NAGRA, Switzerland, as an ultimate test for the performance of geologic disposal in Opalinus Clay, with focus on both the EBS components and the host-rock behavior. It will be one of the largest and longest-duration heater tests worldwide, with focus on both the EBS components and the host-rock behavior. The FE experiment is conducted in a side tunnel at Mont Terri, excavated along the claystone bedding planes, extending 50 m in length and about 2.8 m in diameter (Figure 4-1). Heating from emplaced waste is simulated by three heat-producing canisters of 1500 W maximum power each. The temperature is expected to exceed 100°C, with a target temperature of 125 to 135°C at the inner part of the buffer. A sophisticated monitoring program has been implemented, including dense instrumentation of the bentonite buffer and host rock, and extensive geophysical monitoring.

The experiment will provide data useful for the validation of THM coupling effects regarding the processes in the host rock, while correctly accounting for (and examining) the conditions in the emplacement tunnel temperature, saturation, and swelling pressure. Due to the 1:1 scale of the experiment, it will be possible to achieve realistic temperature, saturation, and stress gradients. It will also be possible to test backfilling technology with granular bentonite, as well as lining technology with shotcrete, anchors, and steel ribs. Processes examined in the test cover many aspects of a repository evolution, such as creation and desaturation of the EDZ during tunnel excavation and operation (including ventilation for about one year), as well as reconsolidation of the EDZ, resaturation, thermal stresses, and thermal pore-pressure increase after backfilling and heating (heating and monitoring period > 10 years).

In 2011, a niche in front of the FE tunnel was constructed, followed by a first phase of instrumentation of the rock mass surrounding the tunnel, using boreholes drilled from the niche. The FE tunnel was excavated by a road-header in 2012, which was followed by another phase of instrumentation. The tunnel was open for a one-year ventilation period. This was followed by emplacing the heaters, bentonite buffer, and a concrete plug, after which the heating was gradually turned on during the fall of 2014 and early 2015, with applying the full heat power of 1350 W at all three heaters (H1, H2, H3) from February 18, 2015 (Figure 4-2). The heating is expected to go on for at least 15 years, with continuous monitoring of THM processes in both the bentonite buffer and a surrounding rock. After over 4 years of heating, the temperature at the heaters is approaching 130°C, and a relative humidity near the heaters in granular bentonite buffer stays low at around 10 to 20%. Some wetting is also taking place of other parts of the buffer, at some point reaching full saturation. No substantial swelling stress has been developed in the granular bentonite section, with stresses reaching at some locations up to 0.4 MPa.

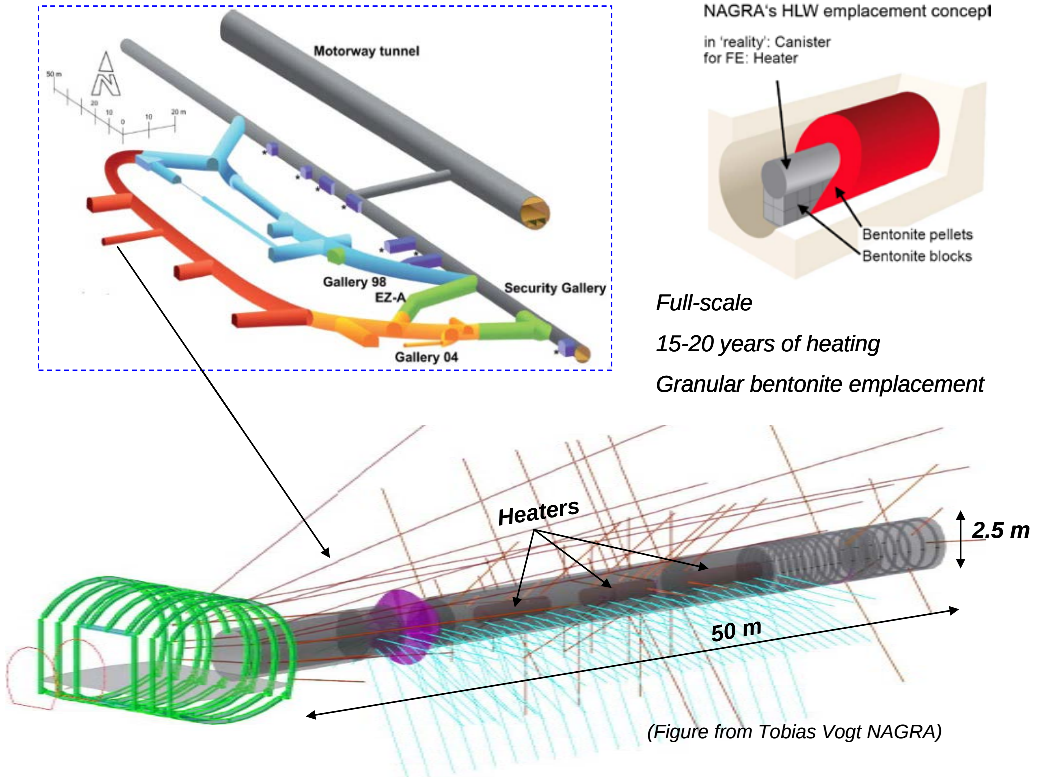

Figure 4-1. Plan view of FE experiment setup and borehole layout.

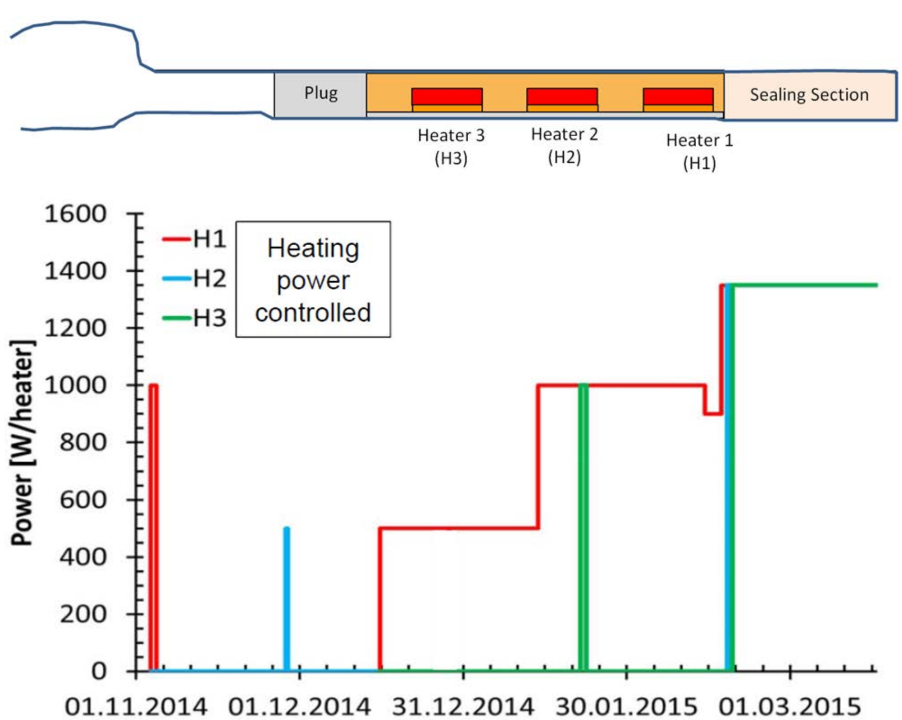

Figure 4-2. Heat power applied to H1, H2 and H3 during heater start-up at the Mont Terri FE experiment.

4.2 Progress of LBNL Modeling of FE Experiment

DOE is one of the experimental partners for the FE heater experiment, and LBNL is one of the modeling teams. In addition to LBNL, six other modeling teams are currently involved in the Mont Terri FE experiment, including Germany (2 teams), U.K., Spain, Switzerland, and Canada.

Each modeling team develops its conceptual models and material properties using available literature on lab experiments and previous Mont Terri *in situ* tests, etc. In the FY2013 UFD milestone report (Houseworth et al., 2013), we also made a first full THM 3D simulation of the FE heater test, including the BBM model for calculating the mechanical responses. These were scoping and preliminary predictions with the material properties available at the time, though in some cases including a different kind of bentonite.

In the FY2015 UFD milestone report (Zheng et al., 2015), we presented simulation results related to the thermal evolution for different heat power schemes. This included a staged heating during the first few months of the experiment. A staged heating schedule was also adopted in the real experiment to be able to use early data for determining the maximum heat load so that temperatures would not exceed certain limits. For example, the maximum temperature should not exceed 150°C as such high temperature could potentially damage the monitoring system. The modeling presented in the FY2015 UFD milestone report indeed showed that temperature could increase to about 150°C if the maximum heat power of 1500 W would be applied on each of the heaters. It was decided by NAGRA to limit the maximum heat power to 1350 W to maintain maximum temperature well below 150°C.

In the FY2016 UFD milestone report (Zheng et al., 2016), we presented the results of initial interpretative modeling of the FE experiment with comparison to field data for the first year of heating. The approach was to use the previously developed 3D model of the FE experiment, but with THM properties updated and determined from the modeling of the smaller scale HE-E experiment. In the modeling, we obtained a good agreement with monitored evolution of temperature and relative humidity, when using an effective diffusivity that was lowered using a tortuosity factor as low as 0.14 (Zheng et al., 2016).

In the FY2017 SFWSD milestone report (Zheng et al., 2017), we updated model simulations with comparison to monitoring data extended to more than two years, including additional comparison for monitoring points located at other sections along the tunnel, i.e., comparisons made at monitoring sections located at all three heaters. The agreement between modeling and experimental data for temperature and relatively humidity was generally good, though some disagreement was found related to the relative humidity evolution in the bentonite blocks below the heaters.

In the FY2018 SFWSD milestone report (Rutqvist et al., 2018), we updated a comparison to about 3.5 years, including additional comparison for monitoring points located in the buffer as well as in the host rock, conducted additional sensitivity analysis, and obtained a better match of relative humidity evolution in the bentonite blocks below the heaters.

In the current report, we present the model and provide a brief update of the simulation results extended to 4.5 years from the start of the heating.

4.3 TOUGH-FLAC Model of the Mont Terri FE Experiment

For the FE experiment modeling, we have developed a conceptual model and modeling approach based on the previous milestone reports (Houseworth et al., 2013; Zheng et al., 2014, 2015, 2016). The host rock is modeled using TOUGH-FLAC with anisotropic properties considering bedding planes of the Opalinus Clay. To accurately model anisotropic thermal and hydrological behavior, we created a TOUGH2 inclined mesh. Anisotropic mechanical material behavior is simulated using the FLAC3D ubiquitous joint model, with initial material properties derived from the analysis of the excavation design of the experimental tunnels. In the ubiquitous joint model, weak planes are assumed along the bedding planes of the Opalinus Clay, in which the shear strength properties are different along and across the bedding (Houseworth et al. 2013). For the bentonite, we started with the BBM model as applied by the Centro De Investigaciones Energéticas, Medio Ambientales Y Tecnológicas (CIEMAT) and Universitat Politècnica de Catalunya (UPC) (Garitte and Gens, 2012), and derived specific input material parameters for the MX-80 bentonite pellets, which are used as the emplaced buffer around the heaters. With this modeling approach, we are able to simulate THM processes in both the bentonite and host rocks, as well as their interactions.

Figure 4-3 presents the 3D TOUGH-FLAC numerical grid of the FE experiment. This model grid includes all material components used for the modeling of the FE experiment, including layered Opalinus Clay host rock, excavation disturbed zone, tunnel, three heaters, bentonite buffer, concrete liner, and a concrete plug. Initial conditions for the model simulation are: 2 MPa pore-fluid pressure, and 15°C temperature for the host rock. The 2 MPa pore pressure does not represent hydrostatic conditions, and the process is affected by the existing tunnel system at the site. In our simulations, we first run a simulation with an open tunnel at the atmospheric pressure for one year, creating a pressure drop and hydraulic gradient around the tunnel. Thereafter, we assume instantaneous emplacement of the heater and the buffer to start the heating simulation.

The thermal and hydraulic material properties for modeling the FE experiment are given in Table 4-1. These properties are based on the modeling studies of several other smaller scale heater experiments at the Mont Terri laboratory, including the HE-D and HE-E experiments described in previous reports (Zheng et al., 2015; 2016). The intrinsic permeability of gas flow in the bentonite is about six orders of magnitude higher than the intrinsic permeability for liquid flow, and this is simulated in TOUGH2 using a high value of the Klinkenberg parameter. The initial saturations in granular bentonite and bentonite block are different than those in the previous HE-E experiment, and are set for the FE experiment set to 16.5% for granular bentonite and to 75% for bentonite blocks.

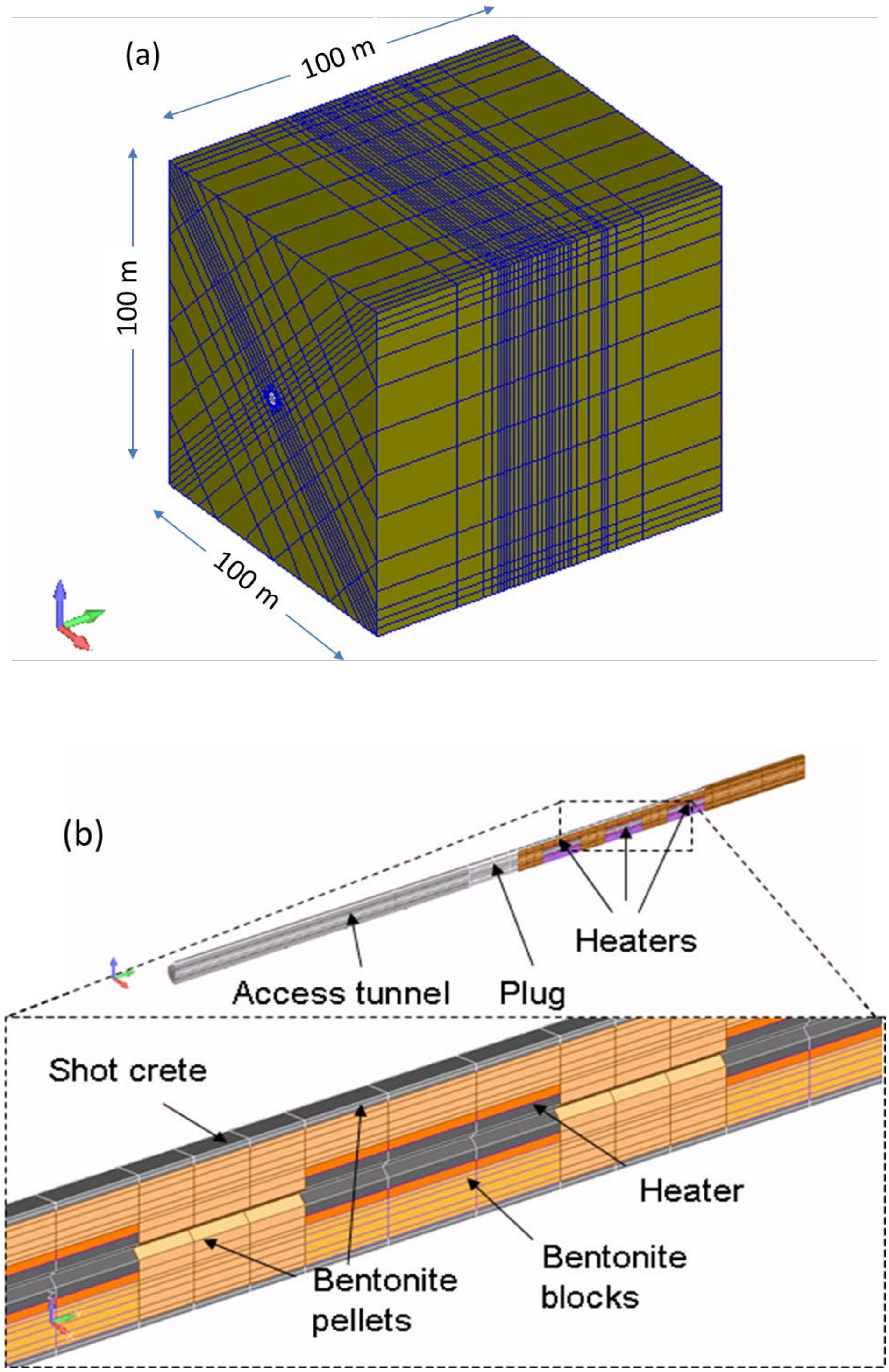

Figure 4-3. TOUGH-FLAC 3D numerical grid of the FE experiment. (a) entire model and (b) details of the materials and gridding of the EBS.

Table 4-1. Parameters used in the modeling of the Mont Terri FE experiment.

Parameters	Symbol	Opalinus Clay	Granular Bentonite	Bentonite blocks	Concrete (shotcrete and plugs)	Unit
Grain density	ρ_g	2.7×10^3	2.7×10^3	2.7×10^3	2.7×10^3	kg/m^3
Porosity	$\O$	0.15	0.46	0.389	0.15	-
Intrinsic permeability	k	5.0×10^{-20}	5.0×10^{-21}	2.0×10^{-21}	3.5×10^{-21}	m^2
Liquid relative permeability (Corey, 1954) $k_{lr}(S_l) = \left(\frac{S_l - S_{lr}}{S_{ls} - S_{lr}}\right)^A$	A	-	5	3	-	-
Liquid relative permeability (van Genuchten, 1980) $k_{lr}(S_l) = \left(\frac{S_l - S_{lr}}{S_{ls} - S_{lr}}\right)^{1/2}\left[1 - \left\{1 - \left(\frac{S_l - S_{lr}}{S_{sl} - S_{lr}}\right)^{1/m}\right\}^m\right]^2$	m	0.52	-	-	0.52	-
Capillary curve (van Genuchten, 1980) $\psi(S_l) = Po\left\{\left(\frac{S_l - S_{lr}}{S_{ls} - S_{lr}}\right)^{-1/m} - 1\right\}^{1-m}$	P_0	1.09×10^7	1.0×10^7	3.0×10^7	1.09×10^7	Pa
	M	0.29	0.4	0.32	0.29	-
	S_{ls}	1.0	1.0	1.0	1.0	-
	S_{lr}	0.01	0.0	0.0	0.01	-
Thermal conductivity (wet)	λ_{sat}	1.7	1.3	1.0	1.7	W/m°K
Thermal conductivity (dry)	λ_{dry}	1.06	0.3	0.5	1.06	W/m°K
Grain specific heat	C	800	950	950	800	J/kg°K

4.4 Simulation Results with Comparison to Monitored Data to 4.5 years

In the FY2016 milestone report (Zheng et al., 2016), a good comparison of one-year simulation results and observations of the relative humidity in the buffer was achieved using a tortuosity parameter as low as $\tau = 0.14$. In the FY2017 milestone report (Zheng et al., 2017), the value of tortuosity of $\tau = 0.14$ was confirmed based on the results of simulations and observations for a period of two years of heating and for a number of monitoring points at all three heaters. In the FY2018 report (Rutqvist et al., 2018), the results of simulations and observations were compared for a period of 3.5 years for monitoring points around the three heaters.

In the current report, the simulation and experimental data are compared for a period of 4.5 years, demonstrating no significant changes in the trends and comparison with field data. Figure 4.4 shows an example of the evolution of temperature and relative humidity at Heater 3 (H3). This data set is chosen because of good field data quality obtained with the sensor working properly for 4.5 years. The time zero in these figures is 12/28/2014, which is just after the start of heating at Heater 1 (H1). The results shown in Figure 4-4 confirm previous results of an excellent agreement in buffer temperature evolution, while some discrepancies are observed regarding the evolution of relative humidity.

The discrepancy between simulated the measured relative humidity is explained by the fact the real distance between the sensor location and the rock wall in the field is not exact in the model. In the modeling, the tunnel is simulated as a perfect circle and the thickness of shotcrete around the tunnel is constant while in the field the shape of the tunnel is not perfectly circular and the thickness of shotcrete is not constant (Figure 4-5). Overall though, the trend of moisture inflow from the rock and the relative humidity evolution are captured in modeling as shown in Rutqvist et al., (2018). In general, the rate of inflow to saturate the buffer is relative slow due to the low permeability of the host rock.

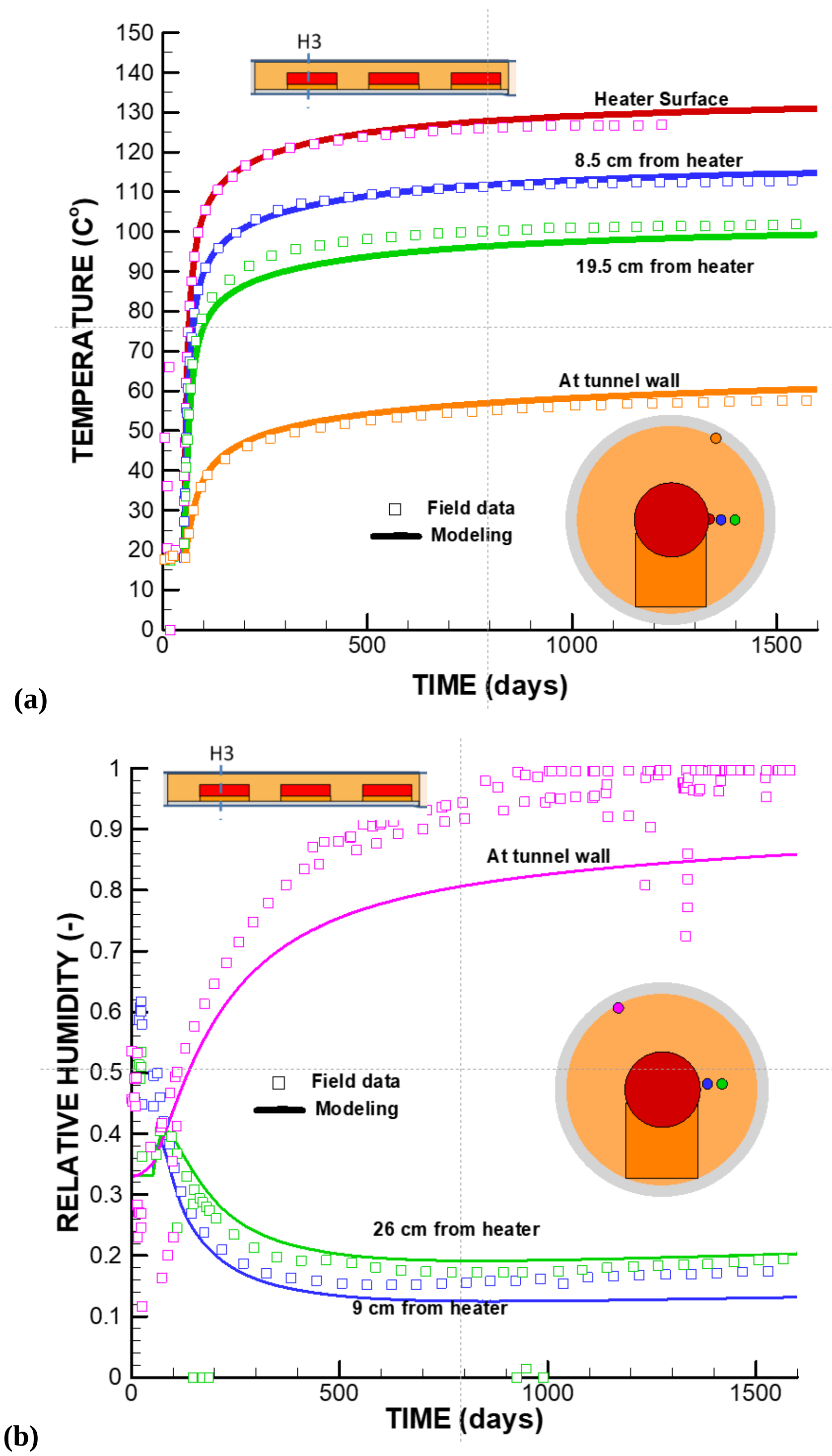

Figure 4-4. Comparison of modeled (lines) and measured (symbols) evolutions of (a) temperature and (b) relative humidity at the monitoring point located in granular bentonite at H3 for over two years of monitoring data.

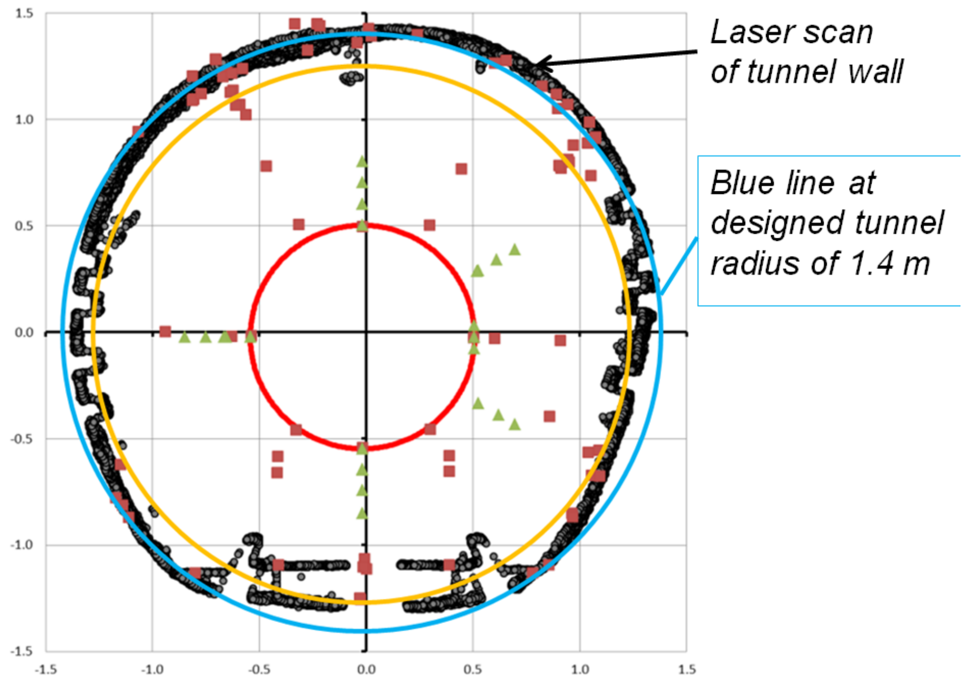

Figure 4-5. Comparison of the actual zigzag-shape cross-section of the tunnel from the laser scan with the circular shape of tunnel used in numerical modeling. The red circle in the middle is the heater. Squares and triangles indicate locations of some of monitoring sensors. Axis units are in meters.

Figure 4-6 shows a comparison of the pressure evolution in the host rock for up to 800 days. The best overall match was by setting the permeability to 2e-20 m^2 and the pore compressibility to 1e-9 Pa^{-1} for monitoring points located along a borehole parallel to bedding (Figure 4-6a). For monitoring points located perpendicular to bedding, permeability was also set to 2e-20 m^2 and a pore compressibility was set to 5e-9 Pa^{-1} (Figure 4-6b). This indicates that the difference between coupled THM responses are mainly due to a difference in fluid storage. Although this was the best overall match in the rate of pressure increase at different points, there are some discrepancies, in particular in the initial pressure values at some points. In future modeling, we will study the phenomenon of anisotropic pressure response in detail and will try to apply and explain these differences using anisotropic material models.

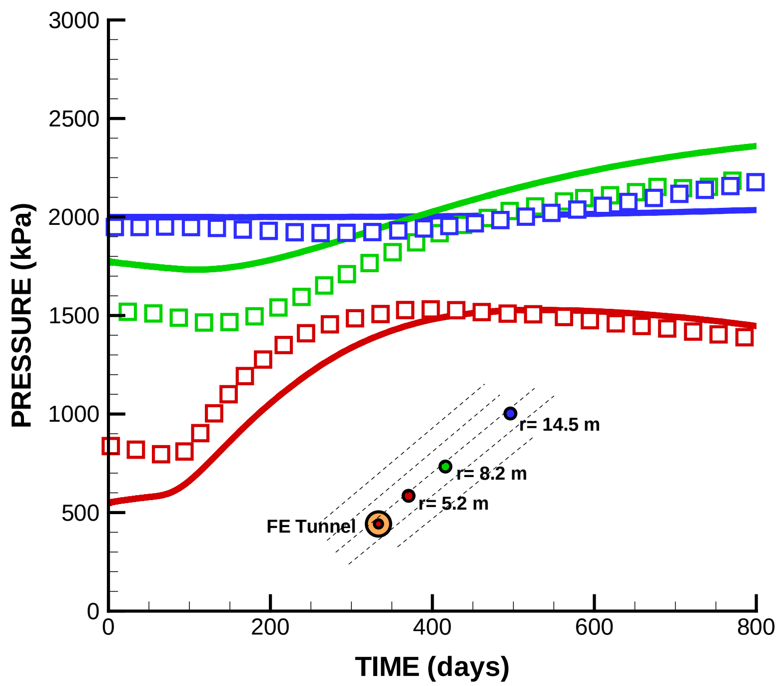

(a)

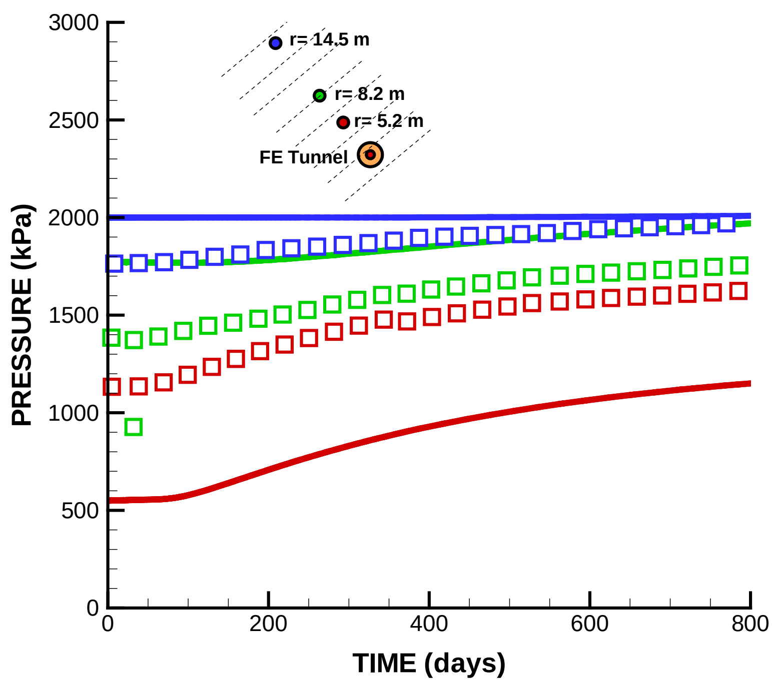

(b)

Figure 4-6. Results of scoping calculation for thermal pressurization effects in the host rock for pressure monitoring points located (a) perpendicular to bedding, and (b) parallel to bedding of the tunnel

4.5 Summary and Status the FE Experiment Modeling

We have conducted various types of modeling over the past few years, including benchmarking, heating design modeling, model predictions and interpretative modeling. Currently, we have interpreted data for up to 4.5 years of heating, including data on temperature and relatively humidity in the bentonite buffer and up to 2.5 years of pressure in the host rock. Some finding and lessons learned of the work to date are as follows:

- A good agreement between modeled and measured evolutions in buffer temperature and relative humidity was achieved at the FE experiment based on a model prediction using properties of bentonite and Opalinus Clay determined from the previous Mont Terri HE-E experiment.
- A value of the effective vapor diffusion coefficient (and the tortuosity factor) were calibrated against measured relative humidity evolution in the granular bentonite, but the value was much lower than used for previous modeling of the HE-E experiment. This difference and the potential role of enhanced thermal diffusion of the early-time TH response in the buffer are open questions that warrant further studies.
- The values of the effective vapor diffusivity coefficient and the tortuosity factors for the bentonite block were determined based on the calibration of model parameters, and these values are much higher than those for the granular bentonite (0.33 for blocks vs 0.14 for granular bentonite).

Still after 4.5 years of heating and infiltration from the surrounding rock, no significant swelling stress has been developed in the bentonite buffer. Measurements show the highest total pressure in the buffer is less than 0.4 MPa. We will continue modeling of the FE experiment along with new monitoring data, focusing more on the mechanical evolution of the buffer and host rock.

5. HEATER EXPERIMENTS AT BURE IN COx CLAY STONE (DECOVALEX-2019)

In this section, we present recent TOUGH-FLAC modeling results related to the *in situ* heater experiment, conducted in Callovo-Oxfordian claystone (COx) at the Meuse/Haute-Marne Underground Research Laboratory (MHM URL) in Bure, France. Modeling of the heater tests is one of the Tasks of the DECOVALEX-2019 project. In the following, we first provide a description of the DECOVALEX-2019 Task E and international modeling teams associated with this task; then provide a description of updated TOUGH-FLAC simulation results, and the comparison to the *in situ* experiments associated in each step.

5.1 DECOVALEX-2019 Task E and International Modeling Teams

DECOVALEX-2019 Task E is a study addressing important issues related to the repository design and safety calculation, as well as problem of upscaling from a sample scale to a repository scale. This study is also focused on the evaluation of the thermally induced pore pressure build-up and stress changes around a repository. The Task is coordinated by ANDRA (French National Radioactive Waste Management Agency), and involves modeling of two *in situ* tests performed at the URL in Bure (France):

- The TED experiment, a small-scale heating experiment focused on the claystone THM behavior of the undisturbed rock mass in the far field; and
- The ALC experiment, a one-to-one scale heating experiment focused especially on the interaction between the surrounding rock and the support (steel casing in this case) in the near field.

Based on the results of modeling of two *in situ* tests, the impact of the heating experiments at the repository scale with several parallel cells will be evaluated. These results will be used to address some key technical challenges, such as the variability of the THM parameters, the determination of appropriate boundary conditions, and the potential thermally induced hydraulic fracturing between canisters. Modeling is used to represent a series of parallel cells.

DECOVALEX-2019 Task E is conducted by a step-by-step approach, from small-scale to full-scale studies (Figure 5-1). It is structured into four main steps:

- Step 1: Simple 3D THM modeling benchmark;
- Step 2: Interpretative modeling of the TED experiment (back-analysis);
- Step 3: Modeling of the ALC experiment
    - Step 3a: Predictive modeling of the ALC experiment using the reference values for the rock mass parameters determined in Step 2;
    - Step 3b: Interpretative modeling of the ALC experiment;
- Step 4: Prediction at the repository scale of an area with several high level waste cells.

The participating groups in the DECOVALEX-2019 Task E are:

- Canada: NWMO (The Nuclear Waste Management Organization);
- France: ANDRA, University of Lille;
- Germany: BGR (Institute for Geosciences and Natural Resources) and UFZ (Helmholtz Centre for Environmental Research), Leipzig;
- UK: RWM (Radioactive Waste Management Limited), Quintessa Ltd;
- USA: U.S. DOE and LBNL.

Currently, Step 1 related to 3D THM modeling benchmark, Step 2 related to interpretative modeling of the TED experiment at Bure, and Step 3 related to blind prediction and interpretative modeling of the ALC experiment, have been completed. Step 4 related to the prediction of the temperature, pore pressure and stresses at the repository scale is ongoing. An interim report regarding Steps 1 and 2 has been completed in 2018. The whole task should be finished before the next DECOVALEX-2019 workshop, which will be held in November 2019.

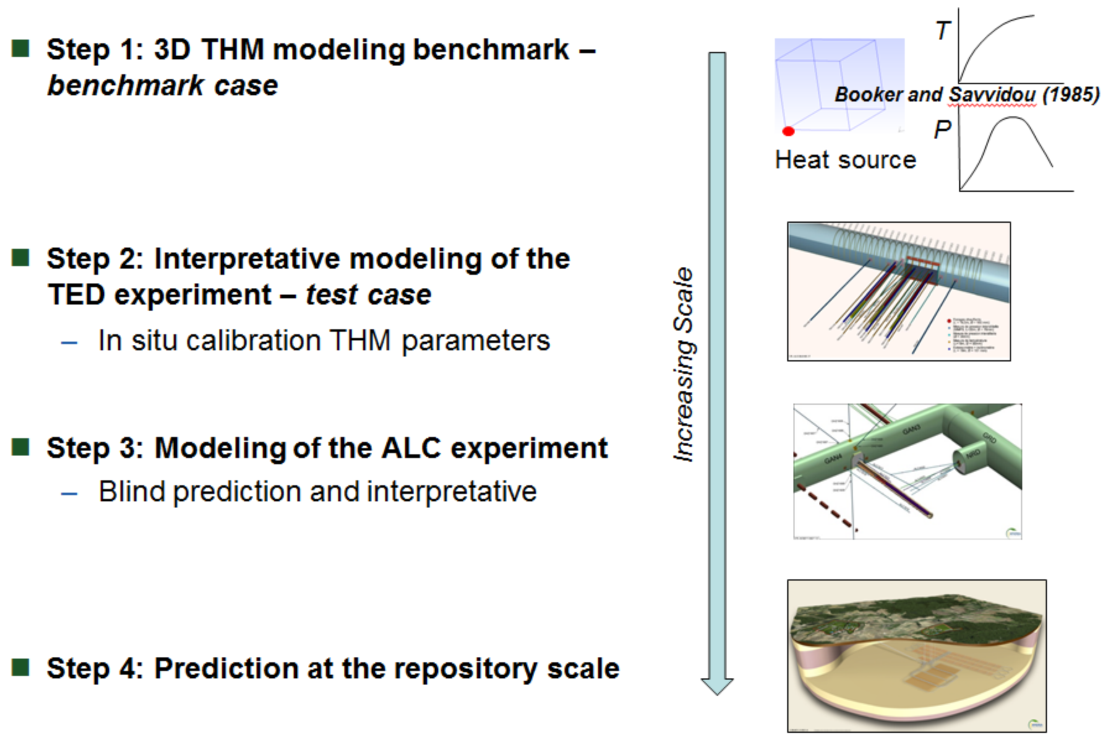

Figure 5-1. Overview of DECOVALEX-2019 Task E, illustrating the increasing scale of investigations.

5.2 TOUGH-FLAC Simulation Results with Comparison to Experimental Data

5.2.1 Step 1: 3D THM modeling benchmark

Step 1 of Task E is a basic benchmark test conducted to assess the consolidation of an infinite homogeneous saturated porous media around a point continuous heat input. Experimental and modeling results were compared with the analytical solution of Booker and Savvidou (1985) developed based on the hypothesis that the pore water and the solid grains are incompressible. The 3D model is generated with FLAC3D, and the simulation is launched with the module EOS1 (Equation of State) in TOUGH2. The detailed model setup can be found in the FY2017 report (Zheng et al., 2017). Comparison between modeling results and analytical solution for temperature, pore pressure, displacements and stresses evolution up to 365 days is provided at certain points in the FY2018 report (Rutqvist et al., 2018).

In previous work as reported in Rutqvist et al., (2018), we have computed the evolution of temperature, pressure, and displacements at certain points. An overall good agreement is reached related to the temperature, pore pressure and displacement evolution between numerical results and the analytical solution, except the displacement in *x*-direction, which is slightly smaller than the analytical solution. Later in this step, the analytical solution of stresses has been derived based on the methodology given in Booker and Savvidou’s paper. The simulated stress results are in a good agreement with the analytical solution, which verifies the correctness of the TOUGH-FLAC code as well as the results of modeling of temperature, pore pressure and displacements.

5.2.2 Step 2: TED experiment

The TED experiment lasted for three years from 2010 to 2013. It involved three heaters at a depth of 490 m, in three parallel boreholes at a separation of about 2.7 m (Figure 5-2). The three heaters were 4 m long and were installed at the end of 160 mm diameter and 16 m long boreholes, drilled from a main drift and parallel to the maximum horizontal stress. This arrangement represented a similar configuration to high-level nuclear waste cells with parallel micro-tunnels, but at a smaller scale. The TED experiment was heavily instrumented with 108 temperature sensors in the rock mass, 69 temperature sensors in 3 heater boreholes, 18 piezometers, 2 extensometers and inclinometers, and 10 temperature sensors recording the temperature at the level of the main drift. The temperature measurements during the TED experiment showed that the rock has an anisotropic thermal conductivity, because at the same distance from the heater, the temperature increase is higher in the bedding plane than that in the perpendicular direction. Observations of pore pressure also showed that its evolution was dependent on the location with respect to the bedding plane, as the pore pressure increased faster in the direction parallel to bedding. The increase of pore pressure in perpendicular direction was slower.

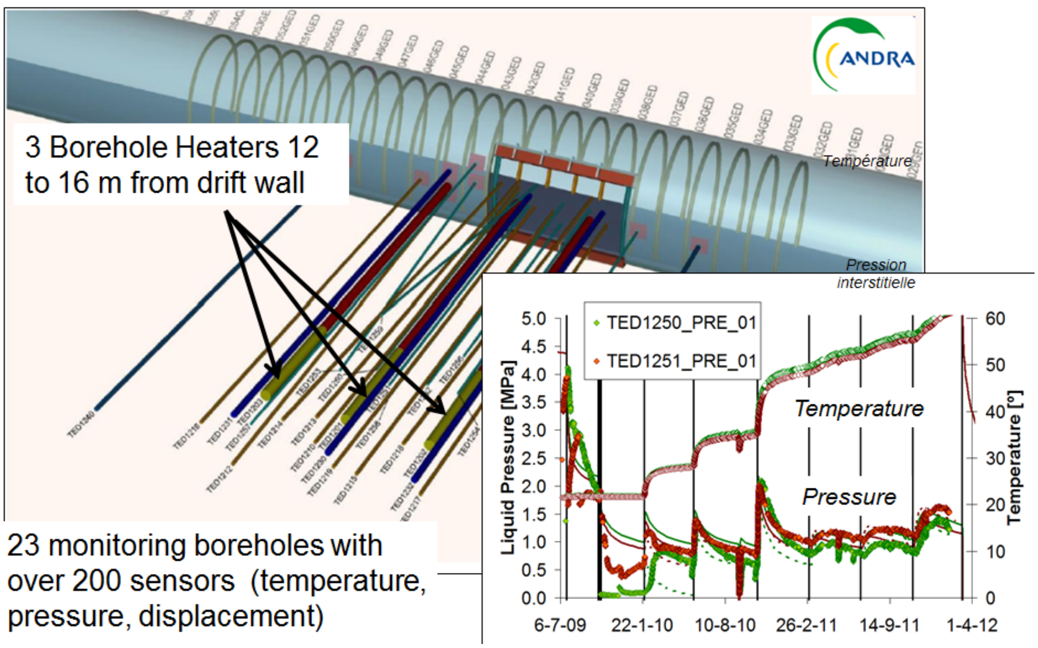

Figure 5-2. The schematic of the TED experiment at Bure. The insert on the figure is the graphs of pressure and temperature evolution, which were used by modeling teams in DECOVALEX-2019 Task E for interpretative modeling.

The purpose of Step 2 is to model the THM response of COx claystone in the TED experiment and to calibrate the numerical models against experimental data. This modeling of the TED experiment will also help improve understanding of physical phenomena observed.

The domain geometry simulated is a cube with a side length of 50 m. The model represents only a half of the GED drift (Figure 5-3). Three heaters are embedded at the center of the domain with surrounded refined grids. For the modeling purposes, it is assumed that the whole domain is saturated and remains saturated during the experiment. In previous work, the model started with instant excavation of the GED tunnel, followed by drilling of other boreholes. Then, at 506 days after excavation, the heating phase started and was running for 1251 days. Heater 1 was turned on first, and it took three steps to reach the planned heat power (600W). After Heater 1 had been turned on for 400 days, Heaters 2 and 3 were turned on to heat the domain, including three heat power steps. The highest power during the heating phase was about 600 W. A cylindrical EDZ of 1m thick was simulated around the GED tunnel. The effect of the variability of permeability due to excavation was simulated (Figure 5-3a). The THM simulations were conducted using the simulator TOUGH-FLAC, using water properties calculated from the steam table equations (IFC-1967). We have recalibrated thermal conductivity, mechanical properties and permeability of COx rock, because we applied other conditions, such as the drainage boundary. All parameters utilized in the current model are summarized in Table 5-1.

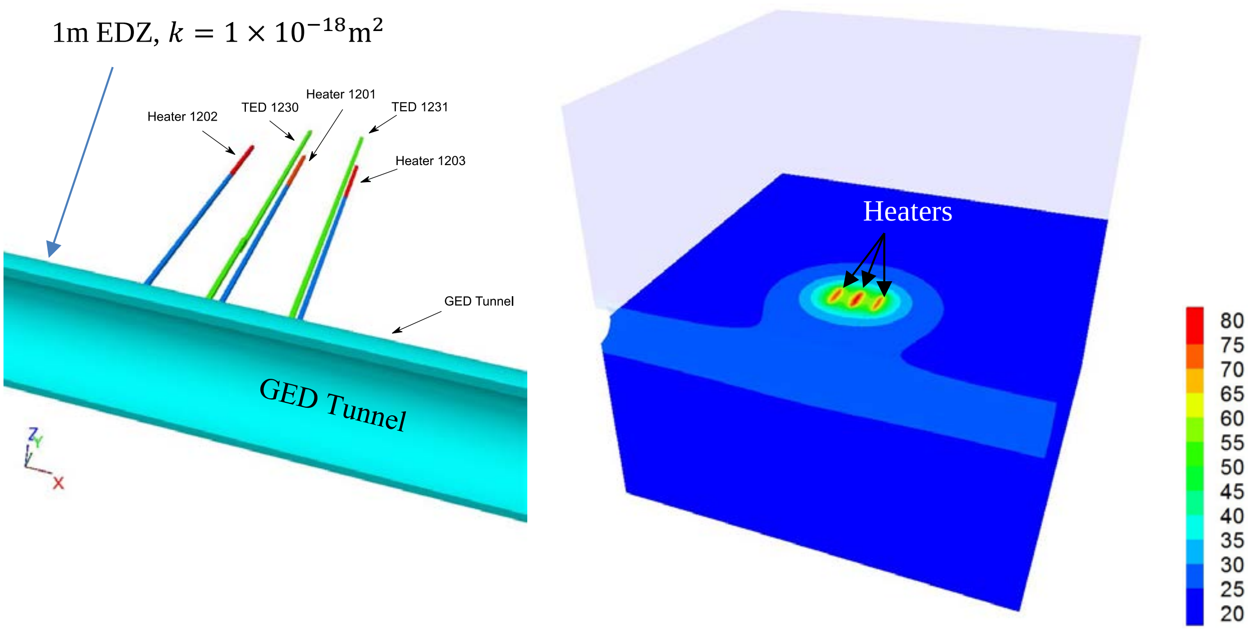

a) b)

Figure 5-3. (a) The model showing the position of heater boreholes (Heaters 1201, 1202, and 1203), extensometer boreholes (TED 1230 and 1231), and GED tunnel surrounded by 1m EDZ, and (b) Temperature distribution at 1509 days.

In TED experiment, six sensors were placed at different boreholes near heaters to measure the temperature evolution during the heating stage. The collected data were used as a basis for calibration of thermal properties. Figure 5-4 displays the recent temperature results based on the results of simulations with calibrated parameters. As the figure shows, a good agreement at Boreholes 1210, 1219, 1250, and 1251 is achieved between the model prediction and the experimental data. The calibration of the thermal properties is generally acceptable, although the model simulation overestimated the temperature by about 3 ^{o}C to 5 ^{o}C at the two points farthest from the heater, Boreholes 1253 and 1258, but the experiment team reported that these two sensors were unreliable.

Table 5-1. THM parameters of Cox Argillite Step 2 used for THM simulations.

Parameters	Values
Porosity [-]	$\phi = 0.15$
Thermal conductivity parallel to bedding [W/m/K]	$\lambda = 2.05$
Thermal conductivity perpendicular to bedding [W/m/K]	$\lambda = 1.15$
Bulk density [kg/m^3]	$\rho = 2400$
Density of solid grains [kg/m^3]	$\rho_s = 2600$
Heat capacity of solid grains [J/kg/K]	$C_{ps} = 800$
Permeability parallel to bedding [m^2]	$K_\parallel = 3 \times 10^{-20}$
Permeability perpendicular to bedding [m^2]	$K_\perp = 0.7 \times 10^{-20}$
Biot coefficient [-]	$b = 0.7$
Volumetric coefficient of thermal expansion of solid grains [1/K]	$\alpha_s = 4.2 \times 10^{-5}$
Young's modulus parallel to bedding [GPa]	$E_1 = E_\parallel = 6$
Young's modulus perpendicular to bedding [GPa]	$E_3 = E_\perp = 3$
Poisson's ratio inside the bedding plane [-]	$\nu_{12} = 0.3$
Poisson's ratio between in bedding plane and out-of-plane [-]	$\nu_{13} = 0.3$
Water properties (ρ_w, c_w, C_{pw}, μ_w, α_w)	(IFC-1967)

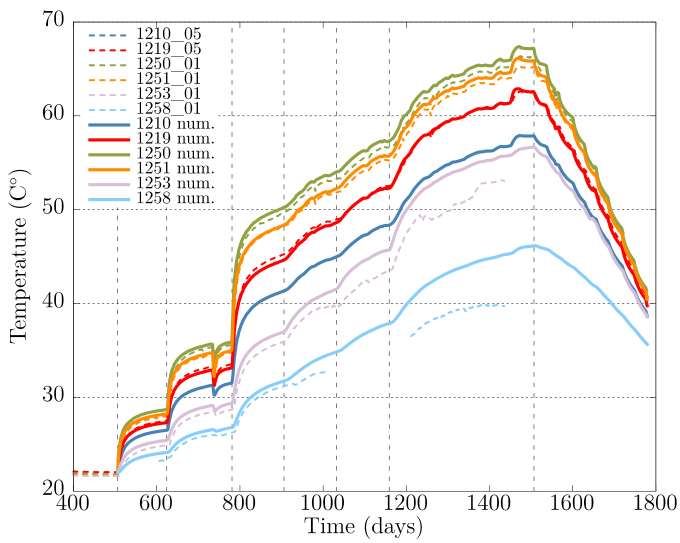

Figure 5-4. Temperature evolution simulated with calibrated thermal conductivity parallel and perpendicular to bedding at measuring points. Dashed lines are measurements at different monitoring points.

Figure 5-5a presents the simulation results and experimental observations of pore pressure at the sensor positions in Boreholes 1253 and 1258. From the figure, the simulated pore pressure at Borehole 1253 is in good agreement with experimental data recorded by the sensor. Although some disagreements of pore pressure at Borehole 1258 are noted, especially the pore pressure at the beginning of the heating phase, but after 800 days the predicted pore pressure agrees with experimental data. Figure 5-5b displays the simulated and observed pore pressure at five sensor positions in Borehole 1240. Compared with experimental data, the trend of pore pressure change has been captured while the magnitude of pore pressure at peak is underestimated. The model simulations with re-calibrated parameters provide a generally good comparison of predictions of temperature and pore pressure, although discrepancies exists especially before 400 days and after 1200 days. However, no measured data on stresses are available.

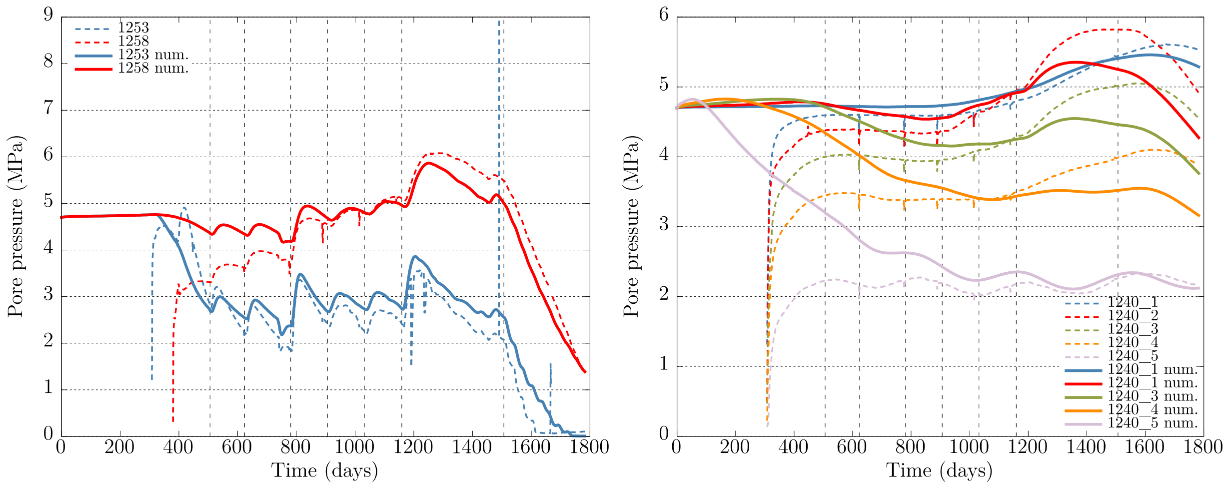

a) b)

Figure 5-5. a) Pore pressure evolution at Boreholes 1253 and 1258. b) Pore pressure evolution at Boreholes 1240.

5.2.3 Step 3: ALC experiment

The heating phase of the ALC experiment in the MHM URL started in 2013, and it is an ongoing *in situ* heating test. The experiment is a full scale representation of a single high-level waste cell in COx claystone. The ALC1604 micro-tunnel was drilled from the GAN drift. It has a total length of 25 m and includes different parts. The heated part in ALC experiment is located in the body part of ALC1604 between 10 and 25 m along the length (Figure 5-6), and is made up of five heating elements. Each element is 3 meters long and has a diameter of 508 mm. The ALC experiment was heavily instrumented with temperature and relative humidity sensors, piezometers, strain gauges, and displacement sensors. The temperature measurements made during the ALC experiment showed a similar phenomenon as in the TED experiment, indicating an anisotropic thermal conductivity. A conclusion about the anisotropy was made because the temperature was different at different locations at the same distance from the heater. In particular, the temperature increase is higher in the bedding plane than that in the perpendicular direction. Observations of pore pressure showed that its evolution is depended on the location with respect to the bedding, and strong hydro-mechanical (HM) coupling induces the opposite pore pressure change near ALC1604 after its excavation. In the vertical direction, the volumetric strain is positive (volumetric expansion), indicating the pore pressure decrease, because in the horizontal direction, the volumetric strain is negative (the volume decreases), causing the pore pressure increase.

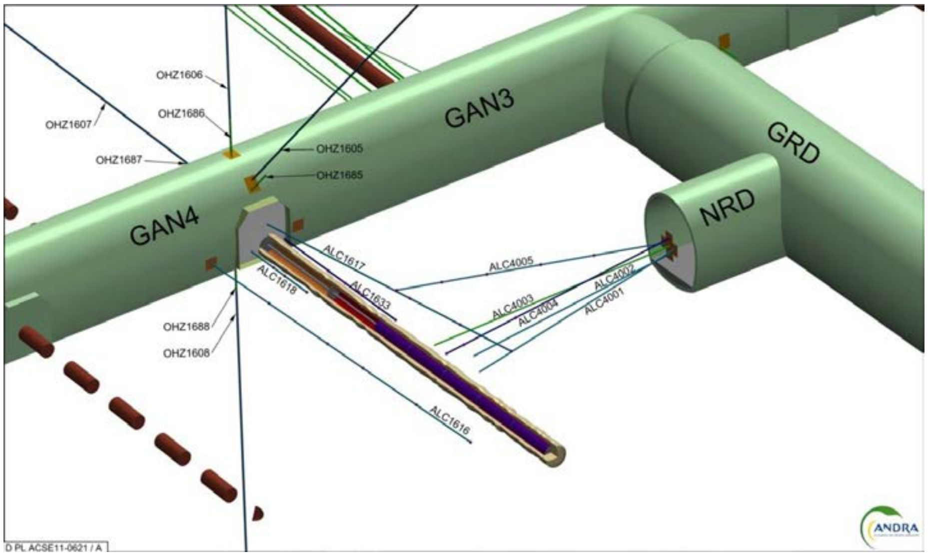

Figure 5-6. The ALC experiment at Bure with various monitoring boreholes and microtunnel ALC1604 that are used in DEOVALEX-2019, Task E, for interpretative modeling.

The purpose of Step 3 is to predict the THM response of COx claystone in the ALC experiment with calibrated material parameters from TED experiment. Modeling of ALC experiment will help investigate the behavior of the cell and the casing under thermal loading, and to understand the THM behavior of the COx and of the interface between the rock mass and the casing.

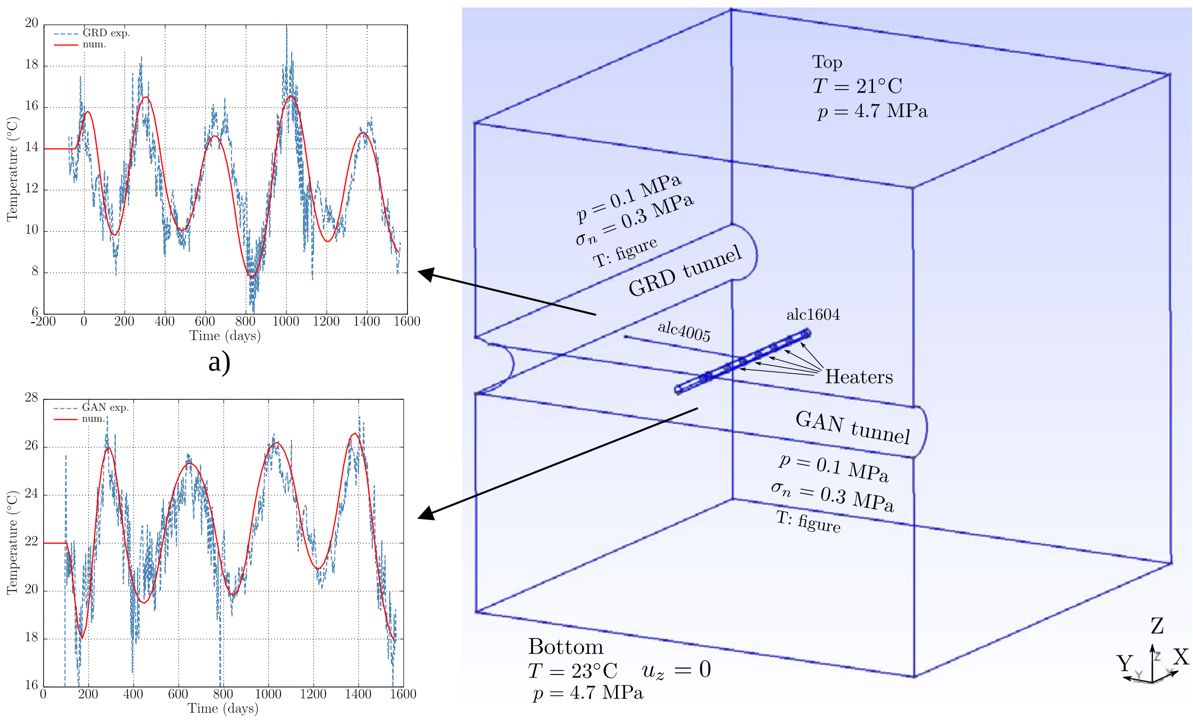

b) **c)**

Figure 5-7. Geometry of the model with boundary conditions: a) Observed and simulated temperature evolution at GRD tunnel; b) Observed and simulated temperature evolution at GAN tunnel; and c) Geometry of the simulation domain and boundary conditions on each surface.

The geometry model domain is a cube with a side length of 50 m centered in height at z = 0, with half of the GAN tunnel excavated along the *y*-direction, and half of the GRD tunnel excavated along the *x*-direction (Figure 5-7c). Five heating elements are located in ALC1604 between 10 and 25 m along *x*-direction. The heaters are discretized with refined elements. Casing and gap inside the borehole are both explicitly discretized (Figure 5-8). For modeling purposes, it is assumed that the whole domain is saturated and remains saturated during the experiment. An additional draining borehole, ALC4005, is explicitly simulated with excavation and drainage as Figure 5-7 shows.

In the simulation, the model started with instant excavation of GAN and GRD tunnels, followed by drilling of other boreholes. Then at 458 days after the excavation, the heating phase started and was running for about 1500 days. The time zero, corresponds to the excavation of tunnels, is at 11/01/2011. A heating test at a very low power (33 W/m, 495 W in total) was conducted between January 31 and February 15, 2013. The main heating phase started on April 18, 2013, at a constant nominal power of 220 W/m (3300 W in total) for the 15 m occupied by the heater elements (i.e., 660W per element). The initial pore water pressure is set constant at 4.7 MPa in the entire domain when excavation started. The initial stress field in the model are the best estimated from field investigations; the major horizontal stress σ_H is set to 16.1 MPa in *y*-direction, and the horizontal minor stress σ_h and the lithostatic stress σ_v are set respectively to 12.4 MPa and 12.7 MPa in the *x*-direction

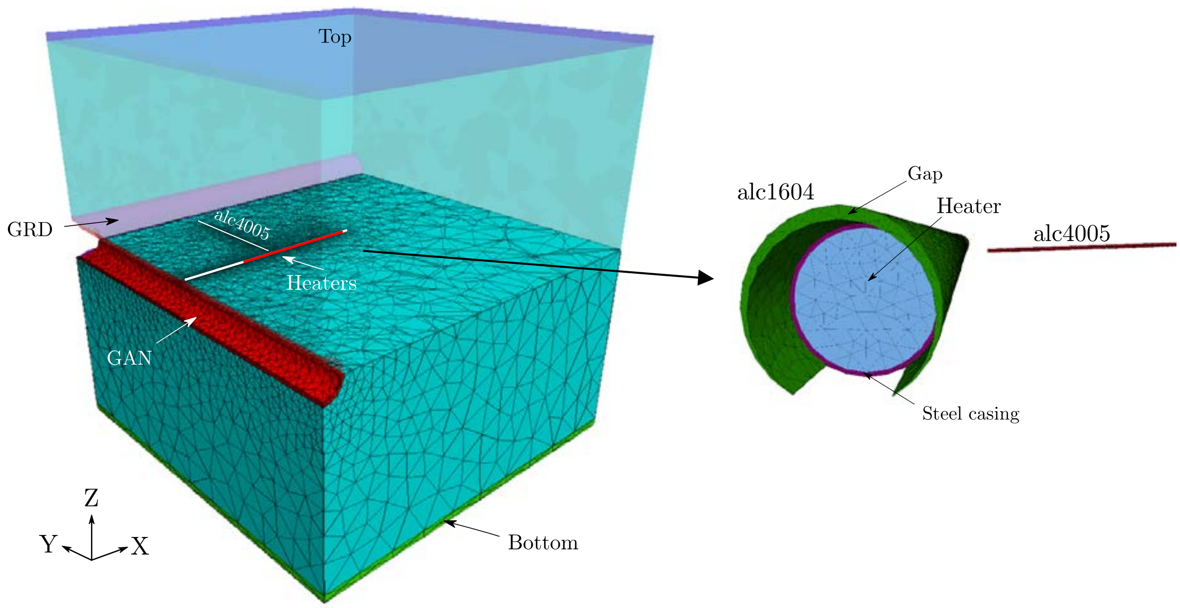

a) b)

Figure 5-8. Mesh generation in simulated domain. a) Mesh in the entire domain. b) Mesh generation for heater, casing and the gap between them.

The THM computation of the ALC experiment is conducted with the parameters, calibrated from the TED test, which are listed in Table 5-1. In the field, six sensors were placed in different boreholes near heaters to measure the temperature evolution during the heating stage. The collected data are used as a basis for calibration of thermal properties. Figure 5-9 displays a comparison of the simulated temperature with experimental data recorded by the sensors. The figure shows a good agreement between the model prediction and experimental data. However, at sensors 1617-1 and 1617-2, the model predicted higher temperature than observed data, while at sensors 1616-5 and 4005-4, the model underestimated the temperature. A possible explanation is that the simulation is based on an assumption of homogeneous host rock, while the in situ COx clay stone is heterogeneous.

In FY2019, we have compared numerical results of pore pressure and experimental field observations. Figure 5-10 presents a comparison of pore pressure monitored by the sensors in the boreholes and numerical results. The figure shows that the pore pressure decreases after the initial excavation of the GAN and GRD tunnels, which is due to the drainage conditions applied at the tunnel surface. Then, around 0 day, corresponding to the day of 10/23/2011, the drilling of the micro-tunnel ALC1604 is computed, and the results indicate the relevant hydro-mechanical (HM) coupling. Volumetric expansion due to excavation of ALC1604 occur at sensors 1617-1 and 1617-2, which are above ALC1604. As a result, pore pressure at these two positions decreases. In the horizontal direction, the volumetric compression occurs at sensors 1616-2 and 1616-5, which raises the pore pressure. After the heating started, the pore pressure increased due to the thermal pressurization, except at sensor 1616-5, which was close to the GAN tunnel, and was affected by the temperature boundary on the tunnel surface. Sensor 4005-4 shows a similar response. Since it is far from the heaters, the temperature changes are small and the peak of pore pressure is lower than that at other sensors. Based on the comparison, a good agreement at sensor 1616-2 during the heating phase is achieved between model prediction and measured data. The other results do not match the observations well enough. Therefore, in order to improve the numerical computation to better capture the evolution of the pore pressure, we launched parametric studies on different rock properties in Step 3, which helps us understand THM processes in COx host rock.

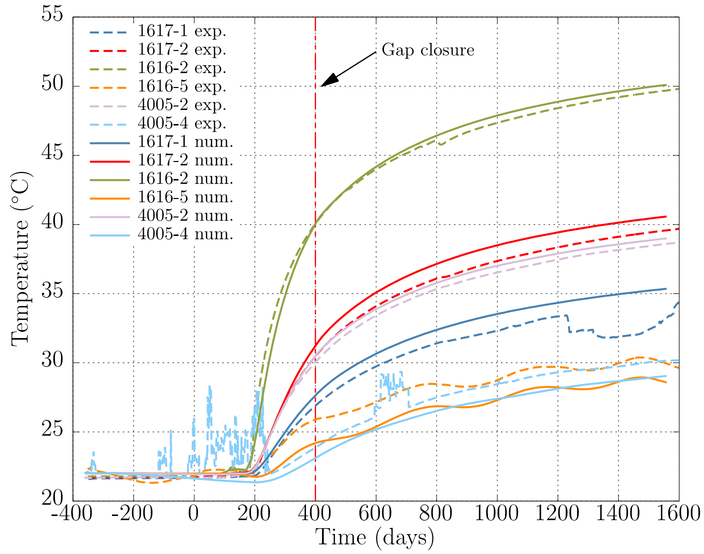

Figure 5-9. Simulated and observed temperature evolution at monitoring points.

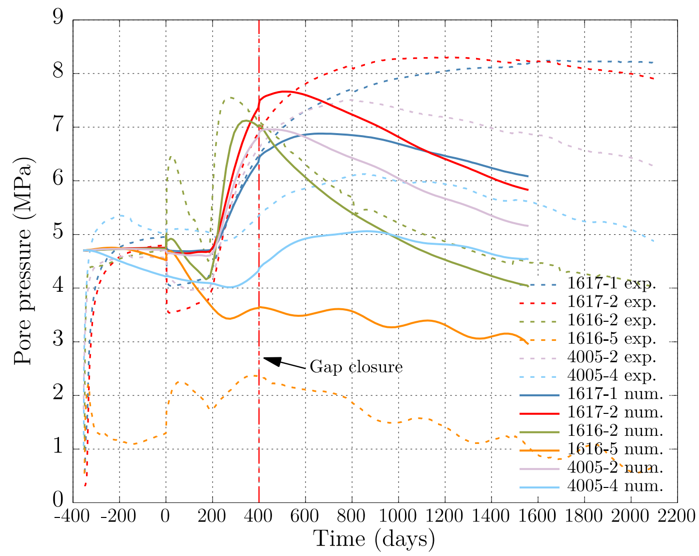

Figure 5-10. Simulated and observed pore pressure evolution at monitoring points.

5.2.3.1 Parametric study

In this section, we present parametric studies on Biot's coefficient, bulk modulus, and permeability of COx claystone, which were conducted in FY2019 to investigate the effects of these variables and to improve the model prediction against the experimental observations. Three Biot's coefficients ($b = 0.6$, 0.7, and 1) were assigned in the COx claystone, and each model was computed with the given value of the Biot coefficient. All other parameters were kept the those listed in Tabel 5-1. Based on the results presented at Figures 5-11a to 5-11f, in general, the peak pore pressure is reduced with the decrease of Biot's coefficient. However, the change of Biot's coefficient does not affect the trend of the simulated pore pressure evolution. Thus, the only change on Biot's coefficient does not help improve the prediction of pore pressure. Figure 5-12a to 5-12f present the parametric study of the effect of the bulk modulus. The previous simulation with $E_1 = 3$ GPa and $E_3 = 6$ GPa is chosen as the basic case. In another case, we increased the horizontal and vertical bulk moduli by the same factor, e.g. a factor of 2 increase, so the claystone keeps the same anisotropy ratio as the basic case (Figure 5-12). The results of modeling show that the increase of the bulk moduli causes the pore pressure to increase during the accumulation process and to decreases during the reduction process. However, the bulk modulus change does not affect the trend of the simulated pore pressure as it was found for the effect of changes of Biot's coefficients. Figures 5-13a to 5-13f illustrate the effect of changes permeability on the pore pressure evolution. In general, the reduction of permeability enhances the pore pressure accumulation but delays the time of the peak of pore pressure. Thus, permeability change indeed affects the pore pressure evolution curve. Through this study, we can expect that lower permeability will help to capture the pore pressure evolution trend at Sensors 1617-1 and 1617-2. However, it will worsen the prediction of pore pressure at Sensor 1616-2. Beside that, too small permeability does not represent the real property of COx claystone. Therefore, with the current parametric studies on Biot's coefficient, bulk modulus, and permeability, we do not achive a good agreement on pore presure between numerical computation and measured field data.

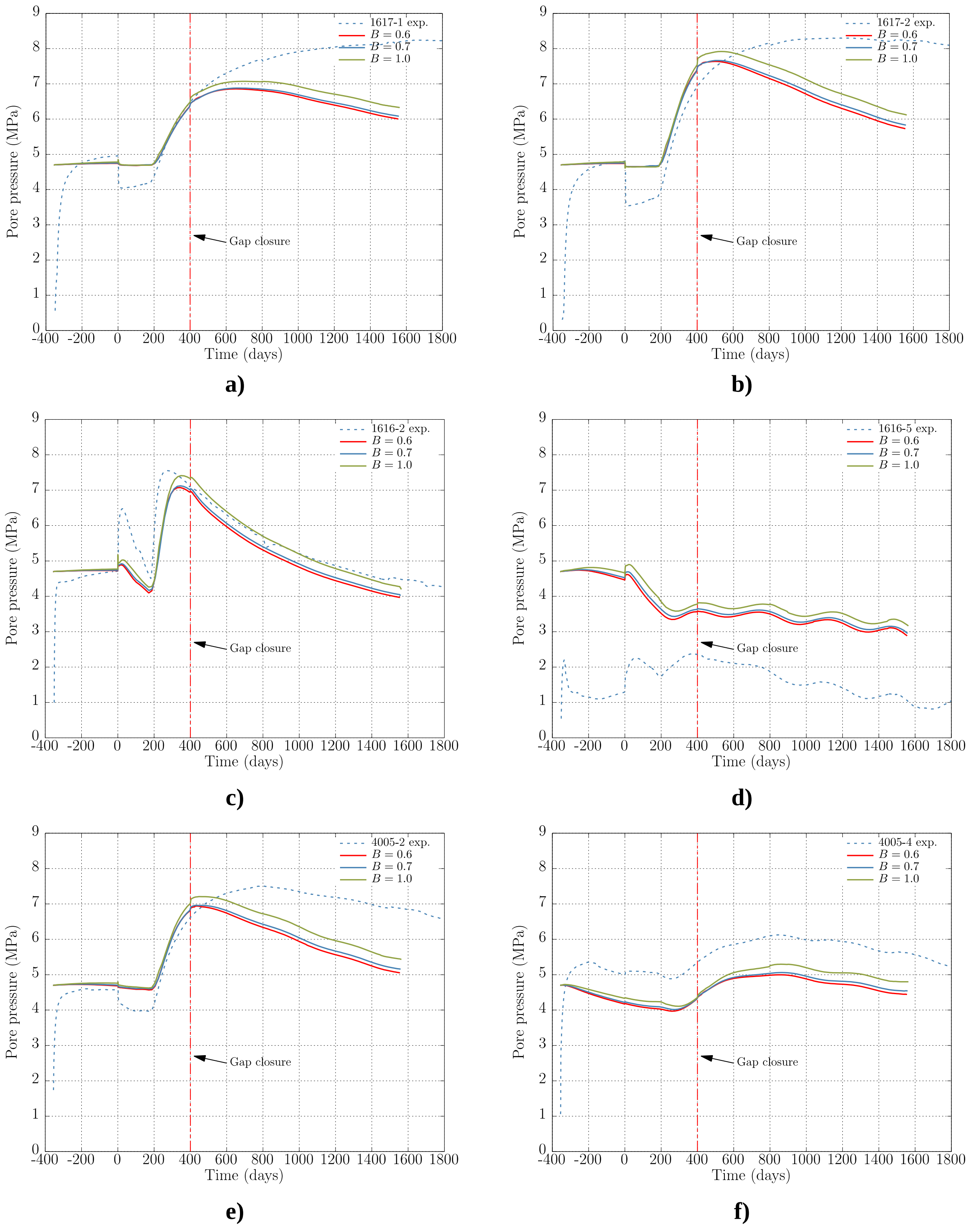

Figure 5-11. Simulated pore pressure evolution for various Biot's coefficients at different sensor points: a) Sensor 1617-1, b) Sensor 1617-2, c) Sensor 1616-2, d) Sensor 1616-5, e) Sensor 4005-2, and f) Sensor 4005-4.

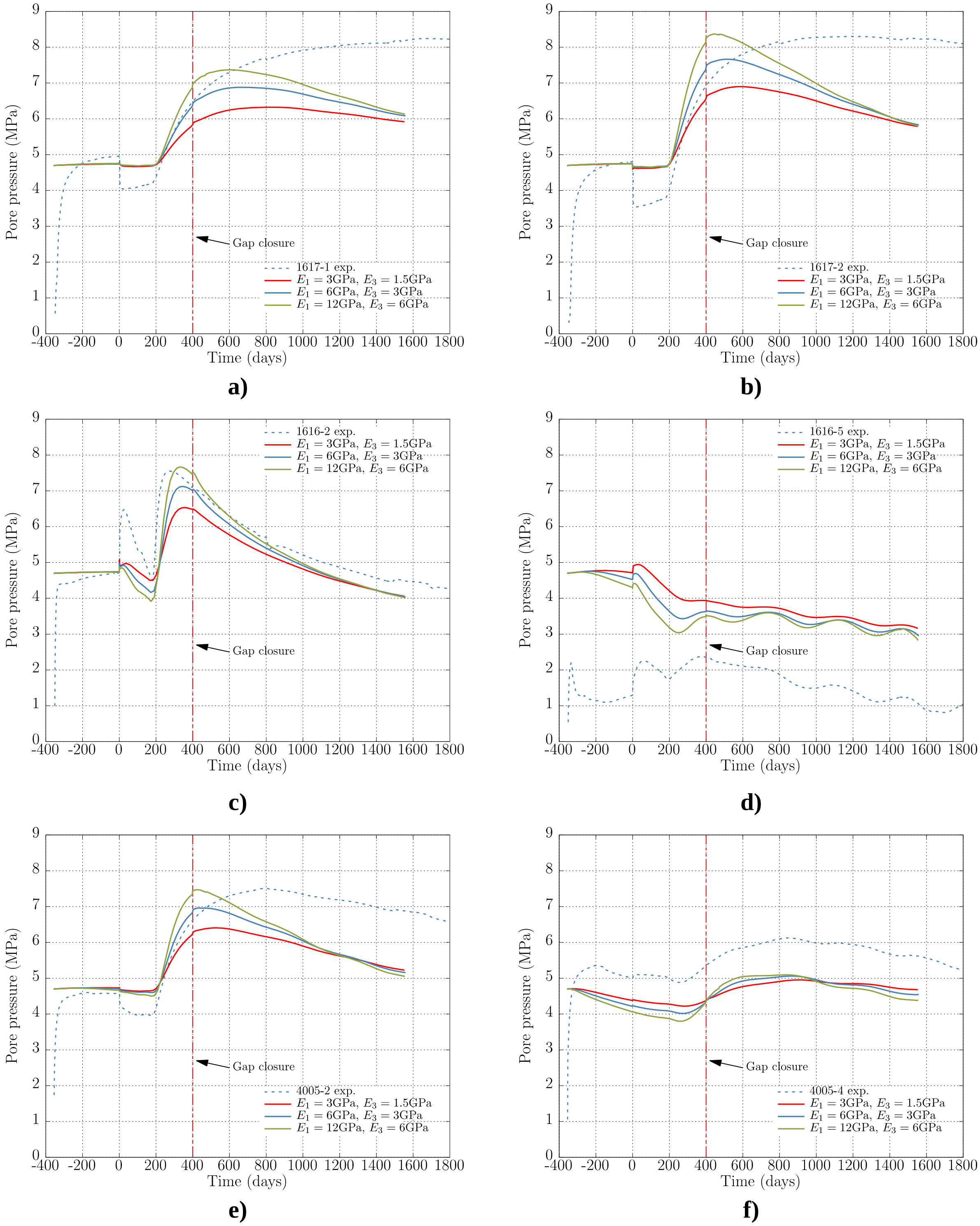

Figure 5-12. Simulated pore pressure evolution for various bulk moduli at different sensor points: a) Sensor 1617-1, b) Sensor 1617-2, c) Sensor 1616-2, d) Sensor 1616-5, e) Sensor 4005-2, and f) Sensor 4005-4.

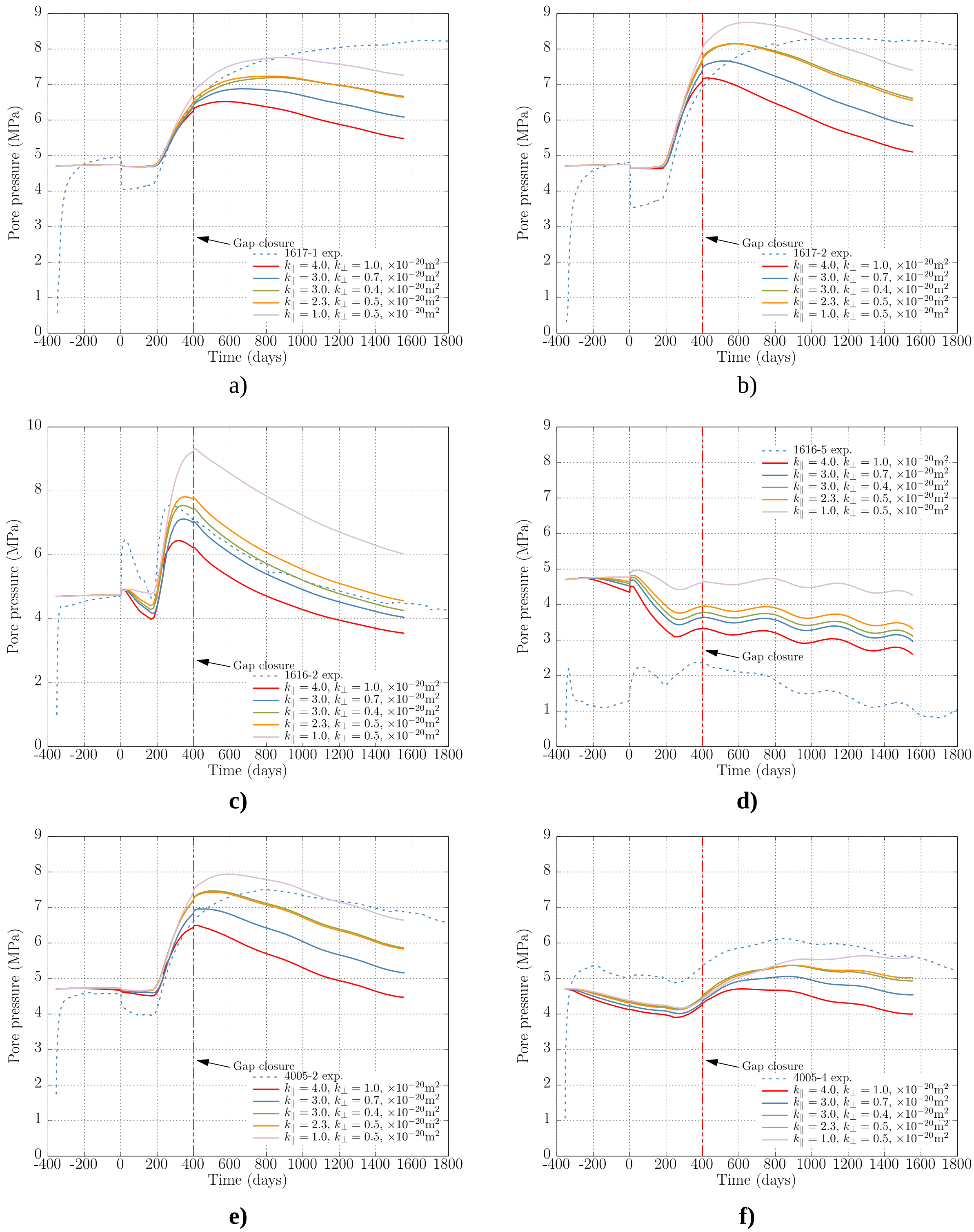

Figure 5-13. Simulated pore pressure evolution for various permeability at different sensor points: a) Sensor 1617-1. b) Sensor 1617-2. c), Sensor 1616-2, d) Sensor 1616-5, e) Sensor 4005-2, and f) Sensor 4005-4.

5.2.4 Step 4: Model at the repository scale

Step 4 is to predict the behavior of claystone with several parallel cells at the repository scale. Following the French concept, the High-Level Waste (HLW) packages will be placed in a set of parallel micro-tunnels of 0.75 m to 0.80 m diameter and 150 m length (Figure 5-14). The HLW zone covers an area of around 8 km². The 3D geological model of the Callovo-Oxfordian has been developed progressively since the start of the 2000s as the field investigations have progressed, based on the results of investigations performed in deep boreholes and at the underground laboratory. The main objective of Step 4 is to investigate how to develop a reliable numerical model for THM simulations at the repository scale (i.e., representative of several parallel cells distributed within several hundreds of meter). This step differs from the previous ones in the way that it is not a benchmark study. This study is focused on modeling to assess differences and impact from different modeling approaches among the different research teams in this DECOVALEX Task.

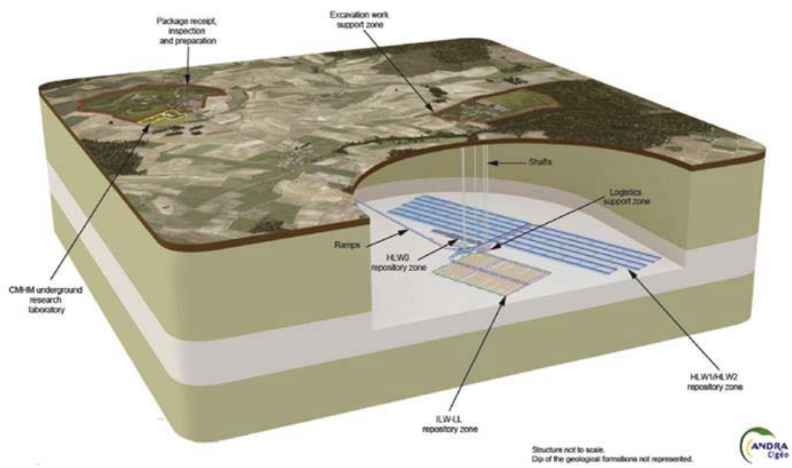

Figure 5-14. Diagram of the facilities of the Cigeo project.

5.2.4.1 Model strategy

We proposed a specific model strategy for Step 4. In the area surrounding the parallel cells, we refined the numerical mesh to allow for a detailed representation of temperature, pore pressure and effective stress, and generated a coarse mesh in the far-field domain. To link the detailed and coarse meshes, we assigned the special interface elements to attach the nodes on both sides. For cells at the edge of the disposal domain, we simplified small cylindrical cell heat sources into one planar heat source to reduce the element number and computational time. The diagram of this model strategy is summarized in Figure 5-15.

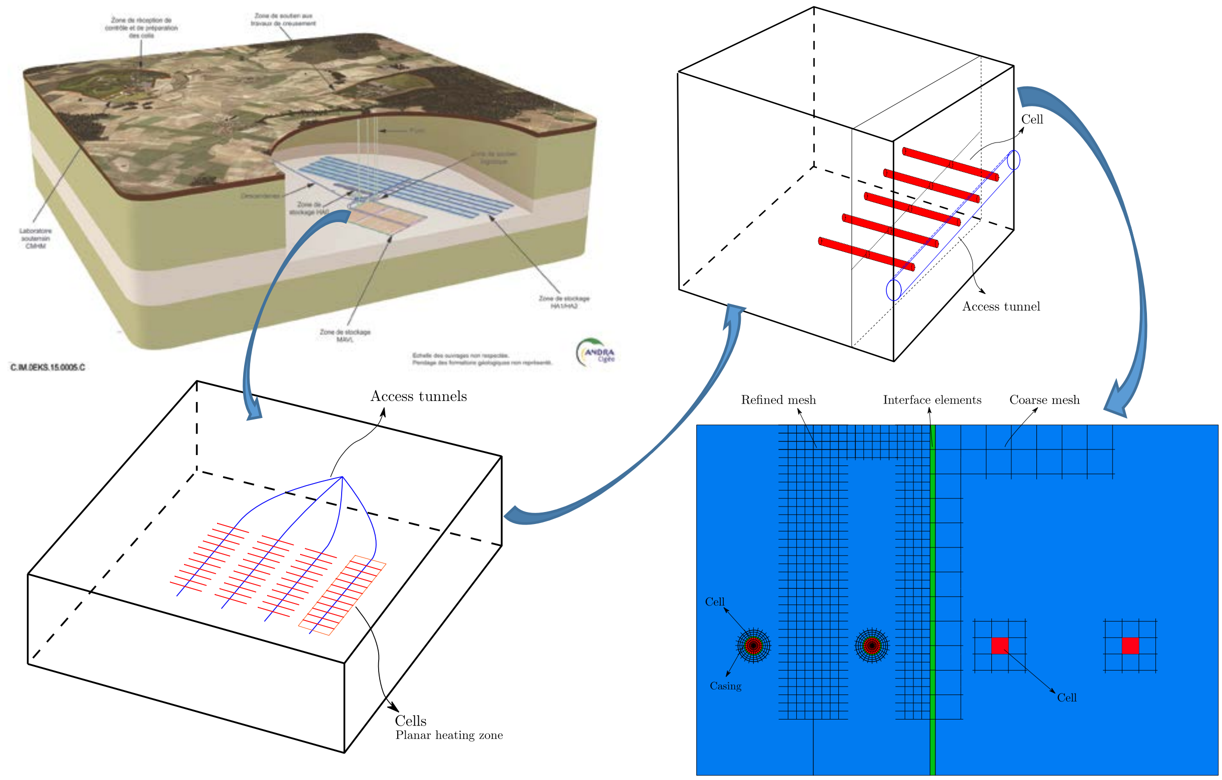

Figure 5-15. Diagram illustrating the development of a conceptual model at the repository scale and a numerical model for the THM simulations at the cell scale.

Vertically, the principal mineralogical phases are sedimented in continuous sequences. The Callovo-Oxfordian formation is predominantly composed of three principal mineralogical phases (UA, UT, and USC) of varying proportions in the thickness of the layer. The detailed THM parameters of the COx claystone and surounding formations obtained in different boreholes in field are measured in the laborotary. The geological information is illlustrated in Figure 5-16 for the 2D model, and Table 5-2 summaries all prameters, which were utilized in the THM simulation for each rock layer. In the developed model, the diameter of the micro-tunnel is 0.8 m, and the distance between two parallel cells is 52.3 m. Currently, the excavated access tunnel is not explicitly presented in the modeling domain. In COx claystone, we placed 16 cells in the layer of UA2-UA3 at the depth of 600 m. Modeling started by simulations of the instant excavation of parallel cells, followed simulations of the drainage of the mirco-tunnels for 2 years before canisters were placed. The heat power is assumed to be 146 W/m at 2 years, then it decays following the pattern shown in Figure 5-17.

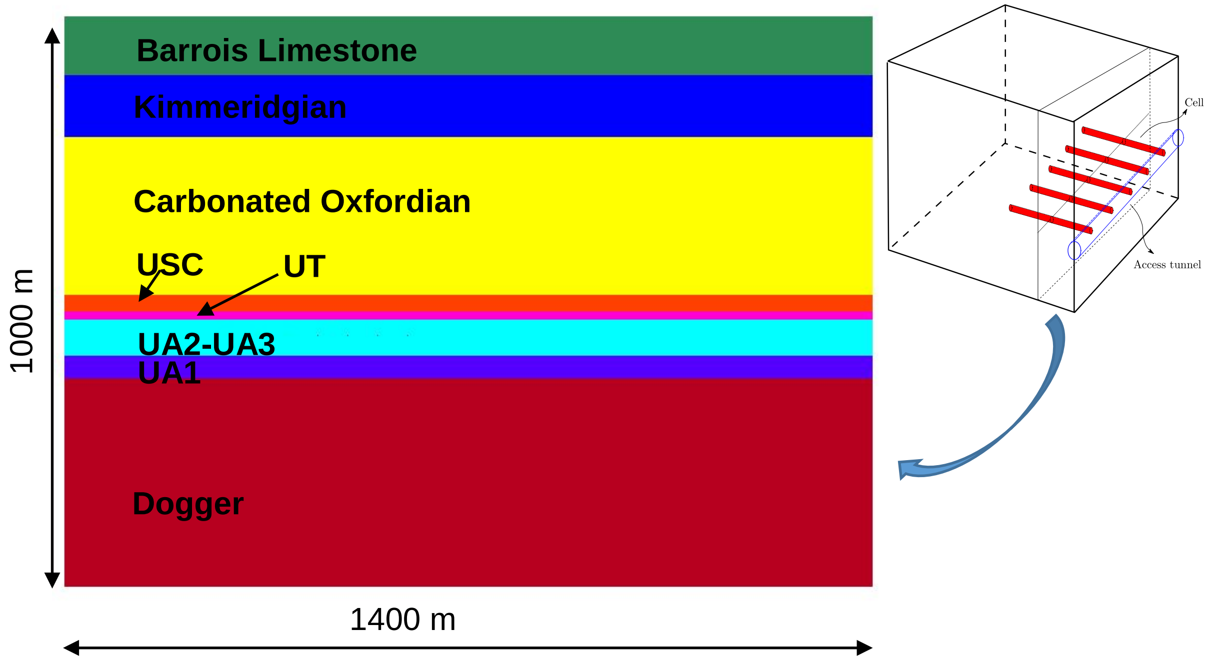

Figure 5-16. Diagram of a 2D model to represent the geological formation.

Table 5-2. THM parameters of different rocks used for modeling in Step 4.

Rocks	n	ρ	b	E	ν	α_s	K	$\lambda_\perp$	$\lambda_\parallel$	C_p	Depth
	-	kg/m^3	-	GPa		1/C	m^2	W/m/K	W/m/K	J/kg/K	M
Barrois Limestone	0.13	2450	0.6	3.6	0.3	2.20E-05	1.00E-19	1.1	1.54	1024	0-103.4
Kimmeridgian	0.13	2450	0.6	3.6	0.3	2.20E-05	1.00E-19	2.1	2.94	1024	103.4-211.4
Carbonated Oxfordian	0.13	2470	0.6	30	0.3	4.50E-06	1.00E-16	2.3	2.3	925	211.4-488
USC	0.15	2480	0.6	12.8	0.3	2.00E-05	5.60E-20	1.79	1.79	978	488-517.4
UT	0.173	2450	0.6	8.5	0.3	2.00E-05	5.60E-20	1.47	2.205	978	517.4-532.6
UA2-UA3	0.193	2430	0.6	7	0.3	2.00E-05	5.60E-20	1.31	1.965	978	532.6-595.8
UA1	0.164	2460	0.6	12.5	0.3	2.00E-05	5.60E-20	1.63	2.445	978	595.8-635
Dogger	0.1	2470	0.6	30	0.3	4.50E-06	1.00E-18	2.3	2.3	925	635-1000

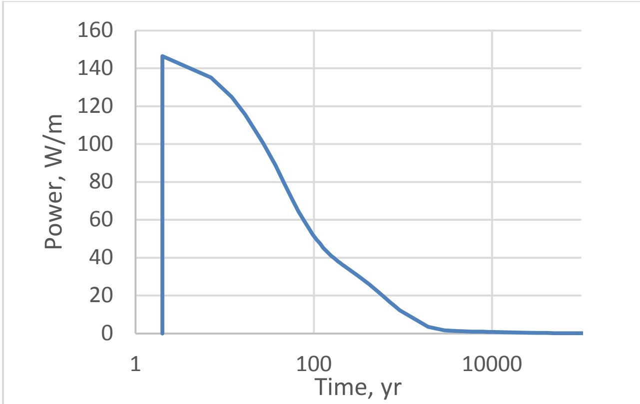

Figure 5-17. The pattern of the planned heat power for each cell.

In this report, we present only the simulated results at in middle cross section (at mesh points from P1 to P9) located between the two adjacent cells as displayed in Figure 5-18.

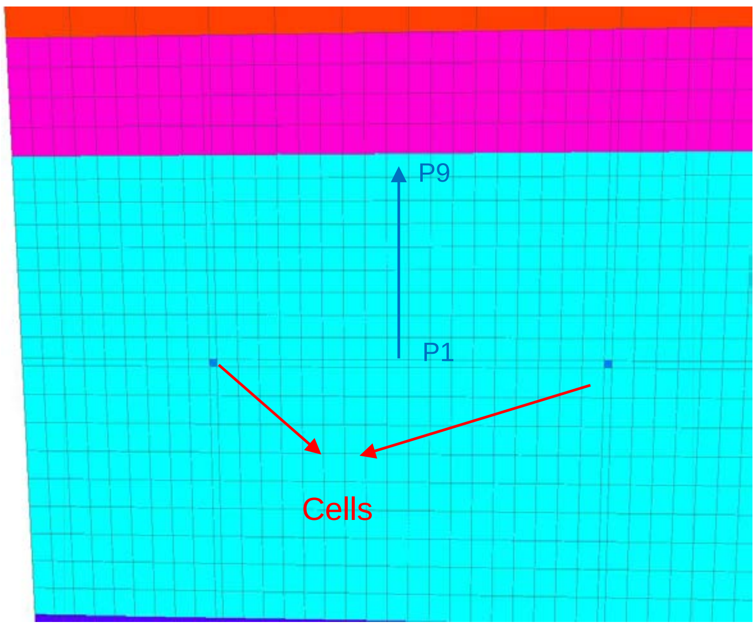

Figure 5-18. Layout of mesh points P1 to P9 used to represent the results of simulations in Step 4.

Figure 5-19 presents the results of simulations of temperature during the heating phase, and it shows that the peak temperature of about 46°C is reached at about 400 years, then it decreases to the background temperature for a long-term period (> 20,000 years). Figure 5-20 displays the simulated results of the pore pressure evolution, and it demonstrates the peak pore pressure is about 10 MPa at about 100 years, which is hundreds years earlier than the moment when peak temperature reaches. Then the pore pressure decreases to hydrostatic pressure in the geological formations. Figure 5-21 presents the Terzaghi's vertical effective stress, which is the different between the total vertical stress and pore pressure, and shows the effective stress reduces from 8 MPa to 4 MPa. As the result of that, the claystone is still under compression, so no hydraulic fracturing happens based on this simulation.

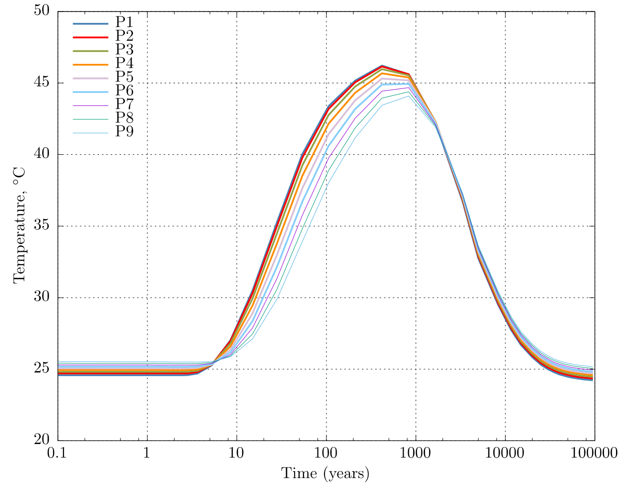

Figure 5-19. Simulation results of temperature at Points P1 to P9 in Step 4.

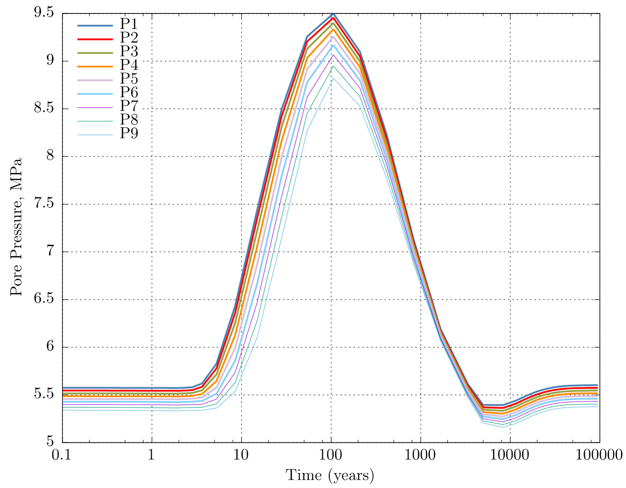

Figure 5-20. Simulation results of pore pressure at Points P1 to P9 in Step 4.

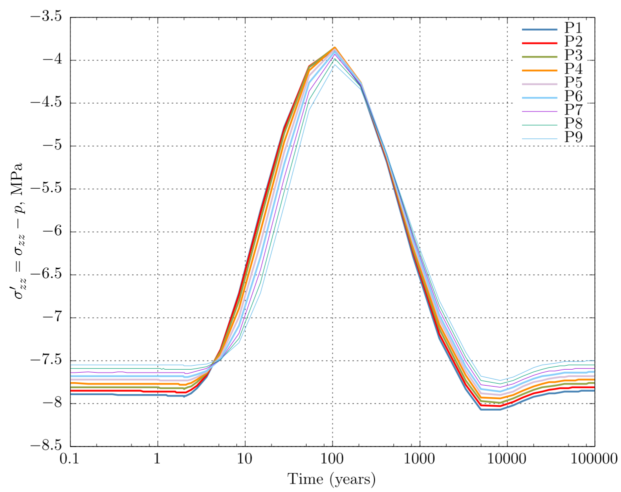

Figure 5-21. Simulation results of Terzaghi's effective stress at Points P1 to P9 in Step 4.

For a 3D model, we extended the 2D slice model along the out-of-plane direction. Because of the symmetric boundary, we considered 4½ heating zones as Figure 5-22 shows. The far-field two heating zones were simplified as two heat planes. The results of simulations obtained for the same mesh points as in the 2D model are plotted in Figures 5-23 to 5-25. From the 3D simulation results, the peak temperature of about 48°C was reached at around 800 years, while the peak pore pressure of about 11 MPa was reached at around 400 years. Figure 5-25 presents the Terzaghi's vertical effective stress, and shows the effective stress reduced from 8 MPa to 2 MPa. Thus, the claystone remains under compression, and no hydraulic fracturing happens based on the results of 3D simulations. The peak temperature in the 3D modeling in higher tha in the 2D modeling, which may be due to the use of planar heating zones, which is an approximation. In future work, we will simulate more cases to determine if the utilization of planar heating zones is suitable to achieve the goal of the development of a reliable repository scale model.

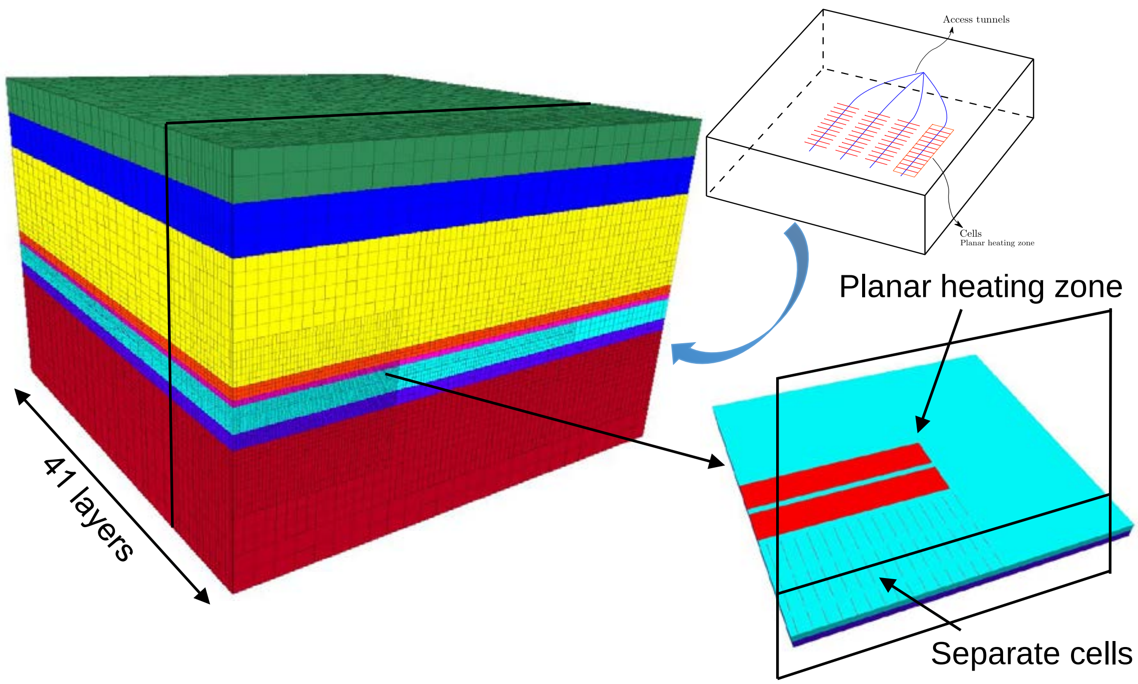

Figure 5-22. 3D model used for simulation in Step 4.

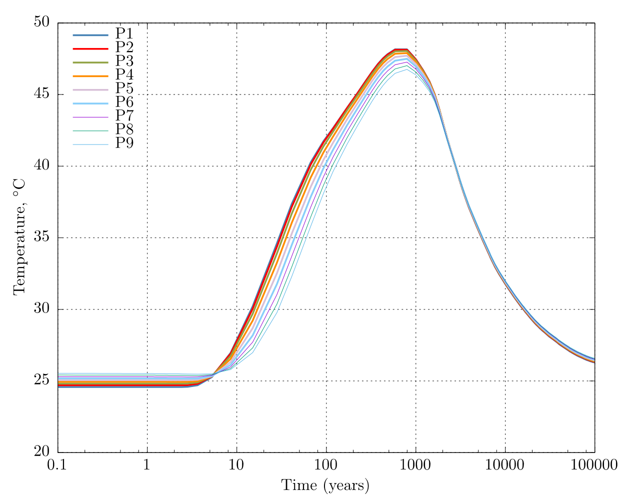

Figure 5-23. Temperature graphs from 3D simulations in Step 4.

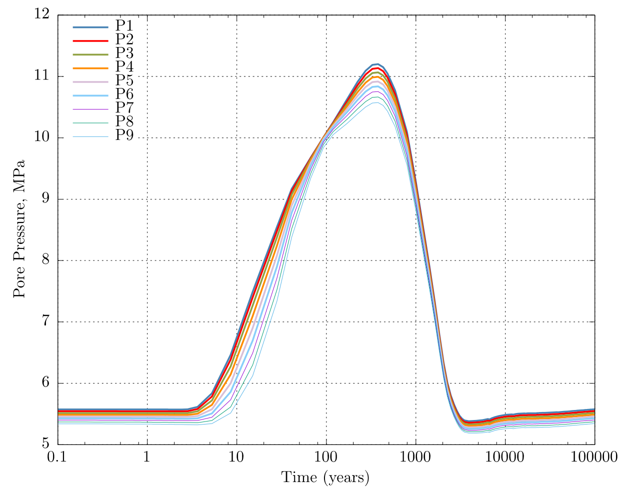

Figure 5-24. Pore pressure graphs from 3D simulations in Step 4.

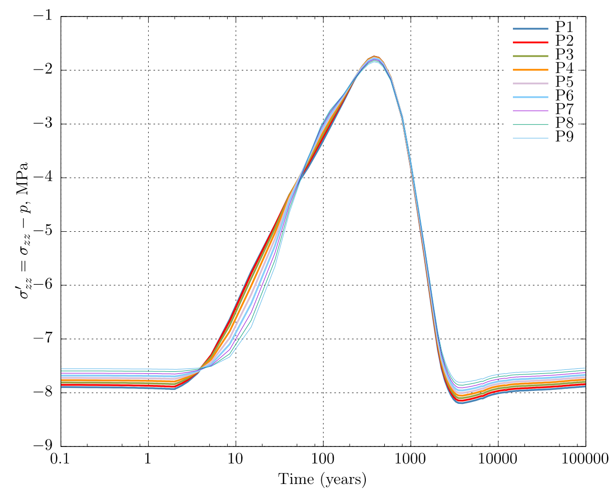

Figure 5-25. Terzaghi's effective stress graphs from 3D simulations in Step 4.

5.3 Summary and Status of the Bure Heater Experiment Modeling

In FY2019, along with Task E of the DECOVALEX-2019 project, we have updated the model to simulate coupled THM processes associated with the large scale ALC in situ heating experiment performed in COx claystone, and conducted new simulations to predict THM processes at the repository scale. The current progress on this task is:

For Step 1, we have achieved a good agreement of temperature, pore pressure, stresses, and displacements between our model simulations and theoretical solutions.

For Step 2, we have determined THM parameters of claystone from the TED experiment, including calibration of the thermal conductivity to match the temperature evolution during the heating phase, and back analysis of the simulation results to determine permeability. The heating phase of the TED experiment has been simulated with TOUGH-FLAC with good match to experimental data.

For Step 3, we predicted the THM behavior of COx claystone during the ALC experiment by utilizing parameters of claystone from those calibrated from modeling of the TED experiment. The heating phase of the ALC experiment has been simulated with TOUGH-FLAC and compared the simulation results with experimental temperature and pore pressure data. We conducted parametric studies of Biot's coefficient, bulk modulus and permeability of COx claystone to investigate their effect on the pore pressure evolution. However, further investigations are needed to improve predictions of the pore pressure.

For Step 4, we have conducted the initial 2D and 3D THM simulations of the parallel cells at the repository scale.

The research for the rest of FY2019 will be focused on simulations related to Step 4 of DECOVALEX-2019 Task E, including model predictions at the repository scale of an area with several high level waste cells, comparison of 2D and 3D models to correctly capture the observed temperature and pore pressure patterns, and evaluation of a possibility of the hydraulic fracturing during the heating phase.

6. MODELING OF GAS MIGRATION IN CLAY USING TOUGH-FLAC AND TOUGH-RBSN (DECOVALEX-2019)

In this section, we present LBNL's activities for modeling gas migration in clay related to Task A of the DECOVALEX-2019 project. This is an international collaborative activity, in which DOE and LBNL gain access to the results of unique laboratory experiments of gas migration. These results are now used for numerical modeling to better understand the processes, to improve numerical models, and which will ultimately be applied in the performance assessment of nuclear waste disposal in host clay rocks and bentonite backfill. The Task A of DECOVALEX-2019 is coordinated by the British Geological Survey (BGS), that is also sharing their extensive data set on coupled THM responses during gas migration in bentonite and clay stone. In FY2019, LBNL has continued to participate in Task A of DECOVALEX-2019 and conducted new simulations of spherical gas flow through bentonite with comparison to the experimental data. In the following sections, we address the issues of gas migration, the description of the Task A experiments, and modeling results compared with experimental data.

6.1 Gas Migration in Clay

Gas migration in clay-based buffer materials has been the subject of a number of international research programmes in the field of nuclear waste disposal, including both laboratory scale and *in situ* experiment (e.g., Horseman et al., 2004; Harrington et al., 2012; Cuss et al., 2014). Substantial insight has been gained in the phenomenology of gas transport processes in bentonite and claystone under different THM conditions. A number of model approaches have been proposed for the interpretation of the experimental results and for the analysis of gas release scenarios from geological repositories in the context of long-term safety assessment. The predictive capability of the gas transport models is yet limited, indicating that basic mechanisms of gas transport in bentonite are not understood in sufficient detail to provide the ground for robust conceptual and quantitative models.

The processes governing the movement of repository gases through bentonite and argillaceous host rocks can be split into two components: (1) molecular diffusion (assumed to be governed by Fick's law), and (2) bulk advection (Harrington, 2016). In repository concepts such as the Swedish KBS-3, corrosion of metallic materials under anoxic conditions will lead to the formation of hydrogen. Radioactive decay of the waste and the radiolysis of water are additional source terms. If the rate of gas production exceeds the rate of gas diffusion within the pores of the barrier or host rock, a discrete gas phase will form. Under these conditions, gas will continue to accumulate until its pressure becomes sufficiently large for it to enter the surrounding material.

Four primary phenomenological models describing gas flow, shown in Figure 6-1, can be defined as following: (1) gas movement by diffusion and/or solution within interstitial fluids along prevailing hydraulic gradients; (2) gas flow in the original porosity of the fabric, commonly referred to as viscocapillary (or two-phase) flow; (3) gas flow along localized dilatant pathways, which may or may not interact with the continuum stress field; and (4) gas fracturing of the rock similar to that performed during hydrocarbon stimulation exercises (Harrington, 2016).

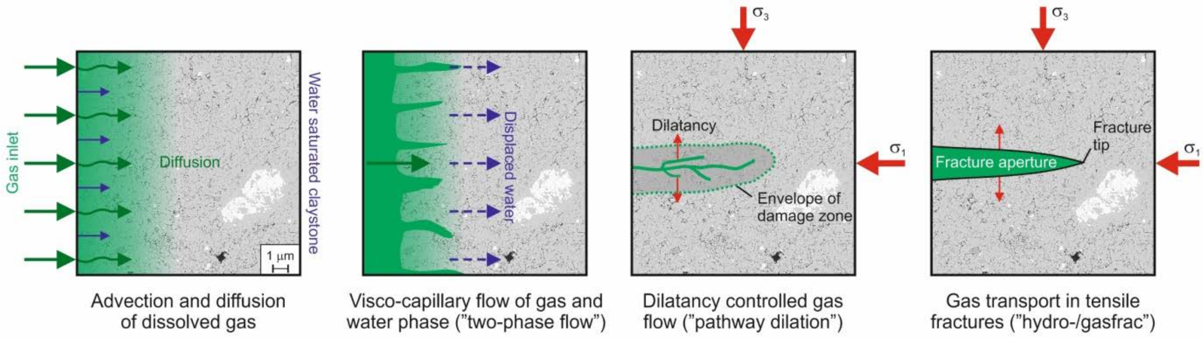

Figure 6-1. Conceptual models of gas flow (Harrington, 2016)

Studies on gas migration in clays (Horseman et al., 1999; 2004; Harrington and Horseman, 1999) indicate that classic concepts of porous medium two-phase flow are inappropriate and continuum approaches to modeling gas flow may be questionable, depending on the scale of the processes and resolution of the numerical model. However, the detail of the dilatant mechanisms controlling gas entry, flow and pathway sealing are unclear. As such, development of new and novel numerical representations for the quantitative treatment of gas in clay-based repository systems is therefore required (Harrington, 2016).

6.2 LBNL Model Approaches for Gas Migration

LBNL is exploring two different approaches for modeling gas migration associated with DECOVALEX-2019, Task A (Figure 6-2):

1) Continuum modeling approach using TOUGH-FLAC simulator (Rutqvist et al., 2011), and

2) Discrete fracture modeling approach using TOUGH-RBSN simulator (Kim et al., 2017)

The two approaches are complementary. The continuum approach is based on current developments and applications of TOUGH-FLAC for the modeling of long-term THM performance of nuclear waste repositories in clay host rocks. The TOUGH2 code and other continuum models have been used in the past to model gas migration in clay considering heterogeneous clay properties with pressure dependent permeability, but without considering geomechanical coupling (e.g., Senger and Marschall, 2008; Senger et al., 2014). In this study, such a continuum approach will be extended to include full geomechanics coupling within the framework of TOUGH-FLAC. The discrete fracture modeling approach is based on current development of the TOUGH-RBSN simulator, in which the opening of grain boundaries for dilatant gas migration is modeled explicitly using a fracture mechanics approach. The TOUGH-RBSN has previously been applied for modeling fluid driven hydraulic fracturing and complex fracturing in clay host rocks (Kim et al., 2017). The TOUGH-RBSN should be suitable for modeling of complex flow paths associated with dilatant gas migration in clays.

In FY2018, we completed the simulations for Stage 1 – 1D gas migration in saturated bentonite samples using both TOUGH-FLAC and TOUGH-RBSN simulators. In FY2019, we have continued to work on Stage 2 – spherical gas migration, for which only the TOUGH-RBSN simulator was employed. In the following section, new model concepts and updated simulation results will be presented.

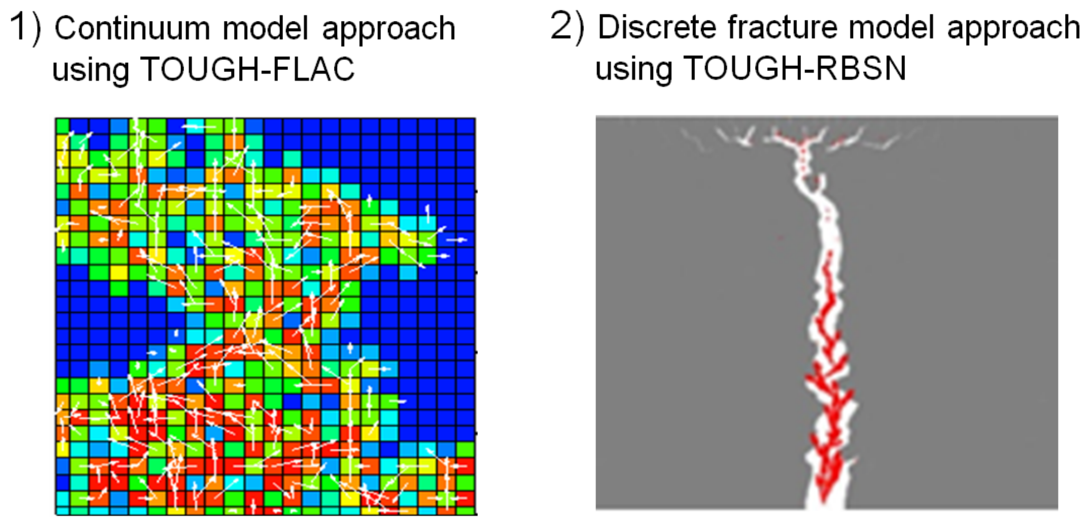

Figure 6-2. Schematic of modeling approaches employed by LBNL for modeling gas migration through clay associated with DECOVALEX-2019 Task A. To the left, the continuum approach using TOUGH-FLAC is illustrated involving heterogeneous properties with the possibility of the formation of dilatant flow paths through pressure or strain dependent permeability in individual cells. The actual color figure to the left is from TOUGH2 modeling in Senger and Marschall (2008), in which the white arrows show gas flow velocity and colors are gas saturation. To the right, the discrete fracture modeling approach using TOUGH-RBSN, involving complex fracturing to simulate the formation of dilatant flow paths. The red shows the fluid flow pathways through the fracture shown in white color.

6.3 Laboratory Experiments of Spherical Gas Migration in Bentonite

Stage 2 experimental data have been collected to describe 3D spherical gas flow through a saturated sample of MX-80 bentonite. The experiment was conducted by BGS, who has also tested the 1D gas flow through bentonite to obtain the Stage 1 experimental data. The experiment is conducted on a cylindrical bentonite sample, 120 mm in height and 60 mm in diameter. The sample is placed in a pressure vessel that allows for monitoring of the evolution of pressure and stress at different locations along the sample, as well as inflow and outflow rates through filters (Figure 6-3).

The gas injection is located at the center of the sample, and staged hydration and gas injection processes have been carefully controlled over 700 days to minimize the perturbation of the system/sample and better reflect realistic conditions of a deep geological disposal facility. The DECOVALEX teams performed numerical simulations of coupled gas pressure and stress responses for the period from 735 to 835 days, when the gas breakthrough occurred.

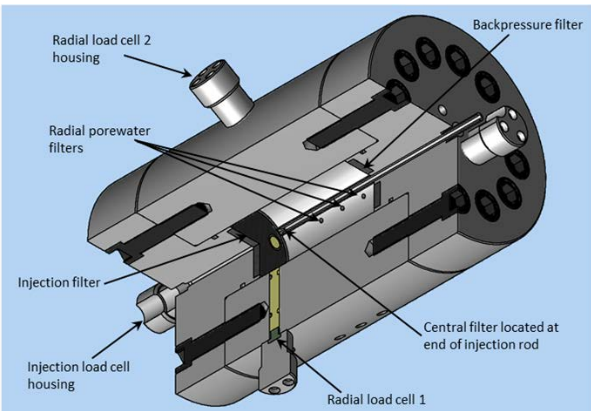

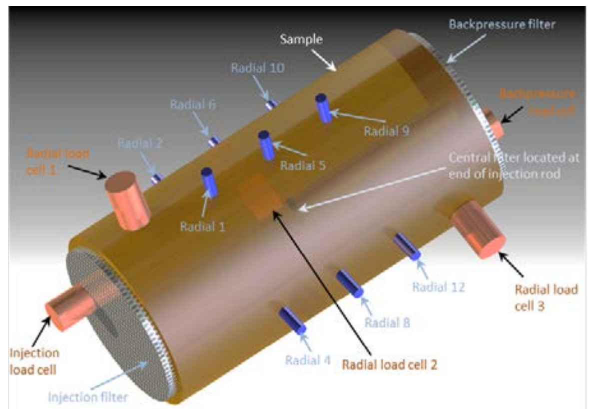

Figure 6-3. Left: Cut-away diagram of the pressure vessel showing the apparatus components and instrumentation. Right: image of the sample showing the relative positions of the load cells and pore pressure filters (Harrington, 2016).

Figure 6-4 shows experimental results of pressure/stress evolutions and inflow/outflow rates between 735 days and 835 days of gas injection. Standard temperature and pressure (STP) are defined as 273.15 K, 101.325 kPa respectively. The peak in gas pressure (around day 767.6) is followed by a protracted negative pressure transient leading to a quasi-steady state by around day 825 (Figure 6-4a). During this period, the change in injection pressure is crudely mirrored by stress which exhibits none of the apparent chaotic patterns observed at earlier breakthrough events. The reduction in the variability of stress from day 768 onwards is accompanied by the development of stable outflow conditions, with flux localized to one drainage array (Figure 6-4b).

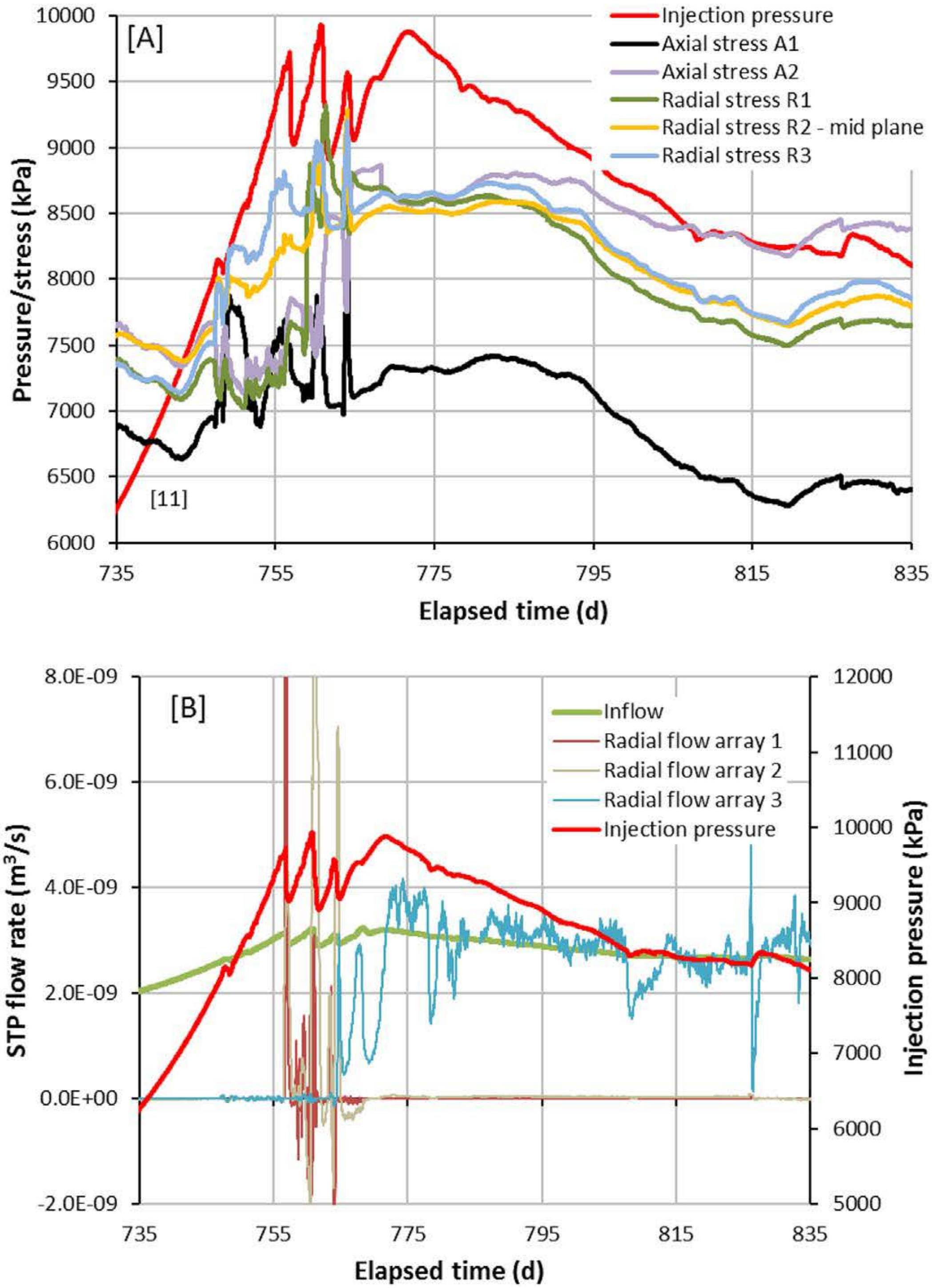

Figure 6-4. Observed 3D spherical gas flow test results: (a) pressure/stress evolutions,and (b) inflow/outflow rates (Harrington et al., 2017).

6.4 TOUGH-RBSN Modeling of Gas Migration Experiments

The TOUGH2 model configuration comprises two types of elements. The first element type is cell elements, whose geometry is associated to the Voronoi cells. The cell elements represent the matrix/grain bulk, for which the porosity-dependent permeability is defined as (Gens et al., 2009)

$$k = k_0 \frac{\phi^3}{(1-\phi)^2} \frac{(1-\phi_0)^2}{{\phi_0}^3} \tag{6.1}$$

where k_0 is the intrinsic permeability, and ϕ_0 is the initial porosity.

The other element type is interface elements, which represent potential fractures or pre-existing fractures embedded in a portion of the matrix volume. It is assumed that the interface element is positioned at the common boundary of two adjacent cell elements, and one fracture plane cut the element into two parallel plates. The permeability is calculated as the sum of two components:

$$k = k_{\text{matrix}} + k_{\text{fracture}} \tag{6.2}$$

where each component is conditionally calculated based on the fracture activation. If an interface element is yet to be fractured, k_{matrix} is calculated as in Equation (6.1) and $k_{fracture}$ is simply assumed to be zero. On the other hand, if the interface element is fractured, $k_{fracture}$ will be predominant to enhance the total permeability, and k_{matrix} is assumed to revert to the initial intrinsic permeability k_0. This conditional expression of the permeability is written as

$$k = \begin{cases} k_0 \frac{\phi^3}{(1-\phi)^2} \frac{(1-\phi_0)^2}{{\phi_0}^3}, & \text{if unfractured} \\ k_0 + \frac{b^3}{12a}, & \text{if fractured} \end{cases} \tag{6.3}$$

where a is the element width, and b is the fracture aperture.

For two-phase flow simulations in TOUGH2, we employed a van Genuchten capillary pressure model (van Genuchten, 1980) and a Corey relative permeability model (Corey, 1954), which are both functions of degree of saturation of local elements. Pressure and flow responses observed from the gas injection experiment interpret that gas only flows into the fully saturated specimen at a certain level of gas pressure or above. This conditional gas penetration is implemented by introducing a gas entry pressure with the corresponding residual gas saturation in the capillary pressure function. The van Genuchten capillary pressure model is used to define the water retention curve as

$$P_c(S) = P'_0\left([S^*]^{-1/\lambda} - 1\right)^{1-\lambda} \tag{6.4}$$

with $S^* = (S - S_{lr})/(1 - S_{lr})$. The relevant capillary pressure parameters are adopted for MX80 bentonite (Senger and Marschall, 2008). For fractured elements, the apparent gas entry pressure P'_0 of the element will be scaled by the function of permeability as

$$P'_0 = P_0 \left(\frac{k_0}{k}\right)^{1/3} \tag{6.5}$$

The relative permeability-saturation relationships of liquid and gaseous phases are parameterized using Corey model as

$$\begin{gathered} k_{rl}(S) = \hat{S}^4 \\ k_{rg}(S) = m_g\left(1 - \hat{S}\right)^2\left(1 - \hat{S}^2\right) \end{gathered} \tag{6.6}$$

where $\hat{S} = (S - S_{lr})/\left(1 - S_{lr} - S_{gr}\right)$ and m_g is an multiplying factor for the enhanced gas permeability. The residual saturations S_{lr} and S_{gr} are provided to limit the mobility of the respective phase, i.e., both liquid and gaseous phases can vary their mobilities only in the range of $S = \left[S_{lr}, 1 - S_{gr}\right]$. To avoid unphysical situation with $P_c = \infty$, larger S_{lr} for the relative permeability is usually chosen as compared to S_{lr} for the capillary pressure (Pruess et al., 2012). S_{gr} can be used to define the air entry pressure in relationship with the capillary pressure function.

In the mechanical simulations, effective (grain-to-grain) stress $\sigma_n{}'$ is calculated from the pore pressure P based on the linear poro-elasticity theory (Biot and Willis, 1957):

$$\sigma_n{}' = \sigma_n - \alpha P \tag{6.7}$$

where σ_n is the total normal stress obtained from overall loading, including external loads; $P = \max(P_g, P_l)$ is taken as the highest pressure between gas and liquid phases; and α is Biot's effective stress parameter. Note that tensile stress is taken to be positive for the sign convention. Also, the shrinkage/swelling effect due to the local changes of liquid saturations ΔS can be taken into account:

$$\Delta\varepsilon_s = \alpha_s \Delta S \tag{6.8}$$

where ε_s is shrinkage/swelling strain; and α_s is the hydraulic shrinkage coefficient. If a poro-elastic geomaterial is subjected to confinement conditions, the stress due to swelling/shrinkage can be calculated as

$$\Delta\sigma' = \Delta\varepsilon_s E \tag{6.9}$$

where E is the Young's modulus.

However, the results of the Stage 2 preliminary simulation, presented in FY2018, revealed a substantial discrepancy of simulated stress-time series data compared to the experiment. Instead of using Equation (6.7), we have introduced Bishop's effective stress calculation, where the pore pressure consists of partial contributions of gas and liquid phases:

$$\sigma_n{}' = \sigma_n - P_g + \chi(P_g - P_l) \tag{6.10}$$

where χ is Bishop's coefficient that is dependent on the degree of saturation of a two-phase system. Here, a general formulation for soil and clay materials, proposed by Khalili and Khabbaz (1998), is used:

$$\chi = \begin{cases} 1 & \text{for } P_g - P_l < P_{ae} \\ \left(\frac{P_g - P_l}{P_{ae}}\right)^{-0.55} & \text{for } P_g - P_l \geq P_{ae} \end{cases} \tag{6.11}$$

where P_{ae} is a gas entry pressure.

The fracture process of a local rigid-body-spring element is simulated by degrading the springs. A fracture event entails a reduction of spring stiffness and a release of the associated elemental forces. For the degraded spring set, the modified stiffness matrix $\mathbf{D}'$ is

$$D' = (1 - \omega)D \tag{6.12}$$

where ω is a scalar damage index with a range from 0 (undamaged) to 1 (completely damaged). For brittle fracturing, which is applied to the cases presented in this report, ω is switched from 0 to 1 once a fracture event occurs (i.e., the stress state of an element violate the failure criteria). The stress criticality of a lattice element is calculated as

$$R_f = \sigma_e / \hat{\sigma} \tag{6.13}$$

where σ_e is the element stress state and $\hat{\sigma}$ is the critical stress defined by failure criteria. In this study, we have used the Mohr-Coulomb criteria to determine the failure of lattice elements.

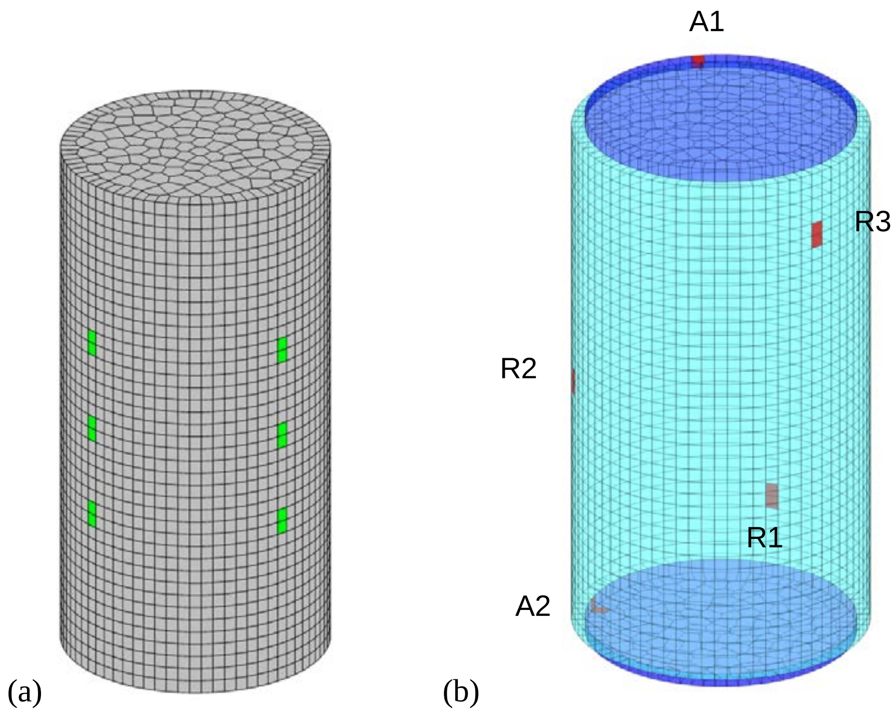

Figure 6-5. 3D Voronoi mesh generation: (a) Mesh discretization of bentonite domain. Six green marks (and six hidden on the other side) indicate the locations of porewater sensors for outflow measurements; and (b) Outer elements are padded for zero-displacement constraints. Red marks indicate the location of load cells, where the local stress values are measured.

For modeling of spherical gas flow in bentonite, we generated a 3D Voronoi mesh of a cylinder with dimensions of 120 mm height and 60 mm diameter, which is composed of 7,856 Voronoi cells and 33,316 element connections (Figure 6-5). Additional padding elements are placed on the axial ends and the circumferential surface to provide a constant volume boundary condition (zero-displacement constraints). Initial mechanical confinement is assumed with the axial stress of 7.25 MPa, the radial stress of 7.75 MP in the sample, and the initial pore pressure of 1 MPa is given for a fully water-saturated state. While the padding elements surrounding the sample domain are hydrologically constrained, a fully gas-saturated element with 168 ml of volume represents the injection system, which is directly connected to the center of the sample domain. A constant injection rate of 2.75×10^{-9} m^3/s at STP is maintained throughout the simulation. Elements at 12 locations on the circumferential surface of the sample, indicated by green marks in Figure 6-5a, are connected to the backpressure boundary element with a constant 1 MPa pressure. Outflow values are measured at the connections between those circumferential elements and the backpressure boundary element. Reactions are measured at the constrained padding elements to derive stress values, which are colored in red in Figure 6-5b.

Model parameters are listed in Table 6-1. The current TOUGH-RBSN model includes all the baseline parameters conforming to the values suggested from the DECOVALEX Task A coordinator from BGS. Pre-calibration processes have been performed to match the experimental data, and the calibrated parameters are given in the notes of Table 6-1.

Table 6-1. Material parameters for TOUGH-RBSN 1D modeling of gas flow through MX-80 bentonite samples.

	Meaning	Symbol [units]	Value
Basic reference values	Young's modulus	E [MPa]	307
	Poisson's ratio	ν [-]	0.4
	Porosity	ϕ_0 [-]	0.44
	Intrinsic permeability	k_0 [m^2]	3.4×10^{-21}
HM coupling parameters	Pore compressibility[1]	c_p [Pa^{-1}]	4.44×10^{-9}
	Biot's coefficient	α_p [-]	1
	Swelling coefficient	α_s [-]	0.0
Mohr-Coulomb failure criterion[2]	Tensile strength	f_t [MPa]	0.001
	Cohesive strength	c [MPa]	0.04
	Internal friction angle	β [deg.]	4.5
van Genuchten capillary pressure model[3]	Apparent gas entry pressure	P_0 [MPa]	18
	Residual liquid saturation	S_{lr} [-]	0.01
	Shape factor	λ [-]	0.45
Corey relative permeability	Residual liquid saturation	S_{lr} [-]	0.8
	Residual gas saturation[4]	S_{gr} [-]	0.0709
	Enhancement factor for k_{rg}	m_g [-]	1

Note:

[1] The pore compressibility is analytically derived from the bulk modulus K: $c_p = \frac{1}{K\phi} = \frac{3(1-2\nu)}{E\phi}$.

[2] The strength parameters are set to match the timing of fracture initiation and gas breakthrough.

[3] The parameters are adopted from Senger and Marchall (2008).

[4] S_{gr}= 0.0709 corresponds to the air-entry pressure P_{ae}= 7 MPa, which is the pressure difference between injection and backpressure points at the breakthrough.

Figure 6-6 presents the injection pressure evolution compared to the experimental result. With a constant injection rate, the pressure of the injection boundary element develops with a decent agreement with the experimental curve up to the peak, and the timing and the level of the peak pressure are comparable to the experimental results. Though the simulation does not demonstrate the multiple pressure drops around the peak in the experiment, the simulated pressure in the post-peak region has similar trend of decrease, and the final pressure is comparable to the pressure evolution in the experiment.

Figure 6-7 shows inflow and outflow rates through the sample. Inflow rate was gradually increasing starting from about 745 days, when the initial gas entry occurred, and then around 761 days jumped to match the level of the injection rate, which implies the gas breakthrough. About one day after the inflow rate jumped, the gas breakthrough affected the flow response through radial pore water arrays. In the experiment, only one radial array took a dominant outflow in concordance with the inflow rate, whereas the simulation exhibits lower outflow rates for all three radial arrays. Multiple lower outflow rates with no dominant flow direction indicate that the inflow diverges to multiple outflows connected through the fractures. For that reason, we plotted the total outflow rate combining the three outflow rates at the radial arrays. Figure 6-8 presents the total gas volume within the sample, which is derived by cumulative integration of flow rates over time. Gas volume suddenly increases and soon levels off at the breakthrough, and then levels up to the end of simulation.

Figure 6-9 shows the stress evolutions measured at the locations of load cells. The stress measurements are well fitted with the experimental data prior to the gas breakthrough, but the increase of stresses looks steep after the breakthrough. Moreover, the simulated stress evolutions plateau out after the gas breakthrough while the experiment exhibits a gradual attenuation of stress measurements to the end. The results can interpret that a new approach with Bishop's equation for the effective stress calculation works well before discrete fractures occur, but it needs to be improved to model the two-phase pressure in the fractured elements.

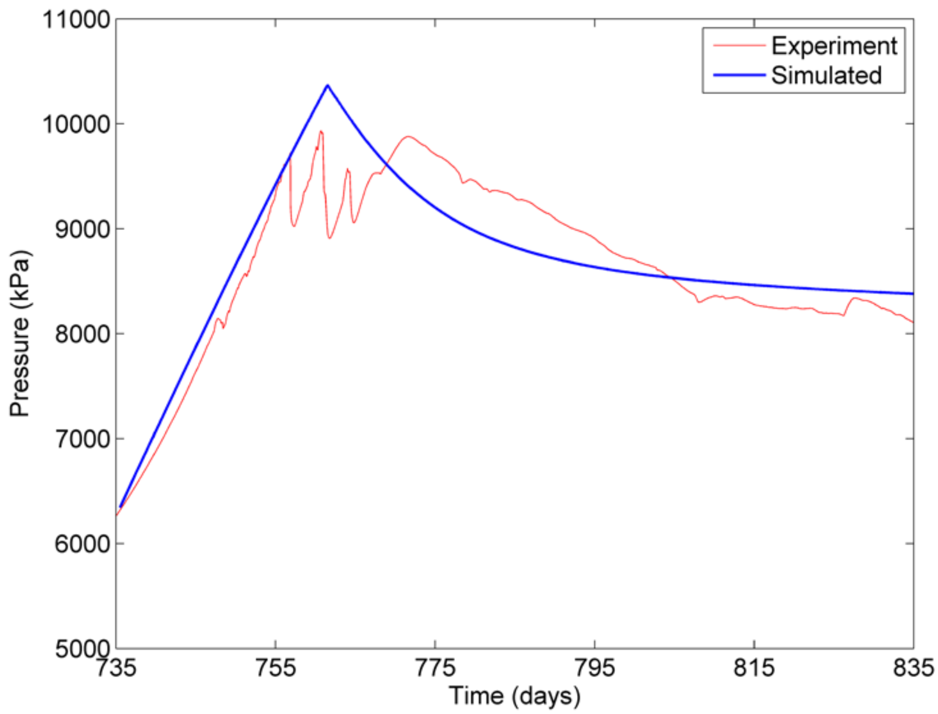

Figure 6-6. Comparison of simulated and experimental injection pressure trends.

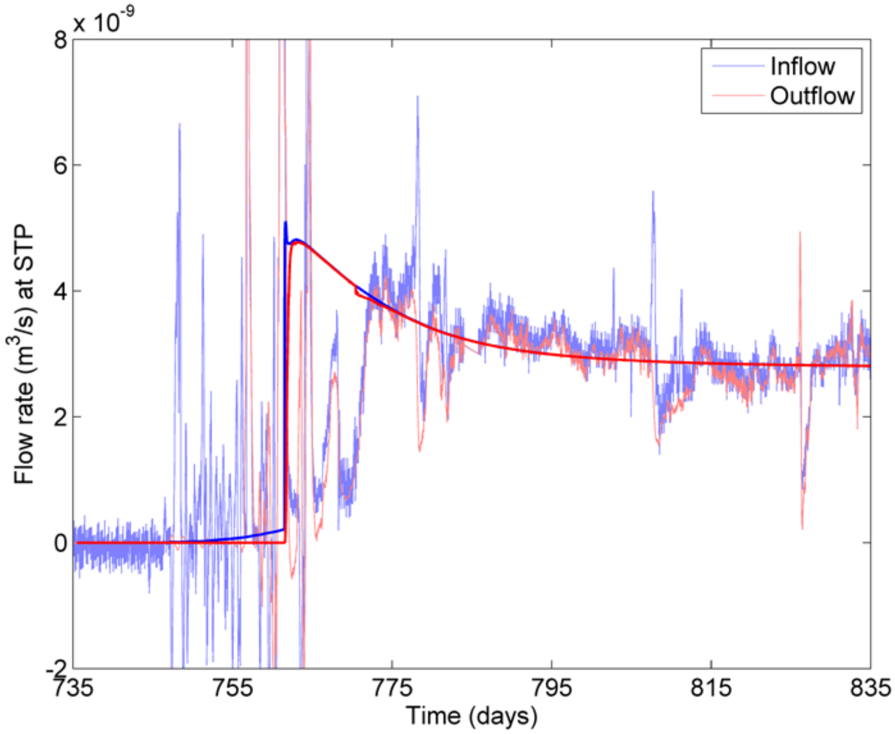

Figure 6-7. Comparison of simulated and experimental flow rate evolutions.

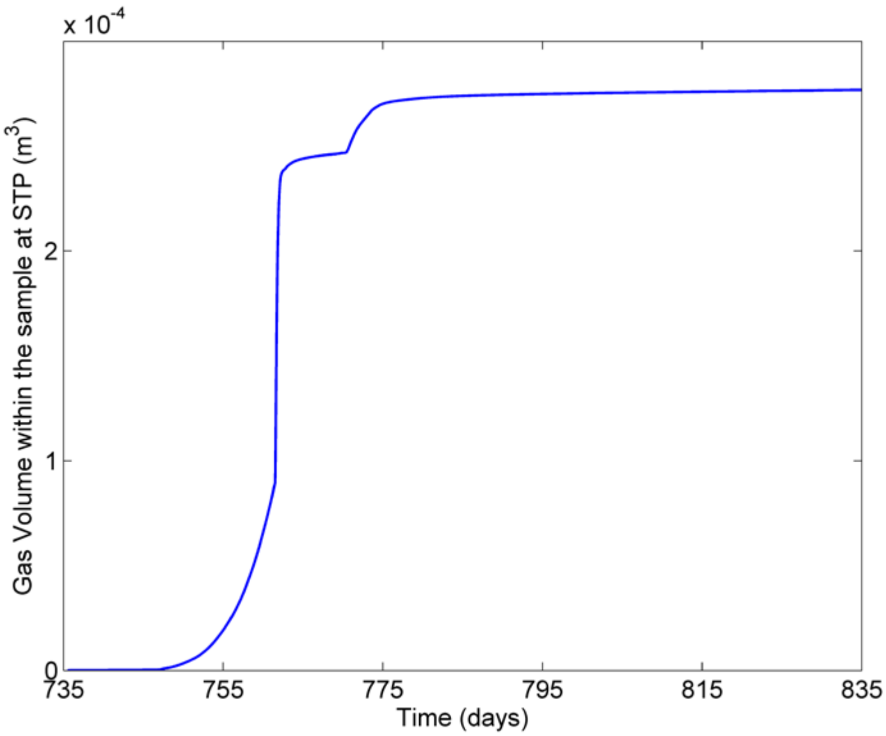

Figure 6-8. Cumulative total gas volume within the sample in the simulation.

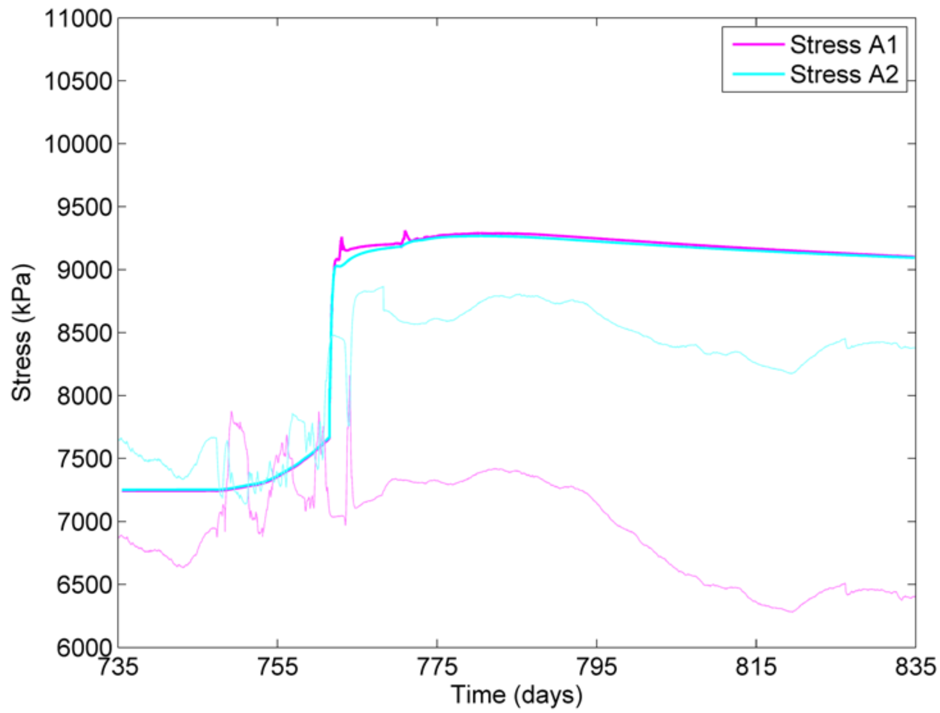

(a)

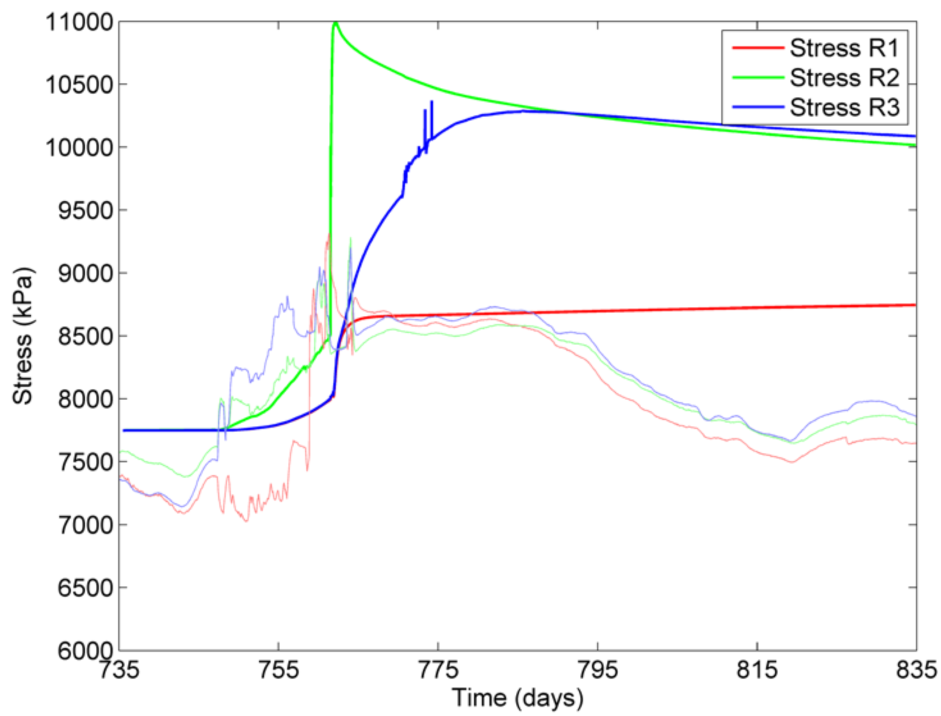

(b)

Figure 6-9. Comparison of trends of simulations and experimental data: of (a) axial stress, and (b) radial stress trends in the experiment and the simulation.

In summary, Bishop's effective stress calculation could improve the simulation results, compared to the preliminary results presented in FY2018, in terms of total stress developments in the early stage before gas breakthrough. The stresses gradually increase due to the gas entry and have a good agreement with experimental data. However, the stress measurements in the post-breakthrough regime deviate from experimental data, of which the level is still high and flat without attenuation.

For the rest of FY2019, we plan to finalize our simulations for the DECOVALEX-2019 tasks. For the final simulations, we will strive to improve the stress responses in the post-breakthrough regime. Possible improvements could include introduction of non-linear elasticity to the model using the Barcelona Basic Model (BBM) or a simpler state surface approach for unsaturated bentonite materials. Avenues for further developments of the gas migration models when looking ahead for FY20 could be

TOUGH-FLAC simulator with Barcelona Expansive Model considering the two structural levels applied to gas migration studies

TOUGH-RBSN discrete fracture model with the addition of long-term sealing and healing of dilated flow paths

However, we recognize that any model needs to be validated against laboratory experiments and if possible field data, to be used for predictions at a large scale. One of the proposed new tasks for the upcoming DECOVALEX-2023 is to model the Large Scale Gas Injection Test (Lasgit) conducted at the Äspö Hard Rock Laboratory in Sweden.

This page is intentionally left blank.

7. MODELING OF MICROSCOPIC PROCESSES AND CONTROLS OF GAS BUBBLE MIGRATION

7.1 Introduction

In nuclear waste disposal systems, the transport of gases that are produced by the metal corrosion (Xu et al., 2008), radiolysis (Christensen and Sunder, 2000) and microbial activities (Pedersen, 1996; Pedersen, 1999) - in the form of discrete gas bubbles or as a continuous phase - has a large effect on their long-term performances (Birkholzer et al., 2012; Claret et al., 2018; Tsang et al., 2015). The gas-water interfaces serve as an important vehicle for the transport of radionuclides and micro-organisms due to preferential flow and preferential sorption (Wan and Wilson, 1994), whereas trapped gas bubbles can result in immobilization of radionuclides. In addition, local pressure build-up due to gas production and accumulation can trigger mechanical responses that reshape pore spaces by deformation or fracturing (Kim et al., 2011).

The migration of gas bubbles is dictated by surface tension, viscous, inertial and buoyancy forces (Cihan and Corapcioglu, 2008), and depends on factors that include imposed macroscopic hydrodynamic conditions, interfacial properties and the structure of the pore spaces.

In argillite, pore diameters are typically below 100 nm (Boulin et al, 2008). As the free path lengths of the gas molecules become smaller than the characteristic length of the pores, molecular interactions at the solid-fluid interface becomes important. Consequently, properties such as viscosity and density deviate from bulk values, and modeling transport of the gas or any other fluid phase requires explicit treatment of molecular scale processes (Wu et al., 2017; Jin and Firoozabadi, 2015).

However, due to processes such as desiccation, fractures are prevalent in clay rocks. The apertures of the cracks are typically on the order of ~10 microns (Fauchille et al., 2016). At this length scale, assuming that gas bubbles are trapped, investigations of how fast they migrate requires understanding of such microscopic processes as snap-off, ganglion mobilization, layer flow, and Haines jumps (Raeini et al., 2014). These pore scale processes not only affect local pressure and velocity, but can also propagate through larger scales and affect macroscopic flow and pressure behaviors (Berg et al., 2013; Armstrong et al., 2015).

For these reasons, direct numerical simulations of microscopic processes in presence of a gas phase has received increasing attention from various communities (Worner, 2012). Pore-scale models provide an investigative tool for the deconvolution of intertwined factors that control gas bubble migration and the interrogation of experimental observations. For example, Khodaparas et al. (2015) investigated the dynamics of isolated air bubbles in liquid flows through uniform microchannels at a range of flow velocities, and Roman et al. (2017) studied snap-offs of gas bubbles going through a constriction in microchannels. The pore scale models also provide the necessary building blocks to improve pore network modeling, and to take into account microscopic phenomena that will be used for macroscopic studies. For instance, a new relationship describing pore-throat conductivity for pore network models was developed based on pore-scale simulations (Raeini et al., 2014).

The overall objectives of this study are to investigate the impacts of pore scale structural heterogeneity and macroscopic pressure gradient (i.e. flow rates) on gas bubble or interfacial migration velocity and local transient pressure variations including shear stress, and to draw implications for dynamic gas bubble formation and consumption coupled with reactions and for larger scale flow behavior, mechanical responses, and radionuclides migration. This chapter reports the results of preliminary investigations, and focuses on the comparison experimental and published experimental data.

7.2 Methods

In this study, two types of approaches are considered: the traditional mesh-based Computational Fluid Dynamics (CFD) approach and the Lattice Boltzmann method. They have different advantages and shortcomings in simulating multiphase flow at low capillary numbers in structures with complex fluid-solid interface, which are commonly encountered in nuclear waste disposal sites. By comparing different algorithms and exploiting their respective advantages, we aim to provide improved insights regarding the physical processes.

7.2.1 Computed Fluid Dynamics (CFD)

For CFD simulations, an open source software package, OpenFOAM (Open Field Operation and Manipulation) and related open source libraries, were used (Jasak, 2009). For two-phase systems, OpenFOAM implements the volume of fluid (VOF) method, which treats the two phases as an effective single phase when solving the continuity and momentum equations:

$$\nabla \cdot \boldsymbol{U} = 0 \tag{7.1}$$

$$\frac{\partial(\rho\mathbf{U})}{\partial t} + \nabla \cdot (\rho\mathbf{U}\mathbf{U}) = -\nabla p + \mu[\nabla\mathbf{U} + (\nabla\mathbf{U})^{T}] + \mathbf{F} \tag{7.2}$$

where **F** is the body force, e.g., surface tension force, and $\boldsymbol{U}$, ρ and μ are weighted average between the two phases based on the volume fraction of the two phases.

$$\boldsymbol{U} = \alpha\boldsymbol{U_w} + (1-\alpha)\boldsymbol{U_{nw}} \tag{7.3a}$$

$$\rho = \alpha\rho_w + (1-\alpha)\rho_{nw} \tag{7.3b}$$

$$\mu = \alpha\mu_w + (1-\alpha)\mu_{nw} \tag{7.3c}$$

where α is the volume fraction of the wetting phase, and the subscripts *w* and *nw* denote the wetting and non-wetting phase, respectively.

The VOF method is referred to as algebraic if the interface is not explicitly reconstructed from the volume fraction field, and is referred to as geometric VOF otherwise. Two algorithms, interGCFoam (https://bitbucket.org/HWUCarbonates/geochemfoam-4.0) and interflow (https://github.com/isoAdvector/isoAdvector) are respective examples of the algebraic and geometric VOF and are compared here.

7.2.1.1 *InterGCFoam*

InterGCFoam builds upon the OpenFOAM solver interFoam, and implements a modified version of the algorithm developed by Raeini et al. (2012) to sharpen the volume fraction field in the calculation of the surface tension force (Maes, 2018).

In the algebraic method, the transport of volume fraction field is solved from the advection equation given by

$$\frac{\partial\alpha}{\partial t} + \nabla \cdot (\alpha\mathbf{U}) = 0 \tag{7.4}$$

In interfoam, the multidimensional universal limiter with explicit solution (**MULES) scheme** was used to compress the interface. The transport equation is given as

$$\frac{\partial\alpha}{\partial t} + \nabla \cdot (\alpha\mathbf{U}) + \nabla \cdot (\alpha(1-\alpha)\mathbf{U_r}) = 0 \tag{7.5}$$

where $\mathbf{U_r}$ is the compression velocity defined as the velocity difference between the wetting phase and non-wetting phase, and the additional term in Equation (7.5) ensures a sharper interface.

To further reduce spurious velocity that arises from local force imbalance, a series of filtering processes were added into interGCFoam. First, the volume fraction field is smoothed by recursively interpolating it between cell centers and face centers:

$$\alpha_{s,i+1} = C_{SK}\langle\langle\alpha_{s,i}\rangle_{c\to f}\rangle_{f\to c} + (1 - C_{SK})\alpha_{s,i},\ \alpha_{s,0} = \alpha \tag{7.6}$$

where the subscript i is the number of iterations, and C_{SK} is a coefficient between 0 and 1.

Normal vector ($\boldsymbol{n_I}$) of the interface is then calculated based on the smoothed volume fraction field α_s and is given by

$$\boldsymbol{n_I} = \frac{\nabla\alpha_s}{|\nabla\alpha_s|} \tag{7.7}$$

The curvature (κ) and the surface tension force at the face centers ($f_{c,f}$) are given by

$$\kappa = \nabla \cdot (\boldsymbol{n_I}) + \boldsymbol{n_I}\nabla\left(\langle\boldsymbol{n_I}\rangle_{c\to f}\right)\boldsymbol{n_I} \tag{7.8}$$

$$f_{c,f} = \sigma\langle\kappa\rangle_{c\to f}\delta_{pc} \tag{7.9}$$

where σ is the surface tension, and the delta function (δ_{pc}) is formulated based on a modified volume fraction field that is curtailed and rescaled using the coefficient C_{PC}, which is between 0 and 1:

$$\delta_{pc} = \nabla\alpha_{pc} = \nabla\left\{\frac{1}{1-C_{PC}}\left[\min\left(\max\left(\alpha, \frac{C_{PC}}{2}\right), 1 - \frac{C_{PC}}{2}\right) - \frac{C_{PC}}{2}\right]\right\} \tag{7.10}$$

To eliminate non-physical velocities parallel to the fluid interface, the components of the surface tension force that are parallel to the fluid interface are filtered:

$$f_{c,f,filtered} = f_{c,f} - f_{c,f,filt\parallel} \tag{7.11}$$

$$\nabla \cdot \nabla P_c = \nabla \cdot f_{c,f,filtered} \tag{7.12}$$

$$f_{c,f,filt\parallel} = \frac{\delta_{pc}}{\delta_{pc}+\epsilon}\left(C_{filt,relax}f_{c,f,filt\parallel}^{old} + C_{filt}\langle\nabla P_c - (\nabla P_c \cdot \boldsymbol{n_I})\boldsymbol{n_I}\rangle_{c\to f}\boldsymbol{n_I}\right) \tag{7.13}$$

where ϵ is a constant on the order of 10^{-4}, $C_{filt,relax}$ and C_{filt} are coefficients between 0 and 1, and P_c is the capillary pressure. The value of $f_{c,f,filt\parallel}$ starts with zero, and the filtering process stops when the components of dynamic capillary force parallel to the fluid interface converges to zero.

The capillary flux (ϕ_c) is further filtered to remove non-physical fluxes:

$$\phi_c = |\boldsymbol{S}|(f_{c,f} - \nabla P_c) \tag{7.14}$$

$$\phi_{c,filtered} = \phi_c - \min(\max\left(\phi_c, \phi_{c,thresh}\right), \phi_{c,thresh}) \tag{7.15}$$

$$\phi_{c,thresh} = C_{\phi,filt}\left|f_{c,f}\right|_{avg}|\boldsymbol{S}| \tag{7.16}$$

where $C_{\phi,filt}$ is a user specified coefficient, and $\boldsymbol{S}$ is the vector area of a face.

In capillary dominated regime, additional filtering based on the capillary pressure gradient is performed as follows. $\phi_{c,thresh} = 1.5 \iint\langle\langle\nabla P_c\rangle_{c\to f}\rangle_{f\to c} \cdot \langle\boldsymbol{n_I}\rangle_{c\to f}$ (7.17)

$$\phi_{c,gPc_{corr}} = \min(\max\left(\phi_{c,filtered}, \phi_{c,thresh}\right), \phi_{c,thresh}) \tag{7.18}$$

7.2.1.2 *InterFlow*

The interflow solver implements the geometric VOF using the isoAdvector algorithm (Roenby et al., 2016). It explicitly reconstructs the interface from the volume fraction field, and the advance of the volume fraction field is based on the advance of the interface.

For each cell in the fluid-fluid interface region (i.e. $\varepsilon < \alpha_i < 1 - \varepsilon$, where ε is a user-defined tolerance value), an isosurface is constructed such that it cuts the cell into two volumes matching the volume fraction value. For this purpose, the volume fraction field is interpolated from cell center to mesh points. The cutting points are determined by going through each edge of the cell and compare the volume fraction of the cell (α_i) and the values on the two vertices (α_k, α_l). If $\alpha_k < \alpha_i < \alpha_l$, a cutting point is introduced with coordinates calculated as

$$\widehat{\boldsymbol{X}}_m = \boldsymbol{X}_k + \frac{\alpha_i - \alpha_k}{\alpha_l - \alpha_k}(\boldsymbol{X}_l - \boldsymbol{X}_k) \tag{7.19}$$

The center ($\boldsymbol{X}_{i,c}$) and normal vector ($\boldsymbol{n}_c$) of the isosurface are determined from the cutting points. Spatial interpolation of the velocity field is performed to calculate the velocity at $\boldsymbol{X}_{i,c}$ ($\boldsymbol{U}_{i,c}$). The isosurface advances at the normal velocity ($U_{i,c} = \boldsymbol{U}_{i,c} \cdot \boldsymbol{n}_c$).

The change of volume fraction in a cell depends on the sum of the volumes of the advancing fluid entering through all bounding faces of the cell.

$$\alpha_i^{t+\Delta t} = \alpha_i^t - \frac{1}{V_i}\sum_{j \in B_i} \delta_{i,j}\Delta V_j \tag{7.20}$$

where $\delta_{i,j}$ is +1(-1) when the fluid moves out of (into) cell i through face j, V_i is the cell volume, and ΔV_j is the volume of the advancing fluid transported across face j and is approximated as follows:

$$\Delta V_j \approx \frac{\phi_j}{|\boldsymbol{S}_j|}\int_t^{t+\Delta t} \hat{S}\,(\tau)d\tau \tag{7.21}$$

where $\boldsymbol{S}_j$ is the vector area of face j, $\hat{S}$ is the surface area of face j within the advancing fluid, and ϕ_j is the volumetric flux through face j.

$$\phi_j = \int \boldsymbol{u} \cdot d\boldsymbol{S} \tag{7.22}$$

The time integral of $\hat{S}$ in Equation (7.21) is the surface area swept by the intersection line between the isosurface and face j. Therefore, by tracking the motion of the isosurface and its intersection with the downwind face j, the volume fraction can be updated according to Equation (7.20).

7.2.2 Lattice Boltzmann Method

Lattice Boltzmann method (LBM) is a numerical method that is used to approximate the Boltzmann's equation. Through consecutive propagation and collision processes of fictive particles over a discrete lattice mesh (Equation (7.23)), numerical approximation of the solution of the Navier-Stokes equation, as Equation (7.2), is reached:

$$f_i(\boldsymbol{x} + e_i\Delta t, t + \Delta t) = f_i(\boldsymbol{x}, t) - \frac{c}{\tau}(f_i(\boldsymbol{x}, t) - f_i^{eq}(\boldsymbol{x}, t)) \tag{7.23}$$

where f_i is the particle distribution function in the ith direction of each lattice, f_i^{eq} is the equilibrium fuction, which is the approximation of the Maxwell-Boltzmann distribution, e_i is the discrete velocity, τ is the relaxation time rate and related to the kinematic viscosity, and $c = \Delta x / \Delta t$.

For the simulations of gas bubble migration, here we focus on the color-gradient LBM and phase field LBM. The color-gradient LBM can simulate high viscosity ratio conditions and generate sharp interface. Some recent development has also enabled accurate representation of contact angle with low spurious current at the interface. Compared to the color-gradient LBM, the phase-field LBM is less established.

But it has great potential in simulating multiphase flow under conditions relevant to geological applications, given its ability in treating high viscosity ratio and high density ratio simultaneously.

7.2.2.1 *Color-Gradient LBM*

Gunstensen et al. (1991) developed the color-gradient method, in which the fluid particles are colored as either 'red' or 'blue.' It has then been improved by Latva-Kokko and Rothman (2005) and Leclaire et al. (2012) to reduce the spurious currents at the interface and the lattice pinning effect. In the current model, there are two collision steps for each fluid given by

$$f_i^{n*}(\boldsymbol{x},t) = f_i^n(\boldsymbol{x},t) + (\Omega_i^n)^1 + (\Omega_i^n)^2 \tag{7.24}$$

The first collision step $(\Omega_i^n)^1$ is the same as the collision step in single-phase flow. The second collision step considers the effect of the surface tension, in which the surface tension can be adjusted independently without changing the thickness of the interface:

$$(\Omega_i^n)^2 = \frac{A_n}{2}|\boldsymbol{f}|\left[w_i \frac{(e_i \cdot f)^2}{|f|^2} - B_i\right] \tag{7.25}$$

where A_n is a parameter related to the surface tension, B_i is the parameter that is dependent on the type of velocity scheme, and $\boldsymbol{f}$ is the color gradient on the lattice.

After the second collision operator is implemented, and the 'recoloring step' is performed to re-evaluate the separation between 'red' and 'blue' fluids:

$$f_i^{r,+} = \frac{\rho_r}{\rho} f_i^* + \beta \frac{\rho_r \rho_b}{\rho^2} f_i^{eq}(\rho, \boldsymbol{u} = 0)\cos(\lambda_i) \tag{7.26}$$

$$f_i^{b,+} = \frac{\rho_b}{\rho} f_i^* - \beta \frac{\rho_r \rho_b}{\rho^2} f_i^{eq}(\rho, \boldsymbol{u} = 0)\cos(\lambda_i) \tag{7.27}$$

where $f_i^{r,+}$ and $f_i^{b,+}$ are the distribution function of 'red' and 'blue' fluids after 'recoloring,' ρ_r and ρ_b are the density of 'red fluid' and 'blue fluid' at the lattice, $f_i^* = \sum_n f_i^{n,*}$, $\rho = \rho_r + \rho_b$, β is a constant between 0 and 1, λ_i is the angle between the color gradient and the direction of discrete velocity e_i, and $\cos(\lambda_i) = \frac{\boldsymbol{e_i} \cdot \boldsymbol{f}}{|\boldsymbol{e_i}| \cdot |\boldsymbol{f}|}$.

To simulate the interaction between fluids and the solid phase more accurately, Xu et al. (2017) and Akai et al. (2018) proposed new methods that modify the color gradient of fluids at the contact line with a given contact angle value for 2D and 3D, respectively. In this case, the geometry of the fluid-fluid interface can be adjusted by the contact angle value. Additional developments include incorporating the surface tension into the collision-streaming process as a force term instead of being the second collision operator given by Equation (7.25) (Halliday, 2007). In this way, the spurious currents at the contact line are reduced as well.

7.2.2.2 *Phase Field LBM*

Phase-field LBM is typically more efficient and more accurate, especially under conditions featuring large density and viscosity ratios. In principle, the phase-field equation governs the evolution of the interface between the two fluids (Chiu and Lin, 2011:

$$\frac{\partial \phi}{\partial t} + \nabla \cdot \phi \boldsymbol{u} = \nabla \cdot M\left[\left(\nabla\phi - \frac{\nabla\phi}{|\nabla\phi|}\frac{[1-4(\phi-\phi_0)^2]}{\xi}\right)\right] \tag{7.28}$$

where ϕ is the phase field value, M is the mobility, ϕ_0 is the average value from two extreme value ϕ_L and ϕ_H, and ξ is the interfacial thickness.

To recover the macroscopic Equation (7.28) from mesoscale to include the effect from forces, the discrete equation on each lattice is used (Fakhari et al., 2017; Fakhari et al., 2018):

$$h_i(\boldsymbol{x} + \boldsymbol{e_i}\Delta t, t + \Delta t) = h_i(\boldsymbol{x}, t) - \frac{h_i(\boldsymbol{x},t) - \bar{h}_i^{eq}(\boldsymbol{x},t)}{\tau_\phi + \frac{1}{2}} + F_i^\phi(\boldsymbol{x}, t) \quad (7.29)$$

$$F_i^\phi(\boldsymbol{x}, t) = \Delta t \frac{\left[1 - 4(\phi - \phi_0)^2\right]}{\xi} w_\alpha \cdot \frac{\nabla\phi}{|\nabla\phi|} \quad (7.30)$$

where h_i is the phase-field distribution function, τ_ϕ is the phase-field relaxation time, $\bar{h}_i^{eq}$ is the phase-field equilibrium function, F_i^ϕ is the forcing term on each discrete velocity direction for the phase-field distribution function, and w_i is the weight coefficient for each discrete velocity direction.

To include hydrodynamic interactions, a velocity-based LB equation is also applied

$$g_i(\boldsymbol{x} + \boldsymbol{e_i}\Delta t, t + \Delta t) = g_i(\boldsymbol{x}, t) + \Omega_i(\boldsymbol{x}, t) + F_i(\boldsymbol{x}, t) \quad (7.31)$$

$$\Omega_i(\boldsymbol{x}, t) = -\frac{g_i - \bar{g}_i^{eq}}{\tau + 1/2} \quad (7.32)$$

$$F_i(\boldsymbol{x}, t) = \Delta t w_i \frac{e_i \cdot \boldsymbol{F}}{\rho c_s^2} \quad (7.33)$$

where g_i is the velocity-based distribution function for incompressible fluids, $\bar{g}_i^{eq}$ is its equilibrium distribution function, $\boldsymbol{F}$ is the sum of forces to fluids, and c_s is the sound speed in LBM.

The interaction between solid phase and fluid are considered in a similar fashion as what was presented in color-gradient LBM. The phase field gradient and the contact angle value are coupled to modify the geometry of the interface (Fakhari et al., 2018).

7.3 Preliminary results

7.3.1 Model verification for the CFD simulators

Chang et al. (2017) performed microfluidic experiments in rough fracture with an average aperture of 2.2 mm, where water was displaced by air at a flow rate of 0.1 mL/hr, i.e. a velocity (v) f 208 µm/s. The capillary number ($Ca = \mu_w v/\sigma$), which measures the relative magnitude of the viscous force (μ_w is the dynamic viscosity of the wetting phase) and the surface tension force (σ is the surface tension), of the experiments is thus on the order of 1e-7. *In situ* images were collected to track the water-air interface and to quantify the migration velocity of the interface. Here, a subsection of the rough-fracture is used for the simulations (Figure 7-1). The length of the subsection is 5 mm, with 0.3 mm patched at the inlet that was initially set as the air phase. The 2D mesh was generated using the OpenFOAM utility snappyHexMesh, with an average grid cell size of 48 µm.

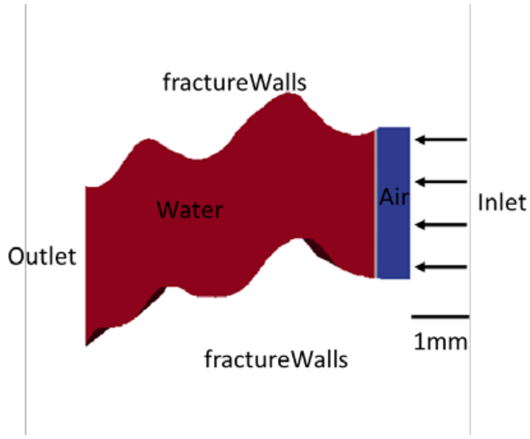

Figure 7-1. Schematic of the computational domain, initial volume fraction and boundary conditions.

The properties of the fluids used in the simulations based on the experimental study are tabulated in Table 7-1. The boundaries conditions are summarized in Table 7-2.

Table 7-1. Parameters used in the simulations of the experiment.

Property	Value
Water density	1000 kg/m^3
Water kinematic viscosity	1.0e-6 m/s^2
Air density	1.2 kg/m^3
Air kinematic viscosity	1.5e-5 m/s^2
Surface tension	0.072 N/m
Contact angle (for water and gas on PDMS)	45°

Table 7-2. Boundary conditions used for the simulations of the experiment.

Boundary Condition	Velocity [m/s]	Pressure [Pa]	Volume fraction of water
Inlet	Uniform fixed value	zeroGradient	Uniform fixed value
Outlet	zeroGradient	Uniform fixed value	zeroGradient
fractureWalls	noSlip	fixedFluxPressure	Constant contact angle

For interGCFoam, the numerical scheme *Gauss linear* is used for the gradient terms, *Gauss linear corrected* is used for the laplacian terms, *Gauss vanLeer* is used for the divergence terms of the volume fraction, and *Gauss SFCD* is used for the divergence terms of velocity. The solver and coefficient information are summarized in Tables 7-3 and 7-4, respectively.

Table 7-3. Solver setup for interGCFoam.

	Pcorr	p	U (laminar)
solver	GAMG	GAMG	BiCGStab
preconditioner	GaussSeidel	GaussSeidel	DILU
tolerance	1e-8	1e-7	1e-6
relTol	1e-5	1e-3	0.1

Table 7-4. Filtering coefficients.

coefficients	**values**
C_{SK}	0.1
Number of smoothing	1
C_{PC}	0.1
C_{filt}	0.1
$C_{filt,relax}$	0.999
$C_{\phi,filt}$	0.01

The simulation results from interGCFoam (Figure 7-2b) show migration of the water-air interface that is comparable to the experimental observations (Figure 7-2a), especially considering that the inlet boundary condition used in the simulation is different from the actual flow conditions at that location during the experiment because of the upstream channel geometry and flow processes. Adjusting the filtering coefficients, especially C_{SK} and the number of filtering cycles, can result in slight decrease in the interface velocity (<5%). Over filtering also results in significant non-zero volume fraction values in the air phase, which is not physical.

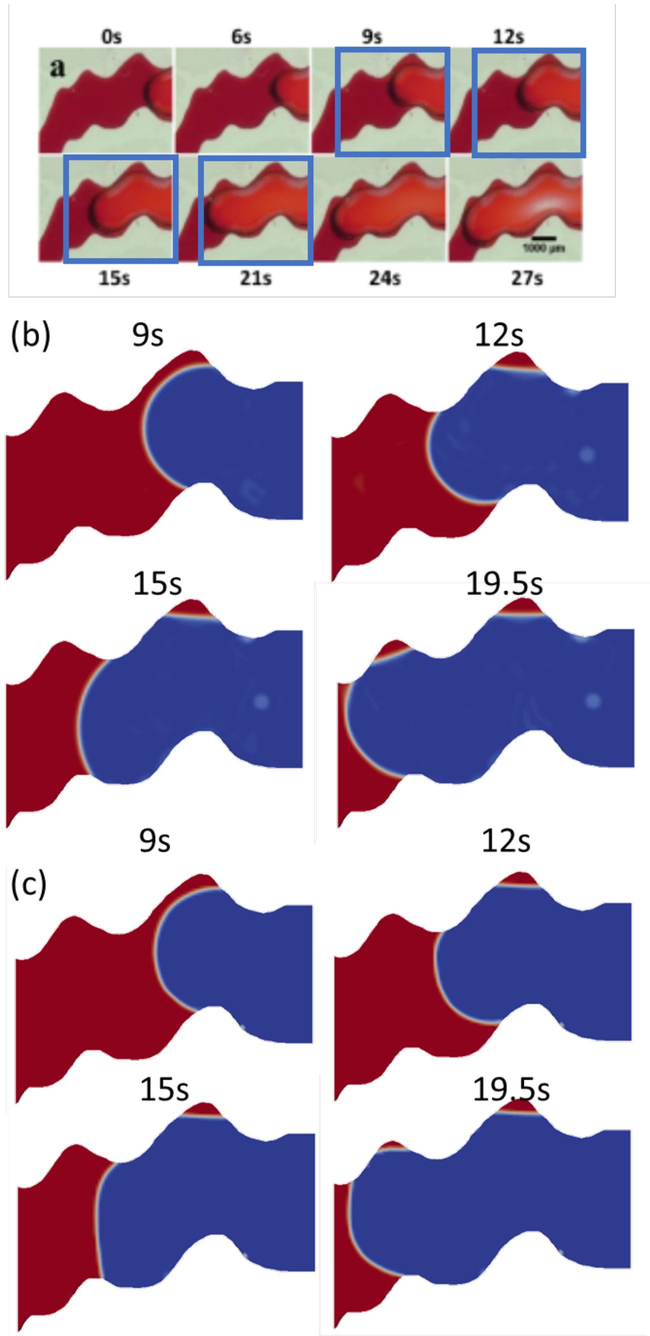

Figure 7-2. (a) Images showing the water-air interface from [34], the blue boxes highlight the computational domain shown in Figure 7-1. (b) snapshots of the volume fraction field from interGCFoam, and (c) snapshots of the volume fraction field from interflow. The blue color represents the air phase ($\alpha = 0$), and the red color represents the water phase ($\alpha = 1$).

For interflow, the numerical schemes used are similar, except for the divergence terms for velocity (*Gauss limitedlinearV).* The solver information is summarized in Table 7-5.

Table 7-5. Solver setup for interflow.

	p_corr	p_rgh	U (laminar)	α
solver	PCG	PCG	PBiCG	PBiCG
preconditioner	DIC	DIC	DILU	DILU
tolerance	1e-10	1e-7	1e-6	1e-6
relTol	0	0.05	0	0

The simulation results give interface migration velocity similar to that of the interGCFoam simulations. But the interface has a shape that is less rounded. This may be caused by the isoAdvector algorithm, which in order to ensure that the isosurface cuts each cell according to its volume fraction value, the isovalue used for determining the isosurface is different across cells, i.e. the isosurface may not be continuous throughout. The interflow solver ensures a sharp interface and eliminates non-physical volume fraction values in the air phase. Reconstruction of the interface is, however, more computational intensive. For the same domain and simulation time (20s), interFoam completes the simulation in 60 hours, which is six times of that of the interGCFoam simulation.

7.3.2 Gas bubble migration in a sinusoidal channel

A sinusoidal channel was also generated, the width of which is between 20 to 40 µm (figure 7-3). This is more comparable to the fracture apertures reported for argillite. The ratio between the maximum and minimum width is comparable to the range of ratios between pore and pore throat.

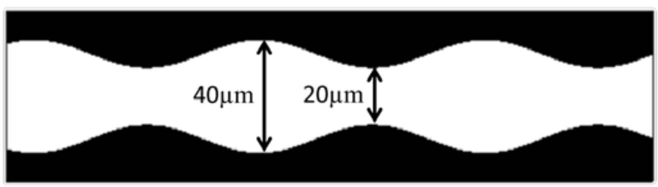

Figure 7-3. Schematic of a sinusoidal channel

Color-gradient LBM simulations were performed to model gas bubble migration through the channel for two viscosity ratios (1 and 50), which confirm the performance of the model at high viscosity ratio. Figure 7-4 shows the simulation results at a Capillary number of 5.6e-3 with a viscosity ratio of 50. The simulations employed a much finer resolution (0.1 µm), and the results captured features such the water film as the bubble migrates through the narrow part of the channel. The velocity profile also showed minimum spurious currents.

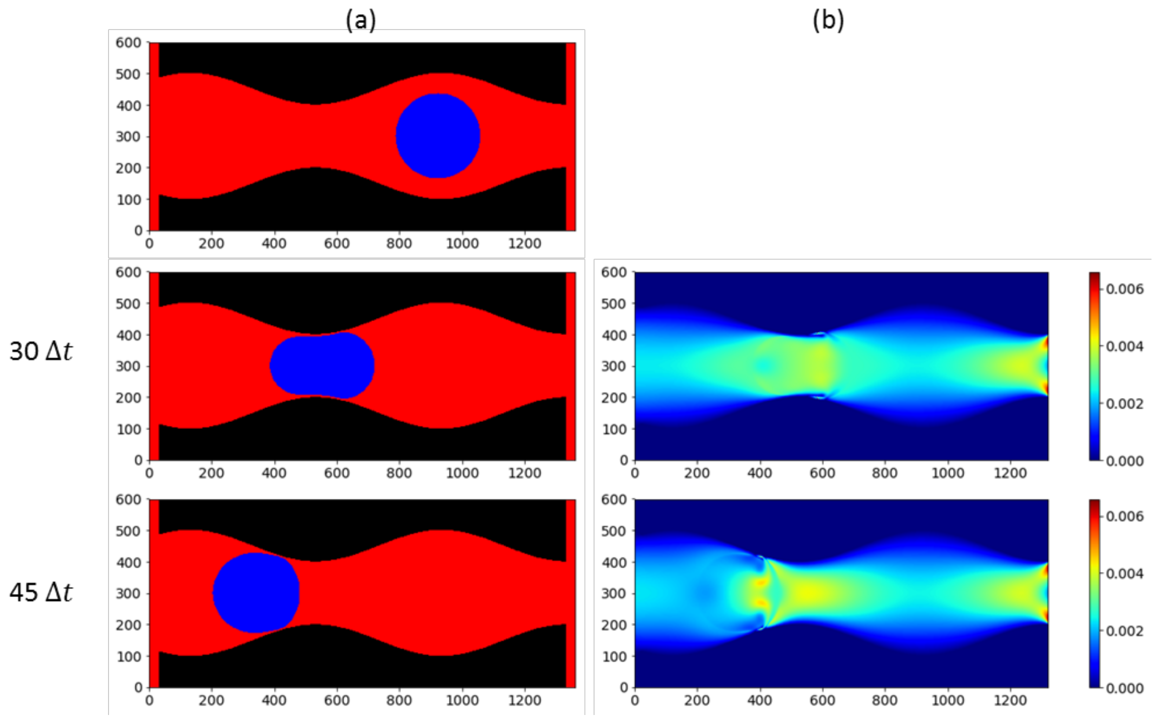

Figure 7-4. (a) Volume fraction field, and (b) Velocity field of the color-gradient LBM simulations at normalized time steps 0, 30, and 45.

7.4 Summary and future work

In this report, different multiphase simulators were tested to simulate gas bubble migration at the microscopic scale. The preliminary simulation results confirmed that the CFD approach and VOF method capture the interface migration velocity reasonably well, even though the current resolution of the mesh does not capture the water film observed in the experiment. Further simulations will be performed to test the impact of the mesh resolution and the potential impact of residual spurious currents on gas bubble dynamics. The color gradient LBM has been demonstrated to work well with large viscosity ratio as expected for gas and water systems. It can also afford much finer mesh resolution given the computational efficiency. Further model development (e.g., phase-field LBM) and test simulations will be performed to benchmark different methods based on published experimental data. Furthermore, without losing generality, simulations based on idealized geometries informed by morphological statistics will be used to investigate gas bubble migration at the microscopic scale with an emphasis on investigating the controls of morphological heterogeneity on the extent of interface velocity and transient pressure variations. In the long run, this study will provide necessary expertise and tools for investigations that are highly relevant to at least two other tasks within the project: (1) dynamic evolution and migration of gas bubbles in presence of abiotic reactions and microbial activities, and (2) local pressure perturbation and the geomechanical responses.

This page is intentionally left blank.

8. SHORT TO LONG TERM HYDROMECHANICAL RESPONSE OF FAULTS AND EDZ IN ARGILLITE HOST ROCK

8.1 Introduction

Faults of various sizes may be reactivated by thermal, hydraulic and mechanical disturbances during operational or post-closure periods. Observations suggest that surface waves produced by distant earthquakes can enhance basin-wide fluid transport extending to depths of a few kilometers. Understanding these phenomena has great importance for the design of geologic disposal of radioactive wastes, because its performance depends on the integrity of the natural system and barriers to contain radionuclides for tens of thousands of years. It is thus crucial that the permeability changes in response to these different types of “weak” loadings, specifically those occurring in fault zones and other preferential subsurface pathways, such as the EDZ, can be better understood and eventually be predicted with confidence. LBNL has been developing a new instrument called Step-Rate Injection Method for Fracture *In-situ* Properties (SIMFIP) that may allow for probing the physical processes affecting fault reactivation in low permeability host rock layers at a field scale. In parallel to instrument development, LBNL is being conducting *in situ* fault activation experiments at depths relevant to nuclear repository sites, using the SIMFIP to probe fault movements and to estimate fault permeability variations.

In this chapter, we first describe the current SIMFIP sensor developments that are conducted within the frame of this project. Second, through field test observations and numerical analyses, we explore how fault permeability can vary with slip and/or slip rate under pressurization in the range that could be expected in a host rock. Because of the very low permeability of the fault zone, fluid injection initially causes a strong pressure increase in the injection well, followed by an overall normal (i.e., ‘opening’) activation of the mechanically weak fault planes connected to the injection source. As the rupture patch increases in size under the influence of a large excess pressure around the injection well, fluid sudden discharge from the injection borehole into the principal shear zone of the fault and generates further fault rupture instability characterized by a large slip event. We demonstrate that the large slip event causes an associated seven-order-of-magnitude permeability increase within the fault. This event appears to be favored by the small difference between principal stresses, by co-rupture stress rotations, and by the geometrical complexity of the fault. Our analysis highlights the importance of considering the detailed fault architecture and heterogeneous hydromechanical behavior of fault compartments when evaluating fault activation and associated leakage in a low permeability host rock. Third, we show some preliminary numerical results of the potential effects of surface waves crossing a critically stressed fault affecting a host rock at a 500m depth. It appears that although these waves are imposing a low dynamic stress loading to the fault, the strong hydromechanical coupled response can lead to a potentially significant change in the fault permeability.

Finally, we describe the perspectives to improve the SIMFIP ability to capture the long term fault displacements and pore pressure variations in very low permeability rocks and to implement the physics of short-to-long term fault pressure and strain/strain rate evolution in numerical model(s) to improve our understanding of fault eventual sealing in response to different types of weak loadings that may affect an argillite host rock layer.

8.2 Development of a New SIMFIP Sensor

8.2.1 Description of SIMFIP technique principles

The SIMFIP (Guglielmi et al., 2015a) technique combines the advantages of a stress relief method (because it allows for constraining the full components of the stress tensor using a 6-component displacement sensor) with the advantages of a hydraulic or sleeve fracturing method (because the sensor is integrated in a straddle packer system that can moved easyly into the borehole). Figure 8-1 shows a photograph of the SIMFIP tool just prior to deployment in a deep mine setting. Figure 8-2 shows a schematic representation of the SIMFIP tool, as well as a representative dataset from a real-world test.

The first SIMFIP instrument developed by Y. Guglielmi has been used for several research experiments in mine-based environments (Guglielmi et al., 2015b). In 2015, the SIMFIP allowed for the first direct *in-situ* continuous measurement of a field-scale fault transitioning from aseismic to seismic slip. Since 2017, further engineering of the SIMFIP performed at LBNL allowed for increasing the pressure under which the SIMFIP can operate, and it is currently being tested in the deep Sanford Underground Research Facility (SURF), which is an underground research laboratory, within the framework of the EGS Collab SIGMA-V project (see Figure 8-1). The current state of the development of the SIMFIP is at a TRL of 3-to-4. It has been tested in field boreholes at more than 20 tests at depths relevant to host rock depository sites. Some tests were performed in argillite in the Underground Laboratory at Mont Terri (Switzerland) and Tournemire (France).

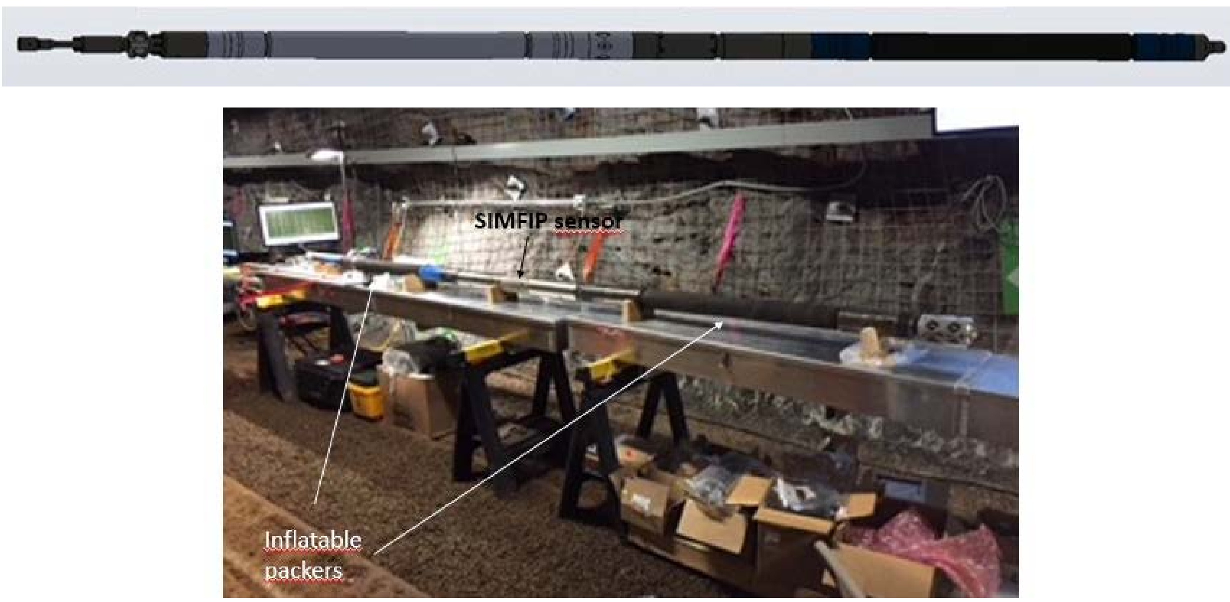

Figure 8-1. SIMFIP probe currently used for the fracture stimulation experiment in the SURF underground research laboratory (fracture pressure applied by the SIMFIP will be about 40MPa). Upper figure shows a Solid Works design of the SIMFIP and the photo shows the current SIMFIP probe.

The SIMFIP borehole probe allows for measuring simultaneously fluid pressure and three-dimensional displacements at high frequency (Figure 8-2). The injection interval is isolated in an open borehole using two inflatable rubber packers. The sealed interval length is currently of length 1.6 m, but can be increased to >20 m long by setting a chain of SIMFIP cages. Each SIMFIP cage is 0.2 m long and 0.1 m diameter pre-calibrated aluminum cage that can either: be connected to two 0.25 m long elements to allow for clamping both ends of the cage on borehole wall—Case 1, or be directly connected to the packers—Case 2. Dimensions of the SIMFIP cage can vary depending on the target borehole conditions. In Case 1, when it is clamped, the cage is disconnected from the straddle packer system. In Case 2, the SIMFIP replaces the mandrel that connects the packers. When packers are inflated, they play two roles: (a) sealing the test interval, and (b) anchoring the SIMFIP cage. Case 2 is the simplest and easiest to set the SIMFIP probe, but the SIMFIP signal must be calibrated to account for the packers' effect during the test (Case 2 results in a relatively lower resolution of the SIMFIP signal, and Case 1 allows for a very high-resolution measurement).

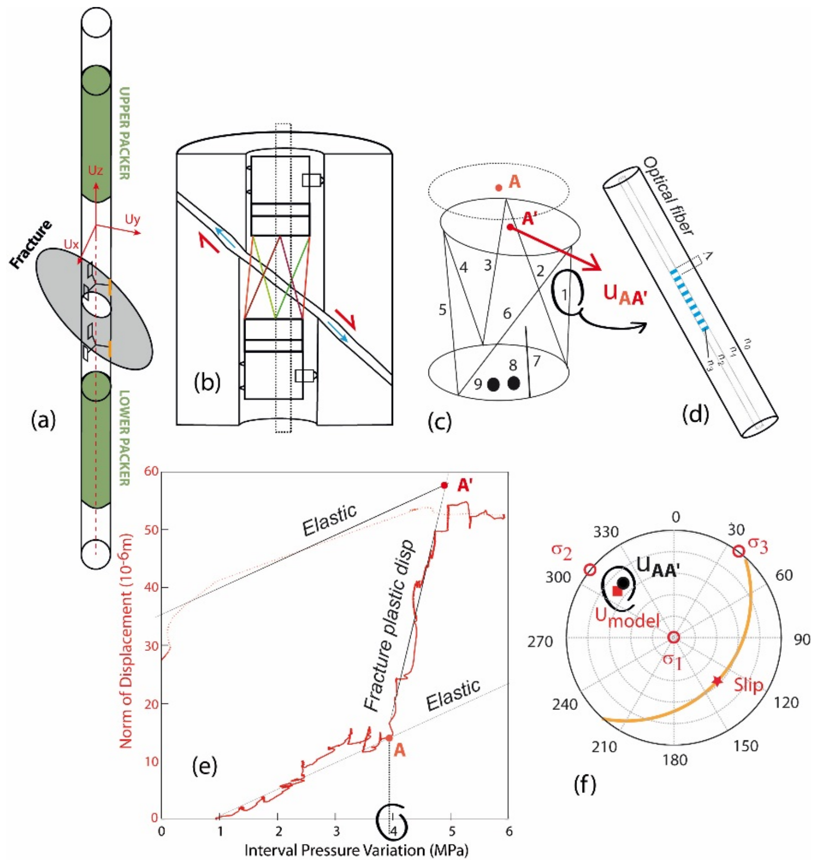

Figure 8-2. SIMFIP probe currently designed at LBNL: (a) Schematic of a typical SIMFIP setting across a natural fracture; (b) Details of the SIMFIP anchoring across the fracture; (c) Principles of the sensor that is a deforming cage in 6 different directions + 1 reference (7) + one pore pressure (8) + one temperature (9); (d) We build all our sensors using Bragg gages all connected on the same optical fiber; (e) Example of a fracture response to a pressure variation in the straddle packer interval, here showing the fracture plastic movement from A to A'; (f) Plastic displacement of the fracture's walls $U_{AA'}$ is plotted in a stereographic projection with the fracture plane orientation. Knowing both the fracture activation pressure and the three-dimensional plastic displacement allows a refined estimation of the absolute values of all the stress tensor components (including SH) by fitting a calculated vector with the measured one.

The SIMFIP is designed to capture micrometer to nanometer displacements of fractures affecting the borehole. In the case of a preexisting natural fracture the SIMFIP will be set across the fracture, anchored on either side of the fracture. A logging OPTV-type tool can be coupled to the SIMFIP probe to target the tested fracture interval in real-time. In the case of an induced fracture, the Case 2 configuration will be used to capture the orientation and the pressure at which the fracture grows from the borehole interval. In both cases, when the fracture is deforming according to the water pressure increase in the interval, the cage allows for obtaining angle dependent strain measurements, which are used to constrain the full three-dimensional strain tensor and the three rotations. The raw data are 6 strain measurements performed with optical fiber Bragg gratings (FBG) that are mechanically clamped on the 6 wings of the deforming cage. In addition, there is a reference FBG that is subject to ambient pressure and temperature, and which remains unstressed. It is used to correct linearly the strain measurements from temperature and pressure variations in the chamber. The 6+1 FBG are distributed along one single fiber that brings the sensor signals to an FBG interrogator set at the surface. A MicronOptics Si155 acquisition system is currently used. This interrogator allows for picking shifts in the FBG wavelength that relate to FBG deformation over a large spectrum of FBG wavelengths.

The 6 components of the tensor describing the relative displacement and rotation between the upper and lower rings are calculated as a linear function of the 6 strain components (named A to F in Equation 8-1). The transfer matrix is calculated as the product of two 6 × 6 matrices calibrated in the laboratory: **A** converts strain data to efforts, i.e., forces and moments applied on the deforming body, and $\mathbf{C_0}$ converts these efforts to the translation and rotation components of the tensor, given by the following equation

$$\begin{pmatrix} u_x \\ u_y \\ u_z \\ r_x \\ r_y \\ r_z \end{pmatrix} = \mathbf{Co} \cdot \mathbf{A} \cdot \begin{pmatrix} A \\ B \\ C \\ D \\ E \\ F \end{pmatrix} \tag{8-1}$$

By convention, uy corresponds to the axial strain, ux and uz to the radial strains. The variables rx, ry and rz are the counter-clockwise rotations (right-hand convention) along the corresponding axes. The displacement range is 0.7 and 3.5 mm in the axial and radial directions of the borehole, respectively; the current accuracy is ± 0.1×10-6 m. A compass set on the probe provides the orientation of measurements with a 0.1° accuracy. The strain data are logged together with pump parameters (pressure and flow rate); water pressure in the anchoring hydraulics and water pressure in the packer hydraulics are measured at the surface. Temperature and pressure are measured in the borehole above, between, and below the packers using specially designed pressure and temperature sensors, which are also based on FBG technology. The chamber P/T sensors are run on the same fiber as the SIMFIP strains. The upper and lower P/T sensors are run on a second independent optical fiber. Ranges can be adapted depending on the depth of tests.

Flowrate, pressure, temperature, and displacement variations from the SIMFIP probe are continuously monitored at a 1000 Hz sampling frequency. Raw data are saved into one ASCII file every five minutes. Pre-processing of the SIMFIP raw data is automated in the acquisition software (written in the LabView format), including the following steps: (1) correction of fiber Bragg gauges measurements from temperature and pressure, (2) detection of the FBG spectra overlapping problems (and filtering), and (3) filtering from outliers using a medium filter (outliers can occur when the interrogator cannot calculate the FBG wavelength because of some wavelength heterogeneity in the assigned FBG spectral region).

8.2.2 New Developments towards a Permanent SIMFIP sensor

The upgrades of the existing SIMFIP mainly concern its transformation into an instrument dedicated to the permanent monitoring of changes in effectives stresses, permeability, elastic and frictional properties of faults and EDZ fractures. The new developments aim to (i) increase the resolution of SIMFIP to nanometer accuracy over a broad band of frequencies [0 - 500Hz] and (ii) enhance the long-term reliability of the SIMFIP sensor.

8.2.2.1 Increasing the sensor’s resolution over a broad band of frequencies.

To increase the SIMFIP resolution we have been engineering very high-resolution clamping systems that optimally bite the borehole wall by applying a force, which is held constant over time. Using Solidworks software (Figure 8-3), we have been exploring a new clamping system that is made of three articulate arms that are deployed to the borehole wall in three radial directions (every 120°) by a hydraulic piston set in a cylinder. When the arms are clamped to the borehole wall, they are immune to any pressure change in the borehole, and we calibrated that they transfer 100±5 % of the formation forces to the sensor. It is a significant improvement compared to the previous system, which transferred about 30 to 60 % of the forces. In addition, the clamps have been designed to house two three-component accelerometers in order to capture dynamic loadings by remote seismic waves. In detail, the whole clamp-SIMFIP assembly is floating around the central steel tube, which is straddling the two packers that are sealing the borehole measuring interval. The assembly is kept central by the centralizing pins when pressure is applied to the unlock direction cylinder, and when deploying into the borehole. When pressure is released from the unlock cylinder and pressure is applied to the lock cylinder, the centralizing pins are released, and the locking arms are deployed. The unlock cylinder pressure is isolated from the zone pressure, so that no zone pressure forces can act on the piston, thereby isolating the clamp behavior from the changes in zone pressure. This has the benefit that the zone pressure does not affect forces directly on the SIMFIP so the SIMFIP, therefore, measures only forces conveyed by the rock. The accelerometer assembly is integrated into the clamp body housing so as to pick up any acceleration conveyed by the rock mass into the clamping assembly.

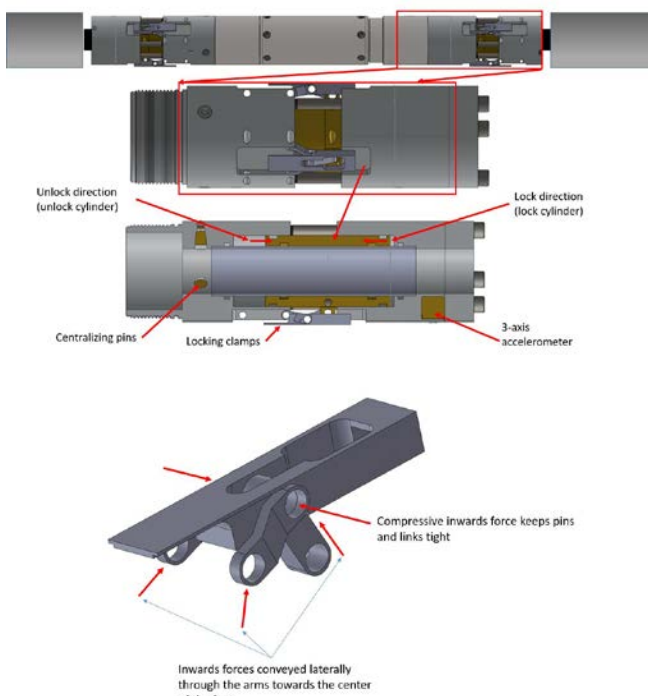

Figure 8-3. Upper figure shows the detailed SolidWorks plan of the SIMFIP anchors developed within the NUMO project. Lower figure shows the locking arm design to prevent link slop and stick slip artifacts from arm links themselves from registering in the SIMFIP data.

To probe a broader band of frequencies, we have designed the integration of the following sensors in a new tool (Figure 8-4):

- A hydrophone set in the monitoring chamber. The hydrophone can capture with high resolution the dynamic changes caused to the fractures flow regime during the passing seismic waves. They will also allow using different types of natural waves such as tube waves induced by natural surface waves “shaking” of fractures to estimate infinitesimal changes in the fractures permeability, thus, potentially contribute to monitoring the eventual sealing of fractures.
- Two 3-component accelerometers such as the ones used in the 6 monitoring boreholes at SURF. If installed in the SIMFIP probe, we would utilize the tight coupling achieved through the clamping mechanisms to obtain very good records of the seismic waves. The central frequency of the recorded activity is on the order of 10 kHz, and does attenuate accordingly over very short distances. Therefore, achieving optimal coupling between the accelerometers and the rock is of great importance. Having two instruments has a number of advantages. First, in case one of the sensors fail we have a redundant second sensor. Second, using two sensors we could use coincidence triggers for processing the waveforms to only consider events that are recorded by both sensors.
- Distributed water electric resistivity measurements. These measurements can give an idea of different types of groundwater moved by the fractures permeability activation, for example if some hydraulic connection between different fault compartments occur or if some dissolved gas leak from the repository site.

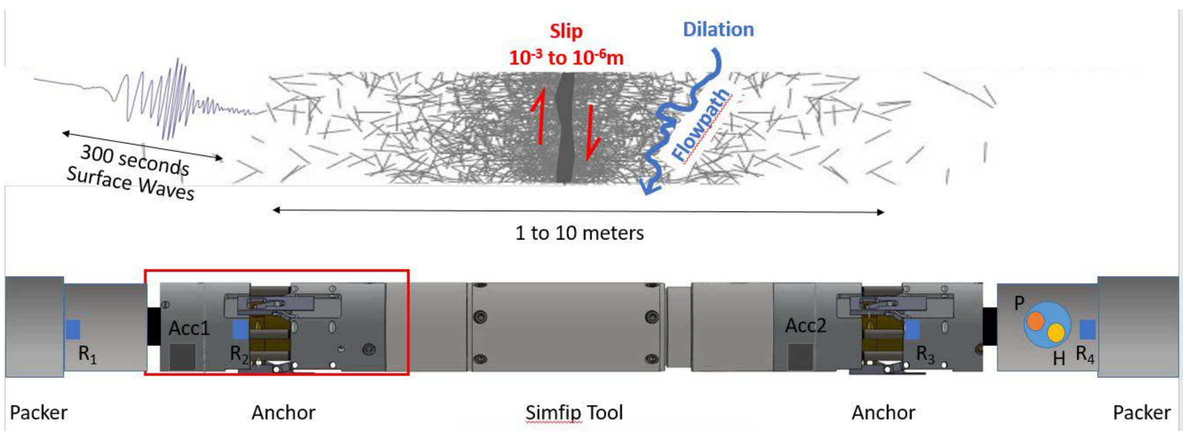

Figure 8-4. Concept of the upgraded SIMFIP tool. Upper figure shows a schematic natural fault zone with a central core surrounded by a fractured damage zone. Middle figure shows the proposed upgraded SIMFIP tool (R1 to R4 are water electric resistivity electrodes, Acc1 and Acc2 are three-components accelerometers, P is a pressure sensor and H is a hydrophone).

8.2.2.2 Long-term reliability of the SIMFIP sensor.

A SIMFIP probe has been designed for long-term monitoring of fault hydromechanical variations around repository sites. Since October 2018, this probe prototype is installed at the Mont Terri underground laboratory (Switzerland), which is built into the Opalinus Clay formation (which is investigated as a potential host rock for deep geologic nuclear waste disposal by the Federal Council of Nuclear Waste Disposal of Switzerland). The laboratory consists of multiple tunnels and galleries located in the SW-NE trending Mont Terri anticline and where the studied fault, although called the "Main Fault" because it is the most deformed zone intersected by the laboratory facilities, it is actually a minor splay. The SIMFIP probe has been installed in a vertical borehole at a depth of 22m below the galleries. It is straddling the entire fault thickness (Figures 8-5a-d). In detail Figures 8-5b,c illustrate that the fault contains complex geological structures characterized by (i) a high density of fractures with orientations mainly ranging from N30 to N70, dipping 20 to 60° SE, and (ii) thick lenses of 'scaly' fabric where 'the rock splits progressively into smaller fish-like flakes.' The fault zone is bounded by two major fault planes, respectively at 21.15 m and 26.15 m (Figure 8-5c).

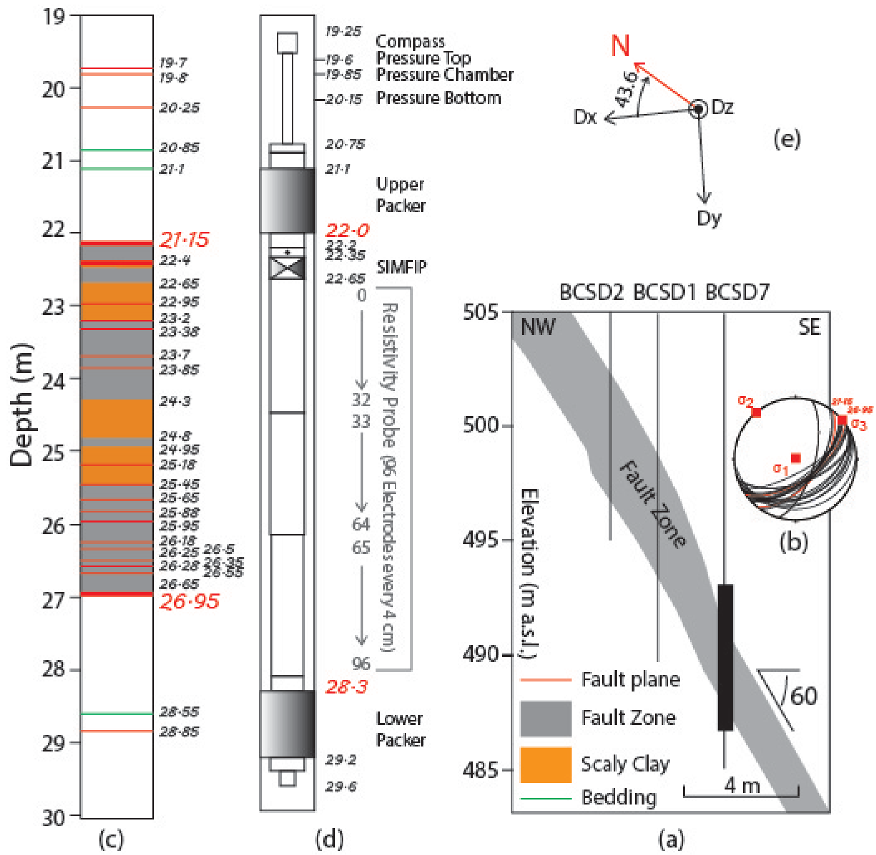

Figure 8-5. (a) SIMFIP probe installation across the Mt Terri Main Fault (black rectangle in borehole BCSD7). (b) Stereographic projection of the Main Fault fractures (the commonly used Mt-Terri state of stress is plotted in red). (c) Detailed log of the borehole Main Fault structures. (d) Plan of the SIMFIP probe. (e) Orientation of the (Dx, Dy, Dz) relative displacements of the upper packer (the lower packer considered fixed).

In order to monitor the hydromechanical behavior of the entire fault zone, a 6.3m long SIMFIP interval has been designed, sealed by two 0.9 m long inflatable packers (Figure 8-5d). In this configuration, the SIMFIP sensor is measuring the relative displacement of the upper packer, the lower packer considered fixed. Thus, the packers play two roles, sealing the interval to isolate fault zone pore pressure variations and anchoring the SIMFIP to measure the displacement of the fault hanging wall relative to the foot wall. A compass set above the upper packer allows orienting the displacement measurements. Borehole pressures are monitored below the lower packer (Pressure bottom), between the packers (Pressure chamber) and above the upper packer (Pressure Top). Finally, water resistivity electrodes have been distributed every 4 cm along the entire length of the SIMFIP chamber in order to localize where eventual leaks could occur from the fault zone into the borehole. We assume that, for example, dissolved gas leak would slightly change the formation water resistivity, enough to be detected by the resistivity probe. An experiment will be made to test this setting by injecting dissolved CO_2 in the fault zone from borehole BCSD1 (Figure 8-5a), while monitoring at the SIMFIP hole. Other gas could eventually be tested, too, in the future.

The SIMFIP probe was installed in the borehole immediately after drilling. Figure 8-6 shows the results of the 5 months monitoring period, which was characterized by an installation phase in October 10th, followed by a period of tuning the packers pressure until December 19th, and finally a period of baseline monitoring until the actual date (monitoring is still permanently running). Periods of packers testing are highlighted by the vertical blue lines in Figure 8-6. The main issue was to maintain a constant packer pressure. For example, during December 2018, packers showed a slow deflation that required several manual re-inflations. The problem was fixed in January 2019 by installing an automatic control of the packer pressure (Figure 8-6a). The four periods of packer pressure variations of January 10th, 16th, February 1st and March 27th correspond to complementary adjustments of the packer system. The control of the packer response is crucial because this probe is equipped with sliding-end packers in order to insure an optimal sealing of the isolated interval that permanently matches with borehole dimension evolution related to interval pressure variation and to borehole clay walls deformations. Thus, because the packers slide while their pressure is varying, it affects the chamber pressure and the displacement measurements (since the SIMFIP is anchored with the packers, Figure 8-6b and c). The packers' pressure increase is inducing a chamber pressure decrease, a SIMFIP vertical extension (positive Dz variation) and an equal radial displacement (Dx = Dy, see, for example, February 2019 packer pressure increase in Figure 8-6a). Interestingly, this response matches with laboratory calibrations, and, thus, any deviation from it observed in the field might highlight a true hydromechanical evolution of the formation.

Interestingly, the chamber pressure increased to 0.583 MPa during the November-December 2018 period. Then, from November 26th to present, pressure decreased to reach a quasi-steady state at about 0.331 MPa in March 2019. In addition, pressure in the lower part of the borehole started to slowly increase, and is still not at steady state (Pbot in Figure 8-6b). These long-term pressure variations are not clearly related to packers' effect (although influence of the packers is observed over shorter periods of time). Both variations might thus be related to borehole pressure equilibration with formation pressure that occurred in about 5 months, given the very low formation permeability. Displacement variations follow these long-term pressure variations. Displacement amplitudes are of 0.3 to 1 mm, the norm of displacement vector in March 2019 being estimated to 0.95 mm after 5 months of monitoring (more than 70% of the displacement occurred after about 1.5 month). These values are in reasonable accordance with strain relaxation effects associated to borehole or gallery excavation observed in other Mt-Terri experiments.

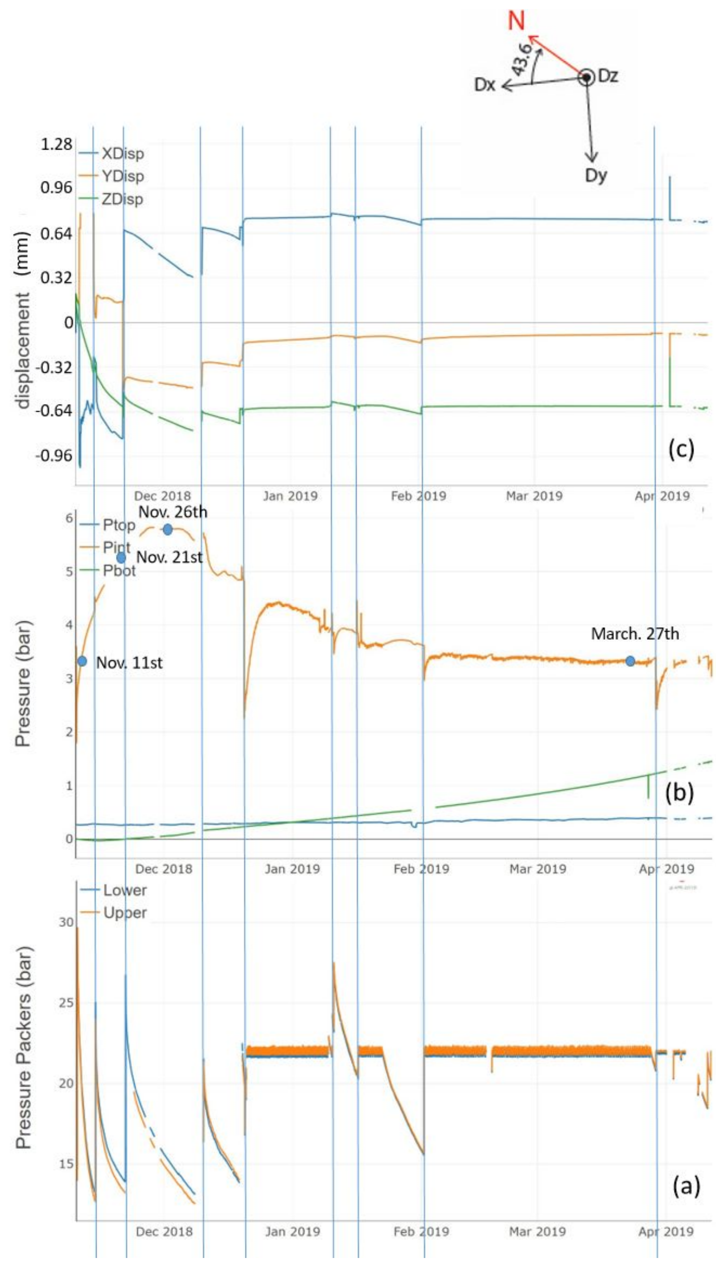

Figure 8-6. Long-term fault zone displacement and pore pressure monitoring: (a) Packer pressure, (b) Chamber pressure (Pint), Bottom hole pressure (Pbot) and Top hole pressure (Ptop), (c) (Dx, Dy, Dz) displacement of the upper packer of the SIMFIP probe (Fault hanging wall).

In Figure 8-7a, we picked the displacements at four points during the rising pressure period (November 11th, 21st and 26th) and during the quasi-constant period on March 27th. The corresponding displacement vectors are plotted in a stereographic lower hemisphere projection (Figure 8-7b), and compared to the orientation of the fault zone fracture and the state of stress (Figure 8-7c). During the pressure rising period, the displacements are oriented N165 to N150 dipping 15 to 45° SE. This is in good accordance with a normal faulting regime characterized by slip along the existing fault zone fractures. After the maximum pressure, there is a drastic rotation of the displacements to N330 - 25º NW, which is in good accordance with a normal closing of the fault zone fractures. These observations show that shearing of pre-existing fault zone fractures may have guided stress relaxation following the borehole excavation. Slip along fractures may have triggered convergence of the chamber walls and explained the initial chamber pressure increase. Slip might also have produced dilation and a slight permeability increase around the borehole, which explains the following chamber pressure decrease until its eventual equilibrium with the formation pressure. The Mohr-Coulomb plot shows that some of the fault zone fractures could potentially be reactivated in shear if we consider the commonly admitted stress tensor and a 0.2 coefficient of friction for fractures. Thus, these long-term observations may show how stress relaxation around a borehole in shales is eventually followed by dilation and drainage.

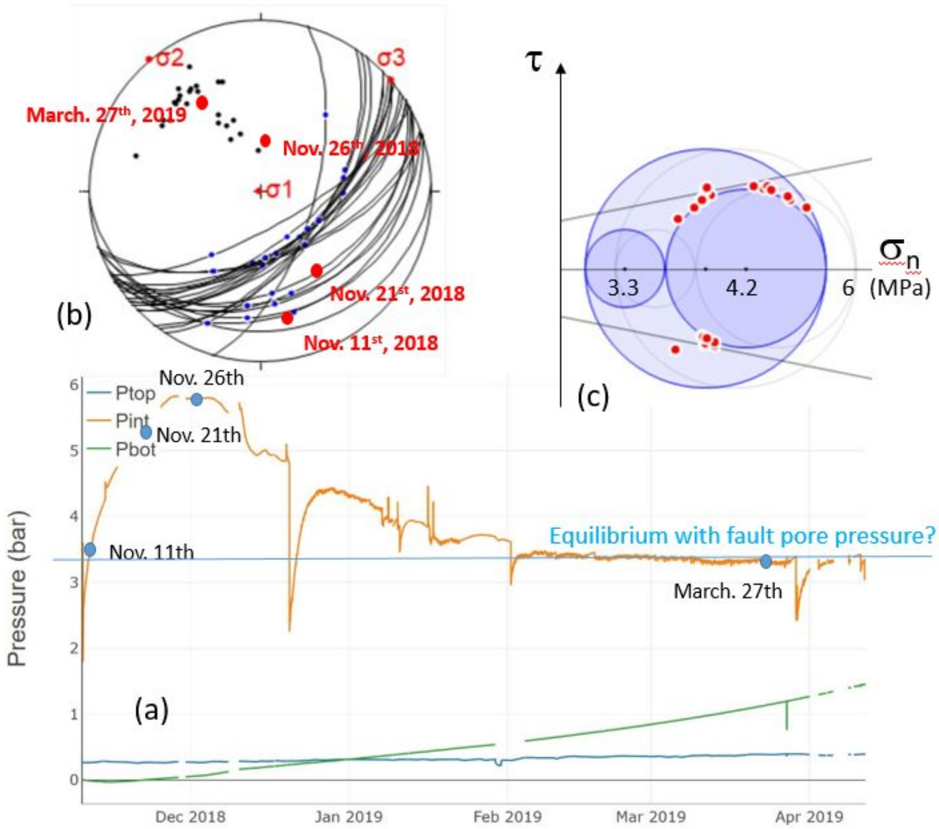

Figure 8-7. (a) Blue points show where the SIMFIP displacements have been picked during the Chamber pressure variations. (b) Stereographic projection of the displacement vectors (red points), fault zone fractures (black lines, black points are the fractures poles) and principal stresses from the Martin and Lanyon tensor commonly used at Mt Terri (blue points on the fracture traces show the orientation of the calculated slip vectors given the considered tensor). (c) Mohr-Coulomb graph of shear and normal stresses calculated on each fracture planes (red points, the inclined lines show the elastic limit given a 0.2 friction coefficient of a no-cohesion fault).

Finally, Figure 8-8 shows the water resistivity variations measured at the 96 electrodes distributed in the SIMFIP chamber (Figure 8-5d) since January 2019. Here data are shown in an arbitrary unit, but they display no significant variation (except two electrode figured in green and yellow that will be removed from the later analyses). This is normal because the chamber is filled with Pearson water in chemical equilibrium with the formation water, to avoid any clay swelling effect. Thus, there is no reason for any evolution of the signal, which, in return, displays a relatively low noise and a reasonable long-term stability. In detail, we expect to detect resistivity variations as low as ~5% of each electrode full scale.

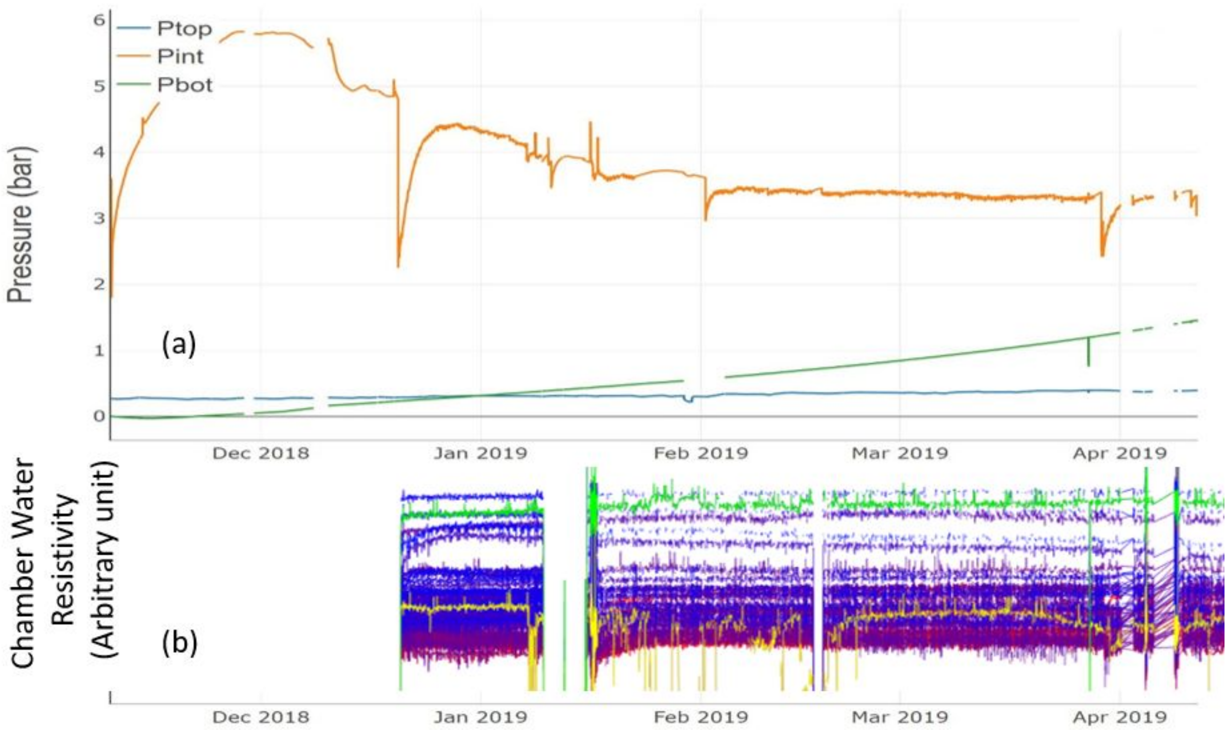

Figure 8-8. Comparison of (a) chamber pressure variations with (b) water electric resistivity variations at the 96 electrodes set in the chamber of the SIMFIP probe.

8.2.3 Conclusions and Perspectives

The preliminary results highlight the potential interest of the new type of SIMFIP instrument, which allows for a refined monitoring of the coupled hydromechanical processes in a small fault zone affecting a clay rich host rock. Results show how the complex equilibrium between borehole pressure and formation pressure may be reached through a several months long stress relaxation accommodated by slip and dilation on the fault fractures. During *in situ* testing, we have developed technical solutions to control the packers pressure in order to improve the resolution of long-term measurements. This allowed for identifying the packers influence on pore pressure measurements in borehole sealed sections in such compliant clay materials. The perspectives are to monitor eventual fault movements and associated changes in pore pressures (i) during local water-with-dissolved CO_2 injections (tests will start around October 2019 and will be repeated over the next two years), and (ii) during the excavation breakthrough of the new Mont Terri gallery, which will occur by the end of May 2019, at about 30 meters from the SIMFIP monitoring zone.

8.3 Observations of the Fault Rupture and Fluid Leakage in Shale

8.3.1 Introduction

Here we report the results of *in situ* experiments conducted to investigate changes in permeability associated with a series of fault movements induced by repeated periods of water injection (and related fluid pressure buildup) in a borehole interval straddling a fault zone intersecting a claystone formation at 300 m depth in the Mont Terri Underground Research Laboratory (Switzerland). The Fault zone is the same as the one described in the previous chapter, but the experiment was different. The one described here, called "FS experiment," was dedicated to short-term hydromechanical testing of the fault zone. Three 30-minute long injection cycles were conducted, each separated by 30-minute long waiting periods without injection. Continuous monitoring of pressure, flowrate and fault displacement was conducted over the entire period at an injection and a monitoring vertical borehole, both drilled about 5 m away across the fault. The injection and monitoring fault intervals were set at 40.6 m and 37.65 m depths, respectively (Figure 8-9).

A very low fault permeability of ~10^{-17} m^2, which is close to the permeability of the host rock, was estimated before activation. State of stress estimated in and around the fault is characterized by a normal regime with the maximum principal stress σ_1 = 5.3±0.2 MPa sub-vertical, σ_2 = 4.5±0.2 MPa sub-horizontal, and striking N310±10° and σ_3 = 3.8±0.2 MPa sub-horizontal and striking N040±10°E.

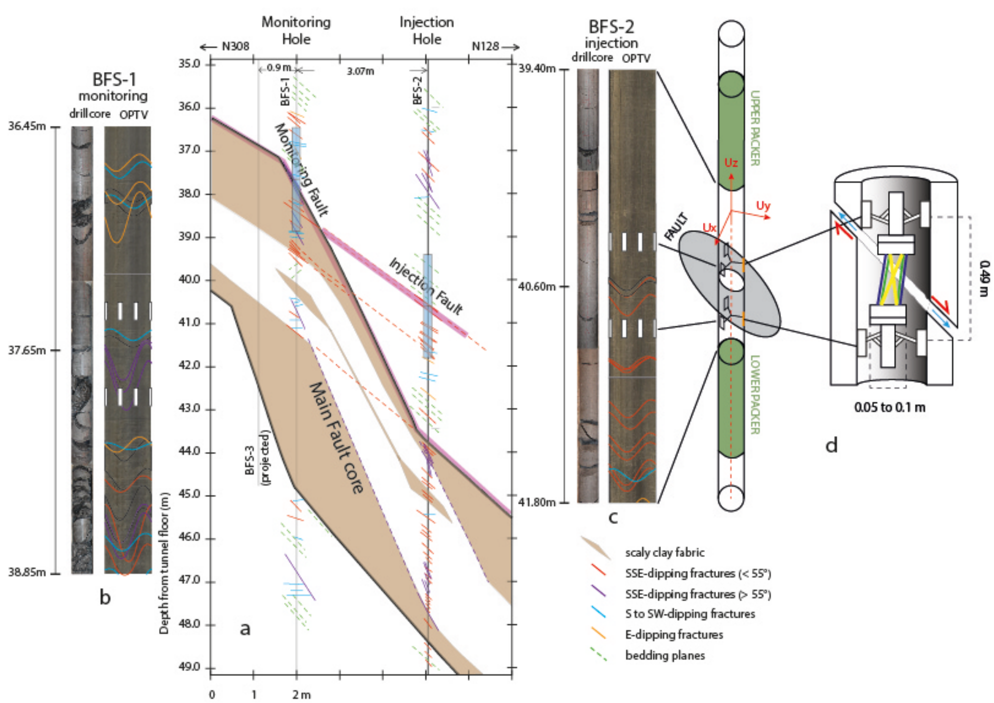

Figure 8-9. (a) Vertical cross-section of the structural setting of the Main Fault activation experiment (blue rectangles shows the location of the test intervals); (b) and (c) Cores and optical log of BFS-1 and BFS-2 intervals (white rectangles on the optical log figure indicate exact locations of the anchors of the displacement sensor); (d) the straddle-packer probe and details of the instrument used to monitor fault displacements at both BFS-1 and BFS-2 intervals. The fault zones across which the SIMFIP sensor is set are named as the injection and the monitoring faults.

Here we report on the complex relationships between fault permeability variations and rupture induced by injection pressures that were set in the range of pressure variations that could, for example, be induced by thermal pressurization of a host rock layer.

8.3.2 Overview of Fault Permeability Variations During the Entire Test Period

In Figure 8-10, we are presenting the graphs depicting the permeability during repeated pressure pulses conducted at the interval located 40.6 m below the galleries (see Figure 8-9a for the location). The upper red and blue curves show the imposed step-by-step pressure variations. Red segments of the pressure curve correspond to time intervals of the pressure increase in the borehole. Blue segments of the pressure curve correspond to the transient pressure evolution caused by the fault hydromechanical response after the pressure was increased in the test interval. Green segments show the fault displacement rate variations measured by the SIMFIP sensor (here it is the rate of the total displacement vector, which was continuously monitored by the SIMFIP during the test). For comparison, the lower graph shows the fault permeability variations obtained from fully coupled hydromechanical modeling with the TOUGH-FLAC simulator.

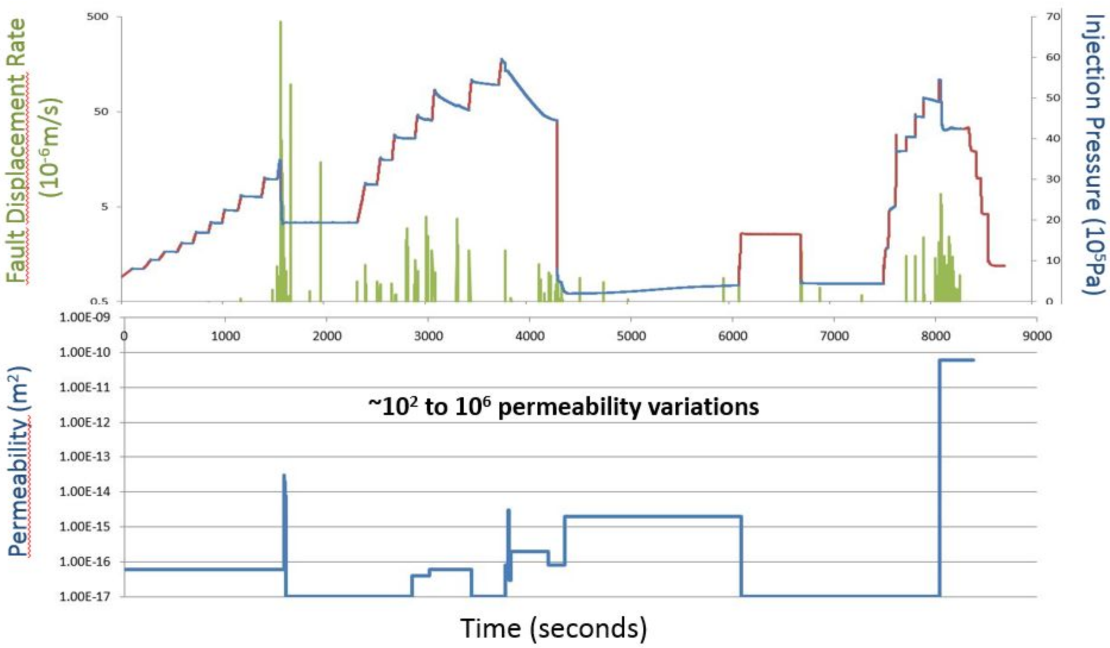

Figure 8-10. Upper graph – pressure (red and blue) and fault displacement rate (green) monitored during pressurization tests in the interval 40.2 m. Lower graph – interval permeability estimated from the fully coupled modeling of the pressure using the TOUGH-FLAC simulator.

Comparison of the upper and lower graphs shows that the large permeability variations correlate with periods of large slip rate events at 1500, 3800 and 8000 seconds, respectively. Interestingly, these permeability changes do not match well with the pressure imposed in the interval. Indeed, the 1500-second event is associated to a factor of 10 larger permeability change than the 3800-second one, although it occurs at a fault opening pressure about 2 MPa lower. This observation reveals that a relatively small pressurization associated with a high displacement rate might produce a larger permeability variation than a high pressurization associated to a small displacement rate. Thus, fault displacement rate might cause the effect of stress on fault reactivation and leakage. This observation also shows that the continuous fault displacement monitored by the SIMFIP sensor allows for tracking changes in faults displacement rates as potential precursors to "large" fault leaks (for simplicity we only show here the displacement rates, which are derived from the SIMFIP measured displacements).

8.3.3 Detailed analysis of fault permeability variation during one pressure cycle

In Figure 8-11, we compare permeability variation to the effective normal stress variation calculated at the injection and the monitoring points using the stress tensor commonly admitted at the Mont Terri site. We used the Thiem solution (Thiem, 1906) to rough estimate the permeability at the injection point during the engine pump test:

$$K = \frac{Q}{2\pi(P_i - P_{r_0})e} \ln\left(\frac{r_0}{r_w}\right) \tag{8.2}$$

With K is the permeability (m^2), Q is the flow rate (m^3/s), r_0 is the radius of influence (m), r_w is the borehole radius (m), P_i the injection pressure (Pa), P_{r_0} is the pressure at the equivalent r_0 radius, and e (m) the interval thickness (here e = 2.4 m). We are aware that using the Thiem solution can only provide a rough estimate of permeability as the formula was developed for steady state flow to fully penetrating pumping well in a confined aquifer.

First, we approximated the value of the radius of influence r_0 considering that the injected volume V followed a radial flow into a single fault zone of aperture b_m, using the following equation:

$$r_0 = \sqrt{\frac{V}{\pi b_m} + r_w^2} \tag{8.3}$$

We considered two b_m values, respectively of 100 and 200 microns, which are in the range of the measured displacement normal to the Main Fault plane during fault rupture (Figure 8-11c). With these values, the calculated r_0 when the pressure starts increasing at the monitoring point is of 3 to 5 m (Figure 8-11b), which is in reasonable agreement with the geometric distance between the two boreholes (Figure 8-9). At the end of the injection, we get r_0 of 13.5 to 19 m, which gives an estimate of the ruptured patch that has been pressurized.

Second, using the pressure measured at the injection and monitoring points (respectively, P_i and P_{r_0} in Equation 8.2), the measured flowrate (Q in Equation 8.2) and the geometrical distance between the two measuring points (r_0 = 4.5 m), we calculated the change in the fault permeability (Figure 8-11b). There is a fast permeability increase to a maximum value of 3.6 x 10^{-8} m^2, when the effective normal stress on the injection and the monitoring faults fall to almost zero and 0.8 MPa, respectively. Then, permeability displays complex variations, finally getting to a value of ~2.2 10^{-9} m^2. Relative to estimated initial permeability values of $\sim(6 - 8) \times 10^{-17}\, m^2$ in the fault, this value corresponds to a seven-orders-of-magnitude permeability increase.

Third, we assumed that fluid flow along the fault is governed by Darcy's law with cubic dependency between flow rate and hydraulic conducting aperture, i.e. the fluid flow per unit width is governed by

$$q = -\frac{b_h^3 \rho g}{12\mu} \Delta h = -T_f \Delta h \tag{8.4}$$

where b_h [m] is hydraulic conducting aperture, ρ [kg/m^3] is fluid density, g is the acceleration due to gravity [m/s^2], h is hydraulic head [m], μ is dynamic fluid viscosity [Pa s], and T_f [m^2/s] is fracture transmissivity. In that formulation, the permeability is given by

$$K = \frac{{b_h}^2}{12} \tag{8.5}$$

Using the previously calculated K and Equation 8.4, we compared the changes in the fault hydraulic conducting aperture b_h with the measured monitoring fault normal displacement (Figure 8-11c). We find that the hydraulic aperture is in a good agreement with the normal displacement measured after fault reactivation. Nevertheless, when injection pressure is stepped down after 1.505 10^4 seconds, there is a sharp decrease in aperture while normal displacement decrease is more progressive, finally stabilizing at a residual value of ~ 85 microns. This shows that even if the hydraulic connection between injection and monitoring points is closed as soon as the effective normal stress is increasing (because of pressure decrease), it does not mean a complete closure of the fault. This is also in good accordance with the no flow-back measurement showing that the injected fluid may remain trapped into the ruptured patch.

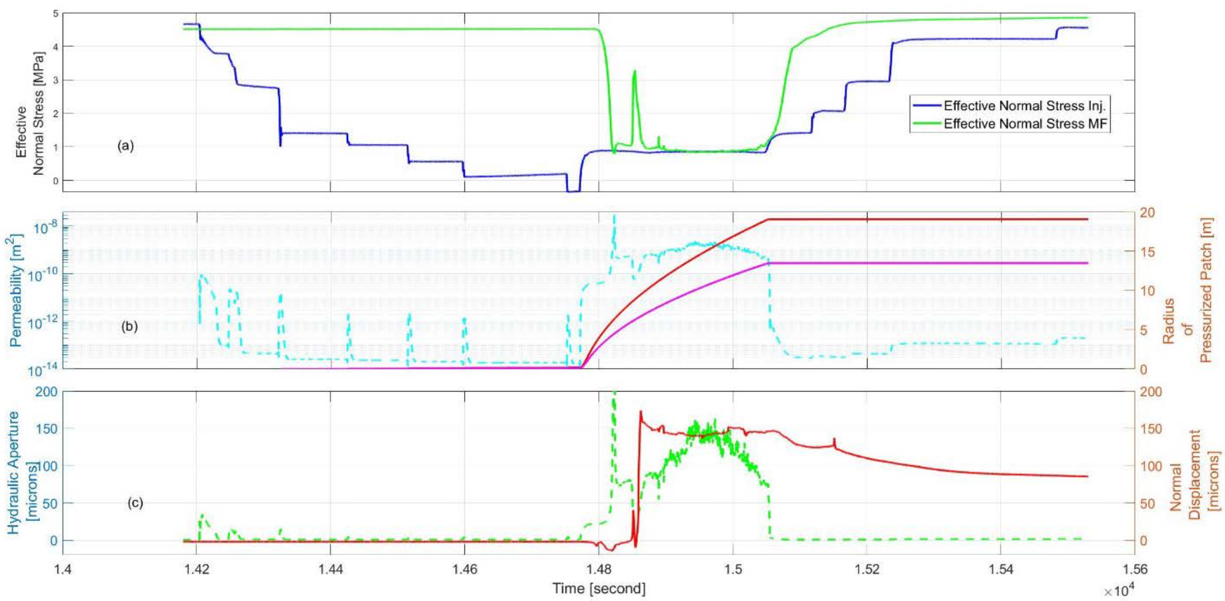

Figure 8-11. (a) Effective normal stress variations estimated at the injection and monitoring points during the engine pump test. (b) Fault permeability (dashed line) and radius of the pressurized patch evolution (red is for b_m = 100 microns and magenta is for b_m = 200 micron). (c) Calculated hydraulic aperture (dashed green curve) and measured fault normal displacement (red curve).

In summary, permeability change is occurring when the injection fault is strongly over-pressurized; highlighting that migration of water through the initially very low permeable fault is only possible at a significant pressure magnitude and gradients. The mechanism of permeability enhancement is related to a large opening of the injection fault, the drop to a zero effective normal stress and the hydraulic aperture that equals the measured fault normal opening potentially indicating that the two walls of the fault may be locally separated.

8.3.4 Relation between permeability variation and mode of fault activation

The estimated permeability increases during the entire test sequence are associated with the stress path evolution at the injection and at the monitoring points during the rupture propagation (Figure 8-12). The shear and the effective normal stresses have been calculated on all the fractures affecting the injection and the monitoring intervals. We used the constitutive strength properties of the intact rock, the bedding planes and the fault that had been determined through direct shear tests conducted in the laboratory (Thoeny, 2014; Amman et al., 2012). These authors defined a bi-linear Coulomb failure criterion characterized by a friction coefficient of 0.19 at the confining stress > 2 MPa, and a friction coefficient of

0.4 to 0.58 below 2 MPa respectively for faults and bedding planes. They attributed this difference in friction coefficients to the high dilatancy at low confining pressure, which favors a friction increase. In addition, they found that bedding planes cohesion was ~0.6 MPa while faults had a less-than-0.1 MPa cohesion. In Figure 8-12a, we hypothesize that the bedding planes and the fault failure envelops define a “strength area,” where discontinuities included in a thick fault zone can rupture in shear. Above this area, is the zone limited by the intact rock strength characterized by (i) a tensile strength of 1.2 to 1.8 and 0.6 MPa parallel and perpendicular to the bedding planes, respectively, and (ii) an average 24° frictional angle.

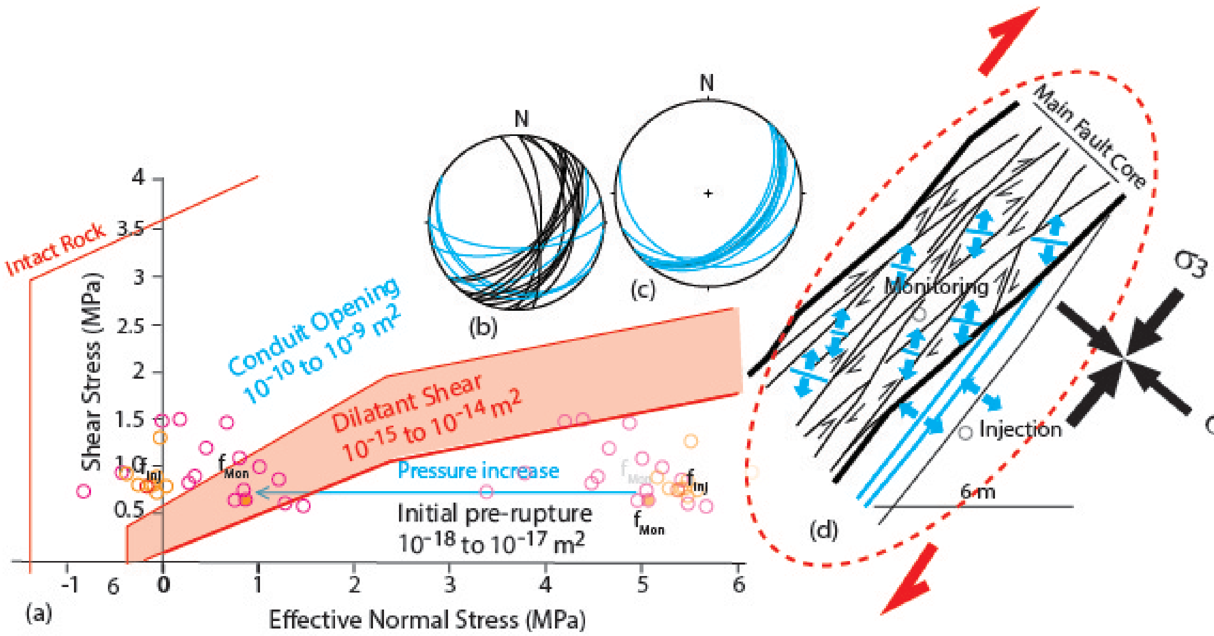

Figure 8-12. Relationship between permeability variation and mode of fault activation. (a) Stress on fractures at the onset of Event 3 and quantitative estimation of permeability variations. (b) and (c) Mode of permeability changes in the Fault core and at the injection point, respectively (blue are fractures that potentially favor conduit opening, black are fractures that potentially favor dilatant shear). (d) Conceptual map view of the Fault activation patch.

Given these fault properties and state of stresses, all the fractures of the injection interval experience an effective normal stress reduction to ~ 0 MPa when the large increase in flowrate is observed (Figure 8-12a and c). Thus, the observed “sudden” permeability increase to ~2.2 10^{-9} m^2 (Figure 8-11) happens above the fault frictional rupture domain defined in Figure 8-12a. It remains below the intact rock failure envelop showing that the overpressure inducing total opening of preexisting fractures might be the most probable mechanism of such large permeability enhancement, which we call “conduit opening” in Figure 8-12a. In the monitoring interval, two potential fracture activation modes coexist when the interval pressure reaches 4.17 MPa (Figure 8-12b). Five fractures are sufficiently well oriented towards stress to experience a ~0 MPa effective normal stress drop and an eventual conduit-opening-like permeability increase. These fractures correspond to a small number of secondary N080 to N110 planes of limited length, which are cut by the main family of N020 to N060 fault planes (Figure 8-12b and d). The remaining majority of fractures potentially experience a reactivation in shear (Figure 8-12a), thus an eventual lower permeability increase from 10^{-18} to 10^{-14} m^2. Indeed, these fractures plot in the dilatant shear zone, where permeability variations were studied by Jeanne et al. (2018).

We can, thus, isolate two regimes of fault permeability variations which successively occur during the repeated pressurization cycles of the initially low permeability clay fault: (1) a transient regime with permeability pulses related to slip induced dilation/compaction, and (2) a “steady state” regime related to over-pressurization and perhaps local separation of fault walls. During the experiment, rupture propagation is mainly associated to the over-pressure regime. We, thus, conclude that rupture propagation must be related to the mode of permeability growth, the presence of strong overpressures favoring a more stable permeability increase than the frictional rupture regime.

8.4 Numerical analysis of key parameters conditioning fault activation induced by pore pressure increase

To investigate the coupling between fault permeability enhancement and slip or slip rate during fluid pressurization, we use the 3DEC code (Itasca Consulting Group, 2016), a distinct element method (Cundall, 1988) to simulate the interaction between fluid flow and fault slip evolution, including hydromechanical coupling, effective stress and friction. To describe the relationship between the fluid pressure diffusion and the permeability change with the fault normal displacement, the model uses the cubic law (Witherspoon et al., 1980). The method has been previously used to understand the hydromechanical behavior of fractured rock and fault zones during fluid pressurization (Cappa et al., 2006; Guglielmi et al., 2008), and to show that the evolution of the fault hydraulic diffusivity is a fully coupled problem depending on stress and fluid pressure (Guglielmi et al., 2015b).

8.4.1 Theoretical analysis of relationship between fault permeability increase and fault slip

We analyzed the influence of fault hydromechanical properties on the growth of injection induced aseismic slip. Using hydromechanical modeling, we show how permeability enhancement, in addition to the background stress and frictional weakening, has an important effect on the pressure diffusion and slip growth during injection. We find that the more pronounced the fault permeability enhancement, the stronger is the growth of the aseismic slip zone. The effect of enhanced permeability is more pronounced when the fault is initially close to failure. Our results show that aseismic slip grows beyond the pressurized zone when the fault permeability increases, while slip remains behind the pressurized zone when permeability does not vary from its initial pre-slip value. Thus, fault permeability increases should be considered as complementary mechanism to current models of fluid induced aseismic slip.

Our 2D model (200 m × 50 m) considers a fluid injection into a horizontal flat fault in homogeneous elastic and impervious media (Figure 8-13a). The remote normal (σ_n) and shear stress (τ) resolved on the fault plane are constant. During injection, the fluid pressure is increased into the fault step-by-step of 0.5 MPa every 150 seconds at the point-source (Figure 8-13b). The total time of injection was 1050 seconds. For numerical accuracy, we used the fine mesh size (0.15 m) along the fault, which was gradually increased to 0.5 m in the direction normal to the fault toward model boundaries.

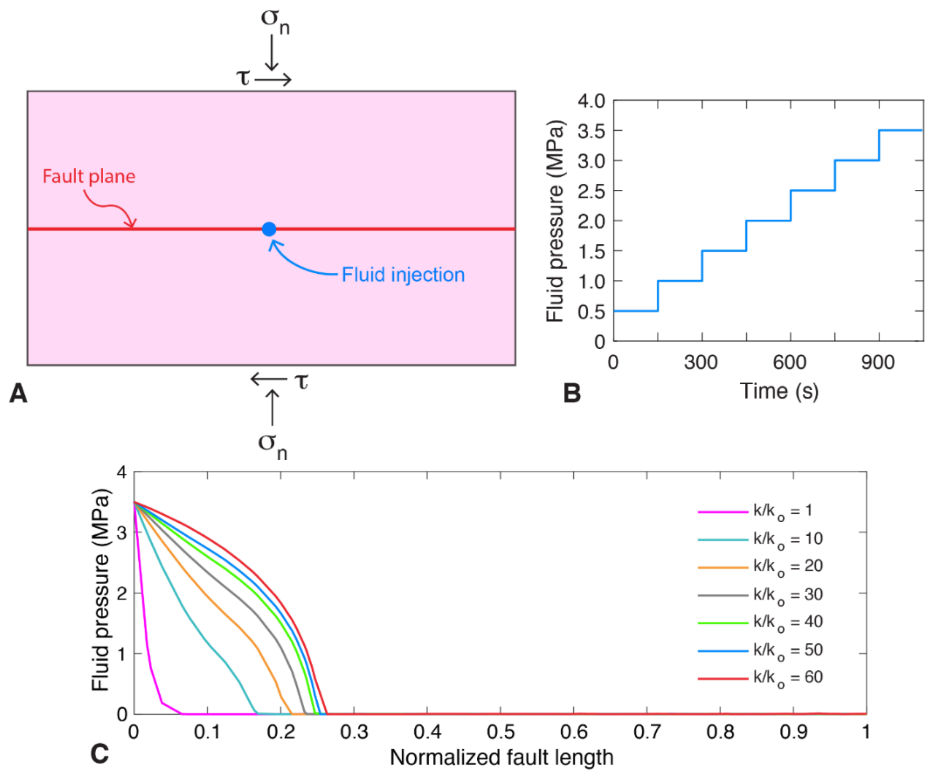

Figure 8-13. (a) Model geometry, and (b) graph of the simulated step-by-step pressure increase into the fault. The remote normal (σ_n) and shear stress (τ) resolved on the fault plane are constant, (c) half-profiles of fluid pressure calculated along the fault, assuming different permeability ratios (k/k_o). The injection point is located at x = 0 along the horizontal axis x representing the distance along fault. Half-profiles are plotted at the end of injection scenario in (b).

In these preliminary tests, we considered the following initial values of the normal stress and the fluid pressure into the fault: σ_{no} = 4.25 MPa and p_o = 0 MPa. We used two different values of shear stress τ_o = 1.65 and 2 MPa to evaluate the effects of different levels of fault criticality to failure, σ_{no}/τ_o = 0.388 and 0.47, respectively. We have tested the effects of different values of permeability changes with fault displacements k/k_o = 1, 10, 20, 30, 40, 50, and 60. The initial hydraulic aperture was assumed to be 9.15 microns (corresponding $k = 7 \times 10^{-12}$ m^2 calculated from the cubic law). Rock elastic properties are K = 20 GPa for the bulk modulus and G = 9 GPa for the shear modulus.

Here, we have tested constant friction and rate-and-state friction (Marone, 1998). For a rate-and-state fault, we assumed the following frictional parameters: μ_o = 0.6, (a-b) = -0.002, and d_c = 10 microns. μ_o is the friction coefficient at a reference slip velocity. The parameter a quantifies the direct effect of a change in slip velocity. The parameter b describes the effect of the state variable (here, we use the "aging law" (Dieterich, 1979)). The characteristic slip distance, d_c, governs the evolution of the state variable. For the fault model with a constant friction, we assumed a static value (μ_s) of 0.6. For simplicity, shear-induced dilatancy is neglected in the simulations.

The modeling results shown in Figure 8-13c revealed that the development of the fluid pressure along the fault varies as a function of different permeability enhancement. Modeling results indicate that both the magnitude and distribution of the steady-state overpressure, as well as the size of the pressurized area, depend on the permeability change. For constant permeability, the pressure perturbation is less pronounced, and the highest pressure and sharpest pressure gradients are situated near the pressurization point. For the modeling scenario with evolving permeability, the pressurization produces a reduction in effective normal stress by increasing the fluid pressure, which leads to opening the fault and increasing its permeability. The size of the pressurized zone is growing significantly with the fault permeability enhancement. Modeling results show that higher the permeability increase, the greater the pressurized area is (Figure 8-13c).

Then, we investigated the effects of the fluid pressure development on the size of the slip zone, and its dependency on the background stress and fault parameters (Figure 8-14). During the fluid pressurization along the fault, the reduction in frictional resistance to sliding, in the presence of a background fault-resolved shear stress, drives the growth of slip. Here, we modeled an aseismic slip (i.e., slow slip without dynamic effects). In Figure 8-14, we compared the slip length as a function of the length of the pressurized zone for a representative range of stress ratio (τ_o/σ_{no}), friction laws and permeability evolution (k/k_o). We found that the slip growth is controlled by a combination of the background stress, frictional weakening and permeability enhancement. For example, a fault with higher background stress and larger enhanced permeability can produce larger slip growth. The background stress affects both the timing of the onset of rupture and the subsequent size evolution of the slip area (Figure 8-14a). Reducing the shear stress delays the onset of rupture and decreases the maximal size of the slip area, whereas the increased shear stress leads to the earlier onset and a larger slipping zone. The effect of the fault friction is also illustrated in Figure 8-14a. Fault frictional weakening using the rate-and-state friction law influences the temporal evolution of the slipping area and may produce larger ruptures. This is expected because friction weakening leads to the reduced fault strength with sequences of accelerated and increased slip, while constant friction tends to stabilize the fault strength, resulting in a less pronounced slip.

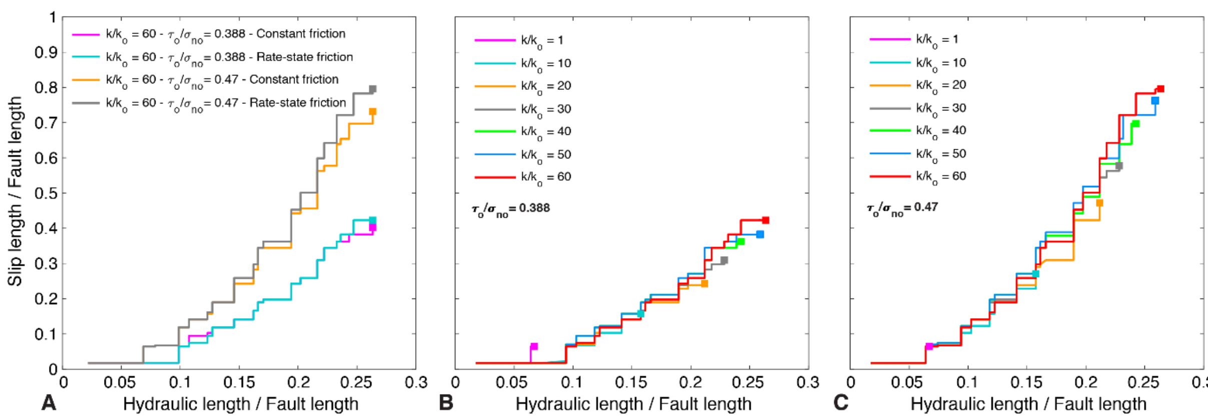

Figure 8-14. Influence of stress conditions and fault-related frictional and hydraulic parameters on the evolution of fault slip. Slip length as function of the hydraulic length for different (a) initial stress ratios and friction laws (i.e., constant friction, rate-and-state friction), and changes in fault permeability for two different stress regimes, (b) τ_o/σ_{no} = 0.388, and (c) τ_o/σ_{no} = 0.47, respectively.

Modeling results also indicate that the permeability evolution affects the spatial extent of the fluid overpressure on the fault, and the fault resistance to rupture; hence, it affects both the maximum diffusion length and the size of slip zone (Figures 8-14b and c). All simulation results, including permeability changes $k/k_o > 1$, show that the growth of the fault slip outpaces the growing fluid pressure front. Higher the increase in fault permeability, higher the growth of the slip front is. In addition, the most noticeable difference between the slip and pressure fronts occurs for the higher, more critical, initial stress ratio τ_o/σ_{no} = 0.47.

In summary, the initial stress on the fault and the change in fault permeability have an important impact on fault slip, which can occur over a zone much greater than the fluid-pressurized zone. For instance, the size of the slip zone is about 1.74 and 3.23 times greater than the size of the pressurized dilatant zone, respectively, for an initial stress ratio of 0.388 and 0.47, respectively (Figure 8-15). Thus, in addition to the fault frictional weakening, the size of the slip zone is controlled by the integral effect of the spatial extent of fluid pressure on the fault. The spatial extent of the largest slip increases with the spatial extent of the largest fluid pressure.

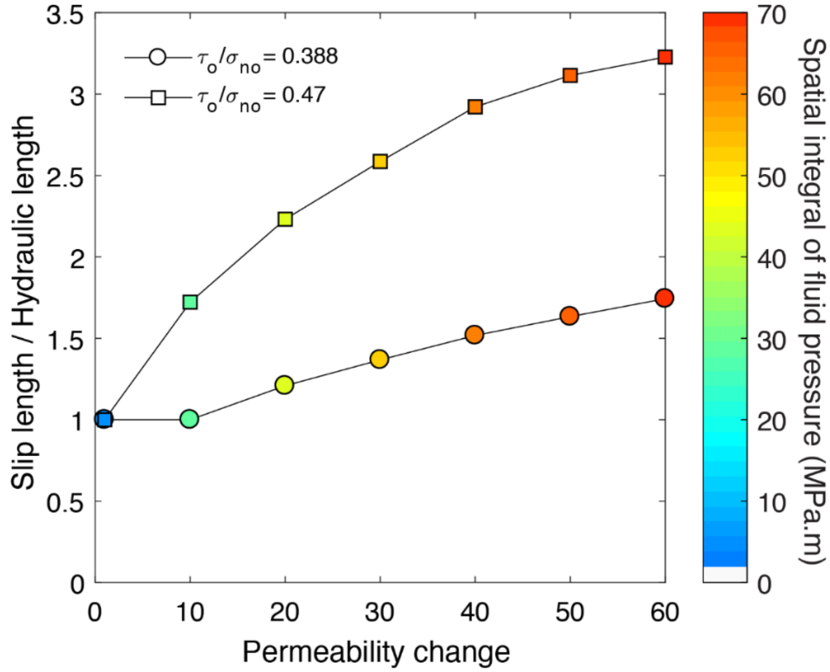

Figure 8-15. Graphs of the maximum slip length over maximum hydraulic length (radius of pressurized area) as a function of permeability enhancement (ratio of current permeability divided by initial permeability). The color bar shows the spatial integral of fluid pressure computed at the end of injection.

8.4.2 Fully coupled numerical analysis of the fault permeability variations observed at field scale (FS experiment at Mont Terri)

8.4.2.1 Context and objective of the numerical approach

The total duration of the injection tests to induce the fault reactivation was about 3 hours. The first injection was conducted with a manual pump to study the initiation of the fault reactivation by creating a rupture patch limited to the nearfield of the injection borehole. No signal was observed in the monitoring borehole. At the injection borehole, a ~60 micron shear slip was measured on the injection fault, associated to a total volume of injected water of ~0.69 liters. Making the approximation of a deformable penny shaped crack, it gives an estimated ~0.5 to 1 m rupture patch radius. At the end of the manual pump test, the injection chamber was opened until the chamber pressure stabilized back to the initial 0.6 MPa pressure. A second pressure increase was then conducted step-by-step with an engine pump in order to propagate the rupture in the fault from the injection to the monitoring borehole. The pressure was increased until a sudden pressure drop occurred in the injection hole followed by a strong pressure signal in the monitoring hole, indicating a hydraulic connection was established. This event was associated with a strong flowrate increase as the engine pump attempted to stabilize the injection chamber pressure. Using an analytical Thiem solution, the radius of influence of this second pressurization was much larger than in the manual pump test, corresponding to an injected volume of 143.1 liters. Here we are interested in modeling the hydromechanical response of the fault zone when there is the hydraulic connection and significant leakage between the injection and the monitoring wells. We developed a three-dimensional model of a simplified fault zone architecture using the distinct element code 3DEC, which allows one to conduct fully coupled hydromechanical analysis of the fault movements induced by the injections.

8.4.2.2 Numerical Model setting

The model includes the injection and the monitoring points (BFS1 and BFS2, shown in Figure 8-16a). The first aim of the modeling is to compare the dependency to stress versus the dependency to strain of fault leakage. The model domain has side-lengths of 20 m and contains three fault families representing the average azimuth and dip of the fault families intersected in the intervals, respectively N50 – 60E (red in Figure 8-16a), N39 37E (yellow in Fig. 8-16a) and N120 25W (grey in Figure 8-16a). The faults are located in this model, which simplifies the reality according to their approximate location in the field.

Fault rupture is described by a generalized Coulomb friction law. In order to figure the sudden changes in fault hydraulic conductivity at failure, the model considers the fault as initially sealed, and allows for fluid flow in the fault only when shear rupture occurs. In detail, at rupture, the hydraulic conductivity of the fault varies (1) as a function of the effective stress ('elastic' equivalent hydraulic aperture u_{he}), and (2) as a function of dilation induced by fault deformation (u_{hs}), as:

$$k_H = \frac{\rho g}{12\mu}(u_{he} + u_{hs})^3 = \frac{\rho g}{12\mu}\left(u_{h0} + \frac{\Delta\sigma_n'}{K_n} + u_{hs}\right)^3 \tag{8.6}$$

u_{hs} is evaluated in a model calibration by matching the measured flowrate and pressure evolution between the injection and the monitoring points during the step rate experiment. We use the hydraulic aperture value 150 microns, which was deduced from the analytical Thiem solution (Figure 8-11). The host rock is assumed to be linear elastic with transverse isotropic properties to figure the Opalinus clay bedding mechanical influence. We used the average values at the Mont Terri URL [Bock, 2009]. The host rock is considered impermeable, which is reasonable considering very low permeability of Opalinus Clay (~10^{-18} m^2) and the relatively short time frame of these experiments. Fault stiffness (K_n, K_s) is estimated to be 300 GPa/m. Fault permeability and friction angle are 8×10^{-17}m^2 (Jeanne et al. 2018) and 18 to 24°, respectively, according to average values from laboratory direct shear tests on Opalinus Clay reconstituted fault gouge samples (Bakker, 2017; Orellana et al., 2018).

To estimate the stress field at the injection and the monitoring points, we started with the commonly accepted stress tensor defined by Martin and Lanyon [2003] with σ1 = 6 MPa sub-vertical, σ2 = 4 MPa N320 sub-horizontal, and σ3 = 2 MPa N052 sub-horizontal. The principal stresses were applied to all the model boundaries (Figure 8-16a). An initial pore pressure of 0.6 MPa was set in the faults in accordance with pore pressure measurements recovered by piezometers set 5 to 15 m away in the fault zone for the purpose of the experiment. The field injection was simulated by applying the time-history of pressure imposed in BFS-2 during the in-situ experiment at the model's fault grid point coordinates (0, 0, 0) (Figure 8-16d). Injected flowrate is then calculated at the same point. Displacements (Ux, Uy, Uz) of the fault-hanging wall toward the footwall and pore pressures are calculated at the injection and the monitoring points (Figure 8-16b,c).

First, the model was run to establish equilibrium of the initial stress and pressure conditions. Then, the injection pressure was applied step-by-step (Fig. 8-16a). Here, we model the injection cycle conducted with an engine pump from 7000 to 9000 seconds as shown in Figure 8-10. Since this cycle is coming after a cycle conducted with a manual pump, where a limited rupture was triggered on the fault, we have figured an initial pre-ruptured patch of 0.5 m radius around the injection point. The principal stresses azimuth was incrementally rotated of an angle α until a best match was achieved between calculated and measured displacement orientations, and the principal stresses magnitudes were varied until fault opening pressure associated to flowrate increase was obtained (Figure 8-16b).

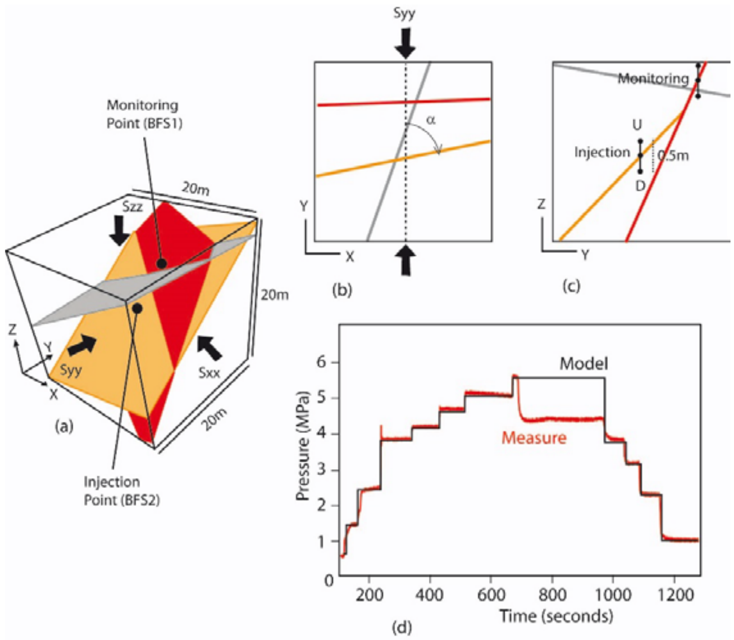

Figure 8-16. Numerical hydromechanical model setting. (a) Three-dimensional view of the model geometry (in red the N50-60E fault, in yellow the N39-37E fault and in grey the N120-25W fault); (b) and (c) present horizontal and vertical cross-sections (in (c) we show how both the injection and monitoring displacement measurement points are reproduced in the model); (d) Pressure loading history (black line is the pressure imposed at the injection point in the model, red is the pressure measured in the field).

8.4.2.3 Best fit case

Figure 8-17 shows the model solution that reasonably matches both measured fault displacements and fault opening pressure (F.O.P) variations with time. The best-fit solution is obtained for σ_1 = 5.3 MPa, oriented sub-vertical, σ_2 = 4.7 MPa, oriented N310 sub-horizontal, and σ_3 = 3.8 MPa, oriented N040 sub-horizontal. The calculated (U_x, U_y, U_z) reasonably match the injection and the monitoring points measurements (Figure 8-17). The calculated fault opening pressure is matching the 5.4 MPa injection point field value, while it is slightly overestimating at the monitoring point with values of 4.3 and 4.1 for the model and the field measurements, respectively. Post-rupture displacements underestimate the measured displacements during the decreasing pressures after 850 seconds (Figure 8-17).

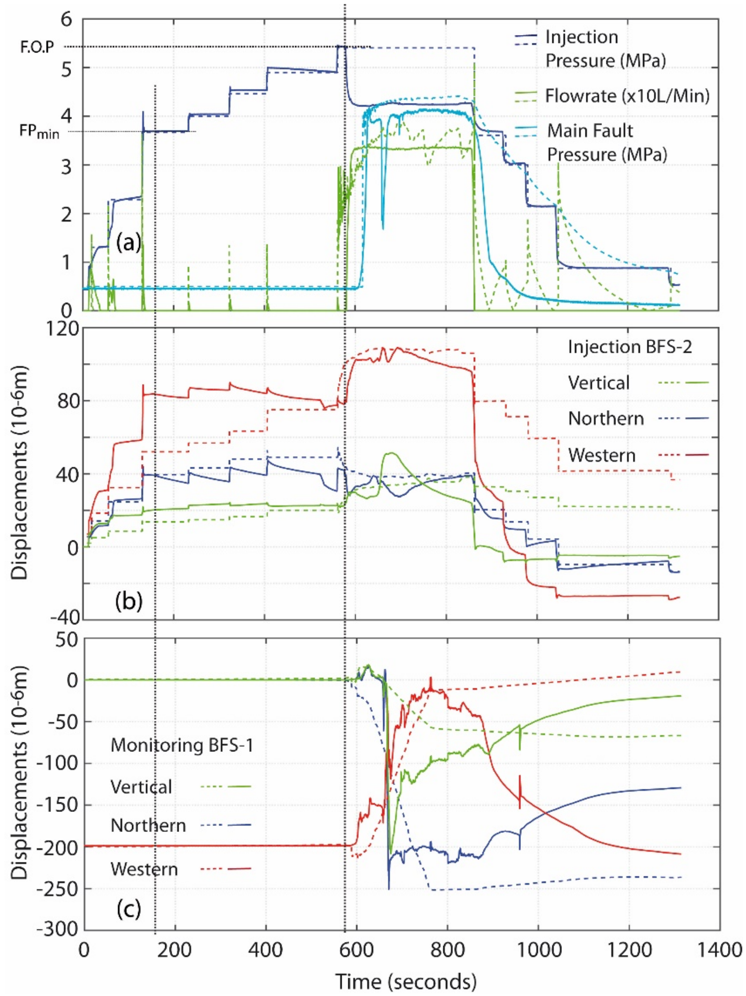

Figure 8-17. Comparison between calculated variations of fluid pressures, flowrate and displacements (dashed lines) and measurements (continuous lines) as a function of time. (a) Pressure and flowrate variations at injection BFS-2 and monitoring BFS-1 boreholes; (b) Displacement variations at injection point BFS-2; (c) Displacement variations at monitoring point BFS-1.

The orientation of the stress tensor derived from the best fit geometry (Figure 8-16) is close to the one commonly admitted at the Mont Terri underground laboratory scale, although the minimum principal horizontal stress magnitude of 3.8 ± 0.1 MPa is larger than 0.6 to 2 MPa commonly estimated (Martins and Lanyon, 2003). Using this minimum principal horizontal stress range of values, from our simulations a fault leakage pressure FOP = 4.4 MPa, which is 1 MPa below the measured one. To discuss the reasons of this large difference in the $\sigma 3$ values, we present a series of snapshots showing the rupture growth with the fault shear displacement and normal opening estimated at the injection chamber (Figure 8-18). As observed in the field, the calculated flowrate increases abruptly when normal and shear stresses fall to zero at the injection point for a fault opening pressure of 5.4 MPa (Figure 8-18b,c). This is associated with a pressure drop at the tip of the rupture patch that was induced during the previous manual pump cycle (pressure at 0.5m from injection in Fig. 8-18c) and to a large increase in shear displacement (Figure 8-18a). The rupture patch then propagates until connecting with the monitoring point (Figure 8-18d-f). Note that a ~0.2 MPa shear stress concentration occurs beyond the tip of the rupture patch, and is thus preceding the effective stress drop and fluid diffusion. This is in good accordance with field observations at the monitoring point that showed deformations preceding pore pressure increase of several seconds.

Below 5.4 MPa, no flow variation is calculated. Elastic re-opening of the patch that ruptured during the manual pump test occurs with step pressure increase. When pressure is increased from 3.9 to 4.4MPa, reopening is associated to elastic shear displacement with an orientation in accordance with the orientation of the stress tensor, and shear stress starts concentrating at the tip of the pressurized patch. Since no flow variation is calculated, its means that pressure might be enough to produce some elastic shear but not enough to promote rupture growth and associated hydraulic opening. Rupture initiation might thus be controlled by the elastic deformation and size of the pressurized patch. The effective stress variation on the fault controls the magnitude and direction of the elastic shear displacement, and consequently the amount of shear stress concentration at the tip of the pressurized patch (which is about 0.5 m away from the injection source point).

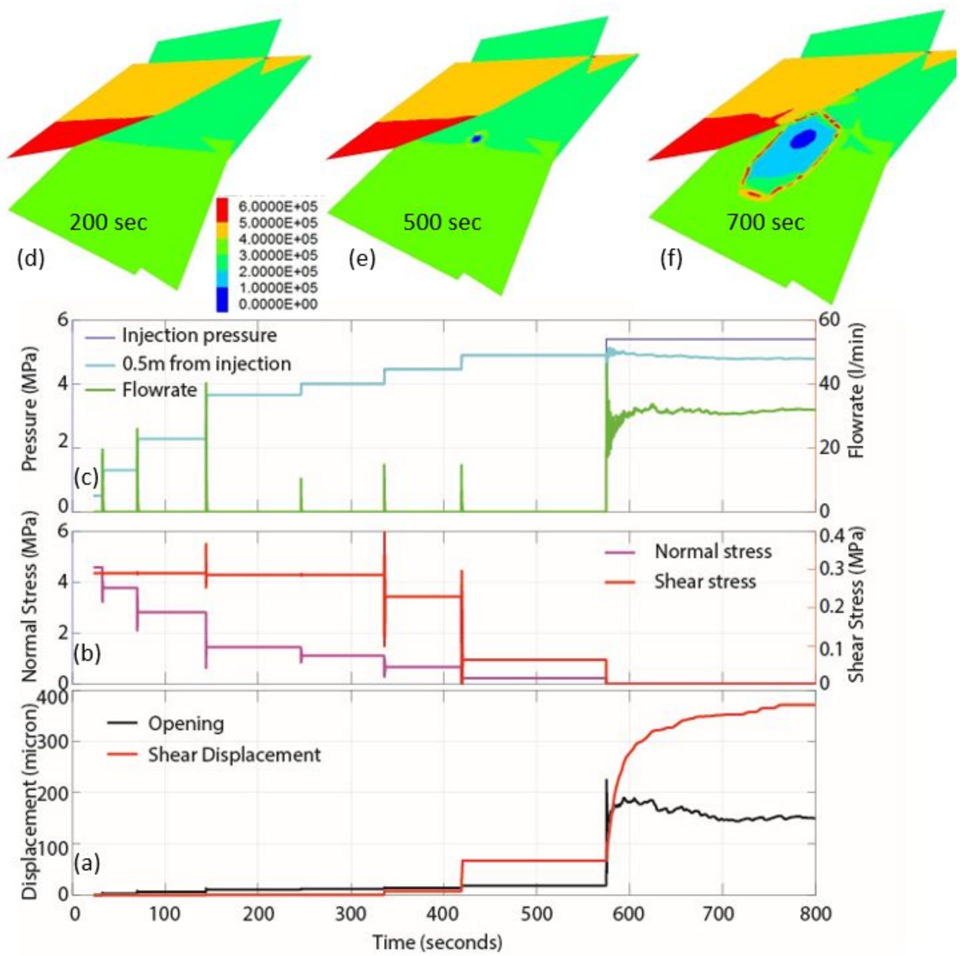

Figure 8-18. Best fit model of fault activation and leakage at the injection point. (a) Normal opening and shear displacements; (b) Effective normal and shear stresses; (c) Injection pressure, pressure at 0.5m from injection and leakage flowrate; (d) to (e) Three snapshots of the model shear stress variations in the fault zone associated to fault rupture growth.

8.4.2.4 Fault leakage sensitivity to stress

To study the fault leakage sensitivity to stress, simulations have been conducted where the horizontal stresses were rotated with increments α=20° and applied to the best fit model geometry (Figure 8-19). First, in Figure 8-19a, we compare the calculated displacement vector picked during the first 6 seconds after FOP with the measured displacements picked during the first 60 seconds after FOP. As expected, the sense of displacement variations depends on the horizontal principal stress orientation (the stress magnitudes being kept the same in all cases). If we compare with the fault zone plane N042-36ºSE orientation considered in the model, it is interesting to observe that most of the calculated displacement vectors do not plot on the plane projection, although shear rupture has been calculated in all the cases (compare for example the best fit case for SH oriented N130º in Figure 8-19a with the slip patch propagation in Figure 8-18d to f). This result highlights the high dilation effect on the displacement vector orientation that is related to the excess of injected fluid pressure within the ruptured patch (highlighted in the model by the effective normal stress drop to zero). These results match well with the field measurements characterized by a scattering of the displacements at failure off the existing natural fault zone planes (larger red and orange circles in Fig. 8-19a). In addition, there is a ~20 to 30º rotation of the measured vectors during rupture which is initiating in the N10 direction during the first 10 seconds after FOP and rotating towards the N110 direction with leakage flowrate increase. The displacements at rupture initiation are reasonably reproduced with a N130 maximum horizontal stress, while the rotation occurring later during leakage flowrate increase would be better reproduced by a N150 maximum horizontal stress. Thus, it means that there is a stress or a strain rotation occurring while fluid is propagating through the activated fault.

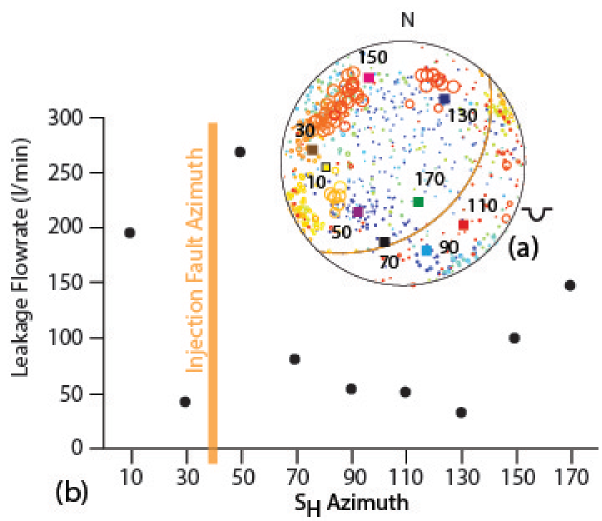

Figure 8-19. Sensitivity study of fault movements and leakage to the orientation of the maximum principal horizontal stress. (a) Colored square points in the stereoplot (lower hemisphere projection) correspond to the plastic vectors calculated for the different stress orientations over the 56 seconds following rupture initiation. The colored circles correspond to field displacements measured druing the 60 seconds following the fault opening pressure (the large the circle is, the larger the displacement). The orange line figures the projected plane of the injection fault considered in the model. (b) Calculated flow rate at 600 seconds after the fault opening pressure for different maximum horizontal stress directions.

Figure 8-19b shows the effects of the different horizontal stress orientations on the fault leakage magnitude. The models show that the fault is opening to flow for any orientation relative to the stress field. The highest value corresponds to SH oriented N050 sub-parallel to the fault N042º direction also corresponding to Sh oriented N140 perpendicular to fault. Thus, in this case the effective normal stress on the fault is the lowest and the leakage flowrate the largest. Nevertheless, the graph shows less straightforward results. For example, it appears that the leakage flowrate is higher when SH is almost perpendicular to the fault direction (N150 in Fig. 8-19) than when it is more oblique. This shows that the full stress tensor magnitude and orientation must be considered in predicting the fault leakage.

8.4.2.5 Sensitivity to the permeability function

Finally, we compared the fault leakage using two different permeability laws in the model (Figure 8-20):

- A conventional permeability law where fault permeability is allowed to increase with effective stress variation and slip induced dilation.
- The best fit model where fluid flow is only allowed in the activated parts in shear or tensile failure of the fault plane, while no flow is occurring in the remaining elastic parts.

Results show that the conventional permeability law cannot explain the abrupt leakage flowrate variation that is occurring at the fault opening pressure, highlighting that fluids may mainly propagate in the ruptured patches of the fault zone with very little leakage in the un-ruptured zones.

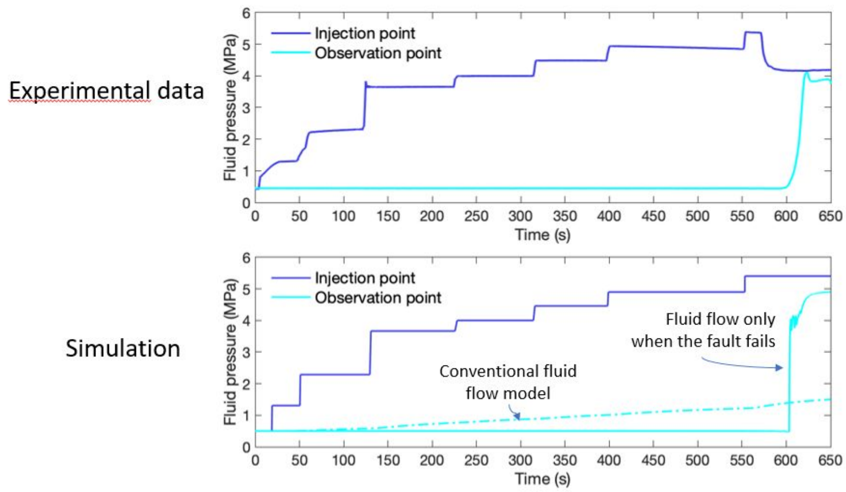

Figure 8-20. Sensitivity study of fault leakage to the permeability law.

8.4.3 Fully coupled numerical analysis of fault permeability variations related to “weak” dynamic loading by surface seismic waves.

8.4.3.1 Introduction

Co-seismic hydrological responses following earthquakes have been documented in a large number of cases over the last decade (Brodsky and Van der Elst, 2014). Observations suggest that large earthquakes with surface waves magnitudes $Ms \geq 8.0$ (local magnitudes of about $M_L \geq 7$) can enhance basin-wide fluid transport extending to depths of a few km, which can have important implications for groundwater supply and quality, contaminant transport, and underground waste repositories. Understanding these phenomena has great importance in particular for geologic disposal of radioactive waste, where the performance depends on the integrity of the natural system to contain radionuclides for tens of thousands of years. It is thus of crucial interest to nuclear waste authorities that the permeability changes in response to earthquakes, specifically those occurring in fault zones and other preferential subsurface pathways, can be better understood and eventually be predicted with confidence.

Here, we show some results of a preliminary analysis of surface waves produced by distant earthquakes and their potential effects on a fault zone located at a shallow ~1km depth. A simple analytical study shows that, at the 250 to 500m depths which are relevant to nuclear repository sites, the estimated maximum dynamic stress amplitudes travelling with Rayleigh surface waves are of σ_{rr} = 0.05 to 0.56

MPa and σ_{zz} = 0.07 to 0.113 MPa, respectively, for the radial and the vertical wave components. We have conducted fully coupled hydromechanical numerical modeling to explore the effects of such dynamic stress variations on pore pressure variations in a small fault zone affecting a low permeable host rock layer at 500 m depth. We explore how important the fluid-mechanical coupling in the fault is to estimate the dynamic effects of seismic waves on fault rupture. These investigations conclude on the possibility for a significant fault permeability co-seismic permanent variation. This result may be considered in estimating the potential loss of integrity of host rocks systems, even those located relatively far from active seismic zones.

8.4.3.2 Numerical procedure

We compare continuum and discontinuum fully coupled hydromechanical numerical dynamic analysis using the finite difference software (FLAC^{3D}) and the distinct element software (3DEC). Both softwares are based on an explicit finite difference scheme that solves the full equation of motion in a fully nonlinear analysis (Cundall, 1988). FLAC^{3D} allows one to consider fluid flow in continuous volumes, while 3DEC accounts for fluid flow in both discontinuities and in continuous blocks bounded by discontinuities. 3DEC also makes it possible to study fracture shear displacements and associated fluid flow induced by both dynamic and static effects, including several fractures more or less interconnected and of different geometries. FLAC3D can only represent very limited fractures geometries (such as a few parallel interfaces), and cannot describe fluid flow in the interfaces.

As a starting procedure, we consider fault plane opening as a result of changed in effective stress and linear elastic normal stiffness, but with a tensile strength of 0 MPa. That is, effective normal stress is governed by (compressive stress negative).

$$\sigma_n' = \sigma_n - P \tag{8.7}$$

where σ'_n and σ_n are effective and total normal stresses, respectively, and P is fluid pressure.

Shear displacement is governed by linear elastic shear stiffness and shear strength based on the Coulomb criterion. Then we have implemented in both 3DEC and FLAC3D the following linear slip-weakening friction law. The linear slip-weakening law assumes that the friction coefficient (μ) depends on the amount of slip (D) and decays linearly from a peak static value (μ_s) to a residual dynamic value (μ_d) over a critical slip distance (δ_c):

$$\mu = \{\mu_s - (\mu_s - \mu_d)\frac{D}{\delta_c}\ D < \delta_c\ \mu_d\ D > \delta_c \tag{8.8}$$

In 3DEC, we assume that fluid flow along the fault is governed by Darcy's law with cubic dependency between flow rate and hydraulic conducting aperture, i.e. the fluid flow per unit width is governed by

$$q = -\frac{b_h^3 \rho g}{12\mu}\Delta h = -T_f \Delta h \tag{8.9}$$

where b_h [m] is hydraulic conducting aperture, ρ [kg/m^3] is fluid density, g is the acceleration due to gravity [m/s^2], h is hydraulic head [m], μ is dynamic fluid viscosity [Pa s], and T_f [m^2/s] is fracture transmissivity. For simplicity we may assume that the hydraulic conducting aperture is equal to a mechanical aperture that is related to fracture normal displacement and that the current hydraulic aperture can be divided into an elastic part b_{he}, and plastic part b_{hs} according to:

$$b_h = b_{he} + b_{hs} \tag{8.10}$$

where the plastic part is considered to be induced by fault slip. Here, hydraulic aperture is equal to the mechanical aperture that in turn depends on opening as a result of reduction in effective stress and fracturing and shear dilation along with fault shearing, where the shear dilation is governed by

$$b_{hS} = u_s \times \tan\varphi \tag{8.11}$$

where μ_s is shear displacement and φ is the dilation angle.

In the simplest version of the model, a fault is figured as a single plane discontinuity or interface (3DEC) or as a thin layer (FLAC3D). The model domains have side-lengths of 20 m and each contain a fault zone dipping ~ 60 degrees (Figure 8-21a). The fault properties used in the model are given in Table 8-1. The host rock is assumed to be linear elastic with isotropic properties. We used the average values determined at the Mont Terri URL (Bock, 2009). The host rock is considered of low permeability (~10^{-18} m^2). Fault stiffness (K_n, K_s) is estimated to be 300 GPa/m. Fault initial permeability and friction angle were given (3-6) × 10^{-11} m^2 and 16 to 18°, respectively, according to average values from laboratory direct shear tests on Opalinus Clay reconstituted fault gouge samples (Bakker, 2017; Orellana et al., 2018).

Table 8-1: 3DEC material properties for benchmark simulations.

Material	Parameter	Value
Fault (Elasto-plastic)	Normal stiffness, kn (GPa/m)	30 – 300
	Shear stiffness, ks (GPa/m)	30 - 300
	Cohesion (MPa)	0
	Static Friction Angle (°)	16-18
	Residual Friction Angle (°)	10
	Critical Slip Distance (microns)	10
	Dilation angle (°)	10
	Tensile strength and Cohesion (Pa)	0
	Initial aperture (m)	(2-6)×10^{-5}
Host Rock Matrix (Elastic)	Bulk Modulus, K (GPa)	5.9-59
	Shear Modulus, G (GPa)	2.3-23
	Bulk density, ρ (kg/m^3)	2,450
	Porosity	0.1
	Permeability (m^2)	10^{-18}-10^{-15}
Fluid	Density (kg/m^3)	1,000
	Compressibility (Pa^{-1})	4.4e^{-10}
	Dynamic Viscosity (Pa s)	1.0e^{-3}

The stress field is simplified with the idea to set the fault zone close to the critical Coulomb stress at the onset of the numerical tests, and at a depth of 500 m which is considered to be the relevant depth for a nuclear waste repository site. Here we considered a maximum principal stress being exactly vertical at 12.0 MPa equal to the intermediate principal stress, whereas the minimum principal stress is oriented normal to the strike of the fault at 9.0 MPa. Initial fluid pressure is 4.9 MPa everywhere in the model. In some 3DEC models, gravity is also applied to the model.

First, a quasi-static consolidation of the model is done. Next, a wave pulse is applied on the side(s) of the model to examine the effects of a transient dynamic loading on fault pore pressure and slip. During this step, the model is run in undrained condition. A velocity history corresponding to different types of a Ricker wavelet in the [0.1, 5 Hz] frequency range and duration of 1 to 40 seconds are used to figure one oscillation of a seismic waveform. To avoid spurious numerical oscillations caused by a rapid change of velocity, the time step is fixed to 5 x 10^{-5} second and the mesh size is 0.5 m.

8.4.3.3 Dynamic response of an undrained critically stressed fault

In this simulation, undrained hydro-mechanical response is assumed, which could be quite realistic in shale of very low permeability. The loading corresponds to a Ricker signal 40 seconds long (corresponding to a 10 second period) with one component perpendicular to the model left boundary and the other component perpendicular to the model basal boundary (Figure 8-21a). A Mohr-Coulomb failure with constant friction is assumed. There is a good correspondence between FLAC3D and 3DEC Model results. A slight delay in seismic velocity occurs when the seismic wave crosses from the hanging wall (y = -5 m red curve in Figure 8-21b) to the foot wall (Y = +5 m, red curve in Figure 8-21c). This is happening from about 20 to 20.3 seconds (compare red and blue curves in Figures 8-21b,c) when a sudden shear slip of 6 mm on the fault is occurring (Figure 8-21d). Supplementary figure S3 shows that the horizontal ($\Delta\sigma yy$) and vertical ($\Delta\sigma zz$) stress waves (stress change) at both hanging and foot wall points pass through the fault without much attenuation, the maximum horizontal stress magnitude ($\Delta\sigma yy$) being equal to that of the input P-wave and the maximum vertical stress magnitude is equal to that of the input Sv-wave. The magnitude of the stress waves is 0.1 and 0.34 MPa for $\Delta\sigma yy$ and $\Delta\sigma zz$, respectively. Thus, the slip event is more visible on the seismic velocities than on the stress changes. In the fault (y = 0, z = 0), Slip and associated shear dilation (normal opening in Figure 8-21d) causes a decrease in fluid pressure, which has the effect of increasing the effective normal stress (Figure 8-21e). These results show the great impact of dynamic hydro-mechanical coupling within the fault. Indeed, during the slip event at 20 seconds, the decreasing fluid pressure and increasing effective normal stress tend to strengthen the fault.

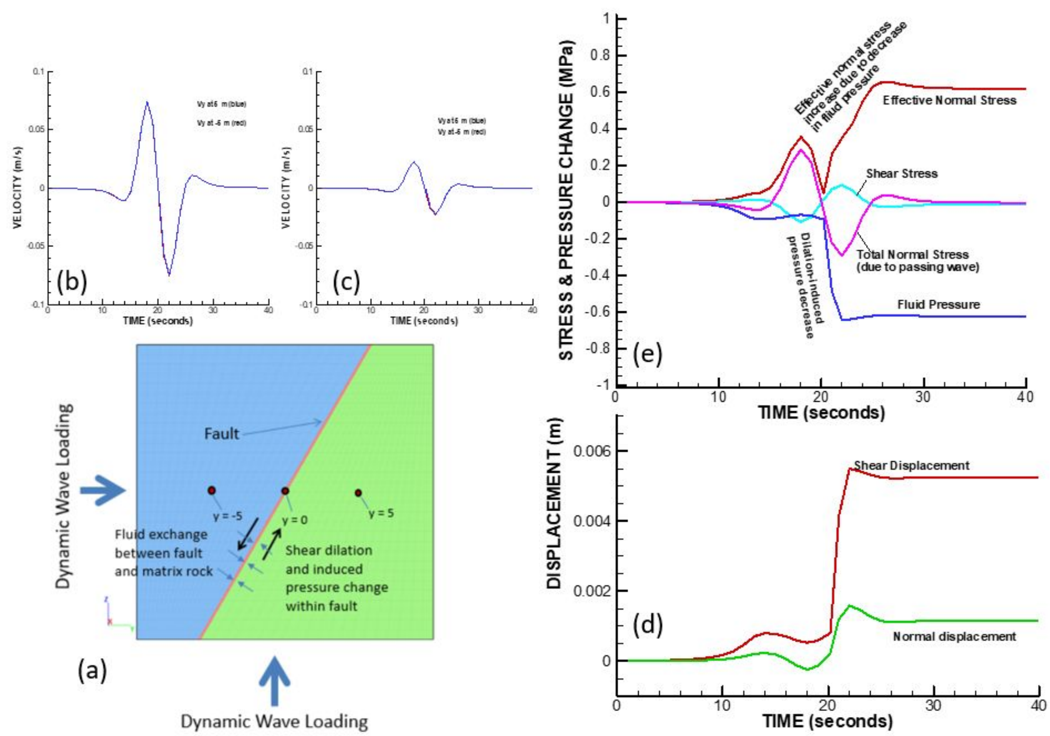

Figure 8-21. (a) Model setting, (b) and (c) v_{rr} and v_{zz} seismic velocities calculated in the fault hanging wall and foot wall, respectively (red curve is at x=-5m, and blue curve is at x=+5m). (d)

Shear slip and normal opening of the fault at point (0, 0), (e) Effective and total stress variations versus time calculated at point (0, 0) in the fault.

8.4.3.4 Influence of the frictional behavior of the fault

We compare an elastic, a constant friction and a slip weakening failure models while applying to the simple fault model a 1second-long Ricker wave. The passing seismic wave can initiate a fast "potentially seismic" slip (~13 mm) only when a frictional weakening (decrease of 5°) occurs along the fault (Figure 8-22a). For a constant friction, the slip is aseismic and its magnitude is small (~ 1 mm) compared to the seismic slip. When the fault is reactivated seismically, there is a rapid shear stress and strength drop (~ 0.45 MPa) starting at about 0.6 s (Figure 8-22d), and an important impact on the hydromechanical fault response. Indeed, the permeability increases of several orders of magnitude (up to 10^{-7} m^2) due to fault dilation (~ 2 mm), and fluid pressure decreases of about 5 MPa (Figure 8-22b and e).

The sensitivity study (not shown in this report) indicates that the hydromechanical fault response is mostly influenced by the friction drop and the dilation angle which affect both the shape and magnitude of fault slip, normal displacement, permeability, fluid pressure, shear and normal stress. For the frictional stability, higher the friction drop is, higher is the fault slip and, lower the dilation angle is, higher is the fault slip. The critical slip distance has a limited effect on the amplitude of displacement, but has an effect on the beginning of inelastic slip, while the linearity or the non-linearity of the friction weakening has no effect of the fault response. Thus, the slip-weakening frictional behavior has an important impact on the fault hydromechanical response to seismic triggering. In particular, the amount of friction drop and of shear-induced dilation influence the fault slip and permeability change. The critical slip distance has a limited effect on the amplitude of displacement, but has an effect on the beginning of inelastic slip.

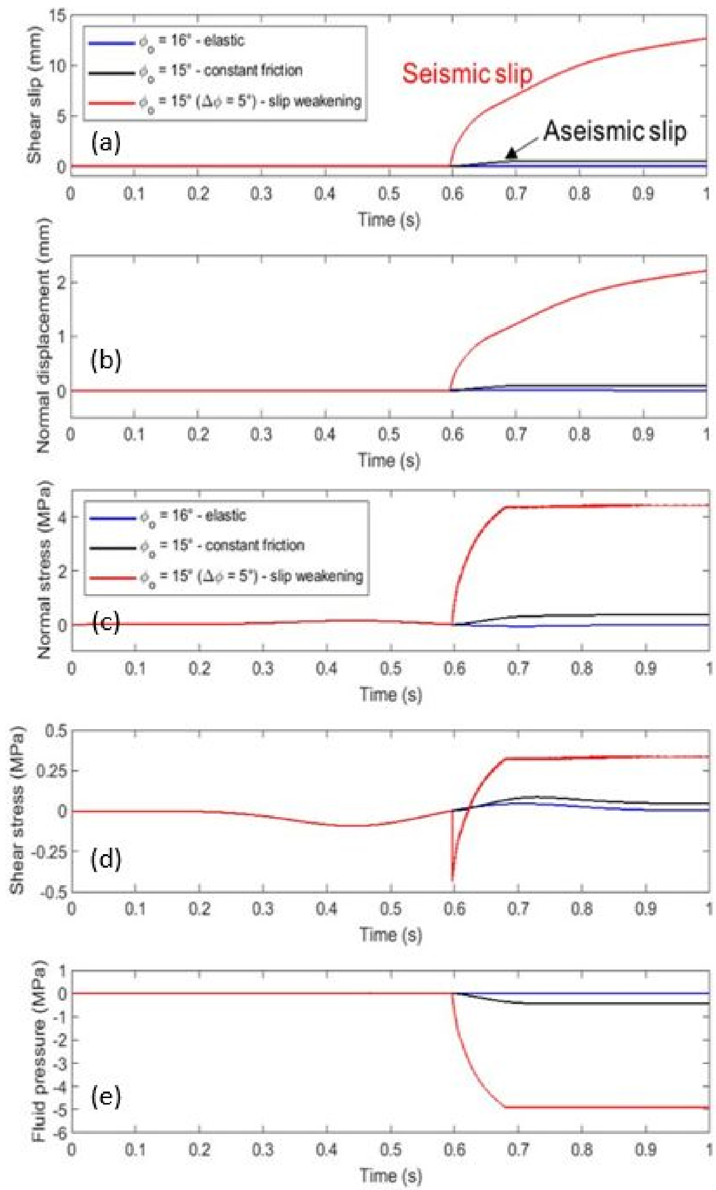

Figure 8-22. Comparison of three different fault friction models: elastic (blue), constant friction (black) and slip-weakening friction (red).

8.5 Summary and future work on fault activation monitoring and SIMFIP tool

8.5.1 Long Term Distributed Pressure-Strain Monitoring

The newly upgraded SIMFIP instrument has been designed, assembled and installed across a fault zone in one Mont Terri borehole (Switzerland) in October 2018. During the first 6 months of *in situ* continuous monitoring, we have developed technical solutions to improve the resolution of the long term measurements. This mainly concerned the long-term packers influence on pore pressure measurements in evolving borehole sealed sections typical of such compliant clay materials. Thanks to these solutions, it has been possible to continuously probe the hydromechanical response of the borehole nearfield during the long term effective stress equilibration with the fault zone affecting the argillite. These observations show that shearing of pre-existing fault zone fractures have guided effective stress relaxation and pore pressure equilibration following the borehole excavation.

Next steps in the sensors developments are the following:

- Designing a distributed SIMFIP monitoring to isolate how heterogeneous the fault zone response is to changes in effective stress and to leakage. Four SIMFIP cages will be distributed along a ~10-20m long interval straddling the entire fault zone. If we consider the concept of a fault zone with a principal shear zone (or core zone) surrounded by a fractured damage zone progressively vanishing in the intact rock, the objective is to continuously probe how fault displacements and leakage distribute in these different zones. We target installing this long chains of SIMFIP at Mont Terri by fall 2019. Overall application of this new instrument could be to allow for monitoring three-dimensional displacements across a canister spacing or across a plurimeter thick fault or damage zone.
- Integration of different strain monitoring systems to better detect fault leakage in Argillite. Thanks to a new experiment in Mont Terri (see chapter 8.5.2 and Fig. 8.23), we have the opportunity to test an integrated network of strain instruments set across and around a fault zone affecting argillites. We will compare, local-to-distributed SIMFIP set in boreholes across the fault zone, distributed strain sensing using fiber optics (Brillouin technology) cemented behind casing in boreholes 5 meters away parallel to the fault zone in the hanging and in the foot walls, and tiltmeters set 20-30m away in the fault hanging and foot walls.

Finally, we will continue the monitoring to capture fault movements and leakage related to different types of events that can potentially modify the long-term hydromechanical properties of fractures and faults affecting argillite host rocks:

(i) Gas leakage. Injections of inert gas and of water-with-dissolved CO_2 injections are planned to start around October 2019 and to be repeated over the next two years.
(ii) Fault response to the excavation breakthrough of the new Mont Terri gallery that will occur by end of May 2019, at about 30 meters from the SIMFIP measuring zone.
(iii) Surface waves effects from eventual distance earthquakes.

8.5.2 *In situ* testing and imaging fault sealing in Argillite (Mt Terri new FS-B experiment)

Our field observations and numerical results highlighted some key points related to fault activation and leakage in argillites:

- The effective stress concept must be considered with care at field scale because the fluid pressure is heterogeneous in the fault zone
- The low permeability of the fault in such materials is a key parameter which favors excess pressures that can induce rupture instabilities
- The fault geometry determines strength weakening processes which overwhelm the frictional rupture processes occurring along the fault

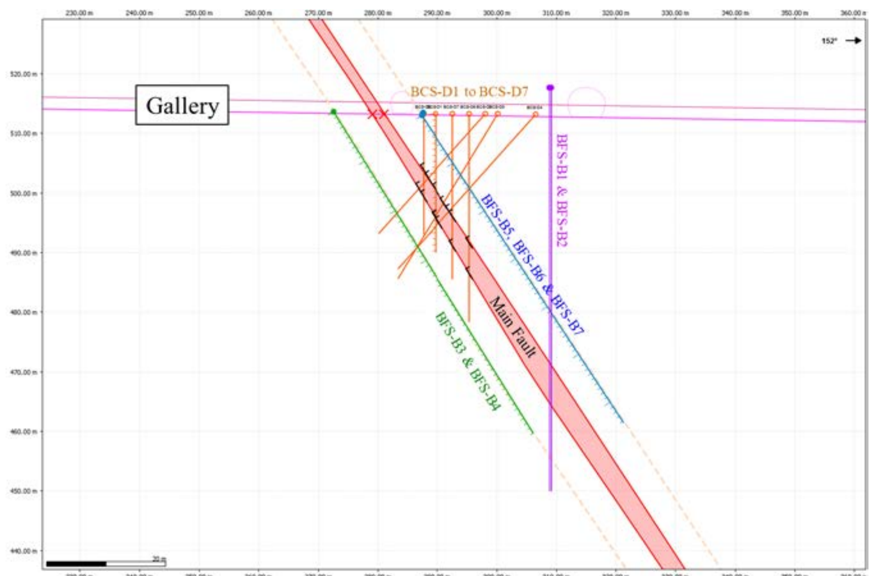

Figure 8-23. Projected vertical section with the current location and details of the CS-D and FS-B boreholes locations at Mont Terri (Switzerland). Hanging wall boreholes (BFS-B5 to BFS-B7) and footwall boreholes (BFS-B3 and BFS-B4) at 5m distance (isopach) from the "Main Fault'' surface are instrumented with the CASSM active seismic monitoring system and with DSS fibers. Vertical boreholes are instrumented with SIMFIP sensors. Tiltmeters are set on the gallery floor at different distances from the fault. Injection will take place in one vertical hole.

Next steps will include the initiation of a new fault activation experiment called FS-B at Mont Terri. FS-B is designed for repeated seismic imaging of fluid flow and stress variations during a controlled fault activation experiment by fluid injection, and monitoring is continued after the activation sequence to characterize the three-dimensional long term permeability evolution of the stimulated fault. Several SIMFIP probes are coupled with cross-hole and vertical passive and active seismic imaging conducted with repetitive seismic sources located in boreholes and on the Mt Terri gallery floor (Figure 8-23). First injection experiment will start in fall 2019. In parallel, we plan to use our improved numerical code to integrate the different datasets of fluid pressure, fault motion measurements and seismic velocities images repeated with time at relatively high frequency. The objectives are to improve our understanding of both the long-term permeability and effective stress changes in a fault zone in an argillite host rock.

This page is intentionally left blank.

9. MODELING MONT TERRI FAULT SLIP EXPERIMENTS (DECOVALEX-2019)

LBNL is a task lead for the modeling efforts for the DECOVALEX-2019 fault slip experiment, and is also conducting model simulations as a research team. Some of these modeling simulations conducted by the LBNL were presented in the previous Section 8, whereas this section provides a brief overview of the Task and modeling work conducted by the LBNL.

9.1 Fault slip experiment at Mont Terri used in DECOVALEX-2019

Figure 9.1 provides an overview of the experiments, which are denoted in the Mont Terri project as the ‘FS Experiment.’ The experiment explores the couplings between fault reactivation in a clay host rock and the potential enhanced fluid displacement through a ow-permeability formation.

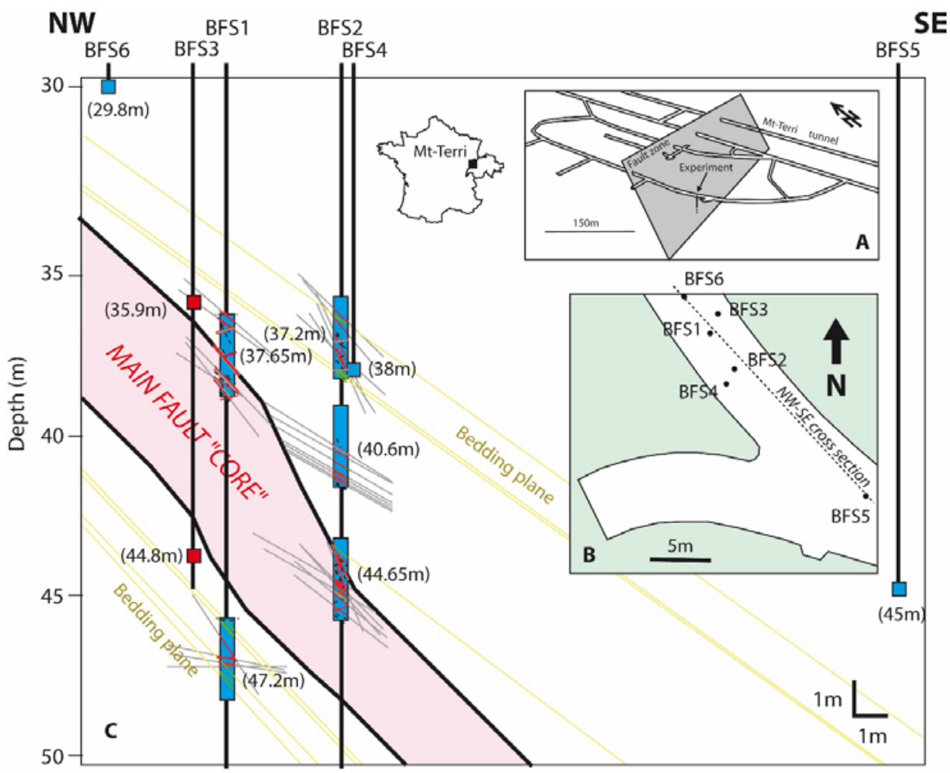

Figure 9-1. Mont Terri fault activation experiment setting. A – Mont Terri main fault with the location of the experiment (red squares-seismic sensors, blue squares-piezometers, blue rectangles-injection and monitoring intervals). B – Cross section of the Main Fault with the locations of the packed-off sections.

At Mont Terri, a total of five injection tests were conducted beneath, within and above the Main Fault during the two measurement campaigns of June and October-November 2015. Two tests related to injection at two difference sections of BFS2 were selected for modeling within Task B of DECOVALEX-2019. The tests were selected as they provided data for fault activation, both at the main fault and a minor fault in the fault damage zone.

9.2 DECOVALEX-2019 Task B Modeling Steps

Task B of DECOVALEX-2019 is conducted in the following three steps with progressively increasing complexity:

Step 1) Model inception: A benchmark calculation of activation of a single fault plane,

Step 2) Minor fault activation: Interpretative modeling of observed minor fault-activation, and

Step 3) Major fault activation: Interpretative modeling of observed activation in a major fault

Step 1 started with modeling of a single fault plane broadly representing the minor fault to be modeled in Step 2. The real step pressure injection scheme was applied during this initial benchmark modeling, and reasonable estimated properties for Opalinus Clay and the minor fault are taken from the site investigations at Mont Terri. Step 3 wss focused on another injection experiment conducted from another section of the same injection borehole, which resulted in shear activation and permeability changes along the main fault.

Figure 9-2 shows the model geometry for Step 1 model inception in the case of a 3D model geometry. The figure also shows some locations where output data from different research teams are compared.

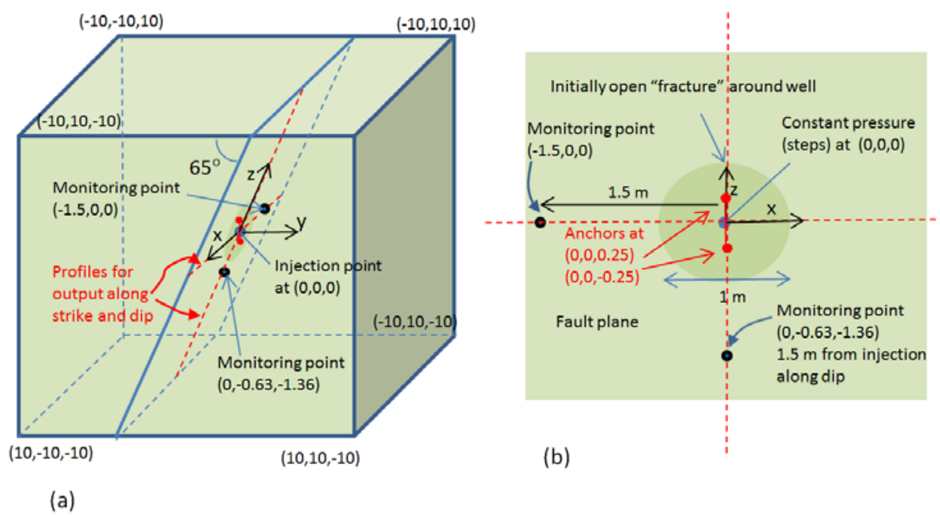

Figure 9-2. Model setup for Step 1 benchmark simulations of DECOVALEX-2019, Task B, using a 3D model. (a) 3D model geometry and locations of output points and profiles. (b) Detailed view of the fault plane near the injection point.

Figure 9.3 demonstrates the step-wise changes of the injection experiment. This injection schedule was also used for Step 2 modeling.

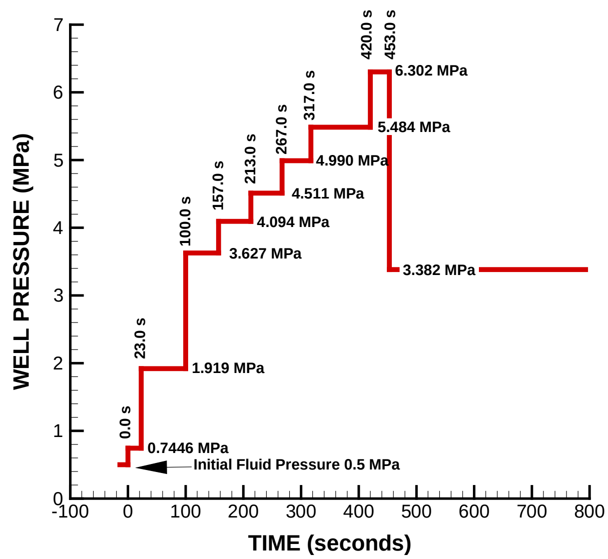

Figure 9-3. Injection pressure steps to be applied at the injection point (x,y,z) = (0,0,0) in the Step 1 benchmark simulations.

9.3 TOUGH-FLAC Fault Activation Model

LBNL uses two modeling approaches for DECOVALEX-2019 Task B. The first modeling approach is using the distinct element model 3DEC as described in Section 8.4.2 above. The second modeling approach is to use TOUGH-FLAC with specially developed capabilities for modeling fault activation. Here we will focus our presentation on the TOUGH-FLAC modeling approach.

Figure 9-4 shows the modeling grid used for the Step 1 simulations. The fault is modeled using finite thickness solid elements that in this case are 8.2 cm thick (Figure 9-5). Fracture like behavior is modeled through equivalent porosity and permeability, considering the cubic law for fluid flow between two parallel fracture surfaces (Figure 9-6). An equivalent mechanical aperture is the sum of elastic aperture change by effective normal stress, shear dilation related to plastic shear strain, and tensile opening related to plastic tensile stain. This is all accommodated through the FLAC3D ubiquitous joint model (Itasca, 2011).

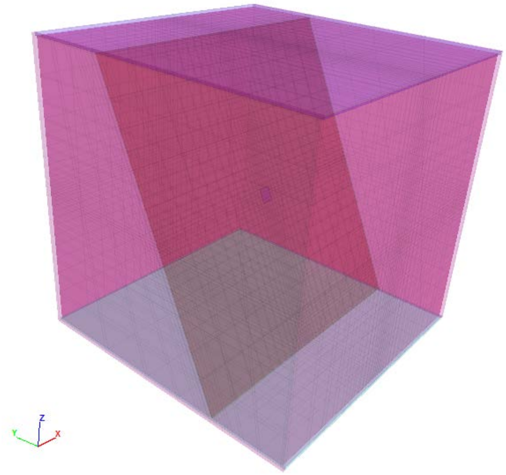

Figure 9-4. 3D TOUGH-FLAC model for Step 1 Benchmark Test simulations.

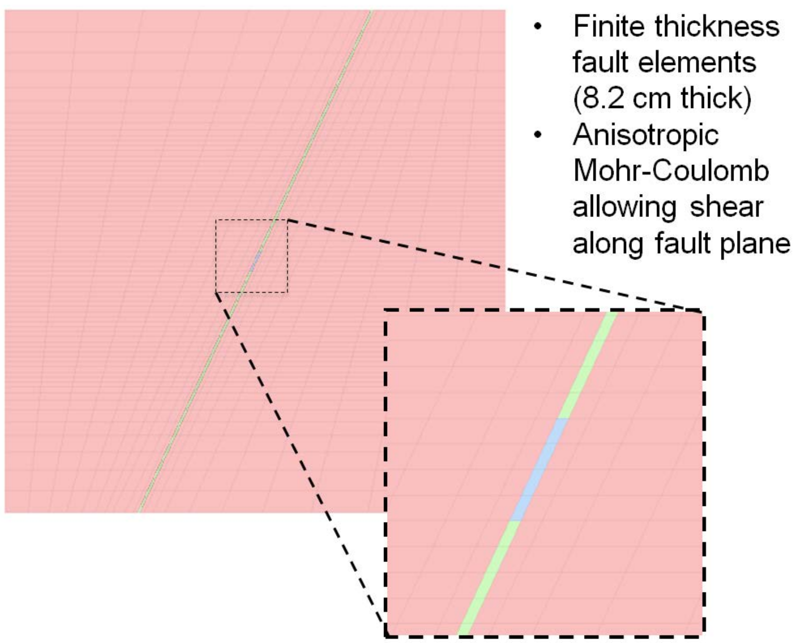

Figure 9-5. TOUGH-FLAC modeling of the fault using finite thickness elements.

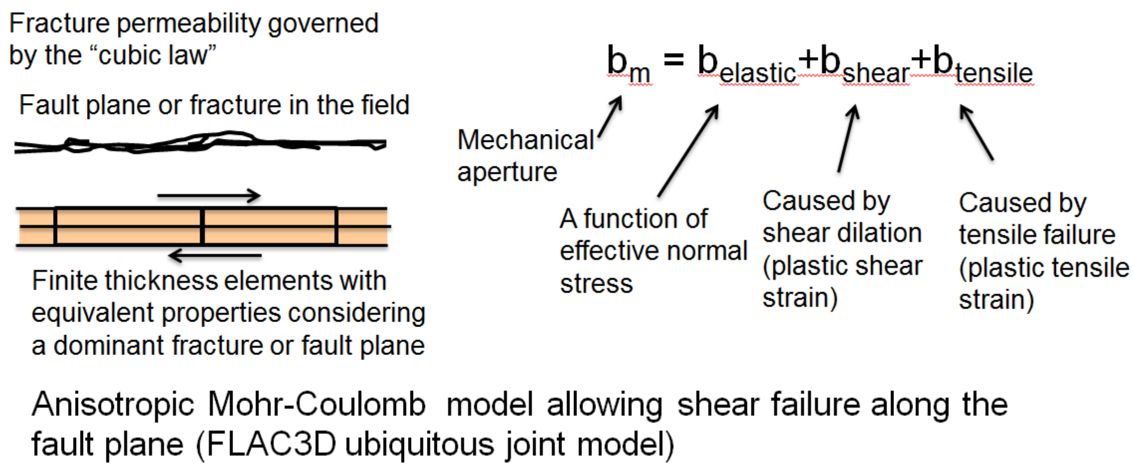

Figure 9-6. Details on the modeling of the fault plane using an anisotropic Mohr-Coulomb model that allows for shear failure along the fault plane, as well as elastic deformation and tensile failure.

As part of the DECOVALEX-2019 Task B, model comparisons are being made among seven international research teams. The modeling approaches may be categorized into those representing the fault as an interface, and those representing them by finite thickness, solid elements. LBNL's two modeling approaches also included both interface elements (in 3DEC) and finite thickness elements (TOUGH-FLAC). The Step 1 modeling revealed some initial disagreements among the modeling teams, and additional simplified benchmark tests were defined within the DECOVALEX-2019 Task B. These additional benchmark tests helped identify the reason for differences. Detailed comparison of the Step 1 results for different teams will be reported in DECOVALEX-2019 joint papers. Here, in this report, a brief summary of Step 2 modeling with TOUGH-FLAC is reported.

9.4 TOUGH-FLAC Modeling of Minor Fault Activation

The minor fault activation, Step 2 of DECOVALEX-2019, Task B, is being simulated with TOUGH-FLAC using a half symmetric model as shown in Figure 9-7. It is symmetric because the stress field is oriented with the horizontal principal stress being approximately parallel and perpendicular to the strike of the minor fault being activated. The LBNL TOUGH-FLAC modeling introduced some important changes to the material properties compared to the Step 1 benchmark simulation in order to match the field data and obtain the best estimate of the stress field at the site. The value of a cohesion of 2 MPa and a tensile strength of 0.6 MPa were used for modeling. The cohesion is necessary to prevent shear activation of the fault prior to injection.

In Step 2, the pressure at the well was simulated according to the schedule shown in Figure 9-3. The simulation started with a pre-existing rupture patch around the well of a radius of 1 m. This initial rupture patch was created during a previous pressurization of the well section. Figure 9-8 shows the simulated and measured pressure evolutions at the injection well (P1) and a monitoring well (P2) located 1.5 m from P1. The pressure is step-wise increasing at the injection well, while no pressure response was recorded at the monitoring will for the first 440 seconds. At 440 seconds, an abrupt pressure response was recorded at the monitoring well (P2). This abrupt pressure increase was also captured in the modeling as a result of an fracture propagation from the 1 m, i.e., the initial fracture radius, to 1.8 m, passing through the monitoring well (P2) located at a radius of 1.5 m.

Figure 9-9 presents a comparison of simulated and measured injection flow rate, demonstrating an excellent agreement between modeling and field data, including an abrupt increase in the flow rate at about 440 seconds. The abrupt increase in pressure followed by an immediate shut down of the injection flow, and the injection well pressure was lowered from 6.3 MPa to about 3.5 MPa. In the modeling, the pressure at this stage was uniform in the fracture from the injection well to the outer radius of the fracture.

Figure 9-10 shows a comparison of mechanical displacements at the injection well. These are relative displacement of the borehole above and below the intersecting fault plane. The locations of the anchors in the borehole are shown in Figure 8-2, which are placed 25 cm above and below the intersecting minor fault plane. The results show a reasonably good agreement between model and measurements until fracture propagation occurred, when the simulated anchor displacement much exceeded the measured anchor displacements. We are currently investigating how to explain this discrepancy in modeling and field data.

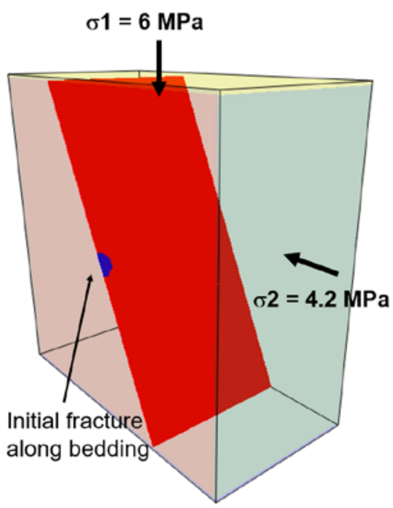

Fault Properties:

Friction angle = **22**
Cohesion = **2 MPa**
Tensile strength = **0.6 MPa**
Aperture of created fracture = 28 Microns
Normal stiffness = 116 GPa/m

Rock Properties:
Permeability = 1e-19 m^2
Porosity = 0.15
Young's Modulus = 6.1 GPa
Poisson's ratio = 0.33

Figure 9-7. Half symmetric TOUGH-FLAC model for Step 2 simulations with applied stress field and some of the basic material properties.

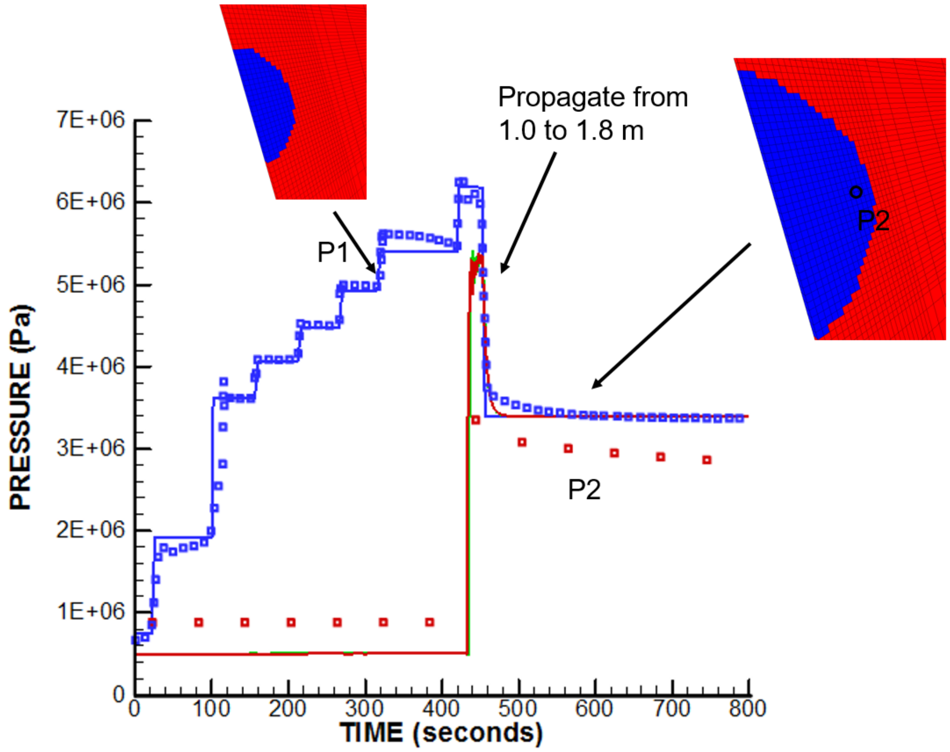

Figure 9-8. Simulated (solid lines) and measured (symbols) pressure evolution at the injection well (P1) and the monitoring well (P2) located about 1.5 m from the injection well.

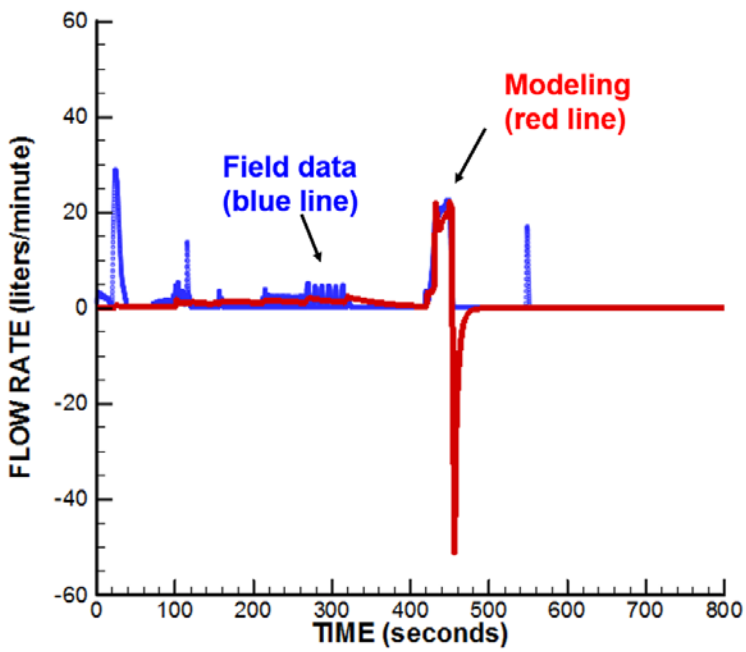

Figure 9-9. Simulated (red line) and measured (blue line) injection flow rate.

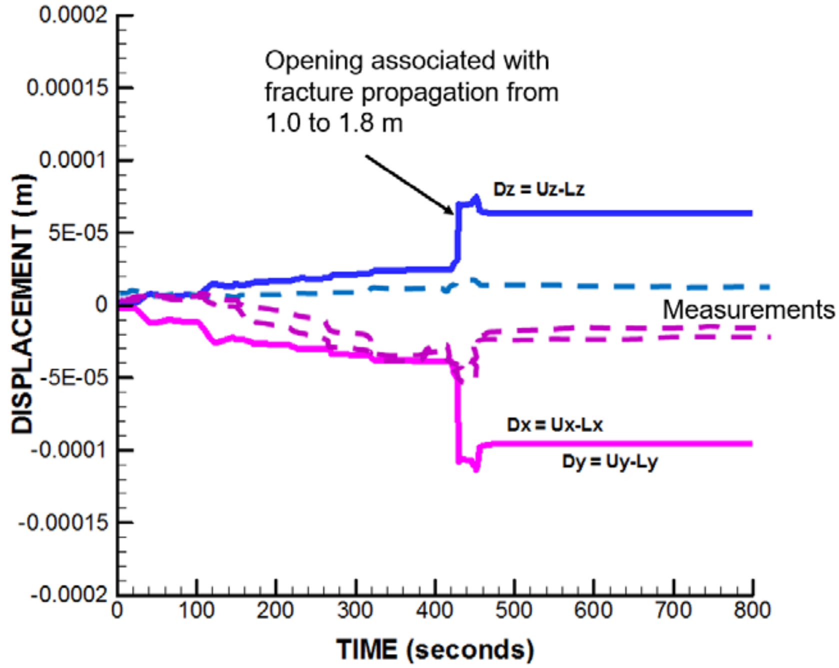

Figure 9-10. Simulated (solid lines) and measured (dashed lines) borehole anchor relative displacments.

In addition to the TOUGH-FLAC simulation presented here, LBNL scientists are also conducting 3DEC model simulations of the minor fault activation. For the rest of FY19, as part of the DECOVALEX-2019 Task B, we are going to summarize the results of investigations in DECOVALEX-2019 reports and joint publications. Also, LBNL will conduct final simulations of Step 2 and 3 for comparison with other research teams within the DECOVALEX-2019. A continuation will be proposed for DECOVALEX-2023, which will focus on the longer term sealing and healing of the created flow path, and may also include simulations of the gas injection.

10. NUCLEATING FRACTURES AND SELF-SEALING: MICRO-CHEMICAL-MECHANICAL MODEL

10.1 Introduction

The evolution of permeability of the Excavation Disturbed Zone (EDZ) in shale is one of the most important aspects for the performance assessment and the safety case. Laboratory and field studies have demonstrated that the EDZ permeability can increase or decrease due to the creation and subsequent long-term sealing and healing of fractures in clay rich rock. Knowledge of the EDZ behavior is essential for any future safety case. Fundamental research needs are: (1) determination of the mechanism(s) of fracture creation and sealing, and (2) development of the capability of predicting fracture creation and sealing caused by chemical, thermal and mechanical stresses.

In recent years, a number of researchers have begun to investigate coupled mechanical-chemical processes in subsurface systems, most commonly focusing on research of reactive fractures (Fletcher et al, 2006; Royne et al, 2008; Ishibashi et al, 2013; Ameli et al, 2014; McDermott et al, 2015). Despite the progress made to date, however, there is the lack of rigorous algorithms for modeling grain contacts, particularly of complex natural geometries for rough surfaces. In addition, the difficulty in addressing the spatial and temporal alteration of the contact surfaces subjected to mechanical and chemical stresses has led to highly simplified treatments and/or weaker coupling approaches. Analysis of small-scale systems has been even rarer. For example, McDermott et al. (2015) presented a model by combining numerical (for flow) and analytical (for chemical-mechanical) methods to simulate small-scale coupled CHM processes, but their model is limited to relatively simple geometries for contact surfaces (parallel edge to edge contacts). Alternatively, upscaled methods with statistical representation or homogenization have been used. Ameli et al. (2014) developed a coupled MC high-resolution model by assuming a fracture as two half-spaces separated by cylindrical asperities that represented the roughness of fracture surfaces. Bond et al. (2017) presented three different numerical models for thermal-hydro-mechanical-chemical (THMC) processes in a single fracture, which were categorized into 2D discretized, simplified models, homogenized models, in which a rough fracture surface is a single entity, and statistical models. To describe mineral precipitation-induced cracking, Ulven (2014) presented a coupled CHM model based on the Discrete Element Method (DEM) for mechanical analysis. This model is most suitable for modeling larger-scale fracturing, however, without consideration of small-scale contact alteration.

The goal of this study is to develop a prototype micro-chemical-mechanical model that handles flow, diffusion, deformation, and chemical reaction in a geometrically simple clay pore environment.

10.2 A New Chemical-Mechanical Model for Microscale Analysis

Modeling Approach

Below is a short description of a modeling approach to a micro-mesoscale (larger than a molecular scale) continuum treatment of coupled geomechanical and geochemical processes. Additional enhancements and modifications are made, particularly for the purpose of simulating microscale to mesoscale MC experiments. The key innovation here is the use of an approach to enable rigorous tracking of evolving grain contact areas subjected to mechanical and chemical stresses, at a variety of scales ranging from a nanometer to a centimeter. The geochemical model will also consider electrostatic effects caused by molecular diffusion and sorption (via the Nernst-Planck and Poisson-Boltzmann equations), thus providing an improved prediction of the solute transfer rates as stressed grain contacts dissolve and the effects on mineral precipitation of local stress.

Contacts of the rough surfaces along grain particles can be altered under the influence of coupled THMC processes such as loading, thermal expansion, fluid flow, and dissolution/precipitation. Modeling such processes at the micro-scale requires a discontinuous representation of the rough surfaces. For each pair (or group) of discontinuous blocks bounded by the rough surfaces, three possible contact states exist, as shown in Figure 9-1 (Hu et al., 2017a). In our approach, the numerical manifold method (NMM, Shi, 1992) is used to analyze these discontinuous and dynamic processes of grain contact alterations induced by MC effects.

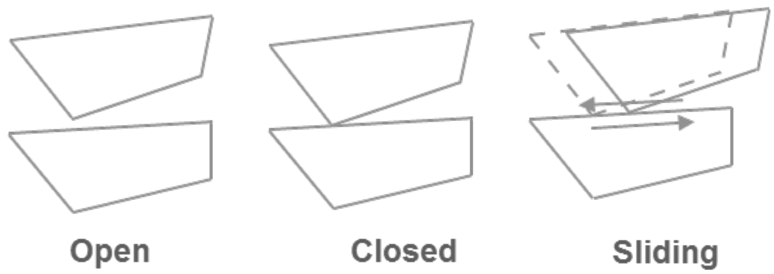

Figure 10-1. Three contact states (open, closed and sliding) considered in NMM (Hu et al., 2017)

The NMM is a promising method to handle problems involving both continuous and discontinuous media and dynamical processes affecting large deformations. The NMM is based on the theory of mathematical manifolds. The numerical meshes of NMM consist of mathematical and physical covers. The mathematical covers overlay the entire material domain, whereas the physical covers are divided from the mathematical covers by boundaries and discontinuities. In the NMM, alteration of contacts can be considered with a rigorous algorithm that includes contact detection, contact enforcement and open-close iteration. In each time step, contact detection is carried out to determine when and where contact occurs among elements divided by discontinuities. Once a contact is detected, constraints are imposed on the elements associated with these discontinuities. For each contact pair (i.e., two elements in contact), the three possible contact states are: open, closed and sliding. Correspondingly, their contact forces are imposed in distinct ways by different constitutive laws. Within each time step, open-close iteration may be carried out several times until the enforced contacts reach convergence. As a result of the coupled MC effects, contact pairs may change and for each contact pair, the three contact states may transfer dynamically. Therefore, the contact iteration involving detection, enforcement and open-close iteration must be repeated so as to ensure convergence. Figure 9-2 shows an example of a simple NMM simulation of contact alteration along two opposing rough surfaces under the impact of loading. In this example, two partially contacting rough surfaces are laterally confined with two plates and fixed at the bottom. After loading is applied (Figure 9-2a), the upper part deforms and moves toward the bottom part until they fully contact (Figure 9-2b). This example involves large deformation (the upper part), dynamic change of contact pairs (such as contact pairs alteration between the left plate and the upper part), and contact states transferring (such as contact states transferring from open to closed states between the upper and the bottom parts). Although this example uses a very coarse mesh (the triangular lines shown in Figure 9-2), such an extreme case demonstrates the capability of NMM for tackling problems of rough surface contacts.

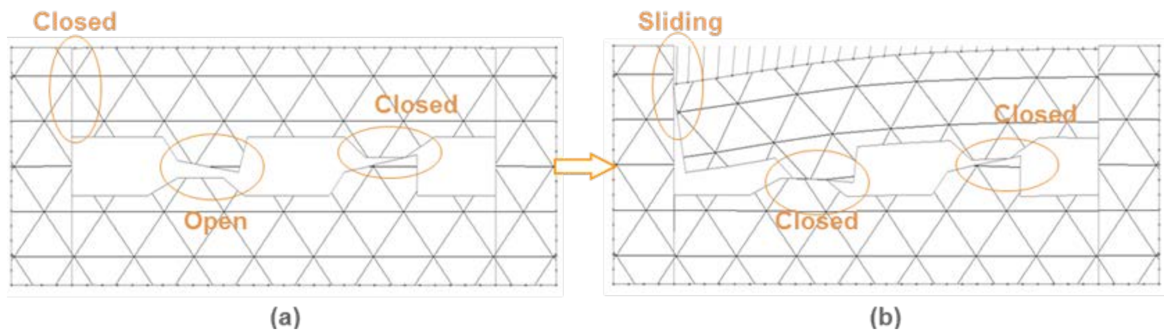

Figure 10-2. NMM analysis of contact alteration along rough surfaces under the impact of loading: (a) before loading, (b) steady sate after loading

The NMM provides a flexible numerical approach to rigorously treat dynamic surface contacts subject to mechanical forces at a range of scales. By using explicit representations of rough surfaces with the above rigorous algorithm for detecting dynamic contact pairs, and their contact states (open, closed, or sliding), the NMM is able to handle microscale interfaces with a large number of asperities, with geometry that can be extracted from laboratory data. Inclusion of a large number of asperities may dramatically increase the computing time on detection of contact pairs and contact iterations, but with high-performance computing facilities that are currently available (primarily NERSC), hundreds to thousands of asperities at a microscale can be handled accurately and efficiently. To incorporate geochemistry, however, it is necessary to couple this treatment to multicomponent reactive transport software.

Coupling of Geomechanics and Geochemistry

The software package CrunchFlow (Steefel et al, 2015) offers a powerful approach to incorporate geochemistry into a microscale coupled mechanical-chemical model through its ability to simulate both the Nernst-Planck equation (with explicit treatment of ions diffusing at different rates and the associated diffusion potential) and the electrical double layer (EDL). The treatment of molecular diffusion, which regulates the transfer of mass from the stressed contact surfaces to free faces, with the Nernst-Planck equation is much more rigorous than is possible with a simple Fickian approach (Tournassat and Steefel, 2015). In addition, the water films separating stressed contacted grains may be as thin as 1-10 nanometers, in which case EDL overlap may occur. The EDL models considered in this implementation of CrunchFlow (Steefel et al, 2015) will be based on both the Poisson-Boltzmann equation and the Mean Electrostatic Potential approach (Tournassat and Steefel, 2015). The various ways to handle EDL processes at the continuum scale are discussed in more detail in the section on Pressure Dissolution.

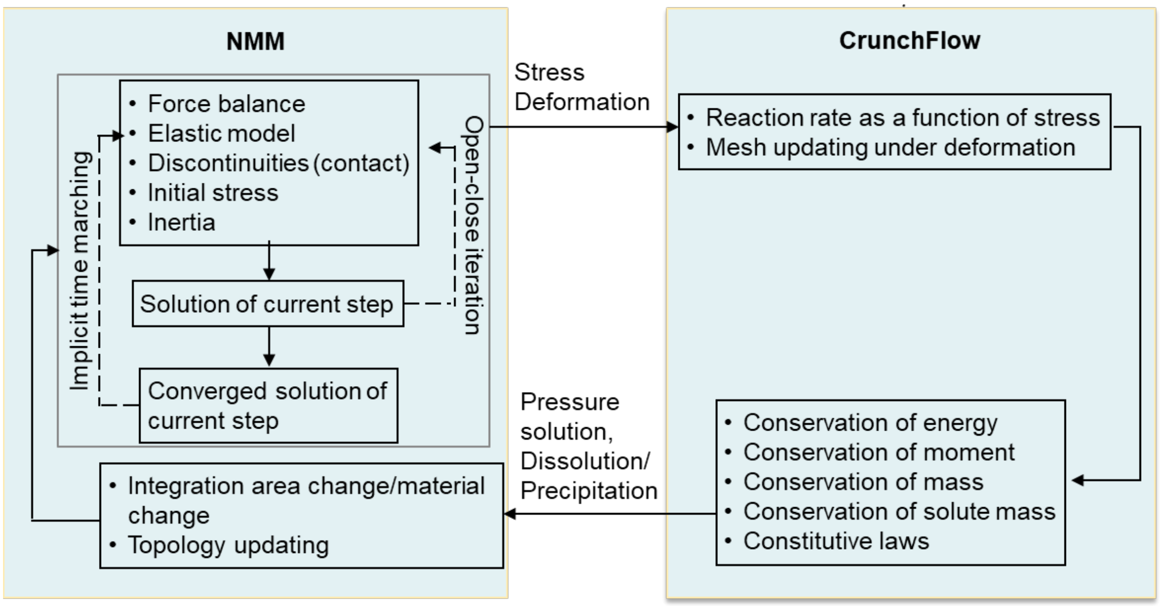

Figure 10-3. Schematic of coupling of geomechanics (calculated by NMM) and geochemistry (calculated by CrunchFlow) for microscale analysis

As shown in Figure 10-3, the mechanics and geochemistry are coupled sequentially by linking NMM to CrunchFlow. In the NMM, force balance equations are combined with elastoplastic constitutive law for continua, and dynamic contact alteration for discontinua are calculated. The calculated stress and deformation are then transferred to CrunchFlow, where the stress effects on rate constants and solubility are incorporated. If large deformation occurs or if fracturing is initiated, mesh updating are carried out in CrunchFlow. In CrunchFlow, diffusive and advective mass transfer from stressed grain contacts are calculated explicitly, and mineral phases are allowed to dissolve (normally, at the stressed contact) and precipitate on free faces where supersaturated. The diffusive mass transfer from stressed to free faces may turn out to be the rate-limiting step in the overall process of pressure dissolution. Similar rate limitations may also apply in the case of mineral precipitation-induced cracking processes. Geochemical dissolution or precipitation in turn will lead to changes in the contact asperities. Depending on the time of prediction, a different number of time steps within each coupling iteration may be required in the NMM and CrunchFlow until a converged solution is achieved.

Mesh Coordination between NMM and CrunchFlow

In previous calculations with the NMM, triangles were used to generate a numerical mesh for linear and second-order interpolations (Hu et al., 2017a, 2017b; Wang et al, 2016). However, in CrunchFlow, rectangles are used as a basis to construct the interpolation based on the finite-different method. In order to coordinate the two approaches with minimal errors caused by mesh incompatability, second-order interpolation based on rectangular mathematical mesh has been developed in NMM (as shown Figure 10-4). The rectangular mathematical mesh leads to a second-order interpolation, as compared to linear interploation using triangles. A new version of the code has been written for the second-order NMM with a rectangular mesh. With second-order interpolation, the orders of integration associated with inertia, strain energy, terms associated with contacts, Dirichlet and Neumann bondary condition items are all increased. By deriving new formulations for higher-order interpolation, all these items will be accurately accounted for. Another issue is associated with the large-deformation when the rough surface is moving or dissolved. This effect will be treated by using stress correction with fixed interpolation (numerical) mesh. As there is no other method capable of calculating the mechanical evolution of rough interfaces, the linear NMM with triangle mesh will be used to validate the new second-order NMM using a rectangular mesh.

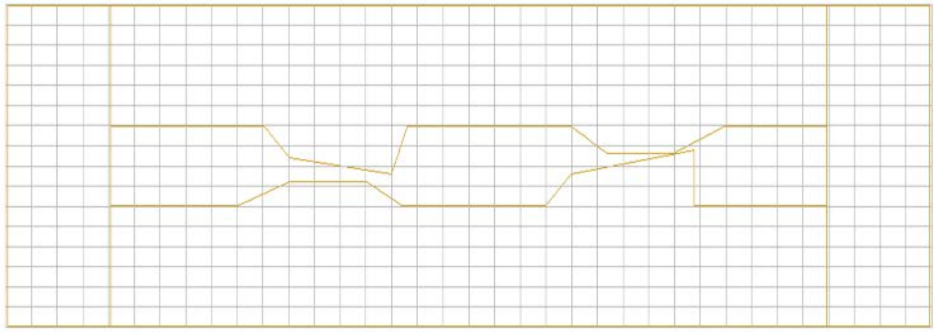

Figure 10-4. Rectangle mathematical mesh generated in NMM

CrunchFlow requires a much finer mesh to calculate reactive transport accurately. Thus, CrunchFlow and NMM will be coordinated by using 4^n times higher resolution than NMM (such as shown in Figure 9-5 for demonstration). Such a treatment will be convenient for data transferring between the NMM and CrunchFlow, when a large number of asperities are involved.

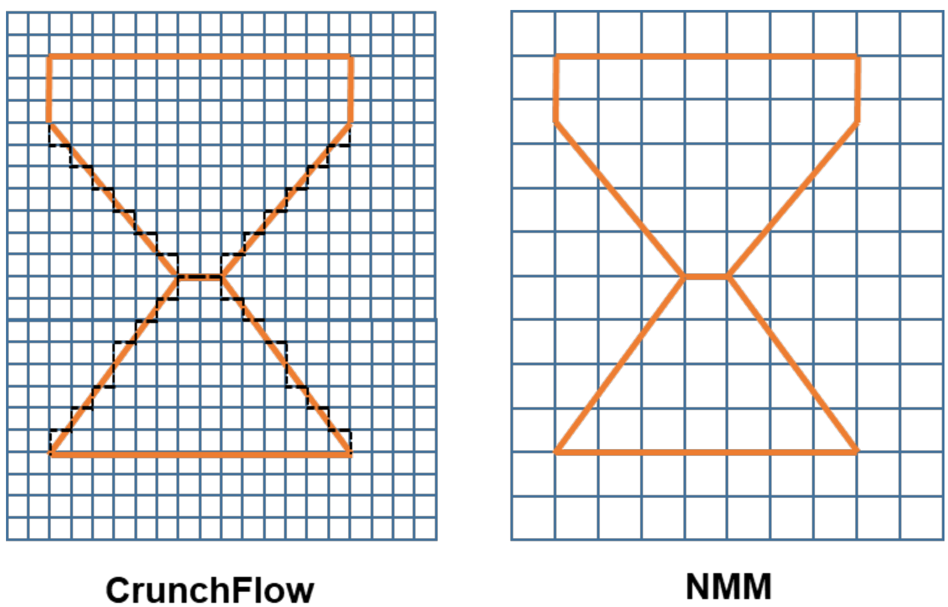

Figure 10-5. Calculation mesh used in NMM and CrunchFlow

Modeling of Mineral Dissolution/Precipitation-Induced Geometric and Mechanical Evolution

The challenge of explicit modeling of the coupled MC processes is to incorporate in NMM the geometric evolution induced by dissolution and precipitation as calculated by CrunchFlow.

As shown in Figure 10-6, dissolution of minerals leads to a reduction in solid material. The geometric evolution in this process associated with discretization in NMM can be categorized into two types: the elements with reduced integration area, and the elements with reduced Young's modulus. The elements with reduced integration area represent the surfaces of the grain, which are dissolved and relocated in the same grid. The elements with reduced Young's modulus represent grain material entirely dissolved in those elements.

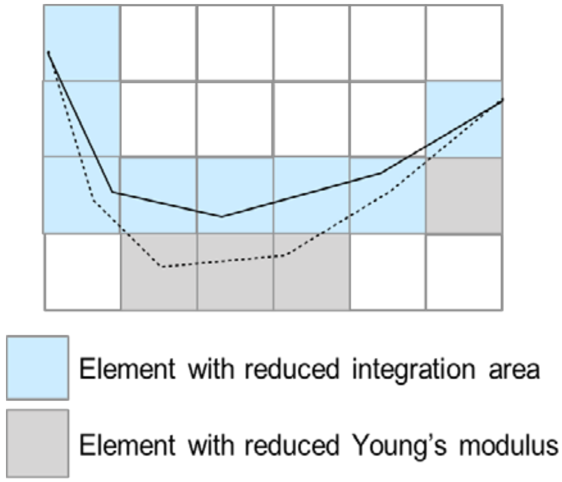

Figure 10-6. NMM Modeling of dissolution impact on mechanics

10.3 Summary

In this Section of the report, we described the ongoing study focused on the development of a novel mechanical-chemical model for micro-scale analysis by linking the geomechanical code NMM to the reactive transport code CrunchFlow. It is the first of its kind approach to rigrously represent the geometry of a microscale structure. The dynamic evolution of grain contacts along interfaces as well as reactive transport will be rigorously simulated. By developing a rectangular mathematical mesh in NMM, it is possible to achieve second-order interpolation and a mesh that is compatible with that used in CrunchFlow. Furthermore, the number of rectangles in NMM and CrunchFlow will be proportional, so that coupling will be more efficiently conducted. Between these two simulators, stress and updated geometry as result of deformation and mineral dissolution will be simulated so as to accurately predict MC behavior.

10.4 Future Study

Future research will include:

- A novel molecular modeling approach that estimates conductivity and dielectric characteristics with nanometer resolution, and passes this to the micro-model so as to approximate spatially-dependent fluid properties by interpolation.
- A new high-resolution fully coupled electrical-hydraulic-chemical-mechanical (EHCM) toolset for analyzing electrical double layer by linking CrunchFlow to NMM;
- With this approach, a sensitivity study can be conducted to investigate how micro-scale contacts impact the mesoscale material behavior, and functions correlating micro-scale contact parameters to mesoscale nonlinear mechanical properties will be provided. By choosing different geometrical settings of the grain boundaries with different stress regimes, a sensitivity study will be carried out to compare with a continuous approach similar to a nonlinear finite thickness zone for fracture analysis (Hu et al., 2017b). The sensitivity study will provide rough relationships between local contact parameters (such as contact aspect ratio, spacing) and the mesoscale nonlinear properties.

11. COUPLED MICROBIAL-ABIOTIC PROCESSES IN EBS AND HOST ROCK MATERIALS

A set of preliminary experiments was completed to assess the potential of important microbial processes being viable within materials used in EBS. The focus was on materials collected from the FEBEX experiment that had been subjected to varying subsurface conditions for extended periods. Details of the sample can be found in Villar et al, (2017) and Villar, (2017) Briefly, the samples were cooled in the formation prior to removal. After removal the samples were transferred to the on-site lab, where subsampling produced samples with and average volume of 18 cm^3. During subsampling external surfaces that had been in contact with removal equipment were removed. Samples were removed from site in 2015, wrapped in plastic, vacuum sealed in aluminized mylar bags, and stored at room temperature.

Experiments were designed to determine if these materials possessed microbial communities capable of metabolizing H_2 and how the FEBEX treatment impacted that capabilities. Two sets of materials were tested from a ‘heater zone’ (BD-48) and from a ‘cold zone” (BD-59) (see Figure 11-1). A sample of each clay type was placed on an autoclaved piece of Al foil in the biosafety cabinet. The sample was then scraped with a sterilized razor blade to remove the outer surfaces. Scrapings and foil were removed and the sample was placed on a new autoclaved piece of foil. A fresh sterile razor blade was then used to remove about 5 g of clay. This ‘fresh’ (newly exposed) layer of clay was mixed and distributed amongst 6 serum vials (6 for each clay type). 10 mL of sterile minimal salts media (Sigma M9 minimal salts, MSM), which contains PO_4^{3-} and NH_4^+. MSM was purchased 5x concentrated (Sigma), so actual addition was 2 mL of medium and 8 mL of DI water. The medium was added to 60 mL serum bottles through a 0.2 µm filter. 15 psi of gas mix was added to each serum bottle. This was done by starting with a full serum bottle of air, adding 7 mL of CO_2, and pressuring to 15 psi with a N_2/5% H_2 mix. All gas was filtered through a 0.2 µm filter. This method provided a consistent gas mix for all bottles, with an average final composition of 5% CO_2, 2.8% H_2, 9% O_2, with a balance of N_2. Sterile control samples (autoclaved clay) and blanks (no clay, only media) were run for comparison purposes.

Samples were placed horizontally on a rocking table and incubated at 35°C. Gas composition of the serum bottle headspace was analyzed periodically to monitor the gas composition. Gas analysis was performed on a Shimadzu GC-8AIT with Ar carrier gas, which allowed for simultaneous quantitative determination of H_2, O_2, N_2, and CO_2. GC conditions were as follows: Ar flow 0.4 kg/cm^2, detector and injection temperature 150°C, Column temperature 35°C, 80 mA current, CTRI packed column. Calibration of H_2, O_2, N_2, and $CO_2$was completed prior to sampling bottles with known concentrations of gases. Samples were analyzed immediately after removing from the incubator and replaced after sampling. To sample, an alcohol saturated wipe was put on the serum stopper for 5 min to sterilize the surface of the stopper. A sterile 22-gauge needle connected to a gas tight syringe was then inserted into the stopper and 100 µL of headspace was removed and injected into the GC. A new needle was used for each bottle when sampled.

The results of H_2 consumption are shown in the Figures 11-2 below. As can be seen no significant H_2 consumption was seen in the BD-48 samples or on the control or blank samples. However, the BD-59 samples showed significant and prolonged H_2 consumption indicating a viable microbial community in these materials capable of H_2 reduction. To assess the potential of whether this result can be due to experimental contamination the results shown in Figure 11-3 shows the responses of the individual replicates for the BD-59 materials. As can be seen, all but one of the replicates show H_2 consumption making the possibility that the results are due to random contamination lower. The samples also show parallel decrease in O_2 concentration (data not shown) further supporting the conclusion of active H_2 metabolism.

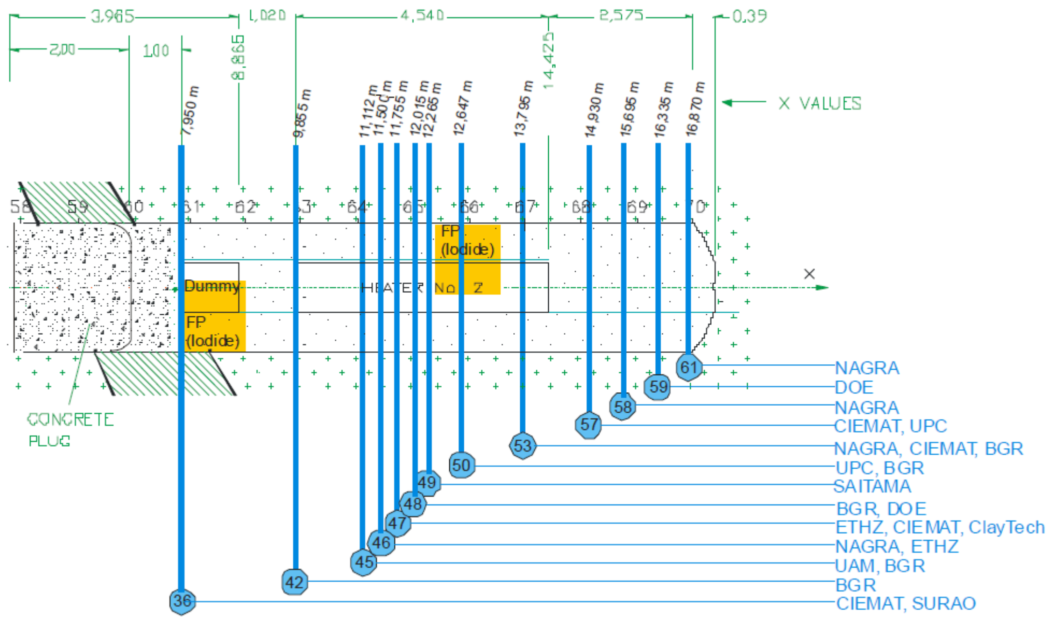

(a)

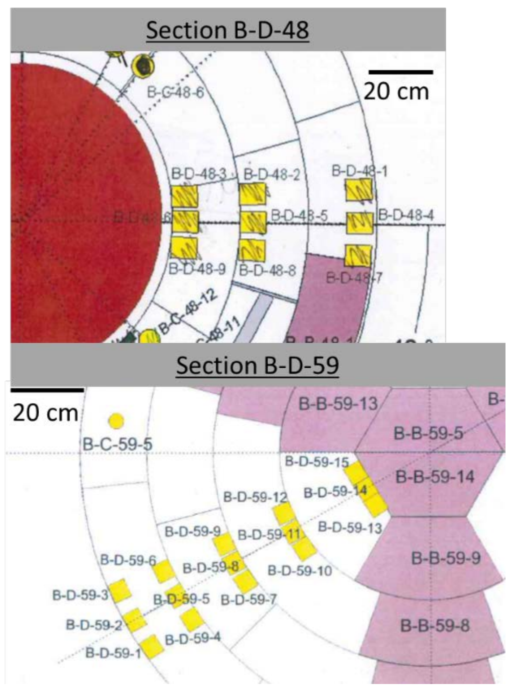

(b)

Figure 11-1. Locations of bentonite samples in original FEBEX experiment. (a) Longitudinal cross-section along FEBEX tunnel and (b) cross-sections B-D-48 and B-D-69 (modified from Villar et al., (2017))

The preliminary results indicate that EBS materials maintain microbial communities with the potential to metabolize H2. However, it is interesting that the material from the hot zone did not show that potential.

Whether that is due to the heating or the drying or both is unknown at this point. While these results are extremely preliminary, at this point they do point strongly to the conclusion that the microbial metabolic potential of EBS materials should be considered in assessing and predicting their behavior in terms of chemical transformations. Planned work for the remained of the fiscal year will focus on the repetition of these experiments in order to verify reproducibility of the results. It will also include the addition of an additional solid material from a 'medium' zone of the FEBEX experiment. There will also be microbial community analysis to better understand the type of microbes present and stimulated during the incubation. Longer term efforts, beyond the current fiscal year, will include the examination of other potential metabolisms, e.g. sulfate or Fe transformation, and how pressure impacts the function of the microbial communities.

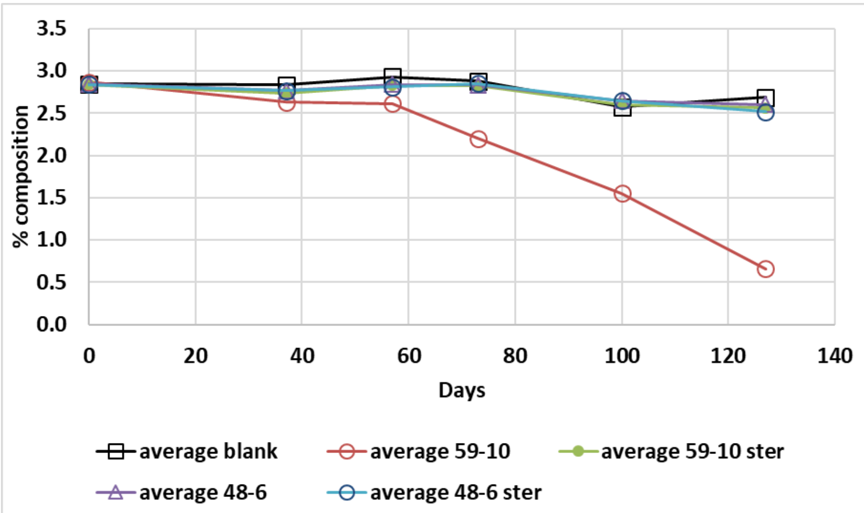

Figure 11-2. Averages of H_2 concentration in each condition. For the 59-10 and 48-6 samples there are 6 replicates, for the sterile control there are 3 replicates, and there are 2 blanks.

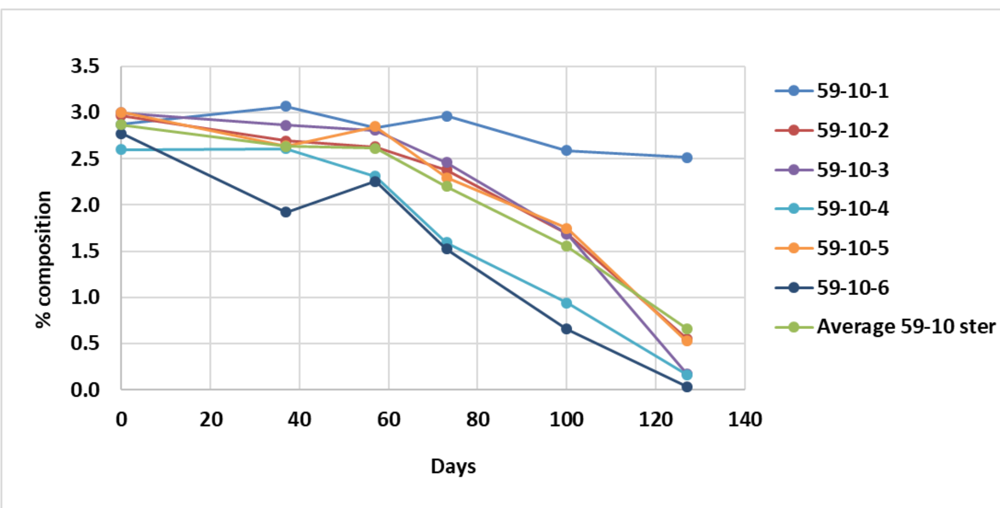

Figure 11-3. Above are individual plots of the six 59-10 bottles. 59-10-1 is showing very little consumption of H2, 59-10-3 and 59-10-5 are showing moderate activity and 59-10-6 and 59-10-4 are showing higher activity. The average is shown here for reference.

This page is intentionally left blank.

12. LINKING THM PROCESS MODELS TO GEOLOGIC DISPOSAL SAFETY ASSESSMENT (GDSA)

A schematic of integration between the coupled THM processes models and a repository-scale model for GDSA and PA is shown in Figure 12-1. The GDSA and PA modeling is conducted with the PFLOTRAN code by Sandia National Laboratories. PFLOTRAN has the capability of modeling coupled TH processes and geochemistry, including radionuclide transport in a high-performance computing environment. The idea is to conduct the GDSA modeling of the entire repository, including all emplacement tunnels. In such a large-scale repository model, it will not be possible to model the detailed thermally driven coupled THM processes occurring in the EBS and near-field during the relatively early repository time period of elevated repository temperature.

An initial approach for linking a coupled processes model to the GDSA could be to use detailed coupled THM process models to simulate near field of emplacement tunnels in different parts of a repository, for different FEPs such as a nominal case or cases of extensive gas generation. The output from such modeling to the GDA and PA model would be the following: (1) changes in flow properties (e.g., permeability and porosity) in the near-field, including the buffer and EDZ, and (2) inform PA about local flow created by coupled processes.

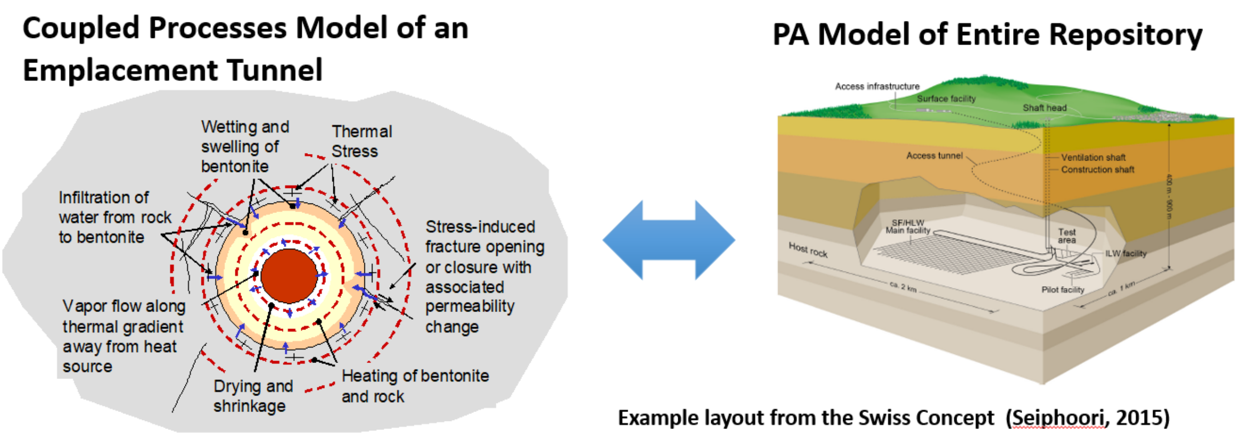

Figure 12-1. Schematic of links between near-field coupled THM processes modeling to repository-scale GDSA and PA models.

Currently, another approach is being developed that would enable inclusion of coupled THM processes into the PFLOTRAN GDSA and PA modeling. This will involve development of an approach to calculate the EDZ permeability evolution as a function of temperature, pressure, and a buffer saturation. The following key observations from the results of modeling of the long-term THM evolution using TOUGH-FLAC (Rutqvist et al., 2014) can be used to develop such an approach:

- The EDZ permeability depends on the effective stress normal to the excavation wall, which is determined by the effective stress of the buffer.
- The effective stress of the buffer can be reasonably well modeled using an analytical model, taking into account that the stress depends on the buffer average saturation and buffer temperature.
- The EDZ permeability evolution can be affectively modeled taking into account the stress tangential to the tunnel opening.

- The tangential stress evolution can be calculated using analytical models, in which the tangential stress depends on pore-elastic and thermos-elastic stresses at the repository level and stress concentrations around the tunnel opening.

Figures 12-2 and 12-3 provide schematics of the conceptual approach, which will be further developed and verified. Figure 12-2 shows the EDZ with different sections that could respond differently as a result of the local stress evolution. In the simplest model, permeability will be determined by the normal stress across the EDZ, which, in turn, is determined by the effective stress within the buffer. The effective stress within the buffer will be determined by the swelling stress during resaturation of the buffer, and, thereafter, the effective stress will be affected by cooling stresses. In a slightly more sophisticated model, the EDZ permeability could depend on three-dimensional stresses. A version of such a model was described by Equation (2.3) in Section 2 of this report. Figure 12-3 shows another view of the link between the detailed THM model and the simplified PFLOTRAN model. In the large-scale PFLOTRAN model, the discretization of the emplacement tunnel is simplified for the purpose of large-scale radionuclide transport simulations. The stress evolution at different EDZ sections in the PFLOTRAN model could be modeled through analytical models, dependent on pressure, temperature and saturation at the different locations in the model (e.g., mid-pillar and buffer).

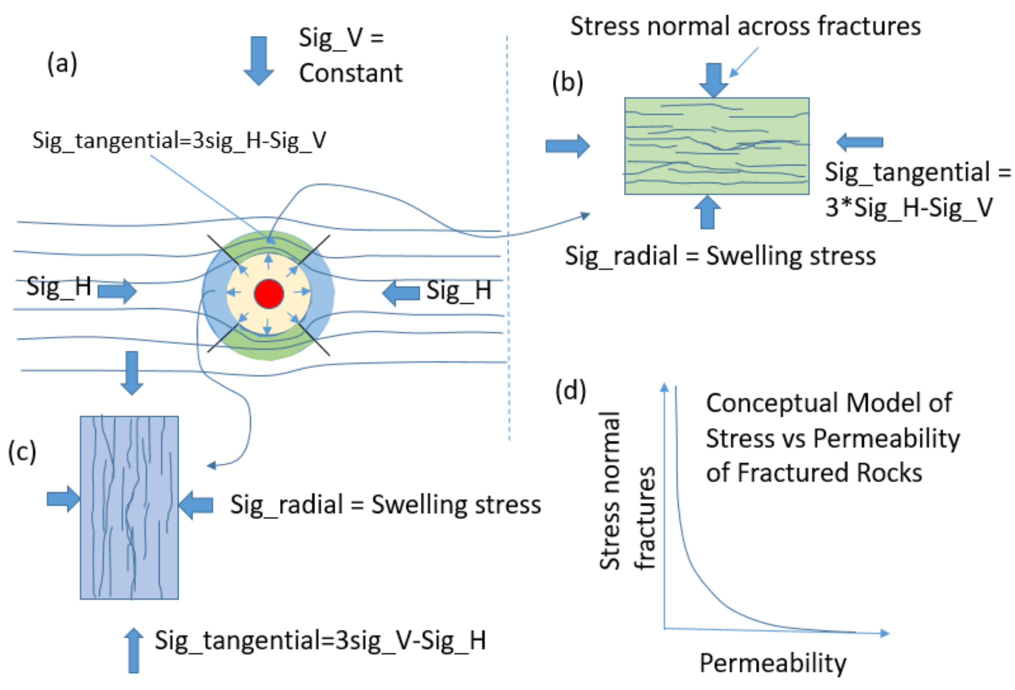

Figure 12-2. Schematic of the EDZ permeability evolution, using a model of an effective stress versus permeability for a fracture rock domain within the EDZ. (a) Different sections of the EDZ evolution on top/bottom and sides of the emplacement tunnel with normal stress from the buffer swelling stress and tangential stress from the horizontal and vertical stress concentrations around the tunnel. (b) EDZ section on the top of the tunnel exposed to radial and tangential stresses. (c) EDZ section on the side of the tunnel. (d) Conceptual model of a normal stress versus permeability for a fracture rocks similar to that shown in (b) and (c).

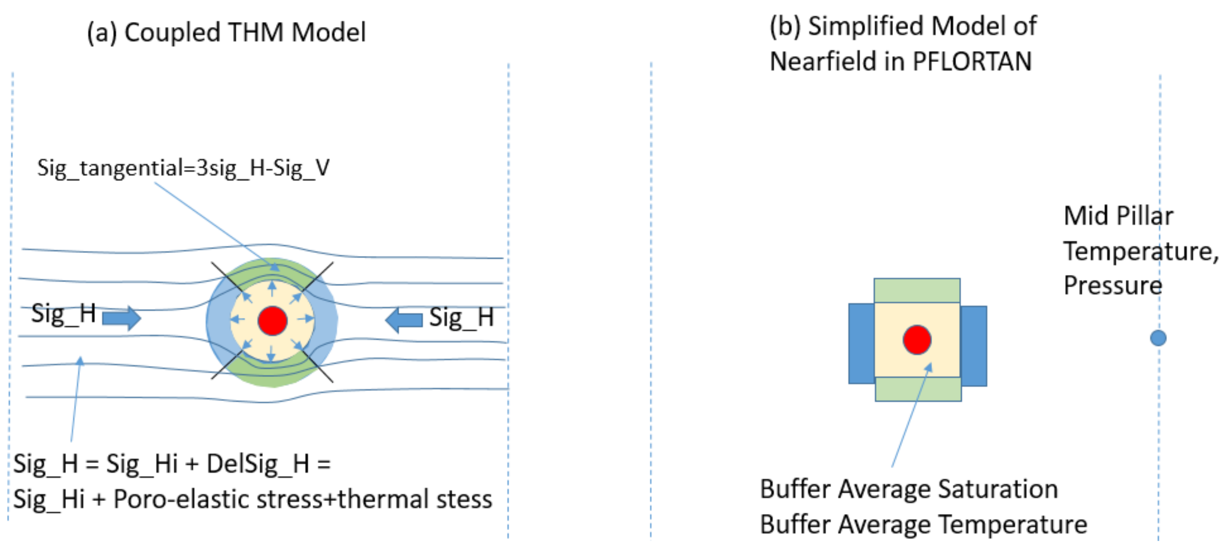

Figure 12-3. Schematic of links between (a) a coupled THM model and (b) PFLOTRAN simplified near field model.

The proposed approach for linking THM process models to GDSA will be further developed and verified during the rest of FY2019. This will be done by comparison of a fully coupled THM solution with the simplified approach of a TH model linked to analytical models for stress and permeability changes. Such a simplified model can then be implemented into PFLOTRAN to calculate the evolution of the EDZ permeability.

This page is intentionally left blank.

13. SUMMARY OF FY2019 PROGRESS

In FY2019, LBNL work on coupled processes in Argillite Rock has continued with a broad research portfolio, including necessary model developments, validations, and applications, along with fundamental studies of Argillite and bentonite-based buffer materials. Details of the progress and planned future work are being provided in Sections 2 through 12 of this report. Below is a brief summary of the different topics:

- Current model developments include moving forward with TOUGH-FLAC, adopting the newly released TOUGH3 and FLAC3D V6 codes, enabling improved performance with parallel processing. Current TOUGH-RBSN developments include improved modeling of hydromechanical coupling associated with fracturing, as well as treatment of anisotropic strength and modulus for applications to shale mechanical behavior. Further testing and documentation of TOUGH3-FLAC6 and TOUGH-RBSN will be performed in the remainder of FY2019.

- TOUGH-FLAC has been continuously validated against major *in situ* heater experiments in argillite at the Mont Terri Underground Research Laboratory (URL) in Switzerland and at the URL in Bure, France. The Mont Terri Full Scale Experiment has now been conducted for 4.5 years, with heating to temperature of up to 130°C in the buffer. The experiments at the Bure URL have been conducted to study processes of thermal pressurization and associated stress changes causing low permeability of argillite host rocks. For the remainder of FY2019, DECOVALEX-2019 tasks associated with Bure experiments will be completed and documented in final reports and journal papers. Continuous participation in the Mont Terri Full Scale Experiment beyond FY2019 will enable us to further investigate a mechanical evolution of the buffer, where swelling stress is now slowly building up. Future work on this topic may include a proposed DECOVALEX-2023 task on fracturing due to thermal pressurization at the Bure URL.

- TOUGH-RBSN has been applied to further study the EDZ at Mont Terri along with modeling of gas migration associated with a DECOVALEX-2019 task. It is the only discrete fracture model applied for modeling gas migration among all the research teams in DECOVALEX-2019. This is complementary to continuum approach of gas migration in TOUGH-FLAC, which might be used at a larger scale for repository performance modeling. Research conducted in FY2019 has also included pore-scale modeling of gas bubble movements. For the rest of FY2019, gas migration tasks associated with DECOVALEX-2019 will be completed and documented in a final report and journal papers. The pore-scale model will be further developed (e.g., phase-field LBM) with benchmarking against different methods based on published experimental data. Future work may include gas migration modeling at a larger scale associated with a proposed DECOVALEX-2023 task, involving the Large Scale Gas Injection Tests (Lasgit), performed at the Äspö Hard Rock Laboratory.

- In FY2019, substantial work has been carried out to study the fracture and fault behavior. This includes studies at the larger scale related to field-scale fault slip experiments at Mont Terri, and at the micro-scale in a new research task related to nucleating fractures and self-sealing, using micro-chemical-mechanical process modeling. In fact, self-sealing has been observed both in field tests at Mont Terri and in laboratory tests on fractured argillite samples, but the underlying mechanisms are not well understood. In the remainder of FY2019, a DECOVALEX-2019 task on modeling of Mont Terri fault activation tests will be completed, whereas experiments on thermal pressurization fracturing at Bure is planned to be evaluated *in situ*. Future DECOVALEX-2023 tasks on fault activation experiments will be focused on the longer term sealing, a topic closely related to the micro-scale self-sealing fundamental studies.

- The FY2019 argillite coupled processes research portfolio also included a research task on the evaluation of coupled microbial-abiotic processes in the EBS and host rock materials. It is focused on consumption of hydrogen gas that could be important in the case of gas generation in the EBS. Preliminary results of laboratory experiments indicate that EBS materials can maintain microbial communities with the potential to metabolize hydrogen. In the remainder of FY2019, the work will focus on conducting recurrent experiments in order to verify reproducibility of results. Future work will include the examination of other potential metabolisms, and how pressure impacts microbial communities and processes.

- Finally, as part of LBNL's Argillite R&D work package, LBNL, in collaboration with SNL, is developing approaches for integrating coupled process models into the Geological Disposal Safety Assessment (GDSA) and Performance Assessment (PA). In FY2019, new ideas have been developed for considering near-field coupled processes in the large-scale PFLOTRAN PA calculations. These ideas, involving a set of analytical functions of coupled geomechanical responses, will be tested and demonstrated for use in the GDSA during the reminder of FY2019 with continuation in FY2020.

14. ACKNOWLEDGEMENTS

This work was supported by the Spent Fuel and Waste Science and Technology Campaign, Office of Nuclear Energy, of the U.S. Department of Energy under Contract Number DE-AC02-05CH11231 with Lawrence Berkeley National Laboratory.

This page is intentionally left blank.

15. REFERENCES

Akai, T., B. Bijeljic, and Blunt, M. J. (2018) Wetting boundary condition for the color-gradient lattice Boltzmann method: Validation with analytical and experimental data, Advances in Water Resources, 116, 56-66.

Alonso, E.E., Gens, A., and Josa, A. (1990) A constitutive model for partially saturated soils. Geotechnique. 40: 405-430.

Amann, F., Thoeny, R., and Martin, C.D. (2012) Rock mechanical considerations associated with the construction of a nuclear waste repository in clay rock. Proceedings of the 46th US Rock Mechanics/Geomechanics Symposium 2012, Chicago, American Rock Mechanics Association, ARMA.

Ameli, P., Elkhoury, J.E., Morris, J.P., and Detwiler, R.L. (2014) Fracture Permeability Alteration due to Chemical and Mechanical Processes: A Coupled High-Resolution Model. Rock Mechanics and Rock Engineering 47(5):1563-1573.

Armstrong, R. T., Evseev, N., Koroteev, D., and Berg, S. (2015) Modeling the velocity field during Haines jumps in porous media, Advances in Water Resources, 77, 57-68.

Asahina, D., and Bolander, J.E. (2011) Voronoi-based discretizations for fracture analysis of particulate materials, Powder Technology, 213, 92–99.

Asahina, D., Houseworth, J.E., Birkholzer, J.T., Rutqvist, J., and Bolander, J.E. (2014) Hydro-mechanical model for wetting/drying and fracture development in geomaterials, Computers & Geosciences, 65, 13–23.

Bakker, E. (2017) Frictional and transport properties of simulated faults in CO2 storage reservoirs and clay-rich caprocks. PHD dissertation, Utrecht Studies in Earth Sciences, N°124, ISBN/EAN: 978-90-6266-4481.

Berg, S., Ott, H., Klapp, S. A., Schwing, A., Neiteler, R., Brussee, N., Makurat, A., Leu, L., Enzmann, F., Schwarz, J. O., Kersten, M., Irvine, S., and Stampanoni, M. (2013) Real-time 3D imaging of Haines jumps in porous media flow, Proceedings of the National Academy of Sciences of the United States of America, 110(10), 3755-3759.

Berton, S., and Bolander, J.E. (2006) Crack band model of fracture in irregular lattices, Computer Methods in Applied Mechanics and Engineering, 195, 7172–7181.

Biot, M.A., and Willis, D.G. (1957) The elastic coefficients of the theory of consolidation, Journal of Applied Mechanics, 24, 594–601.

Birkholzer, J., Houseworth, J., and Tsang, C. F. (2012) Geologic Disposal of High-Level Radioactive Waste: Status, Key Issues, and Trends, Annual Review of Environment and Resources, Vol 37, 37, 79-+.

Bock, H. (2009) RA Experiment - Updated Review of the Rock Mechanics Properties of the Opalinus Clay of the Mont Terri URL based on Laboratory and Field Testing, Technical Report TR 2008-04, Mont Terri Project Underground Rock Laboratory, c/- Project Manager Christophe Nussbaum, Geotechnical Institute Ltd., Gartenstrasse 13, CH - 3007 Bern / Switzerland.

Bolander, J.E., and Saito, S. (1998) Fracture analyses using spring networks with random geometry, Eng. Fract. Mech., 61, 569–591.

Bond A.E., et al. (2017) A synthesis of approaches for modelling coupled thermal-hydraulic-mechanical-chemical processes in a single novaculite fracture experiment. Environmental Earth Sciences 76(1):1-19.

Booker, J.R., and Savvidou, C. (1985) Consolidation around a point heat source. International Journal for Numerical and Analytical Methods in Geomechanics 9, 173–184.

Bossart, P., Meier, P.M, Moeri, A, Trick, T, and Mayor, J-C. (2002) Geological and hydraulic characterization of the excavation disturbed zone in the Opalinus Clay of the Mont Terri Rock Laboratory. Eng Geol 66, 19–38.

Bossart, P., Trick, T., Meier, P.M., and Mayor, J.-C. (2004) Structural and hydrogeological characterisation of the excavation-disturbed zone in the Opalinus Clay (Mont Terri Project, Switzerland), Applied Clay Science, 26, 429– 448.

Bossart, P. (2012) Characteristics of the Opalinus Clay at Mont Terri, http://www.montterri.ch/internet/montterri/en/home/geology/key_characteristics.parsys.49924.DownloadFile.tmp/characteristicsofopa.pdf.

Boulin, P. F., Angulo-Jaramillo, R., Daian, J. F., Talandier, J., and Berne, P. (2008) Pore gas connectivity analysis in Callovo-Oxfordian argillite, Applied Clay Science, 42(1-2), 276-283.

Brodsky, E.E. and Van der Elst, N.J., (2014) “The uses of Dynamic Earthquake Triggering,” Annu. Rev. Earth Planet. Sci., 42:317-339.

Cappa, F., Guglielmi, Y., Rutqvist, J., Tsang, C-F., and Thoraval, A. (2006) Hydromechanical modeling of pulse tests that measure fluid pressure and fracture normal displacement at the Coaraze Laboratory site, France, Int. J. Rock Mech. Min. Sci., 43(7):1062-1082.

Chaboche, J.-L. (1992) Damage induced anisotropy: On the difficulties associated with the active/passive unilateral condition. International Journal of Damage Mechanics 1, 148–171.

Chang, C., Ju, Y., Xie, H. P., Zhou, Q. L., and Gao, F. (2017) Non-Darcy interfacial dynamics of air-water two-phase flow in rough fractures under drainage conditions, Scientific Reports, 7.

Chiu, P. H., and Lin, Y. T. (2011) A conservative phase field method for solving incompressible two-phase flows, Journal of Computational Physics, 230(1), 185-204.

Christensen, H., and Sunder, S. (2000) Current state of knowledge of water radiolysis effects on spent nuclear fuel corrosion, Nuclear Technology, 131(1), 102-123.

Cihan, A., and Corapcioglu, M. Y. (2008) Effect of compressibility on the rise velocity of an air bubble in porous media, Water Resources Research, 44(4).

Claret, F., Marty, N., and Tournassat, C. (2018) Modeling the Long-term Stability of Multi-barrier Systems for Nuclear Waste Disposal in Geological Clay Formations, Reactive Transport Modeling.

Corey, A.T. (1954) The Interrelation Between Gas and Oil Relative Permeabilities, Producers Monthly, 38-41.

Corkum, A.G., and Martin, C.D. (2007) Modeling a mine-by test at the Mont Terri rock laboratory, Switzerland. International Journal of Rock Mechanics & Mining Sciences 44, 846–859.

Cundall, P. A. (1988) Formulation of a Three-Dimensional Distinct Element Model – Part I: A Scheme to Detect and Represent Contacts in a System Composed of Many Polyhedral Blocks, Int. J.Rock Mech., Min. Sci. & Geomech. Abstr., 25, 107-116 (1988).

Cuss, R.J., Harrington, J.F., Noy, D.J., Graham, C.C., and Sellin, P. (2014) Evidence of localised gas propagation pathways in a field-scale bentonite engineered barrier system; results from three gas injection tests in the Large scale gas injection test (Lasgit). Applied Clay Science, 102, pp.81-92, doi:10.1016/j.clay.2014.10.014Harrington J (2016) Specification for DECOVALEX-2019: Task A: modElliNg Gas INjection ExpERiments (ENGINEER). Ref: BGS-DX-v3.

Dieterich, J. H. (1979) Modeling of rock friction experimental results and constitutive equations, J. Geophys. Res., 84, 2161–2168, doi:10.1029/JB084iB05p02161.

Fakhari, A., Mitchell, T., Leonardi, C. , and Bolster, D. (2017) Improved locality of the phase-field lattice-Boltzmann model for immiscible fluids at high density ratios, Physical Review E, 96(5).

Fakhari, A., Li, Y. F. , Bolster, D., and Christensen, K. T. (2018) A phase-field lattice Boltzmann model for simulating multiphase flows in porous media: Application and comparison to experiments of CO2 sequestration at pore scale, Advances in Water Resources, 114, 119-134.

Fauchille, A. L., Hedan, S., Valle, S., Pret, D., Cabrera, J., and Cosenza, P. (2016) Multi-scale study on the deformation and fracture evolution of clay rock sample subjected to desiccation, Applied Clay Science, 132, 251-260.

Fletcher RC, Buss HL, and Brantley SL (2006) A spheroidal weathering model coupling porewater chemistry to soil thicknesses during steady-state denudation. Earth and Planetary Science Letters 244(1-2):444-457.

Garitte, B., and Gens, A. (2012) TH and THM Scoping computations for the definition of an optimal instrumentation layout in the Full-scale Emplacement (FE) experiment NAGRA NIB 10-34, March 2012.

Garitte, B., Shao, H., Wang, X.R., Nguyen, T.S., Li, Z., Rutqvist, J., Birkholzer, J., Wang, W.Q., Kolditz, O., Pan, P.Z., Feng, X.T., Lee, C., Graupner, B.J., Maekawa, K., Manepally, C., Dasgupta, B., Stothoff, S., Ofoegbu, G., Fedors, R., and Barnichon, J.D. (2017) Evaluation of the predictive capability of coupled thermo-hydro-mechanical models for a heated bentonite/clay system (HE-E) in the Mont Terri Rock Laboratory. Environmental Earth Sciences, 76:64.

Gens, A., and Alonso, E. (1992) A framework for the behaviour of unsaturated expansive clays. Can. Geotech. J. 29, 1013–1032.

Gens, A., Sánchez, M., and Sheng, D. (2006) On constitutive modeling of unsaturated soils. Acta Geotechnica. 1, 137-147.

Gens, A., Sánchez, M., Guimaraes, L.D.N., Alonso, E.E., Lloret, A., Olivella, S., Villar, M.V., and Huertas, F. (2009) A full-scale *in situ* heating test for high-level nuclear waste disposal: observations, analysis and interpretation. Geotechnique 59, 377–399.

Guglielmi, Y., Cappa, F., and Amitrano, D. (2008) High-definition analysis of fluid induced seismicity related to the mesoscale hydromechanical properties of a fault zone, Geophys. Res. Lett., 35, L06306, doi:10.1029/2007GL033087.

Guglielmi, Y., Cappa, F., Avouac, J.-P., Henry, P., and Elsworth, D. (2015a) Seismicity triggered by fluid injections induced aseismic slip, Science, 348(6240), 1224–1226, doi:10.1126/science.aab0476.

Guglielmi, Y., Elsworth, D., Cappa, F., Henry, P., Gout, C., Dick, P., and Durand, J. (2015b) In situ observations on the coupling between hydraulic diffusivity and displacements during fault reactivation in shales, J. Geophys. Res., 120, doi:10.1002/2015JB012158.

Guglielmi, Y., et al. (2015a) In Situ observations on the coupling between hydraulic diffusivity and displacements during fault reactivation in shales. Journal of Geophysical Research: Solid Earth, 120, doi: 10.10002/2015JB012158.

Guglielmi, Y., et al. (2015b) Seismicity triggered by fluid-injection-induced aseismic slip. Science, 348(6240), 1224-1226, doi: 10.1126/science/aab0476.

Gunstensen, A.K., Rothman, D.H. , Zaleski, S., and Zanetti, G. (1991) LATTICE BOLTZMANN MODEL OF IMMISCIBLE FLUIDS, Physical Review A, 43(8), 4320-4327.

Halliday, I., Hollis, A.P., and Care, C.M. (2007) Lattice Boltzmann algorithm for continuum multicomponent flow, Physical Review E, 76(2).

Harrington, J.F., and Horseman, S.T. (1999) Gas transport properties of clays and mudrocks. In: Muds And Mudstones: Physical And Fluid Flow Properties (eds A.C.Aplin, A.J. Fleet, and J.H.S. Macquaker). Geological Society of London, Special Publication No. 158, 107-124.

Harrington, J.F., Milodowski, A.E., Graham, C.C., Rushton, J.C., and Cuss, R.J. (2012) Evidence for gas-induced pathways in clay using a nanoparticle injection technique. Mineralogical Magazine. December 2012, Vol. 76(8), pp.3327-3336. DOI: 10.1180/minmag.2012.076.8.45.

Harrington, J. (2016) Specification for DECOVALEX-2019: Task A: modElliNg Gas INjection ExpERiments (ENGINEER). Ref: BGS-DX-v3.

Harrington, J.F., Graham, C.C., Cuss, R.J., and Norris, S. (2017) Gas network development in a precompacted bentonite experiment: Evidence of generation and evolution, Applied Clay Science, 147, 80–89.

Horseman, S.T., Harrington, J.F., and Sellin, P. (1999) Gas migration in clay barriers. Engineering Geology, Vol. 54, 139-149.

Horseman, S.T., Harrington, J.F., and Sellin, P. (2004) Water and gas flow in Mx80 bentonite buffer clay. In: Symposium on the Scientific Basis for Nuclear Waste Management XXVII (Kalmar), Materials Research Society, Vol. 807. 715-720.

Houseworth, J., Rutqvist, J., Asahina, D., Chen, F., Vilarrasa, V., Liu, H.H., and Birkholzer, J. (2013) Report on International Collaboration Involving the FE Heater and HG-A Tests at Mont Terri. Prepared for U.S. Department of Energy, Used Fuel Disposition Campaign, FCRD-UFD-2014-000002, Lawrence Berkeley National Laboratory.

Hu, M., Rutqvist, J., and Wang, Y. (2017a) A numerical manifold method model for analyzing fully coupled hydro-mechanical processes in porous rock masses with discrete fractures. Advances in water resources 102: 111-126.

Hu, M., Wang, Y., Rutqvist, J. (2017b) Fully coupled hydro-mechanical numerical manifold modeling of porous rock with dominant fractures. Acta Geotechnica 12(2): 231-252.

International Formulation Committee (IFC) (1967) A Formulation of the Thermodynamic Properties of Ordinary Water Substance, IFC Secretariat, Düsseldorf, Germany.

Ishibashi, T., McGuire, T.P., Watanabe N, Tsuchiya N, & Elsworth D (2013) Permeability evolution in carbonate fractures: Competing roles of confining stress and fluid pH. Water Resources Research 49(5):2828-2842.

Itasca Consulting Group, Inc. (2003). 3DEC 3-dimensional distinct element code. Minneapolis: ICG.

Itasca, FLAC3D V5.0 (2011) Fast Lagrangian Analysis of Continua in 3 Dimensions, User's Guide. Itasca Consulting Group, Minneapolis, Minnesota.

Itasca, FLAC3D V6.0 (2011) Fast Lagrangian Analysis of Continua in 3 Dimensions, User's Guide. Itasca Consulting Group, Minneapolis, Minnesota.

Jasak, H. (2009), OpenFOAM: Open source CFD in research and industry, International Journal of Naval Architecture and Ocean Engineering, 1(2), 89-94.

Jeanne, P., Guglielmi, Y., Rutqvist, J., Nussbaum, C., and Birkholzer, J. (2018) Permeability variations associated with fault reactivation in a claystone formation investigated by field experiments and numerical simulations. Journal of Geophysical Research, Volume 123, Issue 2, https://doi.org/10.1002/2017JB015149.

Jin, Z. H., and A. Firoozabadi (2015) Flow of methane in shale nanopores at low and high pressure by molecular dynamics simulations, Journal of Chemical Physics, 143(10).

Jung, Y., G. S. H. Pau, S. Finsterle, and R. M. Pollyea. (2017) TOUGH3: A new efficient version of the TOUGH suite of multiphase flow and transport simulators, Comput. Geosci., 108, 2-7.

Khalili, N, and Khabbaz, M.H. (1998) A unique relationship for χ for the determination of the shear strength of unsaturated soils, Géotechnique, 48(2), 681–687.

Khodaparast, S., Magnini, M. , Borhani, N., and Thome, J.R. (2015) Dynamics of isolated confined air bubbles in liquid flows through circular microchannels: an experimental and numerical study, Microfluidics and Nanofluidics, 19(1), 209-234.

Kim, J.-S., Kwon, S.-K., Sanchez, M., and Cho, G.-C. (2011) Geological storage of high level nuclear waste, KSCE Journal of Civil Engineering, 15(4), 721-737.

Kim, K., and Lim, Y.M. (2011) Simulation of rate dependent fracture in concrete using an irregular lattice model, Cement & Concrete Composites, 33, 949–955.

Kim, K., Rutqvist, J., Nakagawa, S., and Birkholzer, J. (2017) TOUGH-RBSN simulator for hydraulic fracture propagation within fractured media: Model validations against laboratory experiments, Computers & Geosciences, 108, 72–85

Kim, K., Rutqvist, J., and Birkholzer, J. (In preperation) Lattice modeling of excavation damage and fracture development influenced by the deformation and strength anisotropy of clay rocks, in preparation.

Kristensson, O., and Åkesson, M. (2008) Mechanical modeling of MX-80 – Quick tools for BBM parameter analysis. Phys Chem Earth, Parts A/B/C. 33, Supplement 1: S508-S515.

Lanyon, G.W., Marschall, P., Trick, T., de La Vaissière, R., Shao, H. and Leung, H. (2009) Hydromechanical evolution and self-sealing of damage zones around a microtunnel in a claystone formation of the Swiss Jura Mountains, *ARMA*, 09-333.

Latva-Kokko, M., and Rothman, D. H. (2005), Diffusion properties of gradient-based lattice Boltzmann models of immiscible fluids, Physical Review E, 71(5).

Leclaire, S., Reggio, M., and Trepanier, J. Y. (2012) Numerical evaluation of two recoloring operators for an immiscible two-phase flow lattice Boltzmann model, Applied Mathematical Modelling, 36(5), 2237-2252.

Liu, H.H., Houseworth, J., Rutqvist, J., Li, L., Asahina, D., Chen, F., and Birkholzer, J. (2012) Report on Modeling Coupled Processes in the Near Field of a Clay Repository. Prepared for U.S. Department of Energy, Used Fuel Disposition Campaign, FCRD-UFD-2012-000223, Lawrence Berkeley National Laboratory.

Maes, J. (2018) GeoChemFoam User Guide

Marone, C. (1998) Laboratory-derived friction laws and their application to seismic faulting, Ann. Rev. Earth Planet. Sci., 26, 643–696.

Marschall, P., Distinguin, M., Shao, H., Bossart, P., Enachescu, C. and Trick, T. (2006) Creation and evolution of damage zones around a microtunnel in a claystone formation of the Swiss Jura Mountains, Society of Petroleum Engineers, SPE-98537-PP.

Marschall, P., Trick, T., Lanyon, G.W., Delay, J. and Shao, H. (2008) Hydro-mechanical evolution of damaged zones around a microtunnel in a claystone formation of the Swiss Jura Mountains, ARMA, 08-193.

Martin C.D., and Chandler N.A. (1994) The progressive fracture of Lac du Bonnet Granite. International Journal of Rock Mechanics and Mining Sciences & Geomechanics Abstract, 31, 643–59.

Martin, C.D., and Lanyon, G.W. (2003) Measurement of in-situ stress in weak rocks at Mont Terri Rock Laboratory, Switzerland. International Journal of Rock Mechanics and Mining Sciences, Volume 40, Issues 7–8, October–December 2003, Pages 1077-1088.

Martino, J.B., and Chandler, N.A. (2004) Excavation-induced studies at the Underground Research Laboratory. International Journal of Rock Mechanics and Mining Sciences, 41, 1413–26.

McDermott C, Bond A, Harris AF, Chittenden N, and Thatcher K (2015) Application of hybrid numerical and analytical solutions for the simulation of coupled thermal, hydraulic, mechanical and chemical processes during fluid flow through a fractured rock. Environmental Earth Sciences 74(12):7837-7854.

McGuire, W. and Gallagher, R.H. (1979) *Matrix Structural Analysis*, John Wiley & Sons, New York.

Nguyen, T.S., Börgesson, L., Chijimatsu, M., Hernelind, J., Jing, L., Kobayashi, A., and Rutqvist, J. (2009) A case study on the influence of THM coupling on the near field safety of a spent fuel repository in sparsely fractured granite. Environmental Geology, 57, 1239–1254.

Nutt, M. (2012) Used Fuel Disposition Campaign Disposal Research and Development Roadmap (FCRD-USED-2011-000065 REV1), U.S. DOE Used Fuel Disposition Campaign.

Orellana, L. F., Scuderi, M. M., Collettini, C., and Violay, M. (2018) Frictional properties of Opalinus Clay: Implications for nuclear waste storage. Journal of Geophysical Research: Solid Earth, 123. https://doi.org/10.1002/ 2017JB014931.

Pedersen, K. (1996), Investigations of subterranean bacteria in deep crystalline bedrock and their importance for the disposal of nuclear waste, Canadian Journal of Microbiology, 42(4), 382-391.

Pedersen, K. (1999) Subterranean microorganisms and radioactive waste disposal in Sweden, Engineering Geology, 52(3-4), 163-176.

Pruess, K., Oldenburg, C.M., and Moridis, G. (2012) TOUGH2 User's Guide, Version 2.1, LBNL-43134(revised), Lawrence Berkeley National Laboratory, Berkeley, California.

Raeini, A.Q, Blunt, M. J., and Bijeljic, B. (2012) Modelling two-phase flow in porous media at the pore scale using the volume-of-fluid method, 5653–5668 pp.

Raeini, A.Q., Bijeljic, B., and Blunt, M.J. (2014) Numerical Modelling of Sub-pore Scale Events in Two-Phase Flow Through Porous Media, Transport in Porous Media, 101(2), 191-213.

Roenby, J., Bredmose, H., and Jasak, H. (2016) A computational method for sharp interface advection, Royal Society Open Science, 3(11).

Roman, S., Abu-Al-Saud, M.O. , Tokunaga, T., Wan, J.M., Kovscek, A.R., and Tchelepi, H.A. (2017), Measurements and simulation of liquid films during drainage displacements and snap-off in constricted capillary tubes, Journal of Colloid and Interface Science, 507, 279-289.

Royne, A., Jamtveit, B., Mathiesen, J., and Malthe-Sorenssen, A. (2008) Controls on rock weathering rates by reaction-induced hierarchical fracturing. Earth and Planetary Science Letters 275(3-4):364-369.

Rutqvist, J., Tsang, C.-F., and Stephansson, O. (2000) Uncertainty in the maximum principal stress estimated from hydraulic fracturing measurements due to the presence of the induced fracture, International Journal of Rock Mechanics and Mining Sciences, 37, 107–120.

Rutqvist, J., Börgesson, L., Chijimatsu, M., Kobayashi, A., Nguyen, T. S., Jing, L., Noorishad, J., and Tsang, C.-F. (2001) Thermohydromechanics of partially saturated geological media – Governing equations and formulation of four finite element models. International Journal of Rock Mechanics and Mining Sciences, 38, 105-127.

Rutqvist, J., Wu, Y.-S., Tsang, C.-F., and Bodvarsson, G. (2002). A modeling approach for analysis of coupled multiphase fluid flow, heat transfer and deformation in fractured porous rock. International Journal of Rock Mechanics & Mining Sciences, 39, 429-442.

Rutqvist, J., and Tsang, C.-F. (2002) A study of caprock hydromechanical changes associated with CO2-injection into a brine formation, Environmental Geology, 42, 296–305.

Rutqvist, J., Börgesson, L., Chijimatsu, M., Hernelind, J., Jing, L., Kobayashi, A., and Nguyen, S. (2009) Modeling of damage, permeability changes and pressure responses during excavation of the TSX tunnel in granitic rock at URL, Canada. Environmental Geology, 57, 1263–1274.

Rutqvist, J. (2011) Status of the TOUGH-FLAC simulator and recent applications related to coupled fluid flow and crustal deformations. Computers & Geosciences, 37, 739–750.

Rutqvist, J., Ijiri, Y, and Yamamoto, H. (2011) Implementation of the Barcelona Basic Model into TOUGH-FLAC for simulations of the geomechanical behavior of unsaturated soils. Computers & Geosciences, 37, 751–762.Rutqvist, J., Ijiri, Y., and Yamamoto, H. (2011) Implementation of the Barcelona Basic Model into TOUGH-FLAC for simulations of the geomechanical behavior of unsaturated soils. Computers &Geosciences, 37, 751-762.

Rutqvist, J., Davis, J., Zheng, L., Vilarrasa, V., Houseworth, J., and Birkholzer, J. (2014a) Investigation of Coupled THMC Processes and Reactive Transport: FY14 Progress. Prepared for U.S. Department of Energy, Used Fuel Disposition, FCRD-UFD-2014-000497, Lawrence Berkeley National Laboratory, LBNL-6720E (2014a).

Rutqvist, J., Zheng, L., Chen, F., Liu, H.-H., and Birkholzer, J. (2014b) Modeling of Coupled Thermo-Hydro-Mechanical Processes with Links to Geochemistry Associated with Bentonite-Backfilled Repository Tunnels in Clay Formations. Rock Mechanics and Rock Engineering, 47, 167–186.

Rutqvist, J. (2015) Fractured rock stress-permeability relationships from *in situ* data and effects of temperature and chemical-mechanical couplings. Geofluids, 15, 48–66.

Rutqvist, J. (2017) An overview of TOUGH-based geomechanics models. Computers & Geosciences, 108, 56–63.

Rutqvist J., Kim K., Xu H., Guglielmi Y., and Birkholzer J. (2018) Investigation of Coupled Processes in Argillite Rock: FY18 Progress. Prepared for U.S. Department of Energy, Spent Fuel and Waste Disposition, SFWD-SFWST-2018-000XXX, LBNL-2001168, Lawrence Berkeley National Laboratory.

Rutqvist J. and Rinaldi A.P. (2019). Fault reactivation and seismicity associated with geologic carbon storage, shale-gas fracturing and geothermal stimulation– Observations from recent modeling studies. Proceedings of 14th Congress of the ISRM, Iguassu Falls, Brazil, Sept 13 - 18, 2019.

Sánchez, M., Gens, A., do Nascimento Guimarães, L., and Olivella, S. (2005) A double structure generalized plasticity model for expansive materials. Int. J. Numer. Anal. Meth. Geomech., 29, 751–787.

Senger, R., and Marschall, P. (2008) Task Force on EBS / Gas Transport in Buffer Material, Nagra Arbeitsbericht NAB 08-24.

Senger R., Romero, E., Ferrari, A., and Marschall, P. (2014) Characterization of gas flow through low-permeability claystone: laboratory experiments and two-phase flow analyses. Norris, S., Bruno, J., Cathelineau, M., Delage, P., Fairhurst, C., Gaucher, E. C., Ho¨hn, E. H., Kalinichev, A., Lalieux, P. & Sellin, P. (eds) Clays in Natural and Engineered Barriers for Radioactive Wast Confinement. Geological Society, London, Special Publications, 400, http://dx.doi.org/10.1144/SP400.15

Shi G (1992) Manifold method of material analysis. Transaction of the 9th Army Conference on Applied Mathematics and Computing. U.S. Army Research Office.

Steefel, C.I., Appelo, C.A.J., Arora, B., Jacques, D., Kalbacher, T., Kolditz, O., Lagneau, V., Lichtner, P.C., Mayer, K.U., Meeussen, J.C.L, Molins, S., Moulton, D., Shao, H., Šimůnek, J., Spycher, N,. Yabusaki, S.B., and Yeh, G.T. (2015) Reactive transport codes for subsurface environmental simulation. Computational Geosciences 19: 445-478.

Tamayo-Mas, E., Harrington, J.F., Shao, H., Dagher, E.E., Lee, J., Kim, K., Rutqvist, J., Lai, S.H., Chittenden, N., Wang, Y., Damians, I.P., and Olivella, S. (2018) Numerical modeling of gas flow in a compact clay barrier for DECOVALEX-2019, Proceedings of ARMA/DFNE 2018 (DFNE 18-623).

Thiem, G. (1906) Hydrologische Methoden. Gebhart, Leipzig, 56p.

Thoeny, R. (2014) Geomechanical analysis of excavation-induced rock mass behavior of faulted opalinus clay at the Mont Terri underground rock laboratory (Switzerland). Thesis, Engineering Geology Geological Institute ETH Zurich Sonneggstrasse 5 CH-8092 Zurich Switzerland, www.engineeringgeology.ethz.ch

Tournassat, C., and Steefel, C.I. (2015) Ionic transport in nano-porous clays with consideration of electrostatic effects. Reviews in Mineralogy and Geochemistry 80: 287-329.

Tsang, C.F., Neretnieks, I., and Tsang, Y. (2015) Hydrologic issues associated with nuclear waste repositories, Water Resources Research, 51(9), 6923-6972.

Ulven O.I., Jamtveit, B., and Malthe-Sørenssen, A. (2014) Reaction-driven fra cturing of porous rock. Journal of GeophysicalResearch: SolidEarth 119(10): 7473-7486.

van Genuchten, M.T. (1980) A closed-form equation for predicting the hydraulic conductivity of unsaturated soils. Soil. Sci. Soc. Am. J., 44, 892-898.

Vilarrasa, V., Rutqvist, J., Blanco-Martin, L., and Birkholzer, J. (2016) Use of a dual structure constitutive model for predicting the long-term behavior of an expansive clay buffer in a nuclear waste repository. *ASCE's International Journal of Geomechanics*, 16, article number D4015005

Villar, M.V., Iglesias, R.J., and García-Siñeriz, J.L. (2018) State of the in situ Febex test (GTS, Switzerland) after 18 years: a heterogeneous bentonite barrier. Environmental Geotechnics, https://doi.org/10.1680/jenge.17.00093

Villar, M.V. (2017) FEBEX-DP Post-mortem THM/THG Analysis Report. NAGRA, August 2017.

Wan, J.M., and Wilson, J.L. (1994) VISUALIZATION OF THE ROLE OF THE GAS-WATER INTERFACE ON THE FATE AND TRANSPORT OF COLLOIDS IN POROUS-MEDIA, Water Resources Research, 30(1), 11-23.

Wang, Y. (2011) Research & Development (R&D) Plan for Used Fuel Disposition Campaign (UFDC) Natural System Evaluation and Tool Development, U.S. DOE Used Fuel Disposition Campaign.

Wang, Y., Hu, M., Zhou, Q., Rutqvist, J. (2016) A new Second-Order Numerical Manifold Method Model with an efficient scheme for analyzing free surface flow with inner drains. Applied Mathematical Modelling 40:1427–1445.

Witherspoon, P.A., Wang, J.S.Y., Iwai, K., and Gale, J.E. (1980) Validity of cubic law for fluid flow in a deformable rock fracture, Water Resources Research, 16, 1016–1024.

Worner, M. (2012) Numerical modeling of multiphase flows in microfluidics and micro process engineering: a review of methods and applications, Microfluidics and Nanofluidics, 12(6), 841-886.

Wu, K.L., Chen, Z.X. , Li, J., Li, X.F., Xu, J.Z., and Dong, X.H. (2017) Wettability effect on nanoconfined water flow, Proceedings of the National Academy of Sciences of the United States of America, 114(13), 3358-3363.

Xu, T. F., Senger, R., and Finsterle, S. (2008) Corrosion-induced gas generation in a nuclear waste repository: Reactive geochemistry and multiphase flow effects, Applied Geochemistry, 23(12), 3423-3433.

Xu, Z. Y., Liu, H.H., and Valocchi, A.J. (2017) Lattice Boltzmann simulation of immiscible two-phase flow with capillary valve effect in porous media, Water Resources Research, 53(5), 3770-3790.

Zheng, L., Rutqvist, J., Steefel, C., Kim, K., Chen, F., Vilarrasa, V., Nakagawa, S., Houseworth, J., and Birkholzer J. (2014) Investigation of Coupled Processes and Impact of High Temperature Limits in Argillite Rock. Prepared for U.S. Department of Energy, Used Fuel Disposition, FCRD-UFD-2014-000493, Lawrence Berkeley National Laboratory, LBNL-6719E.

Zheng, L., Rutqvist, J., Kim, K., and Houseworth, J. (2015) Investigation of Coupled Processes and Impact of High Temperature Limits in Argillite Rock. Prepared for U.S. Department of Energy, Used Fuel Disposition, FCRD-UFD-2015-000362. LBNL-187644, Lawrence Berkeley National Laboratory.

Zheng, L., Kim, K., Xu, H., and Rutqvist, J. (2016) DR Argillite Disposal R&D at LBNL. FCRD-UFD-2016-000437, LBNL-1006013, Lawrence Berkeley National Laboratory.

Zheng L., Kim K., Xu H., Rutqvist J., Voltolini M., and Xiaoyuan C. (2017) Investigation of Coupled Processes and Impact of High Temperature Limits in Argillite Rock: FY17 Progress. Prepared for U.S. Department of Energy, Spent Fuel and Waste Disposition. SFWD-SFWST-2017-000040, LBNL-2001014, Lawrence Berkeley National Laboratory.